Lessons learned from liquefaction of the Canterbury Earthquake Sequence (2010-2011) to inform paleoliquefaction studies

A thesis

submitted in partial fulfilment

of the requirements for the Degree of

Doctor of Philosophy

at

Lincoln University

by

Monica Giona Bucci

Lincoln University

2017

Abstract of a thesis submitted in partial fulfilment of the requirements for the Degree PhD

Lessons learned from liquefaction of the Canterbury Earthquake Sequence (2010-2011) to inform paleoliquefaction studies

By

Monica Giona Bucci

Abstract

Liquefaction affects late Holocene, loose packed and water saturated sediment subjected to cyclical shear stress. Liquefaction features in the geological record are important off-fault markers that inform about the occurrence of moderate to large earthquakes (> 5 Mw). The study of contemporary liquefaction features provides a better understanding of where to find past (paleo) liquefaction features, which, if identified and dated, can provide information on the occurrence, magnitude and timing of past earthquakes. This is particularly important in areas with blind active faults.

The extensive liquefaction caused by the 2010-2011 Canterbury Earthquake Sequence (CES) gave the geoscience community the opportunity to study the liquefaction process in different settings (alluvial, coastal and estuarine), investigating different aspects (e.g. geospatial correlation with landforms, thresholds for peak ground acceleration, resilience of infrastructures), and to collect a wealth geospatial dataset in the broad region of the Canterbury Plains.

The research presented in this dissertation examines the sedimentary architecture of two environments, the alluvial and coastal settings, affected by liquefaction during the CES. The novel aim of this study is to investigate how landform and subsurface sedimentary architecture influence liquefaction and its surface manifestation, to provide knowledge for locating studies of paleoliquefaction in future.

Two study cases documented in the alluvial setting showed that liquefaction features affected a crevasse splay and point bar ridges. However, the liquefaction source layer was linked to paleochannel floor deposits below the crevasse splay in the first case, and to the point bar deposits themselves in the second case.

This research documents liquefaction features in the coastal dune system of the Canterbury Plains in detail for the first time. In the coastal dune setting the liquefiable layer is near the surface. The pore water pressure is vented easily because the coastal dune soil profile is entirely composed of non-cohesive, very well sorted sandy sediment that weakly resists disturbance from fluidised sediment under pressure. As a consequence, the liquefied flow does not need to find a specific crack through which the sediment is vented at the surface; instead, the liquefied sand finds many closely spaced conduits to vent its excess of pore water pressure. Therefore, in the coastal dune setting it is rare to observe discrete dikes (as they are defined in the alluvial setting), instead A horizon delamination (splitting) and blistering (near surface sills) are more common. The differences in styles of surface venting lead to contrasts in patterns of ejecta in the two environments. Whereas the alluvial environment is characterised by coalesced sand blows forming lineations, the coastal dune environment hosts apparently randomly distributed isolated sand blows often associated with collapse features.

Amongst the techniques tested for the first time to investigate liquefaction features are: 3D GPR, which improved the accuracy of the trenching even six years after the liquefaction events; thin section analysis to investigate sediment fabric, which helped to discriminate liquefied sediment from its host sediment, and modern from paleoliquefaction features; a Random Forest classification based on the CES liquefaction map, which was used to test relationships between surface manifestation of liquefaction and topographic parameters. The results from this research will be used to target new study sites for future paleoliquefaction research and thus will improve the earthquake hazard assessment across New Zealand.

Keywords: liquefaction, paleoliquefaction, Canterbury Earthquake Sequence, paleoseismology, earthquake hazard, geomorphology, sedimentology, alluvial environment, coastal environment, Ground Penetrating Radar (GPR), paleoseismic trenches, radiocarbon, seismic CPT thin section analysis, Random Forest Classification

Acknowledgments

First and foremost I want to thank my PhD Supervisors Peter Almond, Pilar Villamor, Carol Smith and Martitia Tuttle. I appreciate all their contribution of time, ideas and funding to make my PhD experience very productive and stimulating. In particular, Peter and Pilar as main supervisors of this PhD project guided me through all the main steps, supporting and constructively criticizing my work to improve it and to encourage me to always do better. Peter and Pilar taught me the scientific rigor in all the phases of the PhD from the stratigraphic observation during the field works through to the logical organization of my writing. Also, Pilar has been an excellent and very patient teacher of English scientific writing. Carol taught me the fascinating aspects of the thin section analysis and she patiently supervised my work especially in the first steps of this analysis. Martitia (Tish) gave me the opportunity to help her in a very interesting field trip in the New Madrid Seismic Zone (USA) to show me impressive liquefaction features and to introduce me to the details of the liquefaction process and of the field observation. All of them have also been very helpful in revising this thesis, giving remarkable advice on the logic structure of the chapters, the clarity of the text and the bibliographic references.

The member of the Soil Department of Lincoln University have all contributed to my personal and professional time at Lincoln and in New Zealand. In particular I want to thank Roger Cresswell for his advice on the health and safety aspects of my field works, Neil Smith for his precious help during the thin section preparations and the cutting of the core tubes, and Amal Torky for her immense support and encouragement through these three years. I want to thank also other members of the GNS Science Institute in Wellington for helping during the first months of this research : Jamie Howarth and Kate Clark for assistance in core sample analysis, William Ries for GIS assistance, Ursula Cochran for diatoms analysis and Kristin Garbett for assistance in bibliographic research. I want to thank also Chris Grimshaw at Canterbury University for allowing me to use the lasersizer machine for grain size analysis.

Several people have been helping during different parts of my field works over the Summer of 2015 and 2016: Remedy Loame (Waikato University), Jody Bourgeois (University of Washington) , Kritarth

Seth, Veronica Penny, Greg Curline, Patil Yadnya (Lincoln University), Matt Watson for Ground Penetrating Radar Survey and the Fugro Team for the geotechnical analysis (CPT) presented in this dissertation. I acknowledge also the Park Supervisors of the Christchurch City Council Ian Jackson, and Dan Cameron from the Waimakariri City Council who respectively allowed our field campaign in the selected study sites.

A thank also goes to other academics from Lincoln University and outside: Miriam Hodge for her advice with the statistical software R and the compositional data analysis, Hannah Buckley and Bradley Case for their support and truly useful discussions on the Random Forest analysis explored in this dissertation, Peter Macdonald (Mc Master University) for solving questions on the use of the R package 'mixdist'.

I am sincerely grateful to Caitriona Cameron for her advice on the scientific English writing especially in the early stages of my PhD, Fiona Shannun for proof reading Chapter 3 of this thesis, and to Zoe Lopes for her friendly and discrete counselling activity and encouragement from the Student Health and Support of Lincoln University.

I gratefully acknowledge the funding sources that made my PhD work possible. I was funded by the New Zealand Natural Hazard Research Platform for the whole period of my PhD.

My time at Lincoln University was made enjoyable in large part due to new friends that became part of my life, in particular Dharini and her family, Amy, Francesco, Tihana and Yuki, and many other people who will always be part of my memories.

Most of all I am truly grateful to my family, for all their immense love and encouragement through the whole PhD journey. For my parents and my sister who tolerate the distance and my ambition to pursue a PhD, they always supported me and taught me the discipline and the self-irony to overcome Life's challenges. Thank you.

Contents

INTRODUCTION

Thesis Background

The 2010-2011 Canterbury earthquake sequence (CES) produced unprecedented extensive liquefaction throughout the Canterbury Plains. The sequence began with the Mw 7.1 Darfield earthquake on 4 September 2010. This event was caused by an unknown, blind fault near Darfield (Figure i), with a hypocentre located at depth 10 km. During the 2010 event the fault ruptured the surface along several faults including the Greendale fault (Basher et al., 2011; Quigley et al., 2012; Van Dissen et al., 2011). The sequence continued in a series of main shocks with their respective aftershocks through 2010 and early 2011 (Bannister and Gledhill, 2012). The only fatal one, the Mw 6.2 Christchurch main shock of 22 February 2011 (Kaiser et al., 2012) caused 185 fatalities and an estimated economic damage of 15-20 billion NZD (Berryman, 2012).

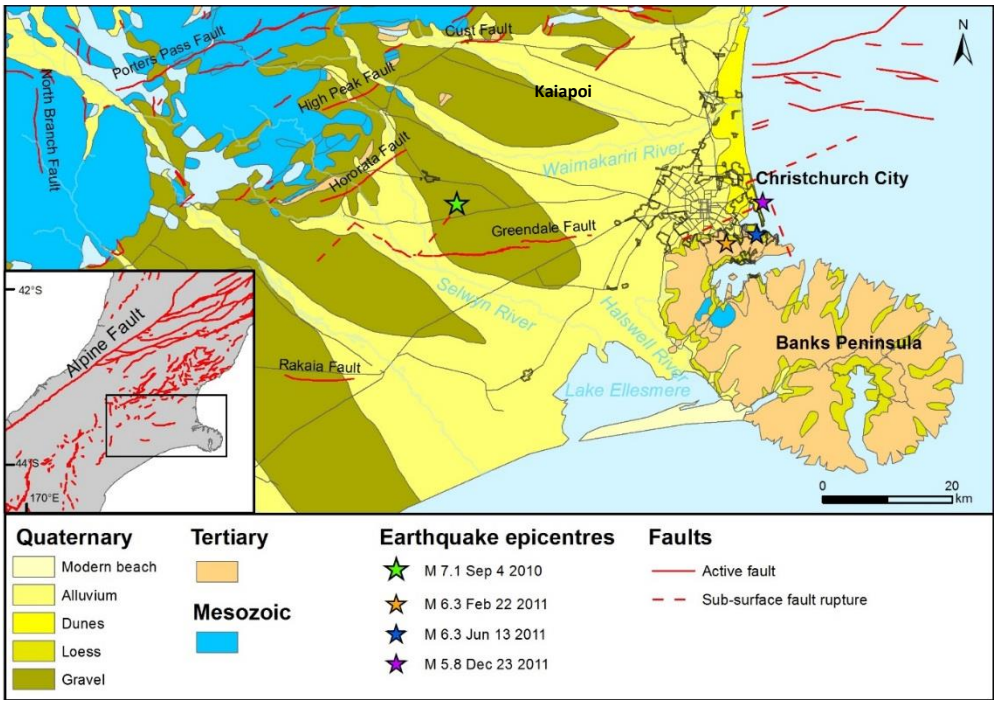

Figure i Location of the main earthquakes caused by the CES on the Canterbury Plains and geology of the Plains with the map of the main faults (from GNS Science Wellington).

None of the historical earthquakes (Fairless and Berrill, 1984) caused as wide spread and recurrent liquefaction in the wider Christchurch city area as the 2010-11 earthquakes. The greater impact during the CES was likely due to their proximity to areas of high liquefaction susceptibility. The September 2010 event was 40 km west of Christchurch (Bannister and Gledhill, 2012; Villamor et al., 2012).

Liquefaction from this event affected residential houses near waterways or streams, wetlands throughout the Christchurch city and the town of Kaiapoi (Cubrinovski et al., 2011a; 2010; 2011b; Orense et al., 2011). The 22 February 2011 event was directly under the city (Figure i) and caused extensive liquefaction and damaging landslides and rock falls in the hills (Bannister and Gledhill, 2012). Numerous large shocks and aftershock (Mw 5.5) produced localized liquefaction (e.g Quigley et al., 2013). The 13 June 2011 caused liquefaction and damage in the eastern suburbs, followed by further events of Mw 5.8 and Mw 5.9 offshore from Christchurch in December (Barnes et al., 2011), increasing the damage in the Canterbury region (Berryman, 2012). The most recent earthquake causing liquefaction in the Canterbury Plains prior to the time of submission of this thesis occurred on the 14th of February 2016 (Giona Bucci et al., 2017; Kaiser et al., 2016).

The extensive liquefaction caused by the CES provided the New Zealand and international geoscience community with a unique and valuable set of data to study new aspects of the liquefaction process, new environments affected by liquefaction, and to test new techniques for liquefaction investigations. For example, after the major liquefaction events aerial photography and LIDAR surveys (light detection and ranging) were flown in response to the earthquakes with the aim of producing detailed mapping of the liquefaction surface manifestation (for a compendium of the liquefaction mapping the reader can refer to Brackley et al., 2012; Townsend et al., 2016).

The first studies in response to the initial investigation of the liquefaction features illustrated the broad association between surface manifestation of liquefaction and geomorphic environments (Almond et al., 2012; Villamor et al., 2016; 2014; Wotherspoon et al., 2012). Also, liquefaction caused by the CES helped scientists in investigating the PGA thresholds for liquefaction surface manifestation in New Zealand (Bastin et al., 2015; Quigley et al., 2013), and in comparison to other worldwide liquefaction events (Tuttle et al., 2017).

This thesis complements the studies mentioned above by investigating the surface manifestation of liquefaction and the detailed sedimentary architecture of those settings more susceptible to

liquefaction in the Canterbury Plains, with the aim of understanding important characteristics such as source layer and/ or the higher susceptibility of certain sedimentary environments, or geomorphic elements within specific environments, to liquefaction. In order to do this, the stratigraphy of trenches excavated in the alluvial setting during a preliminary liquefaction investigation (documented by Villamor et al., 2016; 2014) is analysed in detail; the potential source layer of the liquefaction features is outlined and the characteristics of the sedimentary environment that experienced liquefaction are described by using pedological, geological and geotechnical tools. A detailed analysis of liquefaction features in the coastal setting of Christchurch and its corresponding sedimentary architecture is described and discussed for the first time in this thesis.

Amongst the techniques used for the first time to study liquefaction this thesis reports: i) an application of the 3D GPR to better target subsurface anomalies after 6 years from the earthquakes; ii) a microfabric analysis of the sediment that have liquefied in order to understand the effects of the liquefaction process also at the microscale; iii) and application of machine learning techniques, in particular a Random Forest classification as a pioneer tool for predicting surface manifestation of liquefaction in areas that may have been or may be affected by liquefaction.

The description of the features triggered in the coastal system by the serendipitous Valentine's Day Earthquake is also part of this thesis. The latter event occurred during a liquefaction field campaign to study the legacy of the 2010-2011 liquefaction features in the coastal setting of Christchurch and caused new liquefaction at our trenches. This event improved the understanding of some peculiar features recorded in the stratigraphy of the coastal setting of Christchurch.

Research aim

This thesis investigates the detailed sedimentary architecture of those settings especially prone to liquefaction and subject to the formation of liquefaction features during the 2010-2011 CES. It aims to contribute to the understanding of the liquefaction susceptibility of specific sediment types or

environments of deposition and the geomorphic setting where liquefaction features formed, in order to better predict where paleoliquefaction features might be found.

The research objectives are:

- Objective 1: Understanding correlations between soils and landforms of the Canterbury Plains and the 2010-11 CES liquefaction distribution to identify the range of geomorphic settings affected by liquefaction in the Plains. The outcome of this objective will be the selection of study sites for further detailed analysis.
- Objective 2: Characterization of subsurface sedimentary architecture and sediment characteristics at micro and macro scale at selected sites to gain better understanding of liquefaction susceptibility of different sediment types, to identify the deposits that liquefied, and evaluate factors that influenced the formation of sand dikes and blows at specific locations. An outcome of this objective will be cross sections showing the sedimentary architecture of the study sites in alluvial and coastal environments and the spatial correlation with the surface manifestation of liquefaction, along with a characterization of the source layer.
- Objective 3: Make use of the liquefaction analysis in the selected setting of the Canterbury Plains to develop a model based on microtopographic parameters of the occurrence of surface manifestation of liquefaction. The outcome will be a Random Forest classification of microtopograhic parameters to select new study sites for paleoliquefaction studies in other areas of New Zealand not recently affected by liquefaction. This quantitative classification will further support the more qualitative results gained from our analysis in response to Objective 1 and 2.

The complete study will aid in better discriminating the liquefaction susceptibility and earthquake hazard not only in the Canterbury region but all across New Zealand, improving the liquefaction susceptibility maps.

Thesis structure

This thesis is organized as a cumulative thesis, where each chapter is self-standing. After a discussion of the major literature review on the liquefaction in Chapter 1, Chapter 2 shows a geospatial analysis of the liquefaction surface manifestation during the major earthquakes of the 2010 and 2011 Canterbury Earthquake Sequence and their association with landforms and soils of the Canterbury Plains. Based on this preliminary geospatial correlation the study sites for new liquefaction investigation were selected.

A detailed pattern analysis of liquefaction surface ejection in an alluvial setting was studied in Chapter 3, with the aim of describing the detailed sedimentary architecture and sediment characteristics of a floodplain affected by liquefaction in the Canterbury Plains, and any correlation with liquefaction surface manifestation that occurred during the CES. Chapter 3 describes also the specific geomorphic features of the alluvial setting that are more prone to experience surface manifestation of liquefaction. The potential liquefaction source layer is outlined through visual inspection of cores and grain size analysis. This section is a follow-on of a pioneer and detailed liquefaction study lead by the supervisors of this PhD Thesis and documented in Villamor et al., (2016; 2014). A poster from the preliminary results of this chapter has been presented to the New Zealand Geoscience Conference 2015 (*Detailed pattern analysis of liquefaction surface ejection in an alluvial setting: lessons from the Canterbury earthquake sequence).*

A similar study to Chapter 3 but in the coastal environment is illustrated in Chapters 4 and 5. Chapter 4 is in the form of a short descriptive paper of the liquefaction event triggered by the latest Valentine's earthquake event (14th of February 2016), accepted for publications in the Terra Nova Journal. In this paper there is a detailed documentation of some unique liquefaction features characterizing the coastal setting and their genetic process. Chapter 5 describes the liquefaction features investigated for the first time in the coastal setting of the Canterbury Plains during two field campaigns (summers 2015 and 2016). Chapter 5 highlights the sedimentary architecture of a coastal setting susceptible to

liquefaction and which elements of the sedimentary architecture of the coastal sediment are more prone to liquefy.

While Chapters 3 and 5 describe the settings (alluvial and coastal) more prone to liquefaction at a macro scale, Chapter 6 documents the fabric of alluvial and coastal sediment affected by liquefaction at a microscale. The focus of this chapter is to use the sediment fabric to distinguish between modern and paleoliquefaction and to understand whether there are any differences between the liquefaction features in the different settings selected. An outline of the main findings from this chapter was presented at the New Zealand Geoscience Conference 2015, in Wellington.

The last chapter of this thesis (Chapter 7) explores a potential correlation between the microtopographic patterns associated with liquefaction surface manifestation derived from the alluvial setting analysed in Chapter 3, by using a Random Forest technique. The outcome of the Random Forest algorithm is a geospatial classification that can be applied into a new area (Manawatu Catchment- North Island of New Zealand), in order to target sites for paleoliquefaction investigation, based also on microtopographic patterns. However, the Random Forest analysis proposed is only a preliminary classification and it needs to be improved prior to being used for liquefaction susceptibility maps.

The conclusion chapter summarizes the main findings from this thesis, highlighting what are the main differences in terms of liquefaction susceptibility for the two studied environments (alluvial and coastal), and of sedimentary architectures explored in this dissertation.

Chapter 1
LITERATURE REVIEW

This literature review presents an overview of the liquefaction process to provide a basic understanding of the stresses acting in the soil and causing liquefaction. Factors influencing the liquefaction susceptibility of sediment are discussed, including sediment fabric, depth of water table, and proximity to fault. In addition, the sediment types historically most affected by liquefaction are described. Geotechnical methods most commonly used to assess the liquefaction potential of soils are alsoexplored and a brief summary of empirical relations between liquefaction and earthquake magnitude is presented. Finally, an overview is provided of the main 2010-2012 liquefaction events together with a summary of the historical earthquakes near Christchurch and throughout New Zealand.

1.1 LIQUEFACTION MECHANISMS

This section explains the stresses acting within a soil and those causing the liquefaction process.

1.1.1 Total stress and effective stress

Soil layers are naturally under stress conditions. The main stresses that act on a soil layer at a specific depth are the weight of the column of soil above it (total stress) and the weight of the water column at that depth (pore water pressure) . The intergranular stress is known in soil mechanics as effective stress and it is the stress acting at the particle-particle contact. The effective stress is the subtraction of the porewater pressure (or neutral stress) from the total stress that acts in every directions with equal intensity (Terzaghi et al., 1996) (*Equation 1.1*).

$$\sigma' = \sigma - u \qquad \textit{Equation 1.1}$$

Where σ is the total stress, u is the porewater pressure, σ' is the effective stress.

1.1.2 Stress-strain relationship in the soil

Stress and strain (soil deformation) do not exist independently in materials, but they are linked by an elastic relationship, described by the stress- strain curve. If the soil specimen experiences a big increase in shear stress, it can reach a point where the shear stress does not increase with increasing

strain. This point is the peak of stress after which the shear stress decreases substantially with larger strain . The last value of shear stress is called the ultimate strength and it represents the minimum shear stress value that the soil specimen can carry under unlimited strain (Terzaghi et al., 1996) . At this stage the particles have been ejected at the surface, and soil particles are coming in contact again and starting to form new intergranular contact to build the new effective stress.

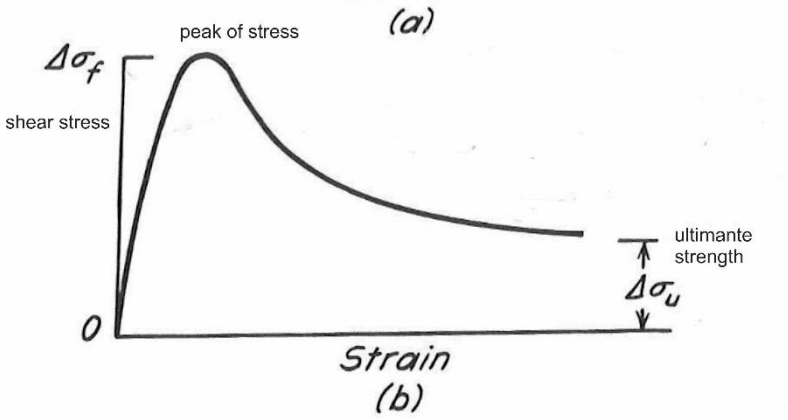

Figure 1. 1 Stress-strain curve for soil, illustrating peak and ultimate strengths modified from (Terzaghi et al., 1996)

The stress-strain curve explains the soil failure mechanism of the liquefaction process. Terzaghi (1996) defined the rapid rate of increase in pore water pressure, great loss of strength (effective stress) and large strains developed under undrained conditions as “liquefaction failure mechanism”. Several triaxial experiments have been carried out to investigate the failure mechanism of the liquefaction process. For example Castro (1969) demonstrated that the liquefaction behaviour occurs in undrained and loose sediment experiencing a contractive behaviour, in other words at a large and sudden increase of porewater pressure the sediment experiences a great loss of strength (effective stress) and a big increase of strain. For further details on the failure mechanism the reader can refer to Mohr’s rupture diagram , and to Coulomb’s equation fully explained in Terzaghi (1996).

1.1.3 Liquefaction Behaviour

Earthquakes triggering liquefaction result in a different mechanism from the monotonic process above explained. Due to the cyclic shear stress occurring during the earthquake, liquefaction can occur also at shear stress values smaller than those in a monotonic condition (Fig 1.1) but larger than those in a

drained condition (no increase in pore water pressure). Figure 1.2 shows what happens during a cyclic shear stress caused by an earthquake.

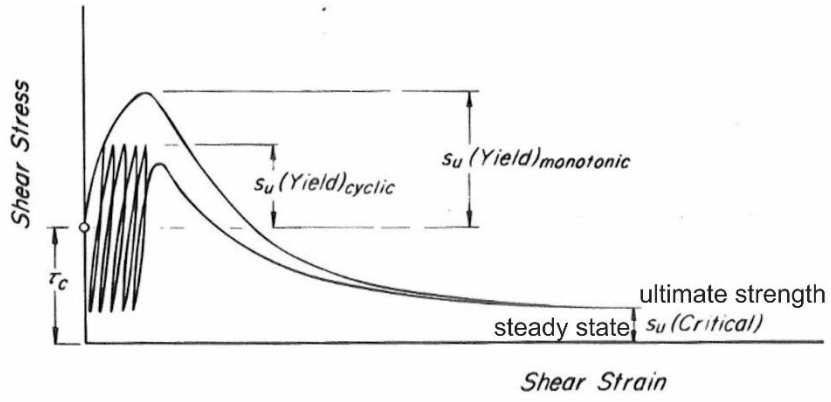

Figure 1. 2 Definition of undrained shear strength at yield and at critical condition. The figure shows the comparison between the monotonic and the cyclic stress that is for instance what happens during the earthquake shaking, modified from Terzaghi et al., 1996.

The cyclic shear stress causes different peaks. At the end of a certain number of peaks the sudden drop in shear stress with large strain causes the ultimate strength or liquefaction failure mechanism. For further details on the liquefaction behaviour the reader can refer to Castro (1969) and Casagrande (1975).

Liquefaction of sand induced by a cyclic shear stress is the most common type of behaviour. However there are other similar processes like cyclic mobility, cyclic softening or flow liquefaction (Figures 1,2 and 3 in Robertson and Wride, 1998; and Figure 1.3 in Tuttle et al., 2017). During the cyclic mobility process sand or gravel with a fines content <50% accumulate small deformation but the soil strength is not significantly reduced. Cyclic softening is a process that occur in clays and silts with a fines content >50%, causing significant deformations. Flow liquefaction occurs in sand and gravel with fines content <50% under monotonic load conditions (e.g. slope) and can cause small or large deformation.

The build-up of pore water pressure is due to cyclic shear stresses caused by the earthquake ground motions. Seed and Idriss (1982) found that the amplitude of the cyclic shear stresses and the number of cycles of shearing contribute to liquefaction. The number of cycles depends on the earthquake

magnitude. The default or reference magnitude value for liquefaction analysis in the U.S. is M.7.5, which is responsible of 15 cycles of uniform stress (Boulanger and Idriss, 2014; Idriss and Boulanger, 2004; Youd, 2001).

1.2 SUSCEPTIBILITY TO LIQUEFACTION

Unconsolidated sediment that is loosely, has a high void ratio, is in undrained conditions (water saturated) and occurs within moderate to high seismicity areas is highly susceptible to liquefaction.

1.2.1 Packing of the sediment

The packing of sediment can be expressed in different ways. A broadly used parameter is the relative density (Dr) which compares the void ratio *e* of the given soil with that of the same soil in its loosest e_{min} and densest e_{max} possible states (*Equation 1.2*) (Terzaghi et al., 1996).

$$Dr = \frac{e\ max\text{-e}}{emax - emin} \qquad \textit{Equation 1.2}$$

The packing (microstructure) of the sediment is studied by using the micromorphology technique (Bullock et al., 1985; Stoops, 1998). In this dissertation the micromorphology technique is used for the first time to study the fabric of liquefaction features, paleoliquefaction features, and undisturbed soil samples. The technique is described in Chapter 6.

1.2.2 Grain size and liquefiable sediment

Grain-size analysis provides a tool to investigate the susceptibility of sediment to liquefaction. In particular, the cumulative frequency curves of the grain size analysis of sediment hosting liquefaction layers and of sediment experiencing liquefaction can be compared with the cumulative curves issued by Tsuchida's (1970). Tsuchida's (1970) study outlined the boundary for "most liquefiable soils" and "potentially liquefiable soils" (Figure 1.3).

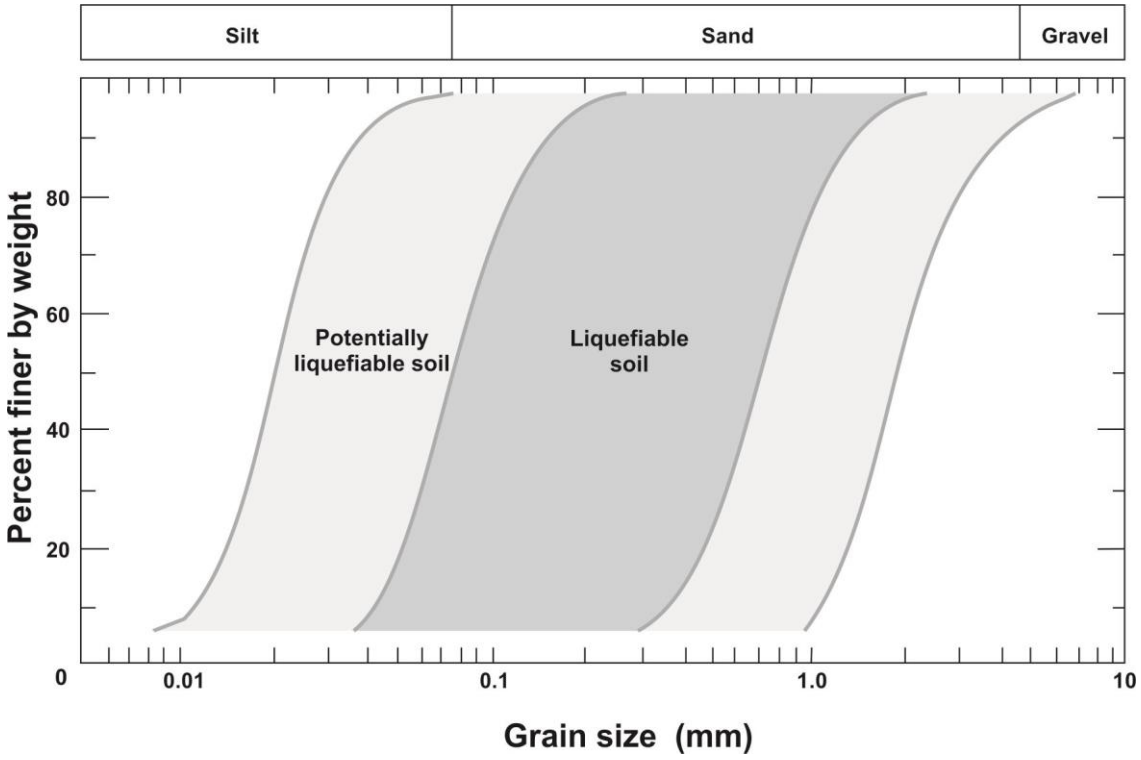

Figure 1. 3 Tsuchida's 1970 liquefaction soil boundaries cumulative curves.

Therefore, performing grain-size analysis and plotting the cumulative curves of sediment sampled at a site allows an investigator to assess their liquefaction susceptibility as well as to study characteristics of the sediment (e.g., sorting, fines content), and to infer the depositional setting, of the sediment.

1.2.3 Water Table

Ground shaking of water saturated sediment is responsible for the increase of pore water pressure during an earthquake. Several studies investigated the influence of depth to water table on earthquake-related liquefaction (Cox et al., 2012; Wang, 2007; 2010). The shallow water table for sediment susceptible to liquefaction is a critical factor also for liquefaction occurrence in the intermediate and far field from the earthquake epicentre. The current published research by Wang and Manga (2010) reports that the earthquake shaking facilitates the opening of cracks and thus some fluid passage. This results in hydrologic responses such as surface manifestation of liquefaction and changes in springs flow even far from the earthquake source.

This hypothesis is also assessed by Cox et al., (2012) analysing the Mw 7.1. Darfield earthquake hydrogeological effects. Cox, et al., (2012) documented how the earthquake increased the piezometric

levels in the unconfined and semiconfined aquifer in proximity of the earthquake epicentre (Darfield-Greendale Fault). The liquefaction in the far field (e.g. Christchurch City and Kaiapoi, 20 km north of Christchurch) and emergence of springs results from the diffusion of the artesian pressure from the intermediate to the shallow water table through fissured confined layers (Cox et al., 2012). This transmission process may help facilitate the liquefaction and spring manifestation in those areas in which there was not awareness of liquefaction hazard.

1.2.4 Cone penetration test

The Cone Penetration Test (CPT) measures the resitance to penetration of subsurface sediment and from these measurements sediment types and stratigraphy are interpreted. The CPT is often preferred to the earlier Standard Penetration Test (SPT) as it provides a nearly continuous record of sediment properties, such as tip resistance, used to assess the liquefaction resistance of soil.

Following the disastrous 1964 **M**w 9.2 Alaska and 1964 **M**w 7.6 Niigata (Japan) earthquake which caused extensive liquefaction and induced extraordinary ground failure, the liquefaction process gained the interest of the geotechnical and engineering communities. A simplified procedure for liquefaction hazard assessment was developed utilising the Cyclic Stress Ratio (CSR) and the Cyclic Resistance Ratio (CRR) (Idriss and Boulanger, 2006; 2008; Seed, 1979; Seed and Idriss, 1982; Seed and Peacock, 1971; Youd, 2001; Youd and Idriss, 1997). The Cyclic Stress Ratio (CSR) is interpreted as the seismic demand on a soil layer (*Equation 1.3)* while the Cyclic Resistance Ratio (CRR) identifies the soil capacity to resist liquefaction (*Equation 1.4*). The CRR can be determined by CPT data (Robertson, 1990).

$$(3)\ CSR = (\tau_{av}/\sigma'_{vo}) = 0.65\ (a_{max}/g)(\sigma_{vo}/\sigma'_{vo})r_d \qquad \textit{Equation 1.3}$$

Where a_{max} is the peak ground acceleration, at the ground surface generated by the earthquake, g is the acceleration of gravity, σ'_{vo} and σ_{vo} are effective and total vertical stress, r_d is the stress reduction coefficient (Youd, 2001).

$$If\ (q_{c1N})_{cs} < 50 \quad CRR_{7.5} = 0.833[((q_{c1N})_{cs}/1000] + 0.05$$

$$If\ 50 \leq (q_{c1N})_{cs} < 160 \quad CRR_{7.5} = 93[((q_{c1N})_{cs}/1000]^3 + 0.08 \qquad \textit{Equation 1.4}$$

Where q_{c1N} is the tip resistance

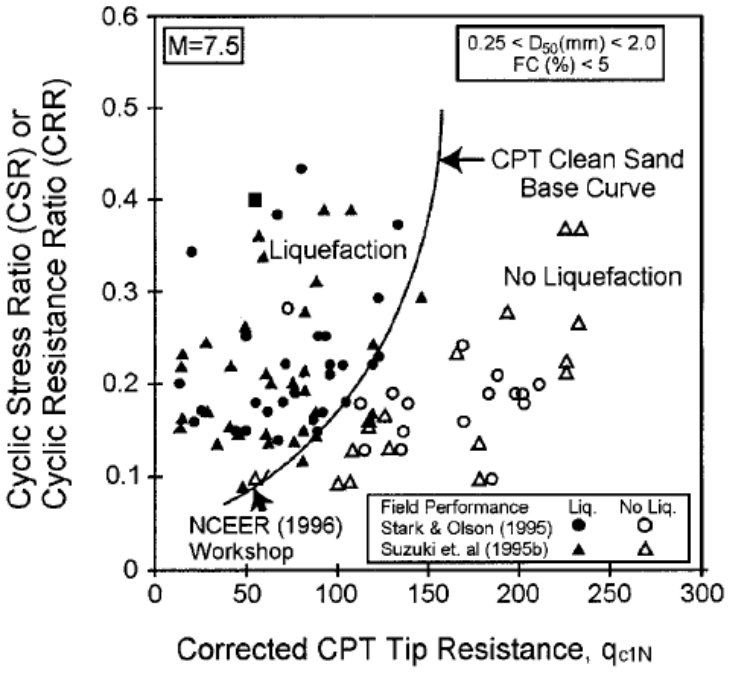

Figure 1. 4 Curve recommended for calculation of CRR from CPT data along with empirical liquefaction data from Youd (2001).

The chart in Figure 1.4 was developed by different CPT data collected including tests from Stark and Olson (1995), Suzuki (1995), Youd (2001). Figure 1.4 shows that the CRR is plotted in function of the corrected and normalized CPT resistance q_{ciN} (Youd, 2001) collected from sites were liquefaction surface manifestation was and was not observed. However, this chart is only valid for clean sand and for earthquake magnitude of 7.5.

Magnitude Scaling Factors (MSF) (Seed and Idriss, 1982) are applied in order to adjust the chart in Figure 1.4 to liquefaction susceptibility assessment triggered by earthquake magnitudes other than M7.5. The MSF are used to correct CSR for different earthquake magnitudes, and they are also important to compute the Factor of Safety (FS). The Factor of Safety is a ratio between CSR and CRR (*Equation 1.5*).

$$FS = (CRR_{7.5}/CSR)*MSF \qquad \textit{Equation 1.5}$$

When the FS is larger than 1 liquefaction is likely to occur; in contrast, when FS is less than 1 liquefaction is not likely to happen (*Equation 1.5*). For a complete review of the MSF see Youd (2001),

and Idriss and Boulanger (2006). The Factor of Safety computation is shown in the Appendix A1, in Chapter 3 of this thesis. For further correction factors useful in engineering practise see Youd (2001).

In conclusion, understanding of the soil mechanical properties through the CPT tests coupled with the magnitude of the earthquake event is critical in order to assess the liquefaction potential at a study site.

The CPT data can also be used to derive a preliminary estimation of the soil layer type. Robertson (1990, 2004) interpreted the soil type by using the CPT friction ratio (sleeve resistance fs normalized at the cone tip resistance q_c), and the normalized cone resistance. This relationship is shown in Equation 1.6.

$$Ic = [(3.47 - \log Q)^2 + (1.22 + \log F)^2]^{0.5} \qquad \textit{Equation 1.6}$$

Where $Q = [(q_c - \sigma_{vo})/P_a]/[(P_a/\sigma'_{vo})^n]$
$F = [f_s/(q_c - \sigma_{vo})] \times 100\%$

q_c is the field cone penetration resistance and is dimensionless,
P_a =1 atm
σ_{vo}= total vertical stress
σ'_{vo} is the effective vertical overburden stress
n=1.0 value for clay soil; 0.5 for sandy soils; 0.5≤n≤1 for silts and sandy silty soils

The friction ratio increases with increasing fine content of the soil, which is responsible for the soil plasticity. From the relationship expressed in Figure 1.6, Robertson derived the index Ic also known as soil behaviour type index which corresponds to the radius of an imaginary circle displayed in Figure 1.5, and calculated in *Equation 1.6*.

The resulting soil chart is not as detailed as a soil type description based on pedological characteristics but it provides a guide to the Soil Behaviour Type (SBT, Robertson, 1990, 2004). For details on the empirical calculation of the Soil Behaviour Type index the reader can refer to Youd (2001) and Robertson (1990, 2004).

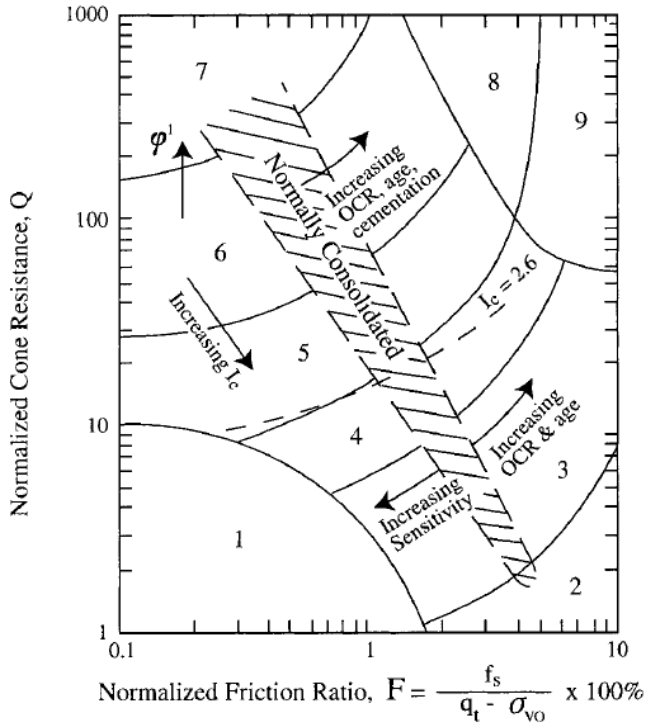

Figure 1. 5 CPT based soil behaviour type chart proposed by Robertson (1990) in which each concentric circle represents a different soil type described in the legend. This concentric area can be used to compute the different behaviour of soil on the CSR (Granted Permission for reuse from the Canadian Geotechnical Journal).

1.2.5 Seismic Cone penetration test

In the Seismic Cone Penetration Test (sCPT), a small velocity seismometer incorporated into the electronic cone penetrometer provides a combination of information for determining strength and shear modulus as well as the stratigraphy at the study site (Robertson et al., 1986).

A shear wave is generated at the surface and the geophone in the borehole measures the time for the shear wave to travel the known distance from the surface to the geophone in the borehole (Figure 1.6). The second geophone, set up vertically 1 m from the first one (in the cone penetrometer) is used to assess the variability of the arrival time[1]. The elastic theory relates the shear modulus G, soil density and shear wave velocity (*Equation 1.7*).

[1] The arrival time is defined in seismology as the length of time between the generation of the wave and it's arrival at the point of measurement .

$G = \rho V_s^2$ *Equation 1.7*

where G is the shear modulus, ρ is the soil density and V_s is the shear wave velocity

The Seismic Cone Penetration Test allows scientists to apply the Elastic Theory and define the shear modulus, knowing the shear wave modulus Vs from field measurements *Equation 1.7*. The shear modulus can be used to calculate the cyclic stress ratio (CSR), as proposed by Andrus and Stokoe (2000). Advantages to using the shear velocity (Vs) to calculate the CSR (Youd, 2001) are as follows: 1) Vs measurements are possible in gravelly soil where CPT or SPT cannot be undertaken; 2) basic soil mechanical properties are related to shear modulus; and 3) the shear modulus is a parameter estimating dynamic soil responses and soil structure interactions.

However, there are drawbacks to using the Vs for liquefaction resistance evaluation (Youd, 2001): 1) Seismic wave velocity measurements occur at small strain, whereas the pore water pressure build- up of the liquefaction process causes large strains; 2) if the measurement interval is large it will not be possible to detect low Vs; 3) there is no classification of soil derived from Vs . As a consequence, it is important to conduct geological drilling or geophysical surveys of the study site prior to the Vs measurements in order to know the location of clay lenses that can yield a Vs value very small. Also, it is critical to interpret Vs and G parameters in light of a geomorphic and sedimentary analysis. By employing both geotechnical and geological methods, it is possible to more accurately identify stratigraphic units and their properties and to better understand the mechanical characteristics of sediment prone to liquefaction.

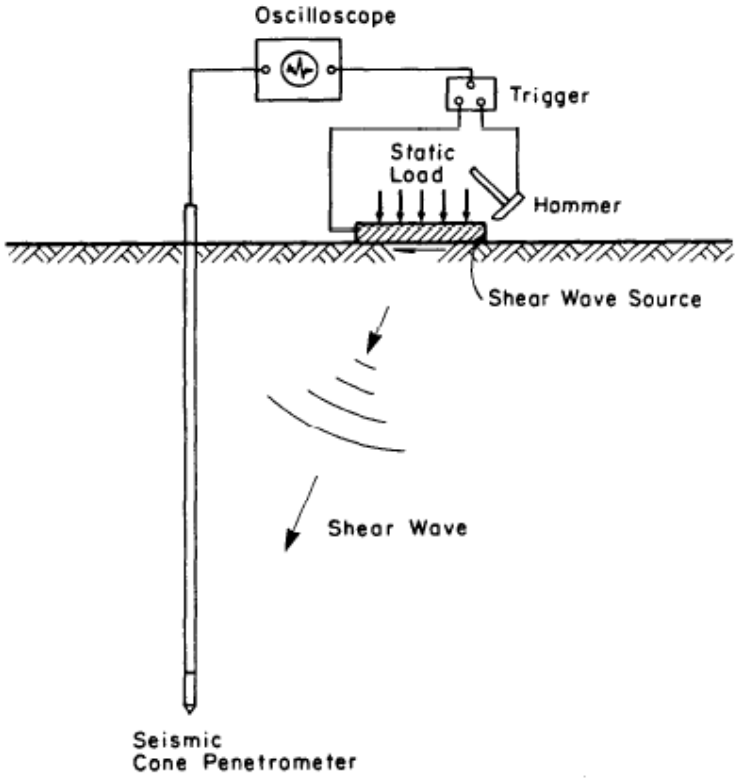

Figure 1. 6 Seismic Cone Penetration test and how it works (Robertson et al., 1986).

1.2.6 Sediment prone to liquefy

The liquefaction susceptibility of different environments of deposition has been addressed by many studies in the geotechnical literature (Bastin et al., 2015; 2016; Bray et al., 2014; Cubrinovski et al., 2011a; Holzer et al., 2010; Papathanassiou et al., 2005; Pirrotta et al., 2007; van Ballegooy et al., 2014; Youd and Hoose, 1977; Youd and Perkins, 1978). These studies highlighted that liquefaction is limited to specific geologic settings, and susceptibility is also conditioned by sediment age, as a result of the aging process. By reviewing several studies of historic earthquakes, Youd and Hoose (1977) identified the following geologic settings prone to liquefaction, ordered from the most susceptible to the least susceptible:

1) fluvial
2) deltaic
3) colluvial and aeolian
4) alluvial fan and alluvial plain, beach and terrace

Likewise, Youd and Perkins (1978) ranked different types of deposits (continental, coastal and artificial)

according to their liquefaction susceptibility, determining the likelihood of liquefaction as a function of geology and age. Later, Holzer (2010) led a study on liquefaction probability for different types of surficial geologic units across the eastern and southern United States. The units consisted of alluvial fan, beach ridge, river delta, aeolian dune, point bar, flood basin, natural river and alluvial fan levees, abandoned river channel, lake and lagoonal deposits, and sandy artificial fill. The liquefaction probability was inferred from the Liquefaction Potential Index (LPI) measured through cone penetration (CPT) tests and scaled for earthquake magnitude (MSF) and seismic demand (PGA, peak ground acceleration, see next section). The liquefaction potential index was formerly proposed by Iwasaki et al., (1978). This index estimates the liquefaction probability surface manifestation as a function of the Factor of Safety (indirect measure of the Cone penetration test, see section 1.2.4) and the depth of the potentially liquefiable layer.

Holzer's (2010) study showed that point bars and aeolian sediment were the most susceptible to liquefaction. There was no consistent variation of liquefaction probability amongst Holocene point bar deposits of different age, at a time scale less than 10,000 years. These conclusions were consistent with other studies addressing the effects of aging, such as Andrus (2009), Hayati (2008) and Youd and Perkins (1978). Youd and Perkins (1978), for instance, presented qualitative estimates of liquefaction susceptibility of soils based on field observation. They concluded that liquefaction susceptibility is high for sediment younger than 500 years; high to moderate for Holocene sediment aged <10,000 years; and very low or non-existent for Pleistocene age sediment. Then, Hayati (2008) analysed the aging effect in order to improve the accurateness of the parameter for the simplified procedure for liquefaction potential evaluation (Seed and Idriss, 1971). The geotechnical studies reviewed by Hayati (2008) (e.g. Arango et al., 2000; 1996; Lewis et al., 1999; 2004; Robertson et al., 2000; Seed, 1979) were summarized in a regression line representing the relationship between sediment strength gain versus time. This relationship showed that liquefaction resistance increased by a factor of 0.17 on a 10 log based scale of cycle of time (as showed in Figure 1.7).

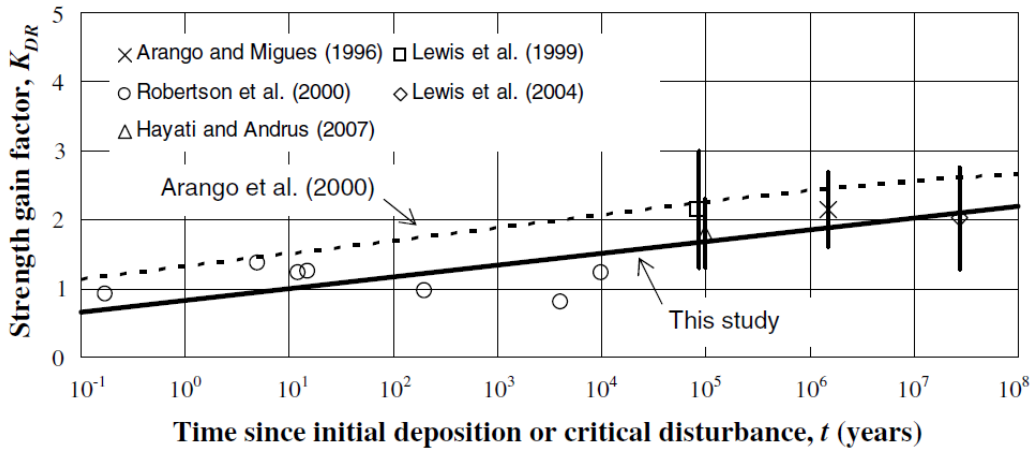

Figure 1. 7 Regression line between strength gain factor (to liquefaction susceptibility) and time by Hayati (2008)

In conclusion, as demonstrated by modern and historical cases of earthquake-induced liquefaction, Holocene aged sediment types are the most likely to liquefy.

1.2.7 Proximity to a fault system and most distal occurrence of liquefaction

Empirical relations on the distance from the earthquake epicentre to the most distal liquefaction features (sand blows) are used in paleoseismology studies in order to estimate the magnitude of paleoearthquakes. Empirical relations were developed using data from modern and historical cases of earthquake-induced liquefaction where the locations and the magnitudes of the earthquakes have been ascertained (Ambraseys, 1988; Papadopoulos and Lefkopoulos, 1993). Some studies on the empirical relations have found that the type of fault (Castilla and Audermard, 2007) or the directivity of the seismic energy (Obermeier, 1996; Tuttle et al., 2002b) can influence the size and the presence of liquefaction features at distance. Tuttle et al (2017) recommend that during reconnaissance surveys only sand blows have to be taken into account for the most distal "surface manifestation of liquefaction" rather than sand dikes. The latter can be formed more easily than the sand blow, and this will cause an over estimation of the paleoearthquake magnitude (Tuttle et al., 2017). The reconnaissance of the most distal sand blow is very often challenging and in most cases it will only be found in areas highly susceptible to liquefaction.

The paleoearthquake magnitude determined from the empirical relations are considered minimum values of the paleoearthquakes since the earthquake epicentre is not known and so the epicentral

distance to the farthest sand blow is likely to be poorly constrained (Castilla and Audermard, 2007; Tuttle et al., 2017). Therefore, seismologists prefer to use the 'energy centre' rather than the epicentre or hypocentre distances for paleoearthquakes, as it is not possible to determine an instrumental epicentre for paleoearthquakes. The distance of the "energy centre" is defined as the centroid of the region that experienced the strongest ground shaking based on regional measurements of liquefaction features size or on back-calculated strength of shaking (Olson et al., 2005a).

Many studies have aimed to reduce uncertainties in the magnitude estimates of paleoearthquakes by performing regional calibration of the magnitude distance relation (Obermeier et al., 2002; Olson et al., 2005a; 2005b). In particular, Olson (2005b) introduced the region-specific-magnitude-bound curve to account for the regional setting and its influence on the liquefaction manifestation. The accurateness of the region-specific magnitude bound curve on predicting earthquake magnitude was also tested by Green (2013) against the site specific geotechnical method (Idriss and Boulanger, 2006; Youd, 2001) using the last Canterbury Earthquake Sequence as a study case. Green's (2013) research assessed the back-calculated earthquake magnitude in two scenarios: known and unknown earthquake source location. This experiment brought to light that the magnitude-bound approach performs well when the earthquake source is known. In contrast, when the latter is unknown the magnitude-bound relations do not result in an accurate location of the earthquake epicentre and this was particularly true for the case of the liquefaction caused by the Darfield earthquake where the area most susceptible to liquefy was far from the earthquake epicentre. Therefore, it is valuable to take into account local conditions of liquefaction susceptibility for a better understanding of the paleoearthquake source, avoiding misinterpretation about the paleoearthquake magnitude.

The liquefaction caused by the last Canterbury Earthquake Sequence contributed to the databases used to develop empirical relations between earthquake magnitude and farthest distance from the epicentre of surface manifestation of liquefaction (Tuttle et al., 2017). Tuttle et al (2017) found that the CES earthquakes induced liquefaction at similar epicentral distances of earthquake of similar

magnitudes. The CES earthquakes plotted above and very close to the lower bound curve of the magnitude epicentral distance produced by Castilla and Audemard (2007) (Figure 1.8, from Tuttle et al 2017, in prep).

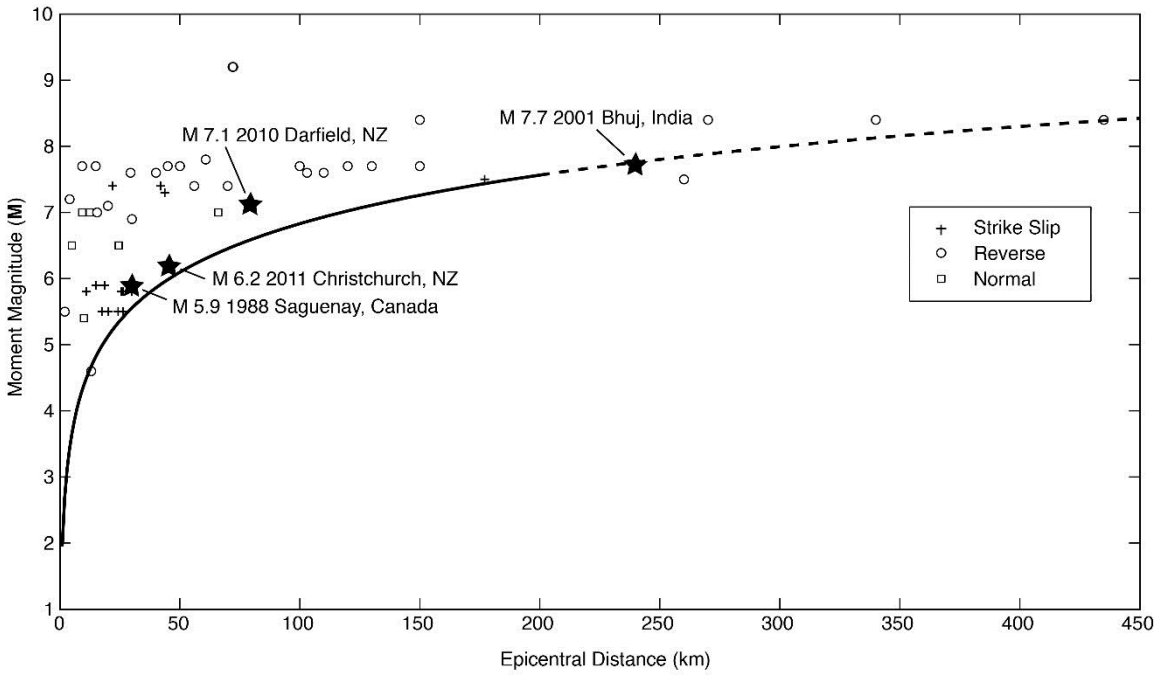

Figure 1. 8 The M 7.1 Darfield and M 6.2 Christchurch earthquakes, as well as other instrumentally recorded earthquakes that induced liquefaction, plot above the lower-bound relation between moment magnitude and epicentral distance to farthest known sand blows (after Castilla and Audemard, 2007, from Tuttle et al., 2017).

This type of analysis will benefit future paleoliquefaction investigations in the Canterbury Plains and through other regions of New Zealand.

1.3 SEDIMENT TYPES AND GEOMORPHIC FEATURES SUSCEPTIBLE TO LIQUEFACTION

In this section the fluvial and coastal dunes environments will be described in detail as they are amongst the most affected environments by liquefaction and also relevent to this research.

1.3.1 Fluvial environment

Within the fluvial environment, the geomorphic features and sediment types most affected by liquefaction are point bars, (paleo)channels and crevasse splays.

Point bar and channel are typical deposits of meander rivers (Allen, 1985; Ricci-Lucchi, 1980). Point bar deposits represent the result of a meandering river lateral migration. Point bar deposits are composed of ridges (also called scroll bars) and depressions (swales).The presence of meanders causes a perturbation in the river flow. The centrifugal force dominates at the surface, pushing the river flow towards the concave edge of the meander. Since the centrifuge force generates high pressure on the outer the meander, there is a lack of pressure on the inside or convex side of the meander. As a consequence, a water gradient is established and the water tends to move from the outer edge towards the inner bank in a sort of helicoidal shape (Figure 1.9). The centrifuge force is dominant at the surface, while the friction force is dominant on the river bed, thus the erosion acting at the surface is compensated by deposition of sandier sediment at the bottom of the meander (Ricci-Lucchi, 1980 Figure 1.9).

The sedimentary structure and the grain size showed in the diagram of Figure 1.9 and 1.10 is a result of the helicoidal movement of the water within a meander section. The grain size fines upward and the structure includes cross-bedding, parallel laminations, and cross-laminations. As the river migrates laterally, point bar deposits are accreted on the inside of the meander, resulting in a profile similar to that shown in Figure 1.9. The geomorphic expression of this sediment architecture is a series of ridges (also called scroll bars) and depressions (swales) between the ridges, both with axes paralleling the channel.

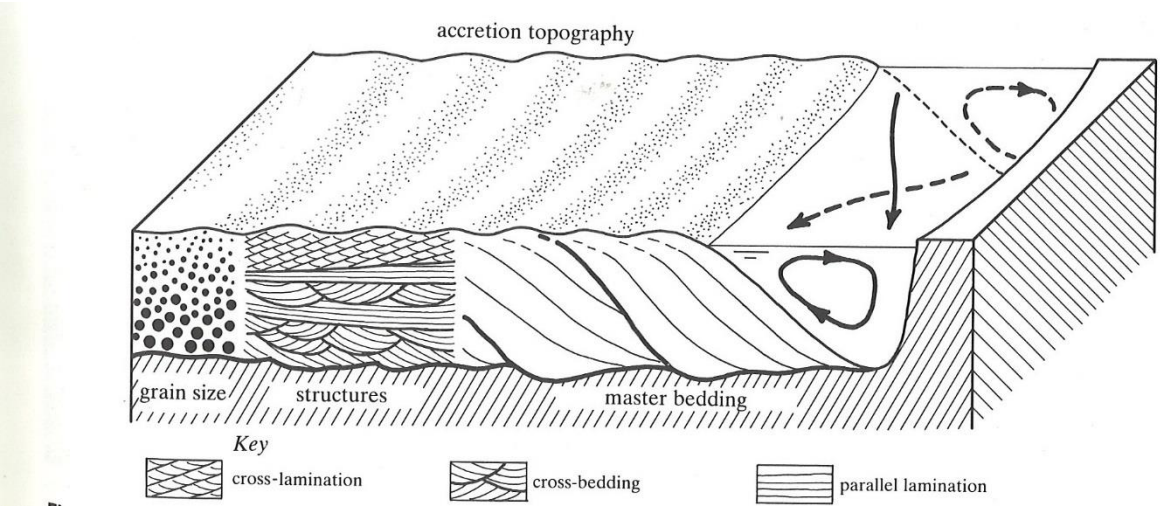

Figure 1. 9 Point bar deposit: grain size, structure and master bedding (Allen, 1985)

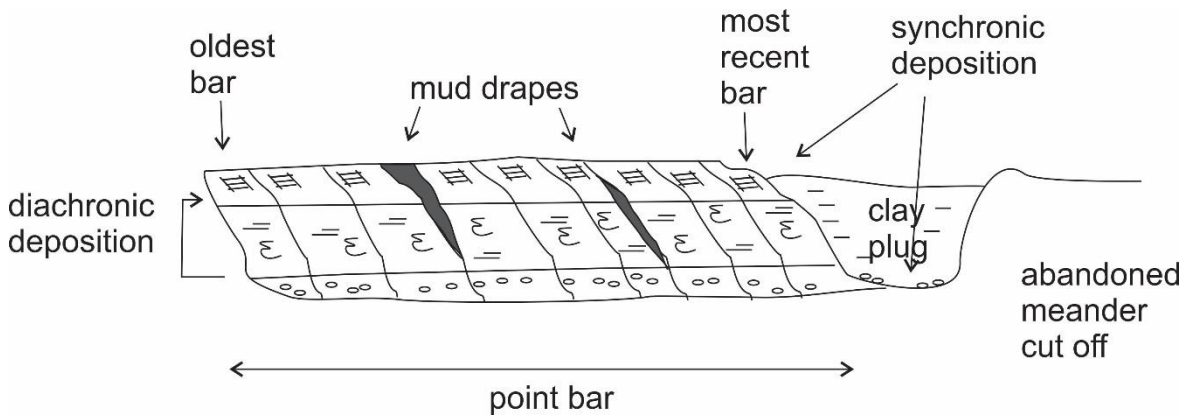

Figure 1. 10 Stratification of point bars deposits from Allen (1970), modified by Ricci-Lucchi (1980). Note how the sediment deposited between two different bars result from a synchronic deposition while the sediment deposited within the same bar result from a diachronic deposition.

In the literature, point bar channel, deltaic, and beach deposits have been the sources of liquefaction and paleo liquefaction features (Amick et al., 1990; Civico et al., 2015; Reid et al., 2012; Tuttle, 1999; Villamor et al., 2016; 2014; Wotherspoon et al., 2012). A good example of the correlation of sand blows and point bars comes from the New Madrid Seismic Zone (NMSZ) in the central U.S. (Tuttle, 2001a Figure 1.11) where sand ejected at the surface appears to be strongly influenced by the curved shape of the underlying point bar deposits.

Figure 1. 11 1964 Aerial photos taken by USDA (U.S. Department of Agriculture) showing light coloured sand blow deposits near the Left Head Chute of Little River that follow scroll bars and natural levee (from Tuttle, 2001a)

Other examples of point bar deposits being prone to liquefaction and the source of sand blows are documented in the literature (Alessio et al., 2013; Almond et al., 2012; Bastin et al., 2015; Berrill et al., 1994; Civico et al., 2015; Fontana et al., 2015; Holzer et al., 2010; Villamor et al., 2016; 2014; Wotherspoon et al., 2012).

Paleo meander channel deposits are abandoned channels caused by river avulsion. The river avulsion can be triggered when the erosion of the outer part of the channel narrows the river neck, eventually breaking through to another portion of the channel and abandoning a portion of the old channel. Over time, the abandoned channel fills in with clay and over bank deposits from the active river. These fine-grained deposits preserve the paleochannel morphology. River avulsion can be a sudden or gradual process, which would result in two different stratigraphic sequences (Ricci-Lucchi, 1980; Figure 1.12).

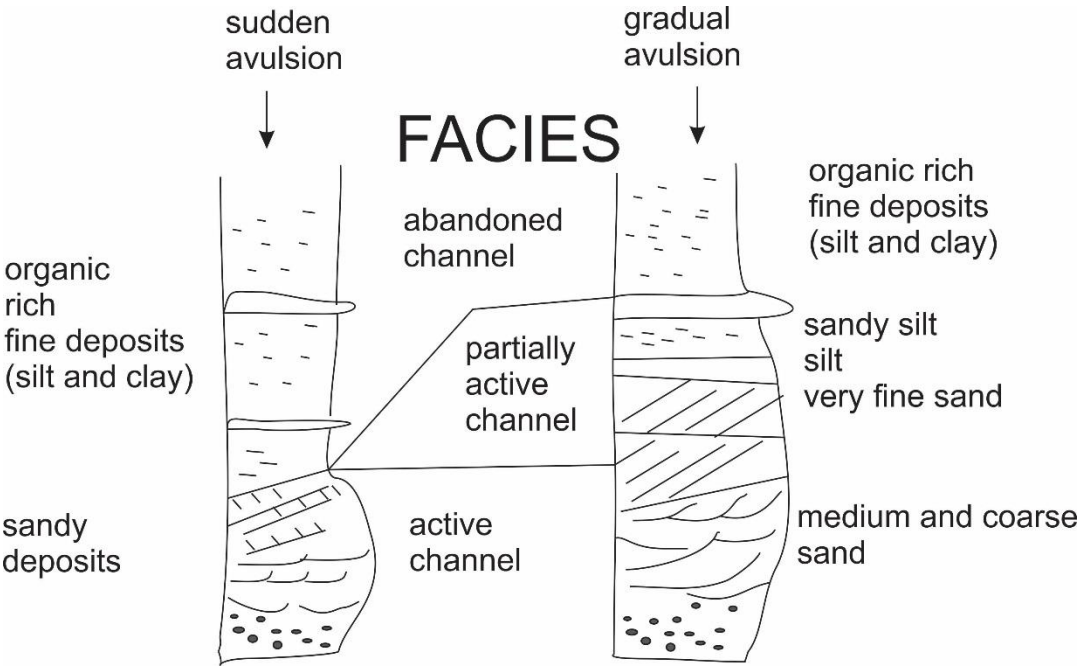

Figure 1. 12 Example of abandoned meander stratigraphy after a quick avulsion or a gradual avulsion, modified by Ricci-Lucchi (1980).

Crevasse splays form during flood events when the river breaches the natural levee creating a fan-shaped deposit. The thickness of crevasse splay can vary but it is usually at least 30 cm. The grain size of crevasse splays is coarser in close proximity of the river and fines away from the river. Presence of pebbles and lack of laminations also characterizes the crevasse splay (Ricci-Lucchi, 1980). Documentation of association between liquefaction surface manifestation and crevasse splay can be found in Villamor (2016; 2014),De Martini (2015) and Civico (2015).

1.3.2 Coastal Environment

The coastal dune setting is characterized by aeolian sedimentation. The sand requires a decrease in wind velocity, in order to be deposited. In a natural coastal environment, wind velocity reduction occurs beside obstacles such as shells, pebbles, and organic debris along the high tide line. According to local wind conditions, sand accumulation as dunes can quickly develop characterized by an upwind gentle slope and a steeper slope on the lee side (Haslett, 2009).

The formation of a coastal dune system requires a single foredune system (Figure 1.13) that is an early dune bridge formed by coalescing embryo dunes, running along the back of the beach (Haslett, 2009).

The morphodynamics of the dune system is also influenced by the amount and the nature of the sediment supplied from the source beach.

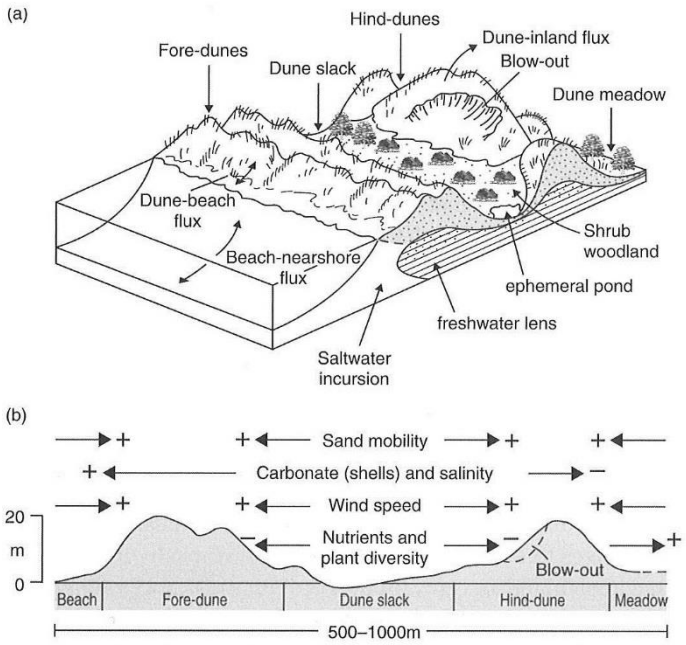

Figure 1. 13 a) Geomorphology of a coastal dune system; b) distribution and influence of the coastal sand dune setting of some environmental parameters (Haslett, 2009).

Depressions between the different crests are called interdune depressions or dune slacks. Here, the water table is shallow and water ponding can occur. In the Jurassic Navajo Sandstone, sand blows have been found in interdune depressions (Bryant et al., 2013; Chan and Bruhn, 2014). Bryant et al. (2013) concluded that sand blows formed in the interdune depressions as a consequence of subsidence related to massive outflow of fluidized sand (Figure 1.14).

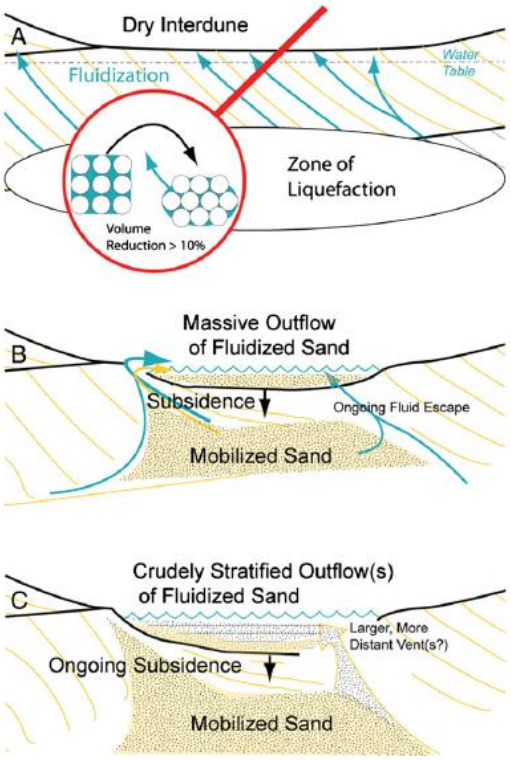

Figure 1. 14 Liquefaction flows in the interdune deposits and pond formation as a consequence (Bryant et al., 2013), permission granted from Sedimentary Geology.

However, a different geomorphic evidence of liquefaction in the dune setting is documented by Chan and Bruhn (2014), showing that the liquefaction flow created a relief inversion (as illustrated in Figure 1.15). In this scenario, sand liquefies below dunes and interdune, but sand blows form in the interdune area where there is less overburden and the water table is shallower.

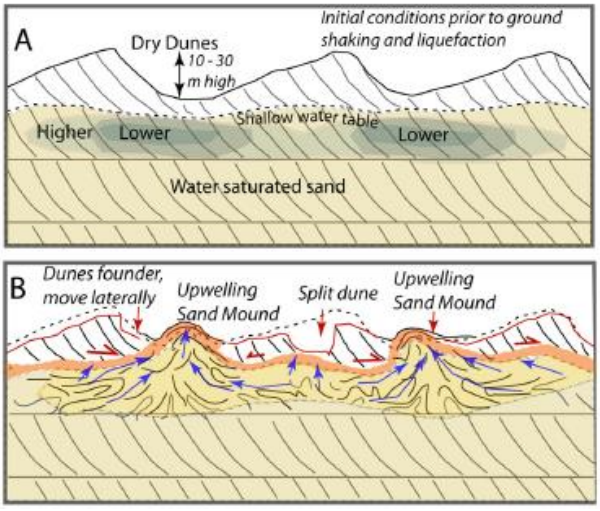

Figure 1. 15 Liquefaction model A) Dry dune conditions and Water table; B) Under strong ground motion the saturated sand liquefied and it comes up forming upwelling sandy mounds. The authors also found out that the lateral spreading was parallel to the dune crest (from Chan and Bruhn, 2014), permission granted for reuse from Earth Surface Processes and Landforms.

Liquefaction manifestation in the coastal setting has also been documented in the eastern of the United States (Amick et al., 1990; Talwani et al., 1999; Talwani and Schaeffer, 2001) however it has not been identified a specific association with a geomorphic feature of the interdune field but instead with the barrier beach setting.

In conclusion, the interdune depressions (lower topographic point in the local geomorphology) are considered the most susceptible geomorphic features to liquefy within the dune setting, due to the shallow groundwater as a driving force. Whereas, in the fluvial setting liquefactions features have been associated with point bars that are higher local topographic points instead of lower topographic points. This means that liquefaction manifestation is not only influenced by overburden pressure (i.e. where there is less overburden pressure there is more surface manifestation of liquefaction) but also by peculiar local topographic conditions that enable the liquefaction flow to be ejected at the surface.

1.3.3 Types of liquefaction features in alluvial and coastal setting

A variety of liquefaction features occur in coastal and fluvial settings.

Sand blows (also named sand boils or sand volcanos)

In the alluvial setting, sand blows are sandy mounds with a sub-rounded shape and a venting area through which water and entrained sediment flow onto the ground surface. The sand blows can vary in size according to the setting where they occur and the magnitude of the earthquake. If they occur above a point bar deposit or along a fissure related to lateral spreading they tend to be elliptical to linear in plan view. The sediment carried to the ground surface varies and depends on the composition of the layer that liquefied and the velocity of the venting water. Generally, sand blows that formed during one event fine upward and fine and thin away from the vent area, though there can be complexities related to pulsing during an event or erosion of channels in the sand blow and deposition of subsequent fans (Tuttle, 1999; Tuttle et al., 2017). If there is standing or ponded water following the episode with fines in suspension, the fines will precipitate out over a period of hours to days to form a silt or clay layer over the sand blow (Tuttle, 1999). The silt or clay layers represent a period of quiescence between events. Compound sand blows thought to have formed as the result of multiple

earthquakes have been documented near the San Andreas fault in central California, in the New Madrid seismic zone in the central U.S, and in the Canterbury area following the CES. In California, the compound sand blows formed during the 1989 Loma Prieta earthquake and aftershock (Sims and Garvin, 1995). In the New Madrid seismic zone, compound sand blows separated by clay layers formed during the 1811-1812 earthquake sequence (Saucier, 1989) and during previous sequences circa A.D. 1450, A.D. 900, and B.C. 2350 (Tuttle, 2010; 2002b). In the Canterbury area, compound sand blows separated by silt layers were documented in Christchurch (Quigley et al., 2013) and near Lincoln (Tuttle et al., 2012 and 2017).

Polygenetic sand blows have also been documented (Rodriguez-Pascua et al., 2015; Tuttle, 2010; Tuttle et al., 2002a), caused by long lasting ground waving and sloshing experienced during an earthquake sequence (Cubrinovski et al., 2010; Yasuda et al., 2012). In particular, these features have been discovered following the most recent Mw 6.3 Christchurch Earthquake 2011 , the Mw 9 2011 Great East Japan Earthquake (Earthquake, 2011) the Mw 5.9 2012 Emilia Romagna Earthquake (Alessio et al., 2013; Chini et al., 2015), and the **Mw** 7.7 2001 Bhuj, India earthquake (Tuttle et al., 2002a). Rodriguez-Pascua (2015) suggested that a single earthquake can trigger polygenetic sand blows due to the undulation of the ground causing several eruptions of sand. Polygenetic sand blows fine upwards as the compound sand blows but the different phases are not separated by silt and clay (Figure 6 B in Rodriguez-Pascua et al., 2015). An effective summary on the formation of polygenetic sand blows is provided in Figure 1.16.

The characteristics of compound and polygenetic sand blows are important in the interpretation of the stratigraphic profile of sand blows in order to assess the number, locations, and magnitudes of paleo-earthquakes.

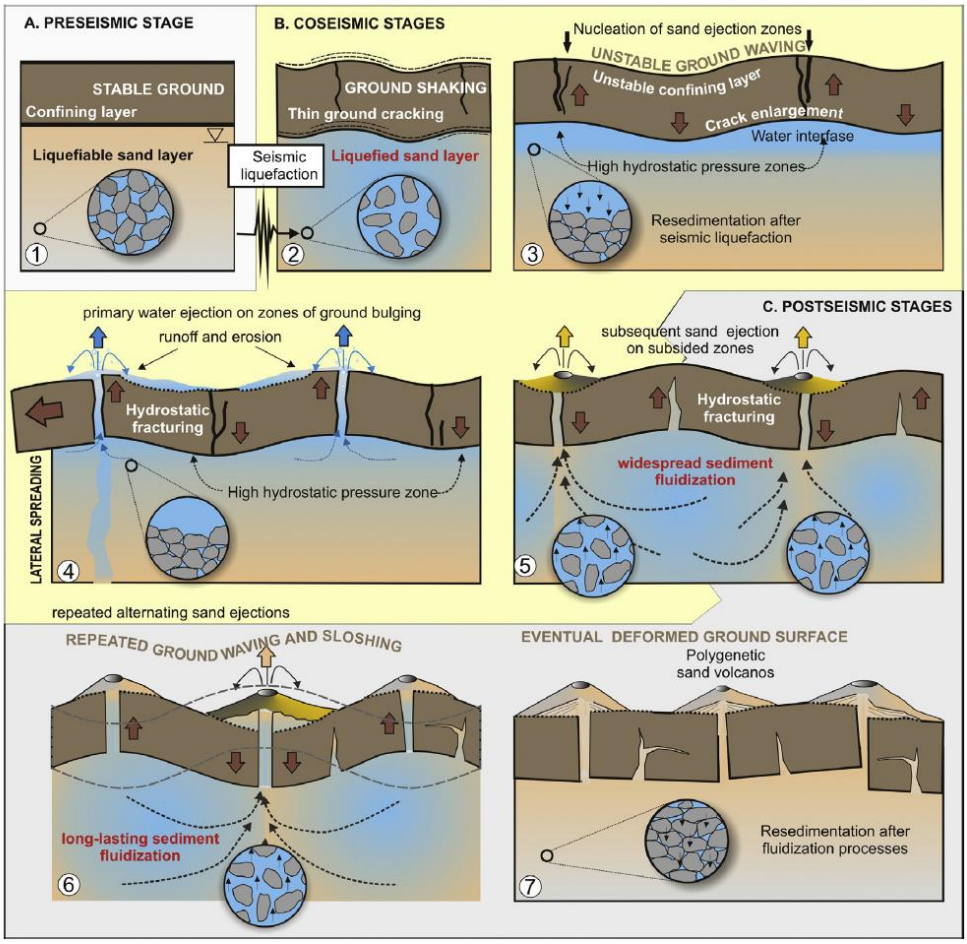

Figure 1. 16 Formation of polygenetic sand blows during the Mw 5.9 Emilia Romagna earthquake (Italy) from (Rodriguez-Pascua et al., 2015). Permission granted from Quaternary International Journal for reuse.

Dikes

Dikes (or neptunian-dikes) are water escape features resulting from earthquake-induced liquefaction, that cross-cut sediment and soil layers. If the dikes reach the ground surface, they are the conduits through which water and sediment travel to the surface, forming sand blows. The grain-size of the sediment carried by a dike depends on that of the layer that liquefied. The dike borders are clearly visible due to the contrast in grain size and sediment weathering with the in situ stratigraphy. Within the dike, some rip up clasts are often visible. The overall colour of liquefaction features, in particular dikes is often gray (or gleyed), indicative of the water saturated condition of the source layer.

Rip up clast

Rip up clasts are fragments of the soil layers disrupted by the liquefaction and dragged in the liquefaction flow.

Sills

Sills are liquefaction dikes injected parallel to the in situ stratigraphic layers.

Blisters

Blisters are subsurface pop-up caused by sills and dikes injected close to the surface (Figure 1.17). Occasionally sand blows form around the base of the mound if the sand dikes reached the surface. Villamor (2014) documented the first example of blisters in the alluvial setting of the Canterbury Plains.

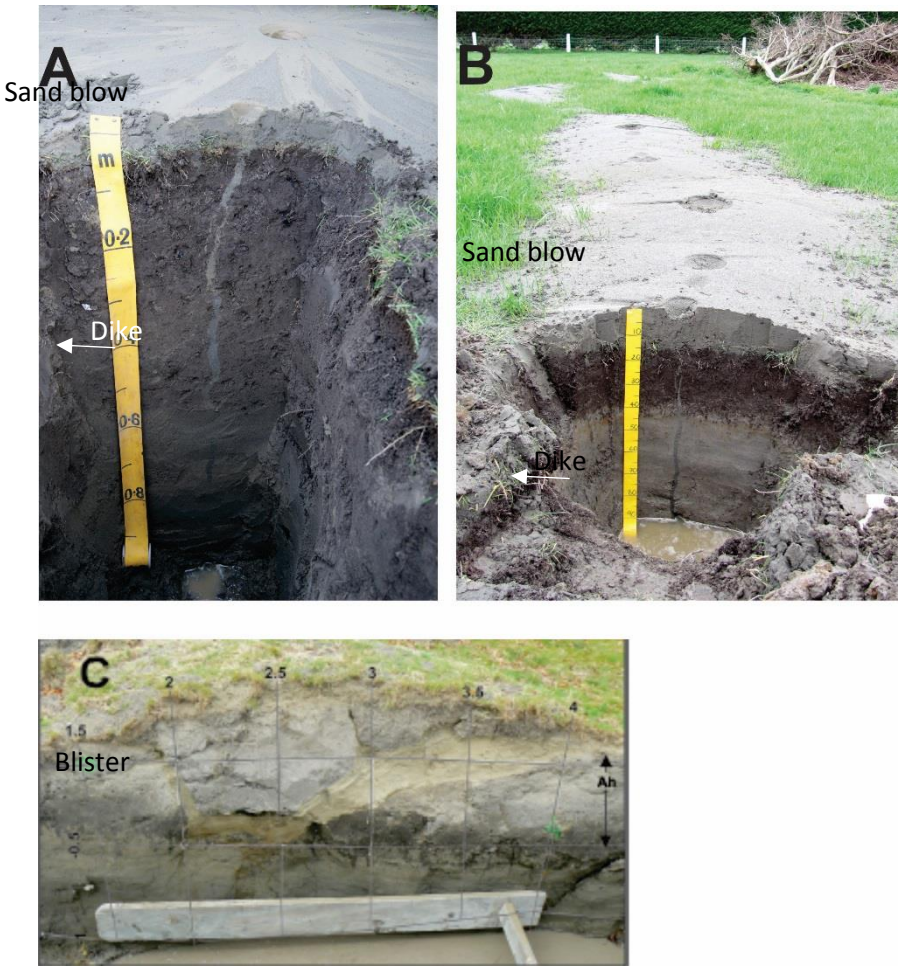

Figure 1. 17 Liquefaction features: a) sand blow and feeder dike; b) sand blow characterized by an elongated shape and corresponding feeder dike-photo credits by Fiona Shannun; c) blister and (yellow sandy sill) from Villamor 2014

In the coastal setting, sand blows explosive craters have been observed and documented by Amick (1990). The exceptionality of these features is imputed to the particular liquefaction susceptibility of the coastal setting (Amick et al., 1990) but also to the possible presence of gas, as discussed by Rydelek and Tuttle (2004) who documented an explosive crater at a site of liquefaction during the Bhuj, India,

earthquake. A diagram showing the four formation phases of the explosive crater is showed in Figure 1.18.

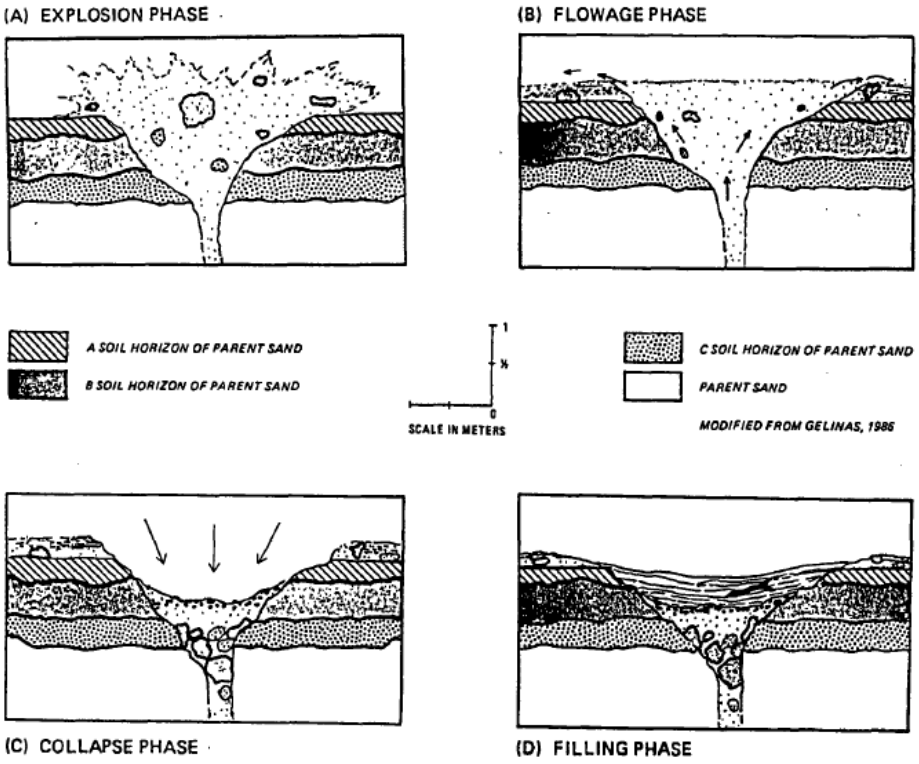

Figure 1. 18 Diagram on the formation of sand blows-explosive craters for more details see Amick (1990)

1.4 HISTORIC LIQUEFACTION AND TYPES OF LIQUEFACTION FEATURES IN NEW ZEALAND

1.4.1 Evidence of liquefaction features across New Zealand

Prior to the Canterbury Earthquake Sequence, there have been more than 30 accounts of liquefaction-related phenomena caused by 10 earthquakes, accompanied by sand blows and water ejection, landslides, foundation failures and flotation of light structures throughout New Zealand since 1843 (Fairless and Berrill, 1984 Figure 1.19). However, this review does not include liquefaction caused by the Edgecumbe earthquake 1987 (Christensen, 1995) and the M_L 6.5 Cook Strait Earthquake of 21 July 2013 (Hancox et al., 2013; Van Dissen et al., 2013).

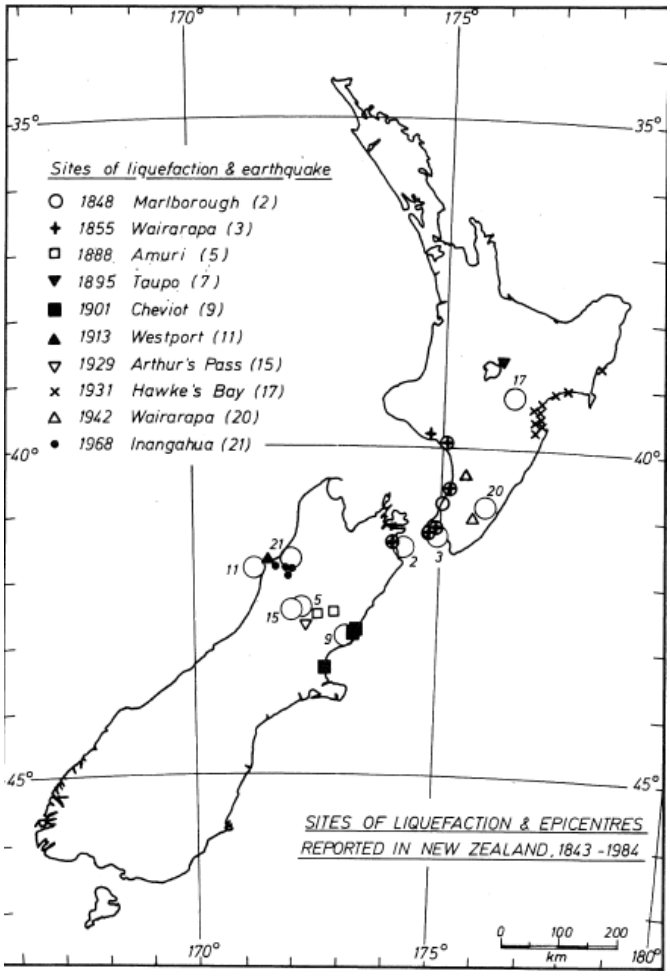

Figure 1. 19 Liquefaction reported throughout New Zealand before the 2010-2011 Canterbury Seqyence. From (Fairless and Berrill, 1984)

A later review of historical earthquakes was undertaken by Downes (2012) based on a Hazard and Risk Assessment Study commissioned by Environment Canterbury (in 1999) and later reported in Stirling (1999; 2001) and Pettinga (2001). That review focussed on the 1869 Christchurch Earthquake

and on the 1870 Lake Ellesmere Earthquake. The magnitude of the 1869 Christchurch earthquake was between 4.5 and 6, while the magnitude of the 1870 Lake Ellesmere earthquake was about 6.5. These two earthquakes were the only evidence of the presence of hidden faults under the Holocene alluvial Plain of the Canterbury Plains before the 2010-2011 Canterbury Earthquake Sequence showing the potential effects of moderate but damaging shaking within the region (Downes and Yetton, 2012). This review brought to light that the 1869 Christchurch earthquake epicentre was located within the Darfield 2010 aftershocks distributed area highlighted by Bannister (2011). A similar relationship was not identified for the 1870 Lake Ellesmere Earthquake and further research is needed also to study other small or moderate earthquakes (e.g. 1895 earthquakes) which might corroborate the presence of other hidden faults beneath the Canterbury Plains. A review of these minor historical earthquakes can be found in Stirling (2008).

The review of historical earthquakes found that liquefaction has recurred at sites underlain by fine, loose sediment and that earthquake hazard assessment within the Canterbury Plains needs to be improved due to the presence of hidden faults beneath Holocene alluvial sediment. In addition, it is highly that the liquefaction was more widespread than documented by Fairless and Berrill (1984) due to the small population and the lack of local reports and investigation in rural areas.

Also, other liquefaction features were discovered by studying the Haast (Berryman et al., 2012) and the Kerepehi faults (Persaud et al., 2016). In both cases, paleoliquefaction features were recognized in the complex stratigraphy along the fault, used to assess the magnitude of the paleoearthquake at the study site, and to corroborate the fault rupture.

Following the CES, other New Zealand regions were targeted for liquefaction and paleoliquefaction investigation, such as Hamilton Region (Kleyburg et al., 2015) and Palmerston North area (Beetham et al., 2011; Dellow et al., 1994).

1.4.2 Liquefaction studies of the Canterbury Earthquake Sequence

The 2010-2011 Canterbury earthquake sequence (CES) induced or triggered liquefaction during the main shocks and aftershocks (Bastin et al., 2015; Quigley et al., 2013; Villamor et al., 2016).

Liquefaction ejecta affected residential houses near waterways or streams, wetlands throughout Christchurch city and the town of Kaiapoi (Brackley et al., 2012; Orense et al., 2011; Townsend et al., 2016). The liquefaction map from aerial photos recorded in the New Zealand Geotechnical Database (CGD0200, 2013) reveals the liquefaction extent in consequence of the main shocks of September 2010, February 2011 and aftershocks of June 2011 (Figure 1.20 A, B, C). Then, in December 2011 two new earthquake events occurred offshore with Mw 5.8 and Mw 5.9 causing new liquefaction (Figure 1.20D). The liquefaction extent varies in function of the earthquake magnitude and the distance from the epicentre, but also as a function of depth to water table and sedimentary facies. Since the Canterbury Earthquake Sequence was characterized by different earthquakes, each with a different epicentre (Bannister and Gledhill, 2012; Beaven et al., 2011; 2012; Quigley et al., 2012; Villamor et al., 2012), the liquefaction extent was different at each event. The sequence continued in a series of aftershocks through 2010 and early 2011 and beyond with the Valentine's Day earthquake in February 2016.

Figure 1. 20 Liquefaction surface manifestation in consequence of the Canterbury Earthquake Sequence 2010-2011 A) September 2010, B) February 2011, C) June 2011, D) December 2011 Map downloaded from the Canterbury Geotechnical Database now renamed New Zealand Geotechnical Database, first download April 2014.

1.4.3 Documentation of Paleoliquefaction features in Christchurch

Initial liquefaction investigations were undertaken soon after the 4 September 2010 Darfield earthquake (Almond et al., 2010a; 2012; Bastin et al., 2015; 2016; Brackley et al., 2012; Quigley et al., 2013; Townsend et al., 2016; Tuttle et al., 2012; Villamor et al., 2016; 2014).

During the preliminary CES investigations of the modern liquefaction features, paleoliquefaction features were identified. Two study sites close to the Halswell River at Greenpark (~28 Km south-west of Christchurch) were selected, in order to investigate the modern liquefaction features and to look for past evidence of liquefaction. The Hardwick site was characterized by an old channel overlain by a crevasse splay, and the Marchand site was characterized by point bar deposits. In two of the eleven

trenches dug between the two sites there was evidence of liquefaction events older than the 2010-2011 Canterbury Earthquake sequence (Paleoliquefaction)(Villamor et al., 2016; 2014). The old features were discriminated by oxidized contours and bioturbation. Also, the cross cutting relationship of modern dikes intruding the old ones proved that prior to the 2010-2011 there was at least one (paleo) liquefaction event.

In particular at the Hardwick site (Figure 1.21) the paleofeatures described included feeder dikes and a related sand blow partially eroded and subsequently buried by a crevasse splay, which was deposited on top of the sand blow. The erosion affecting the sand blow revealed that the feature was exposed to natural weathering before being covered by the crevasse splay. At this site, paleoliquefaction features were dated between AD 908 and AD 1336 (Almond et al., 2012; Villamor et al., 2016; 2014).

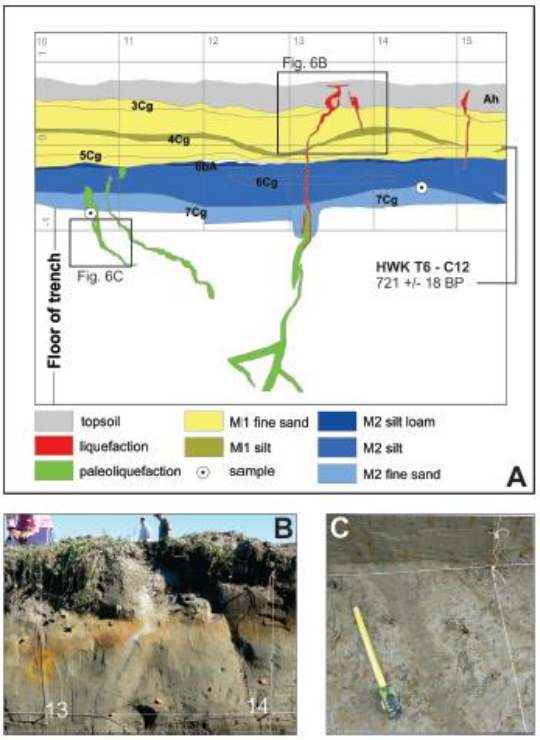

Figure 1. 21 Documentation of Paleoliquefaction at Hardwick site A) Detail of the trench's log showing the soil background, liquefaction and paleoliquefaction; B) Picture of Modern liquefaction (CES); C) Picture of old liquefaction dike coming through the trench's floor (from Villamor et al., 2014).

At the Marchand site (Figure 1.22) the paleoliquefaction features found were weathered sand dikes formed between AD 1017 and 1840 (Almond et al., 2012; Villamor et al., 2016; 2014). Similar to the Hardwick site, the CES sand dikes crosscut the older sand dikes. Further details on the Hardwick and

Marchand study sites and the liquefaction study are in Chapter 3 of this thesis (Almond et al., 2012; Villamor et al., 2016; 2014) .

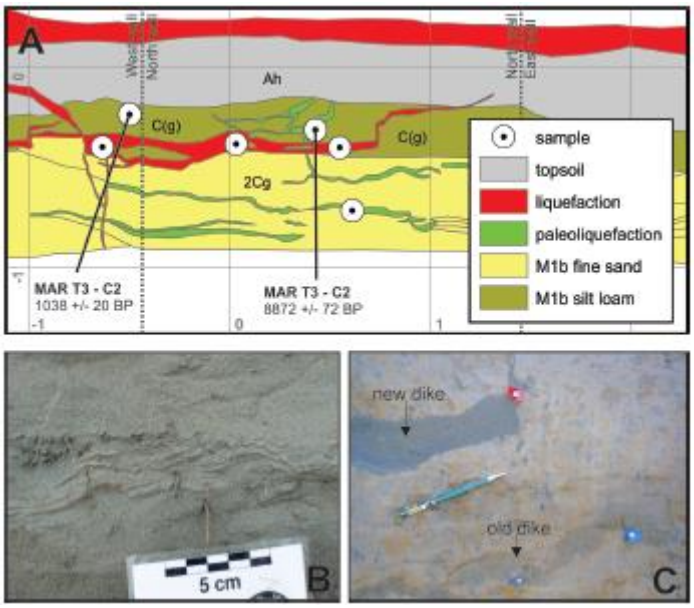

Figure 1. 22 Paleoliquefaction recorded at Marchand's site. A) Detail of the trench's log showing the soil background, liquefaction and paleoliquefaction; B) Detail of the sand blow, lamination and leaves deposition at the contact as a result of the different events happening at the same site; C) Picture of modern and old liquefaction dikes from Villamor et al., (2014)

Due to the proximity of Hardwick and Marchand sites (only 2 km of distance) and the similarities in weathering it has been suggested that the paleoliquefaction features were triggered by the same event between AD 995-1394 (Villamor et al., 2016; 2014).

Other evidence of paleoliquefaction features were found along the Avon River (Avondale) in Christchurch (Bastin et al., 2015; Quigley et al., 2013) dated between AD 1321 and AD 1960 (Bastin et al., 2016). Also, at this study site the main paleoliquefaction feature observed was a paleodike cross cut by a dike of the recent CES. The paleodike looked similar to the modern CES liquefaction features but was bioturbated and oxidised. Other evidence of paleoliquefaction features was documented at Kaiapoi by Bastin et al., (2016), possibly formed in three distinct liquefaction episodes: prior to AD 1458, between AD 1458 and AD 1901, or between AD 1297 and AD 1901.

1.5 IDENTIFICATION OF LIQUEFACTION IN THE GEOLOGICAL RECORD

This section will present the main known techniques used in investigating liquefaction and paleoliquefaction features. These techniques are also used in this research to insure a compounded approach and to guarantee an integration between geology, geophysical and geotechnical investigation.

1.5.1 Paleoseismic trenching and coring

The effectiveness of paleoseismic trenching for liquefaction and paleoliquefaction investigation was ascertained by several studies (Almond et al., 2012; Bastin et al., 2015; Berryman et al., 2012; Langridge and Berryman, 2005; Persaud et al., 2016; Tuttle and Barstow, 1996; Tuttle, 1999, 2001b, 2010; Tuttle et al., 2006; 2002a; Vanneste et al., 2008; Villamor et al., 2016)).

The main advantages of paleoseismic trenches is to be able to confirm that sand dikes are intruded from below (a criteria for earthquake-induced liquefaction features) and to collect samples for dating (Tuttle and Hartleb, 2012a; Tuttle and Hartleb, 2012b). Trenching allows for liquefaction and paleoliquefaction features to be exposed in their whole length; hence it is possible to study in detail the geometry and the cross-cutting relationship within the hosting sediment. Also, due to the length of a paleoseismic trench wall, low- angle dikes can be distinguished from sills and it is possible to better understand the stratigraphic profile.

Coring is also very helpful to explore the stratigraphy at depth, examine sediment for soft sediment deformation (SSD), and possibly identify the layer that liquefied. Piston and vibracores retrieve intact sediment that can allow to collect grain size samples and organic material for radiocarbon dating, and investigate soft sediment deformation at depth.

1.5.2 Ground Penetrating Radar 3D and 2D analysis

The use of the Ground Penetrating Radar, as an effective technique to locate sand dikes and to study the subsurface anomalies, is documented by several studies (Al-Shukri et al., 2006; Lui and Li, 2001; Nobes et al., 2012; Villamor et al., 2014) .

The 3D and 2D Ground Penetrating Radar can assist in targeting the trenching campaign by recognizing the main anomalies in the subsurface. However the 3D radar gives a more accurate image of the subsurface anomalies and their 3-dimensional extent.

1.5.3 Micromorphology analysis

The micromorphology analysis (using microscopes to investigate the detailed sedimentary fabrics) is a post field work technique. It allows for the study of the sediment microstructure and to assess the degree of weathering (textural, organic and excremental pedofeatures). This technique has been used recently in paleoseismic research (Vanneste et al., 2008) but it is broadly used for interpretation of glacial geomorphology processes (Phillips, 2006; Van der Meer and Menzies, 2011). In this dissertation, the micromorphology is used for the first time to study modern and paleo liquefaction features (Chapter 6). The advantage of using this technique in a liquefaction investigation is explained next.

- Detailed analysis of the fabric of the soil experiencing liquefaction;
- Examination of the different liquefaction generations (modern liquefaction vs paleo liquefaction);
- Corroboration of the stratigraphic interpretation after the field work and added information for the interpretation of the formation of geologic structures (e.g., liquefaction features or soft sediment deformation structures) during and after an earthquake event.

Chapter 2

BROAD GEOSPATIAL ANALYSIS TO INVESTIGATE LIQUEFACTION STUDY SITES

2.1 INTRODUCTION

The 2010-2011 Canterbury earthquake sequence (CES) produced extensive liquefaction throughout the Canterbury Plains (Figure 2.1). The Canterbury Plains comprise landforms and deposits of late Pleistocene and Holocene age (Brown and Weeber, 1992), the latter largely occurring on the coastal parts, which were constructed by coastal progradation following the post glacial culmination of sea level rise. These deposits occur in a zone of high water table, and the combination of the sediment age and water saturation make them prone to liquefaction (Brown and Weeber, 1992; Clough, 2005; Elder et al., 1991; Stirling et al., 1999). Preliminary associations between sedimentary environments and liquefaction were documented soon after the CES at Kaiapoi (~ 25 km North of Christchurch Bastin et al., 2016; Wotherspoon et al., 2012) and Halswell/Taitapu area (~ 20 km South west of Christchurch Almond et al., 2012; Tuttle et al., 2017 ; Villamor et al., 2016; 2014) , and in the eastern suburbs of the city (Bastin et al., 2015; Quigley et al., 2013). These studies were focused on small areas or single sites.

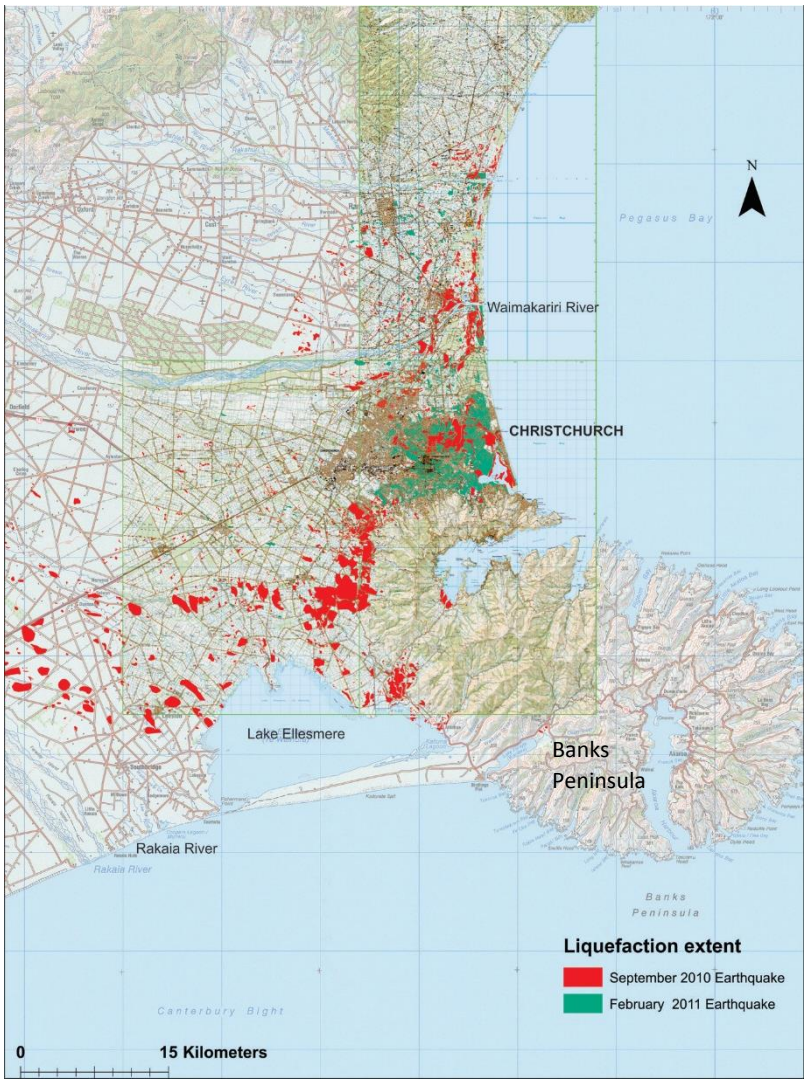

Figure 2. 1 Liquefaction surface manifestation mapped out during the last Canterbury earthquake sequence in the Canterbury Plains. Liquefaction during the Darfield Earthquake (4 September 2010) have been mapped in red, while liquefaction caused during the Christchurch Earthquake (22 February 2011) have been mapped out in green. From Brackley et al., 2012.

This chapter explores the spatial correlation of CES liquefaction features with landforms and soils of the Canterbury Plains at a regional scale. This broad scale analysis assisted the selection of study sites for the research presented in this thesis. The geomorphological and pedological characteristics of the Canterbury Plains are only discussed to the extent needed for studying the surface manifestation of liquefaction.

The susceptibility of sediment to liquefaction is a combined effect of sediment grain size, packing and water table conditions (see section 1.2 and literature herein). The propensity for liquefied sediment

to reach the surface is a function of fluid pressure (earthquake shaking intensity), landform (depth to water table, opportunity for lateral spread or topographic diffusion, type and age of sediment), and surficial soils (crust conditions, drainage). Accordingly, it is expected that meaningful relationships exist between liquefaction ejecta, landforms and soils, and the aim of this study is to use those relationships to identify study sites that are representative of common sets of conditions that precondition for liquefaction ejecta.

To achieve this aim the following objectives are established:

1. Describe the correlation (spatial association) between landforms of the Canterbury Plains and surface manifestation of liquefaction;
2. Describe the correlation (spatial association) between soil series and liquefaction features;
3. Quantify the association between landforms (geomorphic surfaces), soils and liquefaction on the Canterbury Plains within the 2010-11 liquefaction surface manifestation extent in order to characterize the range of geomorphic settings affected by liquefaction during the Canterbury Earthquake Sequence.

2.2 GEOLOGIC FORMATIONS AND SOIL TYPES IN THE CANTERBURY PLAINS

2.2.1 Formation of the Canterbury Plains

The regional boundaries of the Canterbury Plains (Figure 2.1) extend from Timaru (~100 km south to Rakaia River in Figure 2.1) to Waipara River (30 km North of the Waimakariri River marked in Figure 2.1) and east to Banks Peninsula, covering a total area of 7500 km^2 (Browne and Naish, 2003). The geologic basement of the Plains is hard sandstone (greywacke) and mudstone (argillite) of the Torlesse Composite Terrane of Triassic age (Browne et al., 2012). The Plains are formed by a series of coalescing alluvial fans built by the Waimakariri River and other Canterbury rivers coming from the Southern Alps and their foothills (Brown et al., 1988). The building of the Canterbury Plains is related to the events of the late Pleistocene and to the uplift of the Southern Alps during the Kaikoura Orogeny that started at the beginning of the Miocene Period (Soons and Selby, 1985).

The Waimakariri River was the major player in the study area. Postglacial surfaces are found near the lower Waimakariri River as several very young inset fan terraces and abandoned river channels. Some of the currently abandoned channels can be traced through the wider area of Christchurch and were probably active within the last 500 years (Basher et al., 1988). Older channels document avulsions of the Waimakariri River to a channel position south of Banks Peninsula, reaching the sea in the region of the shores of the present Lake Ellesmere.

The Quaternary geologic units on the Canterbury Plains have been described in detail (e.g. Brown and Weeber, 1992; Brown et al., 1988; Gage, 1958; Suggate, 1958; Suggate, 1990, and Figure 2.2). The late Pleistocene units most relevant to the zone affected by CES liquefaction are Burnham, Springston and Christchurch Formations, from oldest to youngest, and are summarized below. Figure 2.2 shows the landforms constructed from the late Quaternary formations described.

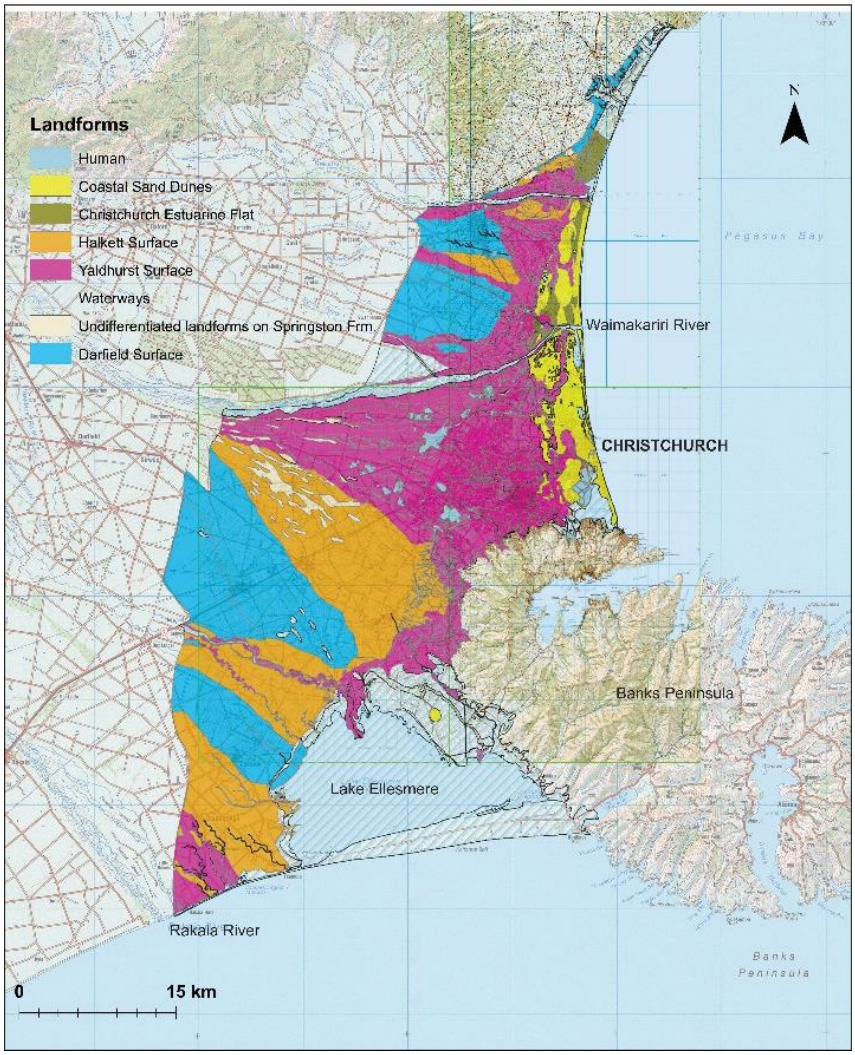

Figure 2. 2 Main landforms on the Quaternary Formation of the Canterbury Plains in the area affected by liquefaction (from Barrell, 2015).

The Burnham Formation, and its lateral equivalent the Riccarton Gravel, (ca 18-25 ka Brown et al., 1988; Oborn and Suggate, 1959; Suggate, 1963; Suggate, 1965, Figure 2.2 and 2.3) represents the last phase of fluvio-glacial aggradation and coastal extension of the Canterbury Plains at the time of the last glacial maximum (LGM) when sea level was about 130 m below present (Brown et al., 1988). According to Browne and Naish's (2003) seismic study in the Canterbury Bight, the Burnham Formation comprises coarse-grained, fluvio-deltaic sediment that forms a regressive systems tract (RST) up to 40 m thick grading to the LGM low sea level stand. On land, the Burnham Formation's Surface is recognised as the Darfield Surface with soils of Lismore age (see below).

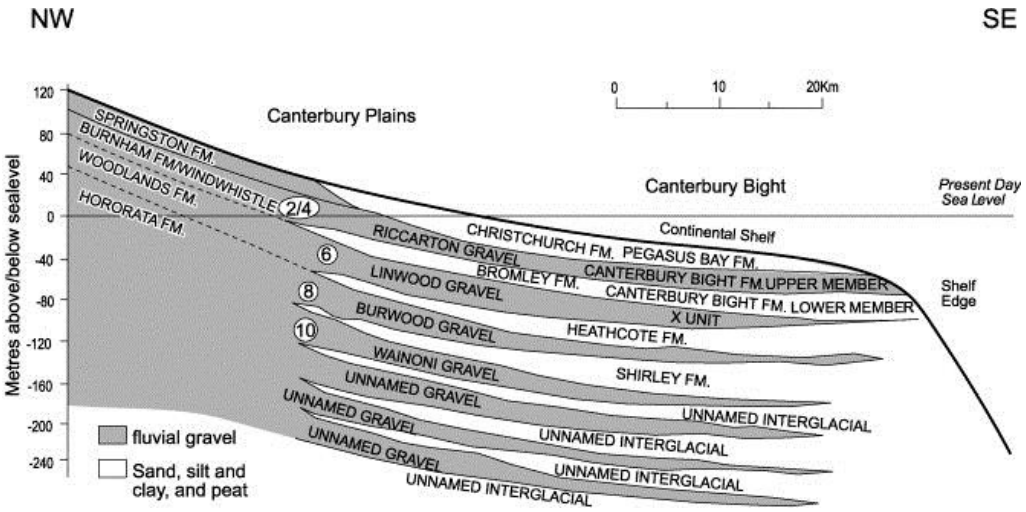

Figure 2. 3 Cross-section through the northern portion of the Canterbury Plains near Christchurch to the edge of the continental shelf showing the stratigraphy of alternating lowland fluvial gravels and highstand sand, silt, clay, and peat (modified after Brown and Weeber, 1992). Numbers refer to inferred oxygen isotope stages based on radiocarbon dating. Burnham formation is the latest fluvio glacial outwash gravel deposited during the last glacial maximum; Springston and Christchurch Formations are the main Canterbury Plains Holocene formations.

Holocene Formations are the Springston and the Christchurch Formations (Figure 2.2 and 2.3) (Brown et al., 1988; Suggate, 1963; Suggate, 1965). The Christchurch Formation began accumulating at the end of the Otira Glaciation about 14,000 years ago (Brown et al., 1988). It is characterized by beach, estuarine, lagoonal deposits, dune and coastal swamp deposits.

The Springston Formation (Figure 2.3) is an aggradational deposit resulting from the Postglacial sea level rise (Suggate, 1963), and it is mainly fluvial sediment, but includes swamp deposits as well. The Springston Formation is inset within channels incised into Burnham Formation in the upper plains, but overlies the Burnham Formation (and its equivalent, the Riccarton Gravel) in the lower plains, and it is interfingered with the Christchurch Formation near the Rakaia River mouth (Figure 4 and Brown et al., 1988). The Springston Formation has a maximum thickness on the west side of Christchurch City of up to 20 m, and its sediment is underlain by several terraces southwards of the Waimakariri River. These terraces, the sediments beneath which are identified as members of the Springston formation, mark different periods of deposition, and are mainly coarse grained deposits. The Springston Formation members are identified on the basis of soil characteristics, for example presence or absence of loess and dune sand, degree of weathering of gravel and matrix, and also by radiocarbon dating.

The members listed in order of decreasing age are: Bleak House Member, Riverview Member, Courtenay Member, Halkett Member and the Yaldhurst member (Brown et al., 1988).

The Halkett member represents younger stages of activity of the Waimakariri and it is capped by numerous sand dunes (Brown et al., 1988). The Yaldhurst member represents the most recent flood and overflow sediment originating from the Waimakariri River when it flooded into the Avon, Heathcote and Halswell Rivers. The Yaldhurst Surface is subdivided (Barrell, 2015) into Yaldhurst 1 Surface, characterized by Waimakariri soil age and Yaldhurst 2 and 3 Surfaces, characterized by Selwyn soil age (Cox and Mead, 1963)[2].

As a consequence of the Canterbury Plains geologic setting, to the west the Plains are characterized by a succession of fan and alluvial gravel forming aquifers. In contrast, to the east a succession of interglacial fluvial, marine and estuarine sediment of silty, clay and peat forms aquitards (Cox et al., 2012) separating a sequence of glacial outwash gravels forming confined and semiconfined aquifers, the youngest of which is the Burnham Formation (Figure 2.4).

In general, the aquifers occur in well sorted and permeable alluvial gravel sediment. Any surface water course is associated with a shallow unconfined aquifer with a water table in hydraulic connection, then intermediate aquifers at depths between 30-80 m and deeper aquifers at more of 80 m depth (Cox et al., 2012). Consequently, to the west the water table lies several meters or more below the surface and away from modern river floodplains. The soils are usually well drained and gravelly. To the east and closer to the coast the water table rises and coupled with fine textured sediment results in poorly drained soils (Brackley et al., 2012).

[2] In this paper Cox and Mead stated that it is possible to recognise four main soil age group on the Springston Formation: Templeton (3-6 k years ago), Waimakariri (700-2400 years ago) and Selwyn (<300). The fourth group is the Lismore (14-20 k years ago) that forms on the Burnham Formation. This thinking has been revised and updated by Basher et al 1988, Webb, 2008, Brackley et al., 2012.

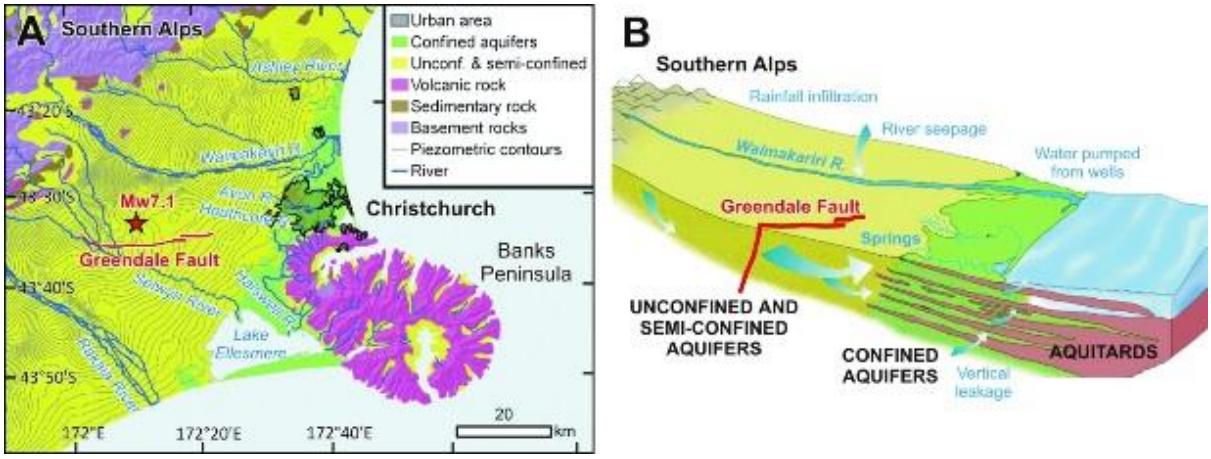

Figure 2. 4 Outline of aquifers and aquitards on the Canterbury Plains and; A, map of the Canterbury Plains with the hydrogeological system in plan view; model of the aquifers and aquitards across the succession of gravel and alluvial sediment through the Plains. From Cox et al., (2012).

2.2.2 The Soils on the Canterbury Plains

In this thesis the soil is considered as a natural body composed by solids (organic matter and minerals), liquid (water, plants exudates) and gas. It is characterized by different horizons or layers which result from addition, losses, mobilization or transformation of energy and matter in order to support the microbial, plant, fungi and animal activity within it. As is the convention with soil survey, the soil that is classified and mapped is restricted to the upper most 1 m or thereabouts. The engineering definition of soil (unconsolidated sediment) is not appropriate in this case.

The mountains composed by Greywacke rocks dominate the landscape in the Canterbury Plains, and they were the source of most of the parent materials. Greywacke rocks and greywacke-derived parent materials contained a high proportion of resistant materials. Weathering of these materials gave rise to sandy and silty soils with minor amounts of newly formed clay minerals and low levels of plant nutrients.

The Canterbury Plains is characterized by sub-humid climate conditions. The rainfall average is between 500 and 750 mm per year and the year average temperature is between 10 and 12 C (NIWA, 2015). Under this rainfall regime Pallic Soils dominate on landforms with adequate time for significant soil development, but Recent or Gley Soils occur where sediment is youthful, or where water

saturation is prevalent, respectively. Some Brown Soils are mapped on well drained, gravelly terraces and on some older sand dunes.

The most important factor determining the soil properties of the Plains is the depth of fine material overlying the gravel outwash (Molloy, 1989). The fine material depth will determine the soil drainage which is also a key factor in determining liquefaction susceptibility. The variation of fine material over the gravel outwash and the corresponding soil series is showed in Figure 2.5. Suites of soils with different grain size and drainage characteristics are defined for surfaces of different age. Figure 2.5 represents these surfaces as terraces as is relevant to where the Waimakariri River (or other rivers) is incised into Burnham Formation. However, this representation is only appropriate for parts of the plains where the postglacial response of the major rivers, such as the Waimakariri, has been degradational (i.e. to the west). Consequently, it only shows subsets of the soil suites; those associated with well drained conditions and coarser grain size. In the east, where a post-glacial aggradational and progradational sequence has formed, successively younger members of the Springston Formation are superposed or on-lapping. In these areas a wider range of drainage and soil grain-size characteristics occur and the soils are more varied (see Table 2.1).

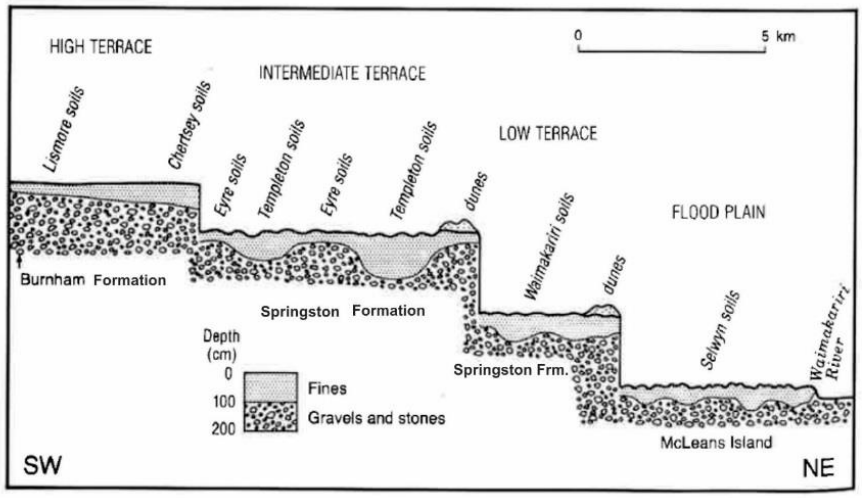

Figure 2. 5 Association between terraces of the Canterbury Plains, Geologic Formations and Soil series, note the variation of depth in fine material. Modified from Molloy (1989).

Four soil age-groups were firstly identified by Cox and Mead (1963) on the Canterbury Plains named Lismore (oldest), Templeton, Waimakariri, and Selwyn (youngest) (Fig. 2.6). Table 2.1 modified from Brackley (2012) and based on Cox and Mead (1963), Basher (1988), and Webb (2008) shows the association between late Quaternary Formations, landforms and soil series.

Lismore and Darnley age groups, associated with the Burnham Formation, include well developed soils. They form in coarse alluvium and are in areas of low water table (usually distant to modern river floodplains). They comprise mainly Argillic Pallic Soils, Orthic Gley Soils and Firm Brown Soils (Hewitt, 2010).

TABLE 2. 1 Key fluvial soil types for the Burnham and Springston Formations on the Canterbury Plains, modified from Brackley et al., 2012.

Geological units	**Springston Formation**			**Burnham Formation**	
Landform	Yaldhurst 2 and 3 Surfaces	Yaldhurst 1 Surface	Halkett Surface	Darfield Surface	
Soil age (years)	<600 (Basher et al., 1988)	700-2400	3000-6000	14,000-20,000	>20,000
Soil age group name	Selwyn	Waimakariri	Templeton	Lismore	Damley
Shallow and stony soils					
Soil types	Rangitata	Rakaia	Eyre	Lismore	Damley
Classification	Fluvial Recent	Fluvial Recent	Orthic Recent	Firm Brown	Argillic Pallic
Deep, well drained soils					
Soil types	Selwyn	Waimakariri	Templeton	Hatfield	Mayfield
Classification	Fluvial Recent	Fluvial Recent	Orthic Recent	Firm Brown	Argillic Pallic
Deep, imperfectly drained soils					
Soil types		Kaiapoi	Wainui	Lowcliffe	Pahau
Classification		Fluvial Recent	Immature Pallic	Argillic Pallic	Argillic Pallic
Deep, poorly drained soils					
Soil Types	Te Kakahi	Taitapu	Temuka	Waterton	Waterton
Classification	Gley Raw	Recent Gley	Orthic Gley	Orthic Gley	Orthic Gley

The Templeton age group comprises soils with a less developed profile formed on mid Holocene fluvial sediment deposited between 6000 and 3000 years ago (Halkett Member of Springston Formation, Cox and Mead, 1963). Soils on this landform are Orthic Recent Soils, Immature Pallic Soils and Orthic Gley Soils. Waimakariri age group is characterised by soils deposited between about 2400 and 700 years ago, and includes Fluvial Recent Soil and Recent Gley Soils. Selwyn age group is the youngest soil group and generally demonstrates minimal soil development. Orders include Fluvial Recent and Gley Raw soils (see Table 2.1 for summary).

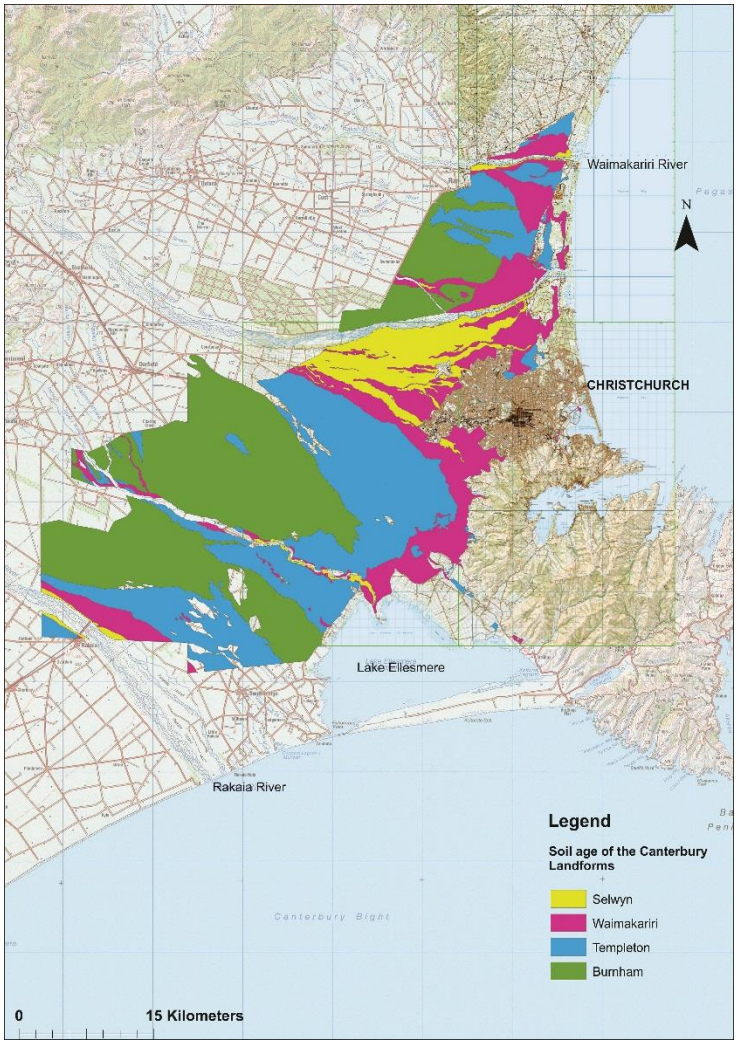

Figure 2. 6 Soil ages mapped out on the Canterbury Plains (from Cox and Mead, 1963)

2.3 METHODS

The analysis of the distribution of surface ejecta and surface water ponding that resulted from the main shocks of the CES includes the spatial pattern of different geomorphic surfaces and soil types. This analysis uses the liquefaction distribution map produced after the September 2010 and February 2011 events (Figure 2.1) produced by a consortium of institutions (GNS Science, Tonkin and Taylor, Lincoln University, Beca, Canterbury University and Geotech consulting). For a compendium of the most relevant maps the reader can refer to Brackley et al., (2012) and Townsend et al (2016).

Firstly the pattern of liquefaction is examined in relation to landforms, and secondly to the soil map (LCR, 2010). Note that the liquefiable subsurface layer is likely to be more extensive than the surface

features mapped, which included ejecta[3] or flooding sediment[4] and flooding water[5] (Brackley et al., 2012; Townsend et al., 2016).

2.3.1 Correlation between landforms of the Canterbury Plains and liquefaction surface manifestation

The geomorphic analysis involved intersecting the combined liquefaction-affected area from the September 2010 and February 2011 earthquakes (Figure 2.1, data from Brackley et al., 2012) with a Canterbury geomorphic map (Barrell, 2015) in a GIS environment. The area of interest is bounded to the north by the Waimakariri, to the east bythe Avon-Heathcote estuary and to the south by the Rakaia River. This area excludes Banks Peninsula to the east and includes the Darfield area on the west.

2.3.2 Correlation between soil series and liquefaction surface manifestation

The soil analysis has been carried out intersecting the soil map for the Upper Plains and Downs of Canterbury (LCR, 2010) and the amalgamated liquefaction extent map after the September 2010 and February 2011 earthquakes (Figure 2.1, Brackley et al., 2012; Townsend et al., 2016) . Two types of analysis were undertaken. The first set of maps illustrates the contribution of each soil series (a soil mapping unit) to the whole liquefied area. That is, of the total area of mapped liquefaction features what percentages are associated with each soil series. The second analysis looks individually at each soil series in the Canterbury Plains and calculates the area that liquefied within the total area covered by that soil.

2.3.3 Association of landforms, soil series and liquefaction surface manifestation

This third step resulted from an intersection of two datasets obtained from the two former analyses: the liquefaction dataset map intersected with the geomorphic map and the liquefaction map intersected with the soil series map. Intersecting these two datasets produced a new dataset which reveals the correlation between landforms and soil series at each liquefaction feature in the

[3] Ejecta are considered those areas in which is possible to identify large sand boils or fissures directly related with a vented area.
[4] Flooding sediments are areas of surface sedimentation for which no vent area could be directly related.
[5] Flooding water is a category that includes standing surface water, saturated ground inferred to be the result of a temporary alteration of water table because of the ground shaking.

Canterbury Plain. This third step was essential to look at both criteria (geomorphology and soils) in the same dataset and to summarize results in order to identify sites most affected by liquefaction in the Christchurch area.

2.4 RESULTS

2.4.1 Correlation between landforms of the Canterbury Plains and surface manifestation of liquefaction

Firstly, the Yaldhurst age surfaces are the most extensive landforms in the Canterbury Plains (28% of the total study area Table 2.2). For mapping purpose the Yaldhurst Surface was subdivided into sub-surfaces: Yaldhurst 1 Surface on the Waimakariri soil age occupies 12% of the area; Yaldhurst 2 and 3 Surfaces on Selwyn soil age occupy 5 and 3% of the respectively. The Halkett Surface represents another extensive landform with 20% of the total study area (Table 2.2). The Darfield Surface on Burnham Formation covers 19% of the total study area (Table 2.2). Coastal Sand Dune landforms represent only 4% of the aerial extent of the Canterbury Plains.

TABLE 2. 2 Summary of the main landforms present on the Canterbury Plain.

Landforms	**Brief physiographic description**	**Aerial Extent ha (%)**
Darfield Surface-fluvial	Glacial outwash derived river deposits (Brown et al., 1988)	10 %
Halkett Surface	Earliest stages of incision of the Waimakariri includes numerous sand dunes (Brown et al., 1988)	9 %
Yaldhurst 1 Surface	Flood and overflow surfaces with few sand dunes (Brown et al., 1988)-Waimakariri soil age	6 %
Yaldhurst raised channel	Flood and overflow surfaces (Brown et al., 1988)-	5 %
Halkett Surface (Rakaia)	Evidence of stages of incision of the Waimakariri in the Rakaia setting	5 %
Halkett Surface (Selwyn)	Evidence of stages of incision of the Waimakariri in the Selwyn setting	4 %
Yaldhurst 2 Surface	Flood and overflow surfaces with few sand dunes (Brown et al., 1988)- Selwyn soil age	4 %
Coastal Sand Dunes	Sand Dunes on the Heathcote and Avon estuarine	4 %
Yaldhurst 1 Surface interchannel/alluvial flat	Interchannel and alluvial flat on the Waimakariri flood and overflow surface, Waimakariri soil age	4 %

The map produced through the GIS analysis is a new map that shows the proportion of each landform affected by liquefaction (Figure 2.7 and Table 2.3). Yaldhurst landforms and coastal sand dunes experienced the highest proportion of surface ejecta cover. Despite its wide extent within the study area and its proximity to the epicentre of the Darfield Earthquake, the Darfield Surface was minimally affected by liquefaction ejecta when compared to the Holocene landforms. The Halkett Surface across the older member of Springston Formation was little affected (4%) by surface ejecta despite also being widely represented in the study region.

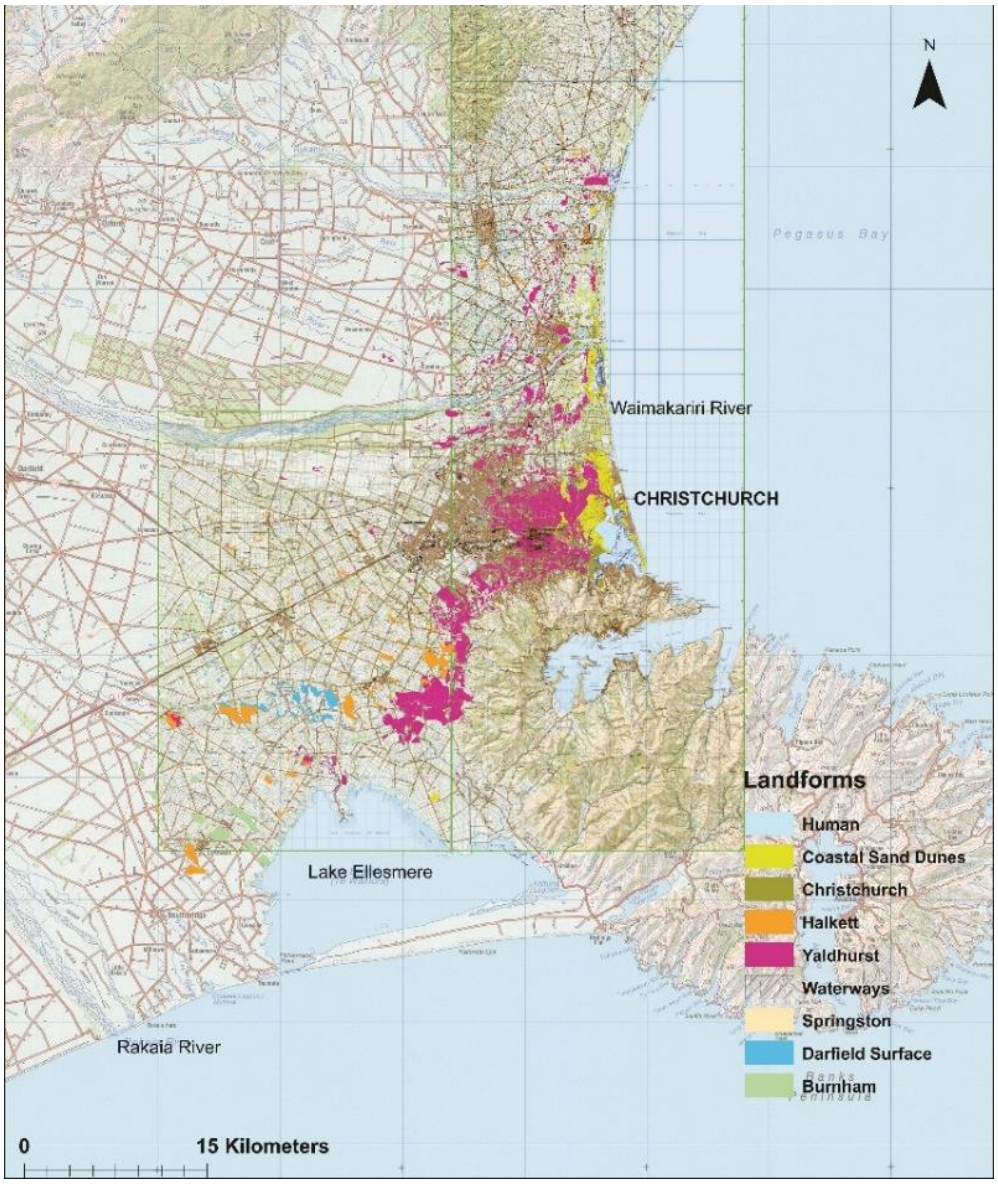

Figure 2. 7 Liquefaction occurrences coded by the landform they occur on. This map reveals that the main surfaces experiencing liquefaction were the Yaldhurst and Coastal landforms.

TABLE 2. 3 Aerial proportion (%) of landforms affected by surface ejecta

Landforms	**ha (%)**
Yaldhurst raised channel	14 %
Yaldhurst flood basin	12 %
Yaldhurst 1 Surface	16 %
Coastal Sand Dunes	10 %
Yaldhurst 2 Surface	4 %
Lake Ellesmere bed	4 %
Halkett Surface	4 %
Darfield Surface	4 %

2.4.2 Correlation between Soil series and Liquefaction surface manifestation

The soil map intersected with the liquefaction map resulted in the dataset shown in Figure 2.8. The main soil orders affected by liquefaction are the Gley and Recent Soils. Table 2.4 lists the soil orders experiencing liquefaction, describing also the soil series affected. Gley Soils are characterized by the presence of high water table and have generally poor drainage.

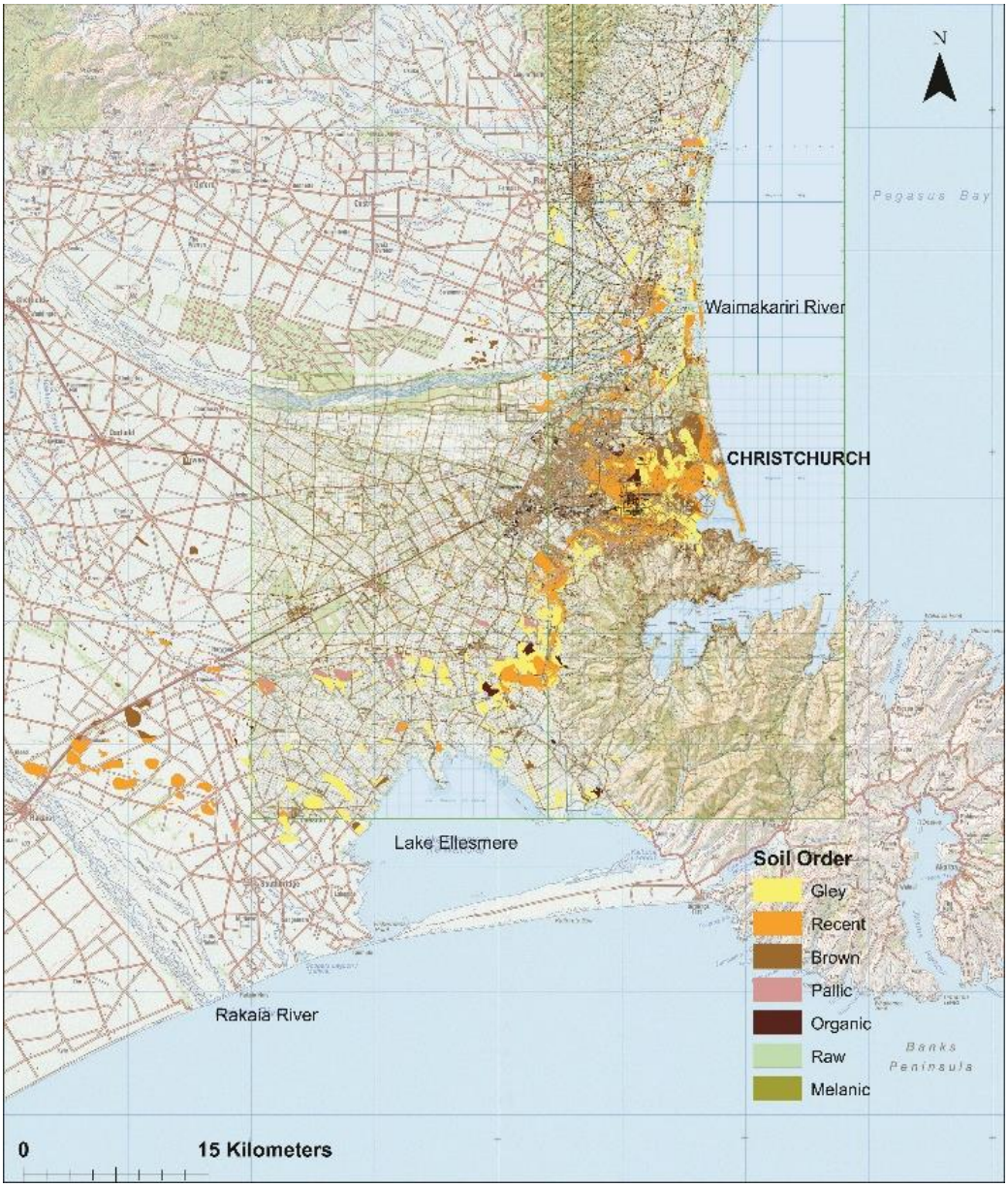

Figure 2. 8 Liquefaction occurrences coded by the soil order they occur on.

Within the Gley order, Taitapu and Temuka soil series are associated with liquefaction. Taitapu is a Recent Gley Soil and Temuka is an Orthic Gley Soil. Within the Recent Soil order, Kaiapoi, Kairaki, Waimakariri, Eyre soil series are associated with liquefaction. Within the Brown Soil order, the Waikuku and Lismore soil series are associated with liquefaction. This result is somewhat unexpected but may be explained as follows: the Waikuku soil, although well drained and formed in sand dunes, likely has saturated sands in the subsurface; and liquefaction associated with the Lismore soil was largely flooding water associated with a raised water table rather than ejection of liquefied sediment.

TABLE 2. 4 Contribution of the soil series most strongly affected by liquefaction to the total liquefied area.

Soil series	Dominant Soil Order	Area ha	Percentage
Taitapu	GLEY	3,220	16%
Kaiapoi	RECENT	2,802	14%
Temuka	GLEY	1,632	8%
Kairaki	RECENT	1,363	7%
Eyre	RECENT	1,325	7%
Waimakariri	RECENT	1,126	6%
Waikuku	BROWN	961	5%
Lismore	BROWN	824	4%

The results presented provided a relationship between liquefaction and soil type considering the proportion of a given soil type that was affected by liquefaction. Table 2.5 ranks the 10 most strongly affected soil series according to this metric. This analysis quantified which kind of soils liquefied and what their extent was in the liquefied area.

TABLE 2. 5 Rank of soils series in the broad liquefaction region that experienced intense liquefaction.

Soil map unit	Dominant Soil Order	Percentage	rank
Aranui complex	GLEY	63 %	1
Kaiapoi + Waimakariri	RECENT	60 %	2
Rangitata + Kaiapoi	RECENT	48 %	3
Taitapu	GLEY	30 %	4
Wakanui+Templeton	PALLIC	29 %	5
Kairaki	RECENT	28 %	6
Kaiapoi + Taitapu	RECENT	26 %	7
Kaiapoi	RECENT	26 %	8
Greenpark	RECENT	24 %	9
Taitapu+ Waikuku	GLEY	23%	10

The percentage value is a ratio between the total liquefaction area which affected a specific soil series and the total soil series area.

The second step of this analysis quantifies the proportion of a specific soil in the liquefaction-affected area relative to its total extent within the region of interest.

A comparison of the results of both analysis (Table 2.5 and Table 2.6) shows that the soil series that are largely present in the liquefied area (Table 2.6) are not the same series that were most strongly affected by this phenomenon (Table 2.5).

TABLE 2. 6 Soil series present in the liquefied region.

Soil series in study area	ha	Percentage of each soil series in the study area
Lismore	50,486	20.98%
Templeton	15,750	6.54%
Eyre	15,202	6.32%
Waimakariri	15,073	6.26%
Temuka	13,439	5.58%
Rangitata	10,910	4.53%
Kaiapoi	10,787	4.48%
Taitapu	10,578	4.39%
Waterton	8,849	3.68%
Rakaia	8,760	3.64%
Motukarara	7,169	2.98%
Darnley	6,220	2.58%
Kairaki	4,866	2.02%
Wakanui	4,825	2.00%
Waikuku	4,634	1.93%
Rangitata+Selwyn	3,467	1.44%
Mayfield+Darnley	3,094	1.29%
Mayfield	2,601	1.08%
Pahau+Darnley	2,546	1.06%
Waimairi	2,484	1.03%
Takahe	2,478	1.03%
Paparua	2,369	0.98%

Selwyn	2,300	0.96%
River Bed+Rangitata	2,218	0.92%
Mairaki+Ashley	2,113	0.88%
Hatfield	2,101	0.87%
Greenpark	2,035	0.85%
Darnley+Mayfield	1,633	0.68%
Eyre+Templeton	1,270	0.53%
Waimakariri+Rakaia	1,265	0.53%
Paparua ?	1,176	0.49%
Darnley+Pahau	1,164	0.48%
Horotane	1,133	0.47%
Fereday	1,013	0.42%
Halkett	939	0.39%
Cashmere	901	0.37%
Evans	826	0.34%
Mairaki	782	0.32%
Windermere	770	0.32%
Te Kakahi	759	0.32%
Rakaia+Waimakariri	734	0.31%
Templeton+Eyre	712	0.30%
Taitapu+Motukarara	689	0.29%
Hatfield+Lismore	687	0.29%
Kaiapoi+Taitapu	666	0.28%
Taumutu	585	0.24%
Temuka+Waterton+Windermere	562	0.23%
Scarborough	483	0.20%
Kaiapoi+Waimakariri	476	0.20%
Lowcliffe+Templeton+Waterton	424	0.18%
Temuka+Windermere	404	0.17%
Taitapu+Kaiapoi	389	0.16%
Aranui complex	383	0.16%
Coastal sand and gravel	325	0.13%
Lowcliffe	247	0.10%
Templeton+Halkett	220	0.09%
Halkett+Eyre	214	0.09%
Kiwi	182	0.08%
Heathcote	180	0.07%
Templeton+Taitapu	176	0.07%
Selwyn+Kaiapoi	149	0.06%
Taitapu+Waikuku	144	0.06%
Rakaia+Kaiapoi	113	0.05%
Selwyn+Rangitata	103	0.04%
Halkett+Templeton+Eyre	92	0.04%
Wakanui+Templeton	85	0.04%
Wakanui+Pahau	78	0.03%
Rangitata+Kaiapoi	48	0.02%
Pahau	43	0.02%
Constructed Wetland within dunes	41	0.02%
Eyre+Halkett	38	0.02%
Templeton+Wakanui	25	0.01%
Taylors Mistake	6	0.00%
Wakanui+Temuka	4	0.00%
Total	240,690	100.00%

While the Taitapu and Kaiapoi series contributed 13 and 15%, respectively, (Table 2.6) to the total area of interest, they were affected by liquefaction to a level of 30% and 26%, respectively (Table 2.5) of their total extent. In contrast, the Aranui complex (typic sandy gley soil, occurring on the aeolian deposit) was affected much more intensely: 63% of its area was covered by ejecta despite its extension in the total area considered being limited to 0.16% (Table 2.6). In other words, some of the soils have very limited aerial extent but their liquefaction susceptibility is enhanced by other factors such as their location close to the faults, or being underlain by liquefaction-prone sediment, and in undrained condition. However, because of the limited aerial extent of these soils (Table 2.6) they were not represented in our first analysis (Table 2.5).

2.4.3. Association of landforms, soil series and liquefaction surface manifestation

This final analysis brings to light that the soil series most affected by liquefaction are those on the Yaldhurst surface which is the youngest landform of the Springston Formation. Tables 2.7 and 2.8 list the proportion (%) of the area of the Gley Soil order and soil series affected by liquefaction according to the main landforms on the Canterbury Plain.

TABLE 2. 7 Proportion (%) of the Gley Soil order affected by liquefaction on each of the main surfaces on the Canterbury Plains

GLEY SOIL ORDER AFFECTED BY LIQUEFACTION	
Landforms	**Percentage**
Christchurch Estuarine flat	4.2%
Coastal Sand Dunes	3.7%
Darfield Surface	3.9%
Halkett Surface	5.7%
Human	3.2%
Undifferentiated landforms on the Springston Frm.	0.04%
Yaldhurst Surface	68.7%
(NA)	10.6%
Grand Total	100.0%

TABLE 2. 8 Proportion (%) of soil series belonging to the Gley Soil order affected by liquefaction per each of the main Canterbury Plain landforms

LANDFORMS	Taitapu	Temuka	Grand Total
Christchurch estuarine flat	2.47%	2.19%	4.65%
Coastal Sand Dunes	2.86%	0.39%	3.25%
Darfield Surface	0.00%	2.53%	2.53%
Halkett Surface	1.62%	5.00%	6.62%
Human	1.31%	0.76%	2.07%
Undifferentiated landforms on the Springston Frm.	0.01%	0.00%	0.01%
Yaldhurst Surface	69.22%	7.07%	76.29%
(blank)	4.29%	0.29%	4.58%
Grand Total	**81.77%**	**18.23%**	**100.00%**

This confirmed that Taitapu and Temuka soil series are the series with a stronger association with liquefaction within their order and both of them lay on the Yaldhurst surface.

Likewise within the Recent Soil order (Table 2.9 and 2.10) the soil series most affected by liquefaction (Kaiapoi, Kairaki, Waimakariri) occur on Yaldhurst (~78%) and Coastal Sand Dunes (8.4%).

TABLE 2. 9 Proportion (%) of Recent Soil order affected by liquefaction organised by main landforms of the Canterbury Plains

RECENT SOIL ORDER AFFECTED BY LIQUEFACTION	
LANDFORMS	**Total**
Christchurch estuarine flat	3.53%
Coastal Sand Dunes	8.40%
Darfield Surface	0.08%
Halkett Surface	1.33%
Human	1.47%
Undifferentiated Landform on the Springston Frm.	0.08%
Yaldhurst Surface	77.96%
(blank)	7.13%
Grand Total	**100.00%**

TABLE 2. 10 Proportion of soil series within the Recent Soil order affected by liquefaction partitioned by the main Canterbury Plain landforms.

Order	**Recent**				
	SOIL SERIES				
LANDFORMS	**Eyre**	**Kaiapoi**	**Kairaki**	**Waimakariri**	**Grand Total**
Christchurch estuarine flat	0.00%	1.41%	2.44%	0.46%	4.31%
Coastal Sand Dunes	0.00%	0.61%	9.11%	0.49%	10.20%
Darfield Surface	0.06%	0.00%	0.00%	0.02%	0.08%
Halkett Surface	0.94%	0.11%	0.00%	0.14%	1.19%
Human	0.00%	0.36%	0.36%	0.65%	1.38%
Undifferentiated Landform on the Springston Frm.	0.08%	0.00%	0.00%	0.01%	0.09%
Yaldhurst Surface	0.11%	54.77%	1.86%	19.32%	76.05%
(blank)	0.00%	3.95%	1.27%	1.49%	6.71%
Grand Total	**1.20%**	**61.20%**	**15.03%**	**22.57%**	**100.00%**

In addition, the Brown Soil order shows similar results (Tables 2.11 and 2.12) and its soil series most affected by liquefaction (Lismore and Waikuku) occur on Yaldhurst and coastal landforms (43% and 36%, respectively, see Table 2.12).

TABLE 2. 11 Proportion (%) of Brown Soils affected by liquefaction organised by each of the main Canterbury Plain landforms

BROWN SOIL	
General	**Total**
Christchurch estuarine flat	4.66%
Coastal Sand Dunes	42.08%
Darfield Surface	5.51%
Halkett Surface	0.85%
Human	1.91%
Undifferentiated Landform on the Springston Frm.	0.42%
Yaldhurst	31.20%
(blank)	13.38%
Grand Total	**100.00%**

TABLE 2. 12 Proportion (%) of soil series within the Brown Soil order affected by liquefaction organised by each of the main surfaces of the Canterbury Plains

LANDFORMS	**Lismore**	**Waikuku**	**Total**
Christchurch estuarine flat	0.00%	4.73%	4.73%
Coastal Sand Dunes	0.00%	42.72%	42.72%
Darfield	5.54%	0.00%	5.54%
Human	0.26%	1.68%	1.93%
Springston	0.00%	0.04%	0.04%
Yaldhurst	0.60%	31.03%	31.63%
(blank)	2.66%	10.74%	13.41%
Grand Total	**9.07%**	**90.93%**	**100.00%**

2.5 DISCUSSION AND CONCLUSIONS

The geospatial analysis undertaken in this chapter illustrated that certain landforms and soils are over-represented (relative to their extent) with respect to liquefaction surface features following on from the September 2010 and February 2011 earthquakes of the CES. The combination of Gley or Recent soils on landforms associated with the most recent depositional events on the Canterbury coastal plain (Yaldhurst Surface and Coastal Dunes) shows the strongest affinity with liquefaction surface features. This is likely due to the sediment's age, which implies consolidation, and the presence of a near surface water table. Gley Soils directly reflect undrained condition, whereas the Recent Soils affected by liquefaction, by definition imperfectly drained, presumably overlie a shallow water table that only reaches the surface for limited periods of time, but which predisposes deeper sediment to liquefaction.

On the alluvial Yaldhurst surface, the analysis identified soils of the Waimakariri age group (700-2400 years), particularly the Taitapu (Gley Soil) and Kaiapoi (an imperfectly drained Recent Soil) soil series as being the most represented in the areas affected by liquefaction. On the Coastal Dunes Kairaki soil series (Recent Soil) was most represented.

The analysis presented in this chapter provided a basis for selection of study sites according to their landform-soil associations, highly susceptible to liquefaction, on the Canterbury Plains. An area on the floodplain of the Halswell River at Greenpark, comprising two individual sites, studied by Villamor et al. (2016; 2014) occurs on the Yaldhurst (2) surface and is dominated by Taitapu soils (700-2400 years, Waimakariri age). The Halswell River site is adopted as one of the study sites for this thesis because of its representativeness of liquefaction-affected sites in the alluvial setting. The coastal setting of the Canterbury Plains is the other important landform-soil association, but no pre-existing detailed studies were available. Three new individual sites were

selected on the coastal setting, all involving Kairaki soils with or without Waikuku soils (an older Brown Soil). Wainoni and QEII Parks, occurred within the urban area and although demonstrating significant surface liquefaction effects had been modified by land development. Consequently, a third site at Featherston Avenue Reserve near Kaiapoi was chosen because it preserved the original geomorphology.

The alluvial site in Greenpark experienced liquefaction during September 2010, February 2011 and June 2011 events, whereas the coastal sites in Christchurch experienced liquefaction during February 2011, June and December 2011. Featherston Avenue Reserve site was the most susceptible site since it experienced liquefaction during all the events of the 2010-2011 earthquake sequence: September 2010, February, June and December 2011, and also in February 2016. A full description of these sites will be addressed in Chapters 3, 4 and 5.

Chapter 3
DETAILED PATTERN ANALYSIS OF SURFACE MANIFESTATION OF LIQUEFACTION IN AN ALLUVIAL SETTING: LESSONS FROM THE CANTERBURY EARTHQUAKE SEQUENCE

3.1 INTRODUCTION

Liquefaction caused by the 2010-2011 Canterbury Earthquake sequence (CES) affected low elevation areas of the Canterbury Plains, such as alluvial, coastal and estuarine settings (see Chapter 2). Liquefaction in the alluvial setting has been widely investigated worldwide. For instance, previous research has documented the influence of the spatial relations, permeability, and thickness of sedimentary deposits on the location and mode of liquefaction-related ground failure (Tuttle and Barstow, 1996) as well as the association of liquefaction ejecta with specific parts of the alluvial setting, such as point-bar deposits (Holzer et al., 2010; Tuttle, 2001a). Recent research on earthquake-induced liquefaction in the Canterbury Plains provides information about the geomorphic setting most affected by liquefaction (Almond et al., 2012; Townsend et al., 2016; Villamor et al., 2016; 2014), the PGA (Peak Ground Acceleration) threshold of liquefaction (Bastin et al., 2015; Quigley et al., 2013; Villamor et al., 2016; 2014), and the land damage caused by liquefaction (Bray et al., 2014; Cubrinovski et al., 2011a; 2010; 2011b; Orense et al., 2011; van Ballegooy et al., 2014). However, none of these Canterbury studies investigated *why* surface manifestation of liquefaction occurs in specific geomorphic settings and what role their subsurface sedimentary architecture plays in determining surface ejecta patterns.

Therefore, the aim of the research presented here is to assess the geomorphic elements most affected by liquefaction in the alluvial system and the sedimentological control on liquefaction and its surface manifestation.

In order to achieve this aim, four objectives are undertaken:

1) Document the spatial correlation between surface manifestation of liquefaction and geomorphic elements of the Halswell River on the lower Canterbury Plains;

2) Identify subsurface source layers of liquefaction features;
3) Evaluate the influences of subsurface sediment architecture on surface manifestation of liquefaction;
4) Develop a conceptual model of the causative relationships between alluvial sedimentation, floodplain construction and surface liquefaction manifestation.

A detailed understanding of the liquefaction phenomenon within the alluvial system will be useful to better understand and map liquefaction susceptibility in conjunction with traditional geotechnical investigations. It will also aid selection of sites for paleoliquefaction studies. A wide range of techniques have been used to investigate liquefaction in the alluvial setting in this study (including those used by Villamor et al. 2016, 2014). An evaluation of the effectiveness of these techniques is provided in Section 3.5 in order to select the most appropriate techniques for future (paleo) liquefaction studies.

3.2 METHODS

The methods used to achieve the four objectives listed in the introduction are as follows:

- Objective 1 is achieved through mapping of the surficial deposits at the Halswell River and detailing the 2010-2011 liquefaction features at the surface.
- Objective 2 is achieved through grain-size analysis of sediment samples collected from the sand blows and dikes combined with visual inspection of retrieved sediment cores (presence of soft sediment deformations) and seismic cone-penetration test (sCPT) data to identify the layer(s) that liquefied and from which sediment the liquefaction features were derived.
- Objective 3 is achieved through collection of information from paleoseismic trenches, hand piston cores, seismic CPT stratigraphic profiles, ground penetrating radar (GPR), radiocarbon dating and geomorphological analysis. This information is gathered into a sedimentary cross section of the Halswell alluvial system (at both sites).

- Objective 4 is achieved through integration of results from objectives 1, 2, and 3, in order to better understand the sedimentological influences on the liquefaction process and its surface ejecta.

3.2.1 Halswell River Geomorphic map and spatial distribution of the 2010-2011 liquefaction features

The study sites along the Halswell River (Greenpark, 24 km southwest of Christchurch, Figure 3.1) were selected because they are in a greenfield area where at least three liquefaction events, related to the September 2010, February 2011, and June 2011 earthquakes, were documented by aerial photos (Almond et al., 2010a) and local reports(Villamor et al., 2016; Villamor et al., 2014).

Surface analysis of a 1 m resolution DEM (digital elevation model derived from LIDAR of the Selwyn District Council taken in 2008) shows a gentle topography (highest elevation of about 6 m a.s.l.) characteristic of a complex braided stream system (Figure 3.1). This complexity is not related to the current Halswell River but to an older and bigger river system, the Waimakariri River, now flowing north of Christchurch (Basher et al., 1988). The surficial Halswell River deposits have contributed to form the Yaldhurst surface (David Barrell, personal communication), hosting Waimakariri-age soils (Springston Formation-Holocene) from 700 to 2400 years old.

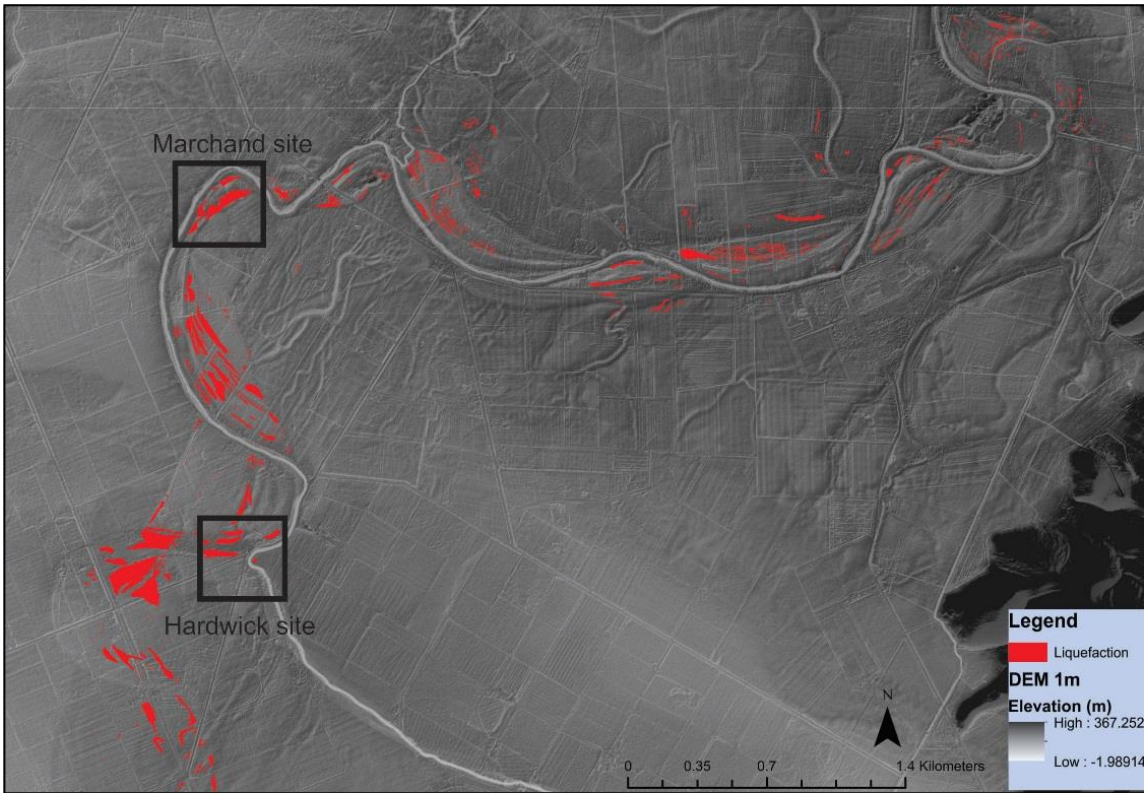

Figure 3. 1 Digital elevation model of the Halswell River landscape from LiDAR data and liquefaction features mapped from aerial photos. Note the subtle topography and the complex meandering system, with crevasse splays, raised channels and levees. These features were formed by the Waimakariri River in the late Holocene.

In proximity to the Halswell River, we identified two study sites, the Hardwick and Marchand properties (Figure 3.1). The Hardwick site was characterized by liquefaction located along an abandoned channel overlaid by a crevasse splay, whereas the Marchand site was characterized by liquefaction associated with a point-bar.

A detailed geomorphic map of the alluvial system of the Halswell River was produced, together with a map of the 2010-2011 liquefaction features. The detailed liquefaction map presented in this dissertation is an update of a former liquefaction map presented in Villamor et al. (2016; 2014). The detailed map is used to show the spatial association of the surface manifestations of liquefaction with landforms of the alluvial system (e.g. point bars, abandoned river channels, etc). The associated landforms may be the source of the sediment that liquefied, the overlying medium that suffered ground failure and through which sand dikes intruded, or the surface sediment on which water and entrained sediment vented.

Aerial photos from 2010 and the 1 m DEM previously used by Villamor, et al. (2016; 2014) were used to map landforms. The liquefaction ejecta were then mapped from aerial photos acquired by Almond et al (2010b).

3.2.2 Sedimentary analysis in the Halswell alluvial system

One stratigraphic cross-section at the Hardwick site, and two cross sections at the Marchand site were built to define the subsurface stratigraphy and its relationship to liquefaction. The cross sections together with the geomorphic maps illustrate the 3D architecture of the landforms of the Halswell River and provide the framework for evaluating liquefaction patterns.

The landforms identified on the geomorphic maps (e.g. crevasse splay, point bars, paleochannel) were used to infer the geometry of the stratigraphic units in the subsurface and to interpret their possible origin, together with information from trenches, hand piston cores, seismic CPTs and ground-penetrating radar (GPR). Radiocarbon ages also provided support for correlation and boundary delineation. Some details of the techniques used are described next.

3.2.2.1 Paleoseismic trenches and cores

Eleven trenches were excavated at the Hardwick and Marchand properties and nearly 18 m of core sediment (up to 5 m deep) were retrieved at these sites. A complete documentation of the trenches and core stratigraphy can be found in Villamor et al., (2016; 2014).

A stratigraphic transect created with auger hole information, parallel to the trenches, was also constructed at the Marchand site. The auger holes were up to 3 m deep (Almond et al., 2010a).

Trenches, cores and auger holes along the transects provided information on sedimentology of the upper 4-5 m of sediment. They were visually inspected and described according to standard soil description methods . Trenching and coring was carried out as part of an earlier study by Villamor et al. (2016; 2014); however, they focussed only on the information from the upper 2 meters with occasional consideration of information from greater depths. This chapter provides a more complete stratigraphic framework of the sites derived from core and GPR data from greater depths. Grain size of sediment samples collected by Villamor et al. (2014) are also analysed in Grain size analysis from Hardwick site and Marchand site. Some additional radiocarbon samples were collected from the cores and added to the existing chronostratigraphy from the two sites (See Appendix A2).

3.2.2.2 Ground-Penetrating Radar

The results of a GPR survey undertaken during the field campaign led by Villamor et al.(2014) are here used to inform the stratigraphic unit outline, in particular within the first 1.5 or 2 m depth. Two different GPR systems were used with two different types of antennas. Prior to trenching, a MALÅ GPR with a 100 MHz shield antenna and 250 MHz shield antenna were used. The control unit was a MALÅ ProEx. Initial GPR imaging had the objective of identifying subsurface disruption and deformation related to liquefaction. This information was used to site geologic trenches in order to examine subsurface liquefaction features. After the trenching campaign, SIR-3000 GPR with 400 MHz and 1.5 GHz antennas were employed in order to collect more detailed profiles to map stratigraphic units. GPR scans were recorded at intervals of 1 cm (100 scans/metre), which was achieved by using a digital survey wheel for pulse triggering. A track log was recorded at the same time using differential GNSS (Global Navigation Satellite System). Data were processed in RADAN 6.7 software, which involved

frequency filtering, horizontal background removal, predictive deconvolution, and gain adjustments. Topographic corrections were not applied in the results of this dissertation.

3.2.2.3 Seismic CPT descriptive columns (Soil Behaviour Type SBT)

The seismic CPTs were used to explore the stratigraphy at depth (up to 15 m) and to define the stratigraphy beyond that revealed in the cores. The seismic CPT descriptive columns, known also as soil behaviour types (SBT) (Robertson, 1990), were used to correlate deeper subsurface units with the units identified in cores and trenches.

3.2.3 Identifying the potentially liquefiable layer

Identification of the layer(s) that could have liquefied during the 2010-2011 events serves to refine the relationship between alluvial sedimentary facies, their liquefaction susceptibility, and surface manifestations of liquefaction. However, the spatial coincidence of landforms and liquefaction ejecta must be interpreted with caution when trying to identify the origin of liquefiable source layers. Floodplains are characterized by superposition of different sedimentary facies; consequently, surficial landforms do not necessarily correspond with the subsurface sediment that liquefied. For example, Villamor et al. (2016) demonstrated that although there was a strong spatial correlation of 2010-2011 liquefaction ejecta with a mapped crevasse splay, the source layer of the ejecta or the sediment that liquefied occurs below the crevasse splay and within a channel deposit. In the present study, the same study sites are explored to greater depth and with a larger suite of techniques (discussed below) in order to define with more confidence the sediment that liquefied during the 2010-2011 earthquakes.

3.2.3.1 Visual inspection of hand piston cores

The cores were numbered according to the corresponding trench, the core location, and the tube collected. For example, core number T5C1T1 indicates Trench HWK5, core location 1,

tube 1. The sediment retrieved in the core was visually inspected and grain size samples were collected (Tables 3. 1, 2, 3, 4, 5, 6). The samples collected from the cores were then named using the core/tube identifier and adding the depth of the sample within the tube (e.g. T5C1T120 indicates sediment sample collected from Trench 5, core 1, tube 1 at 20 cm depth along the tube).

3.2.3.2 Grain size analysis

Grain size analysis was used to assess liquefaction susceptibility of *in situ* sediment in trenches and cores, and also as a forensic technique to link (near) surface ejecta with subsurface sediment. The analysis consisted of 3 steps:

1) Determination of the grain-size distribution using a Micromeritics Saturn Digisizer II 5205 at Canterbury University;
2) Comparison of the cumulative grain-size distribution curves of samples collected from trenches and cores with Tsuchida's (1970) soil behaviour boundaries to provide a preliminary liquefaction susceptibility assessment;
3) Characterisation of grain-size subpopulations using statistical analysis in the R mixdist package (Du, 2002) (https://cran.r-project.org/web/packages/mixdist/mixdist.pdf). Grain size distribution curves of fluvial sediment are commonly multimodal (multigaussian) in nature (Haberlah and Mctainsh, 2011; Leys et al., 2005) (Figure 3.2). Hence mixdist was used to resolve each sediment distribution into its component subpopulations assuming log normal grain size distributions. The resulting grain size distribution curve was used as a "spectrum" to image the component subpopulations. The grain size spectrum was then used as a 'fingerprint' for identifying the source sediment of the surface ejecta. The similarity between ejecta and potential source sediment was quantified using a similarity metric, *S*, defined by Equation 3.1 as,

$$S = \frac{n_1}{N} \qquad Equation\ 3.1$$

(N) is the number of core modes, identified by mixdist, *and* n_1 = number of core modes identified by mixdist in the sand blows. A ratio *S* = 1 implies a perfect match where all the modes in the ejecta occur in the potential source sediment. However, sorting of grain-size subpopulations during liquefaction and flowage would produce a value of *S* <1 when comparing ejecta with its actual source sediment.

The subpopulation matching results were expressed in a two-way table in which the similarity metric was classified using a scale of colour (red, best correlation, S > 0.8; yellow, moderate correlation for S between 0.8 - 0.4; green for poor-no correlation with S < 0.4). Sand blow as well as dike samples were used to mitigate grain size sorting biases during the liquefaction process.

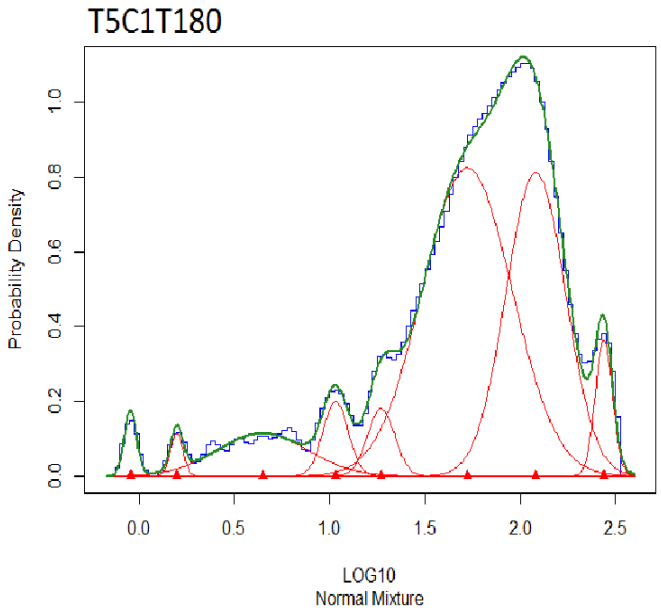

Figure 3. 2 Example of multigaussian grain size distribution curve and its decomposition from a core sample taken from Trench HWK5.

3.2.4 Factor of Safety (derived Seismic CPT)

The seismic cone penetration test (sCPT) is used to assess the mechanical properties of sediment and to ascertain liquefaction susceptibility. The Factor of Safety (FS) against liquefaction was determined from the seismic CPT data using the analyses of Idriss and Boulanger (2006; 2008) and Youd (2001). Where FS < 1, liquefaction is likely to happen, whereas liquefaction is not likely to happen where FS > 1. The FS computation used the PGA (Peak Ground Acceleration) recorded at LINC seismic station. Although the station is ~ 3 km away from the study site, it is underlain by a similar soil type (Villamor et al., 2016; 2014). The PGA values were 0.42g for the September 2010 (Darfield) event, 0.12g for the February 2011 event, and 0.06g for the June 2011 event. The MSF (Magnitude Scaling Factors) used for the computation of PGA magnitude-weighted values are from Idriss and Boulanger (2008). The results of the computations are tabulated in Appendix A1).

3.3 RESULTS

The Hardwick site

3.3.1. Geomorphic association

At the Hardwick site, Villamor et al., (2016; 2014) reported that surface manifestation of liquefaction was spatially associated with a crevasse splay of the Halswell River (Figures 3.3 and 3.4). The crevasse splay overlies an abandoned meander channel and associated point-bar deposits. They found that liquefaction ejecta was not sourced from the crevasse splay but from layers, 4 m deep, that were not exposed in the trenches.

The detailed liquefaction map (Figure 3.3), developed as part of the present work, suggests that the source of the liquefaction features is likely to be the abandoned meander channel below the crevasse splay. This interpretation is based on the detailed spatial pattern of the mapped sand blows and the shape of the paleochannel. More specifically, a) the sand blows are aligned parallel to the paleochannel margin near the northern part of the crevasse splay; and b) the sand blows form arcuate lineations likely reflecting point bar deposits along the inside bend of the buried paleochannel. The crevasse splay appears to have contributed to the infilling of the paleochannel and burial of the point bar deposits (Figure 3.3 B).

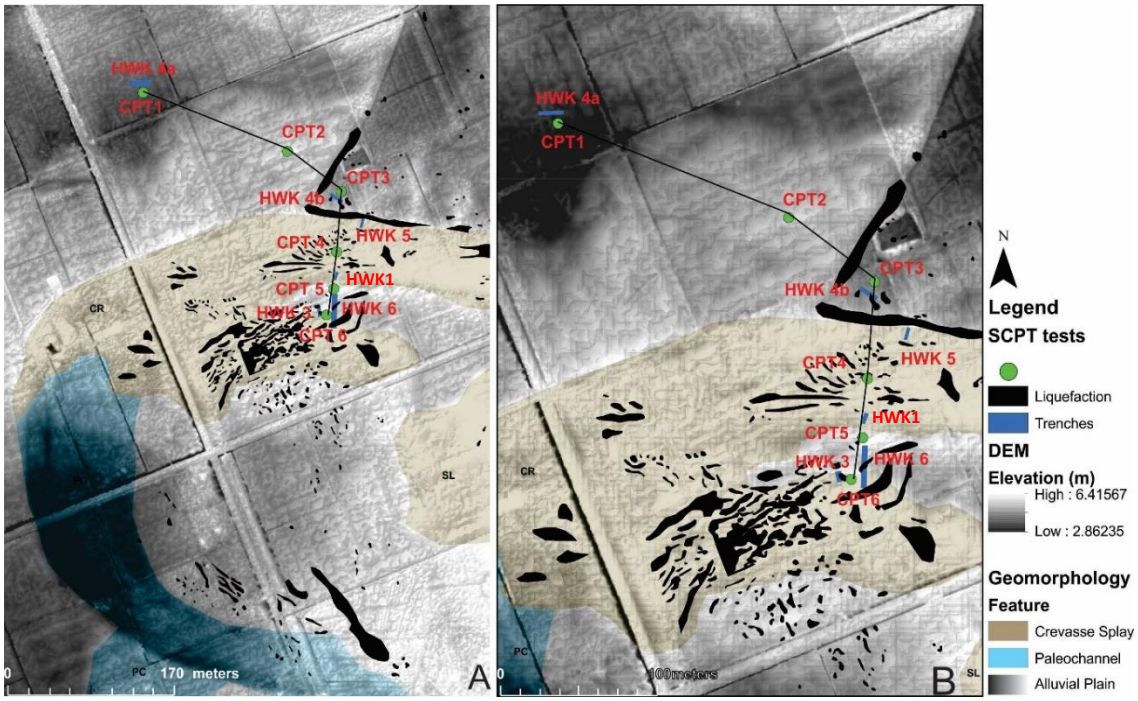

Figure 3. 3 Geomorphic map and September 2010 liquefaction surface manifestation (in black) at the Hardwick site (Halswell River, Greenpark 24 km southwest of Christchurch). The geomorphic map was built using the aerial photos of Tai Tapu area (Almond et al., 2010b) and the digital elevation model obtained from LIDAR. A. Liquefaction is localized on the crevasse splay deposit (coloured in light yellow) that buries the northern half of the abandoned meander channel. Note minor liquefaction in the inner part of the southern half of the meander (outside the crevasse play). B. Detail of the liquefaction surface manifestation in the area of detailed field studies. Note the trend of mapped liquefaction ejecta, parallel to buried meander channel edge and delineating trends similar to point bar shape in the inner part of the meander. The stratigraphic transect is the black thin line with location of sCPT and trenches shown.

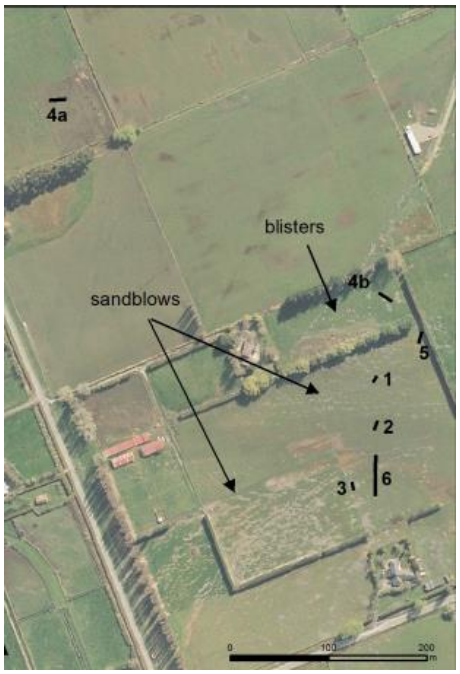

Figure 3. 4 Aerial photos of the Hardwick property in Greenpark area, taken after the liquefaction occurred during the September 2010 earthquake event. This photo shows sand blows within the abandoned channel and associated point bar deposits. Blisters cannot be seen in the aerial photo but were identified at the edge of the relict channel in the field inspection. The locations of the 2012 field campaign trenches are also shown.

3.3.2 Sediment architecture

At the Hardwick site, a 586-m-long stratigraphic cross section was developed (Figures 3.5-3.6) in order to understand the sediment architecture. The transect at the Hardwick site has a northern trend originating at Trench HWK6, passing through Trenches HWK1, HWK5, HWK4b, and finishing at Trench HWK4a on the floodplain (Figure 3.5). The highest topographic area of the transect coincides with the crevasse splay (5.4 m a.s.l.) while the lowest area (4.2 m a.s.l.) corresponds with the floodplain to the northwest of the crevasse splay.

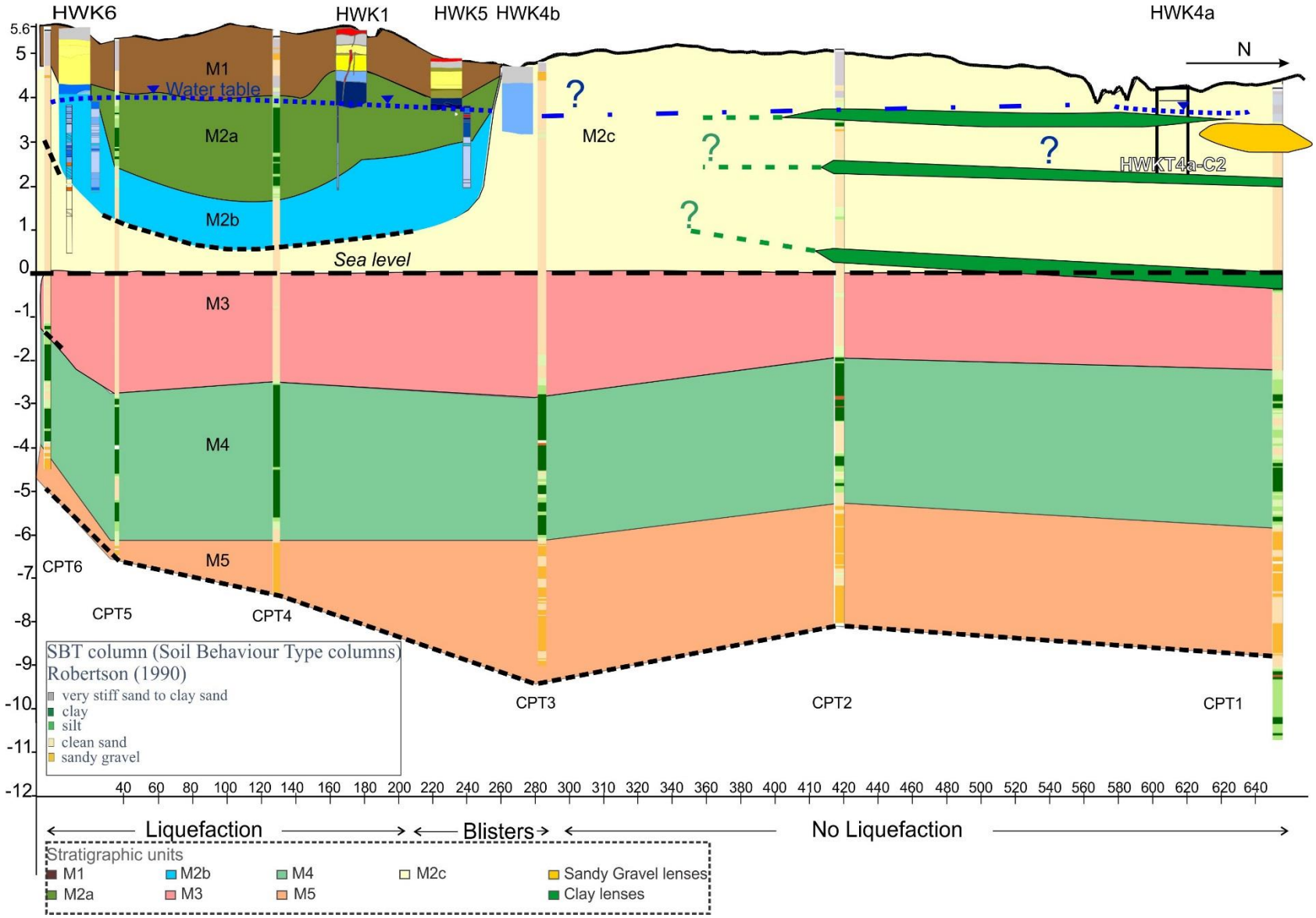

Figure 3. 5 Stratigraphic cross section at Hardwick site based on information from trenches, hand piston cores and seismic CPTs. The black frame highlights the location of Figure 3. 6. Elevation in meters on the vertical axis and Distance in meters on the horizontal axis.

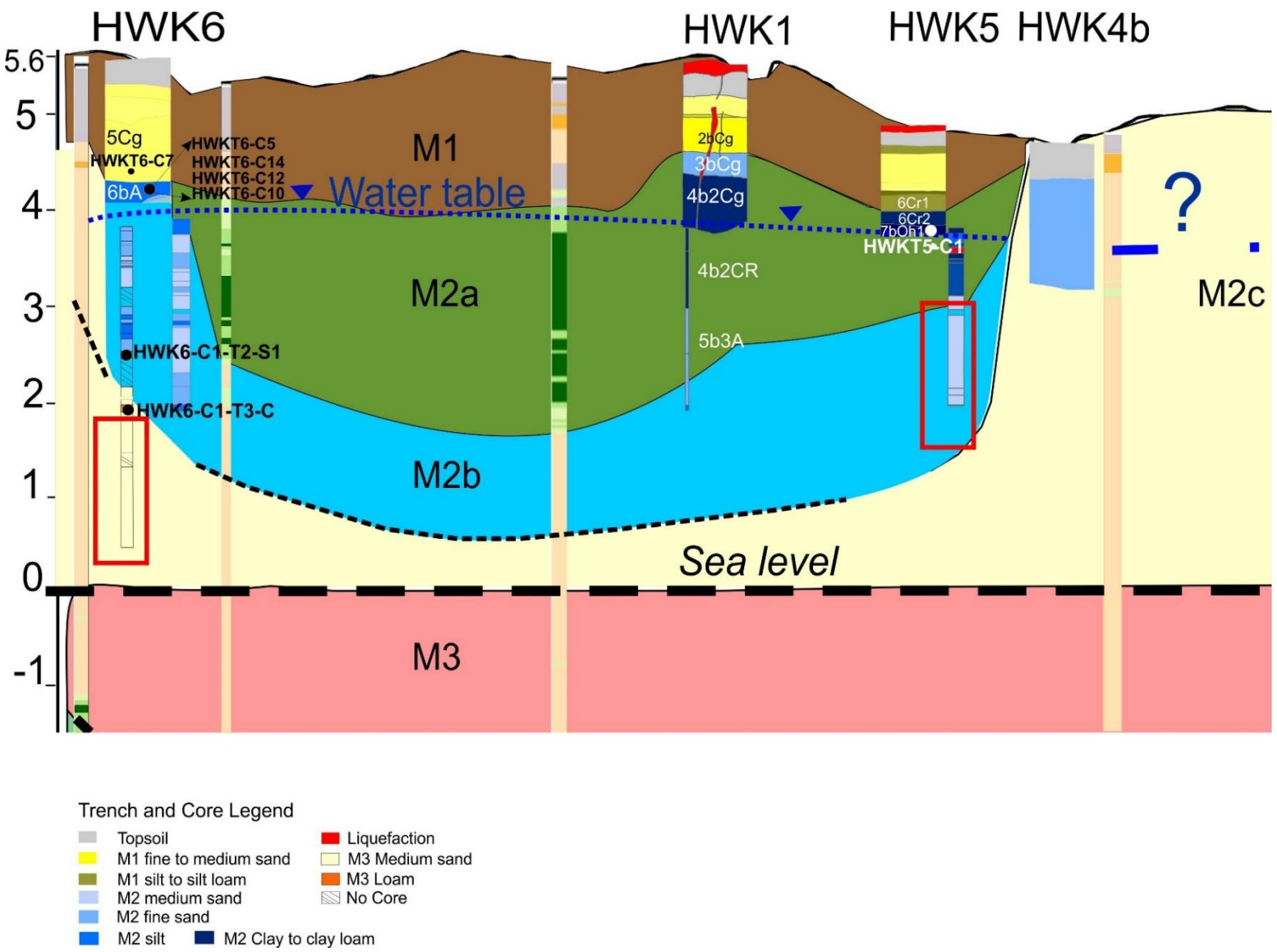

Figure 3. 6 Detail of the stratigraphic cross section across the paleochannel at the Hardwick site. Note the trench stratigraphy is very simplified with only some of the units named to match stratigraphic units defined in the text. For full details on the trench stratigraphy and the soil profile the reader can refer to Villamor et al 2014, 2016. The red frame shows the possible liquefied layer according to the grain size analysis (see text). Elevation in meters on the vertical axis and Distance in meters on the horizontal axis.

The stratigraphy is divided into units M1, M2a, M2b, M2c, M3, M4 and M5. Units M1, M2a, M2b, M2c, M3 observed in the trenches and the cores correspond with, or are subdivisions of, units M1, M2 and M3 of Villamor et al. (2016; 2014). Units M4 and M5, defined here for the first time, are based on the soil behaviour column (SBT) derived from the sCPT data (Appendix A1). A summarised description of these units and their origin is presented next.

3.3.2.1 Crevasse splay (M1)

The crevasse splay is characterized by an organic rich topsoil and an alternation of loamy silt and very fine sandy layers in the subsoil (Taitapu family LCR, 2016). This unit varied in colour from yellowish to grey with common redox segregation features. The crevasse splay deposits form the uppermost unit that underlies the higher southern part of the cross-section. The crevasse splay deposit lower boundary was identified as: an abrupt erosional contact beneath soil unit 5Cg in Trench HWK6; the lower boundary of soil unit 2bCg in Trench HWK1 (down to 94 cm depth); and the lower boundary of soil unit 6Cr1 in Trench HWK5 (down to 1.59 m depth) (Figure 3.6) Villamor et al (2016; 2014). This contact could also be identified on the GPR profile (Figure 3.7) as a strong reflector between 0.7 and 1 m depth corresponding with an organic rich layer directly underlying the crevasse splay sediment.

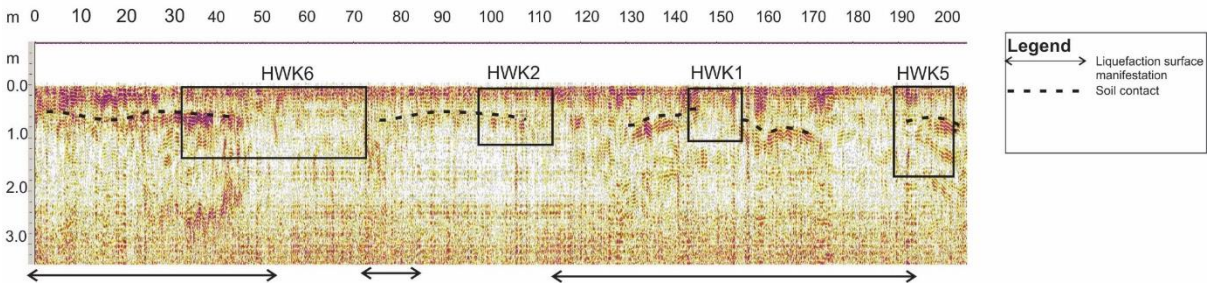

Figure 3. 7 500Hz GPR image at Hardwick site. Black rectangles indicate trench positions. Dash black line is the strong soil reflector due to a change in geophysical properties at nearly 1 m depth. The boundary is inferred to represent the base of

crevasse splay deposits (M1 macrounit). Depth from the ground on the vertical axis in meters and Distance in meters on the horizontal axis.

3.3.2.2 Abandoned meander channel (M2)

Unit M2 represents sediments associated with the abandoned meander channel. Two types of deposits were identified: the upper section was characterized by channel fill deposits (M2a); while the bottom section was characterized by paleochannel floor deposits grading into point bar deposits on the southern margin (inner part) of the paleochannel meander bend (M2b).

3.3.2.2.1 Channel-fill deposits; M2a

The upper section of the paleo channel was occupied by fine sediment such as clay and silty clay. The upper layer of unit M2a is identified as: the sandy layer 3bCg which grades into a silty loam layer of 4b2Cg of Trench HWK1; and the silt loam layer 6Cr2 of Trench HWK5. The lower boundary of this unit was identified as: the base of the silty clay and peaty mixtures recorded from the seismic CPTs 4 and 5; the silty layer identified in Core 2 of Trench HWK6; the silty clay unit identified in the auger of Trench HWK1 (auger units 4b2CR, 5b3A); and the peaty clay layer in the first section of the core of Trench HWK5 (unit 7bOh and blue core portion beneath it, Figure 3.6). The steep inclined edge in Figure 3.5 and 3.6 of unit M2a is delineated based on the lack of silty and clay layers in Core 1 of Trench HWK6, and also on the geomorphic location of the abandoned meander channel margins from the geomorphic map (Fig. 3.3).

3.3.2.2.2 Paleochannel floor deposits; M2b

Unit M2b had a sandier texture than M2a, varying from very fine sand to fine sand. Unit M2b was identified as: the soil layers 6bA-6Cg at Trench HWK6 (Figures 3.5 and 3.6, and Figure 3.8 for more details on Trench HWK6); the sandy soil units of Tube 1 and Tube 2 of Core 1

between 3.8 and 2.0 m a.s.l.; and the second section of Core 1 at HWK5 between ~ 2.8 and 1.5 m a.s.l. .

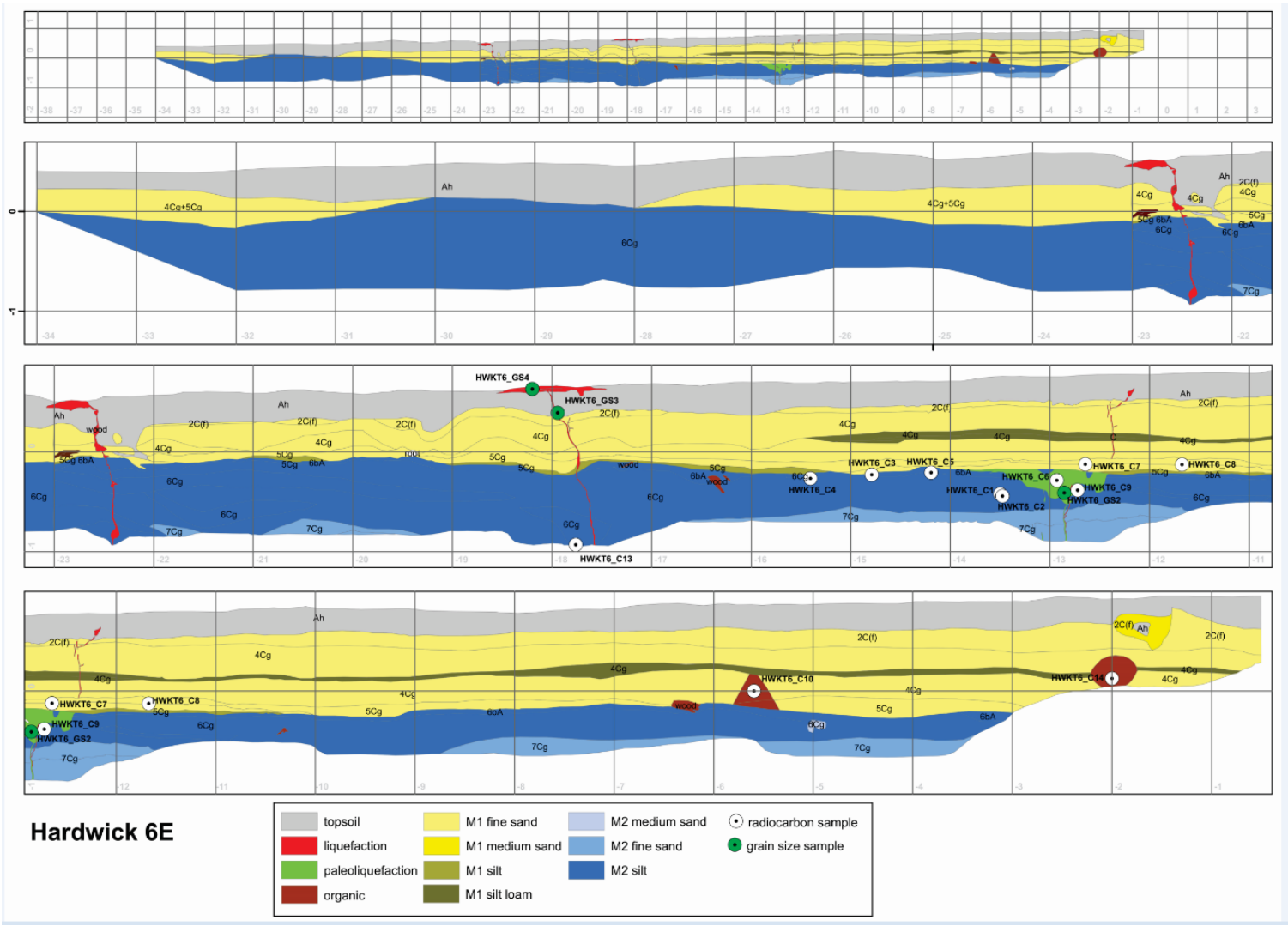

Figure 3. 8 Log of Trench HWK 6 (E, east wall) (from Villamor et al., 2014). Note that the crevasse splay deposit (M1 in text) is composed of units M1 fine sand, M1 medium sand, M1 silt, and M1 silt loam in the figure. Units M2 medium sand, M2 fine sand and M2 silt in this figure correspond to M2a in text. Note modern liquefaction on top of the crevasse splay in red.

It was not possible to clearly outline the bottom boundary of unit M2b across the SBT columns 4 and 5, since the seismic CPT profiles do not record subtle changes in texture. Hence the bottom boundary of the M2b unit is dashed in Figs 3.5 and 3.6. As per unit M2a, the steep lateral margins are inferred from the channel boundaries delineated in the geomorphic map.

3.3.2.3 Floodplain deposits (M2c)

The channel deposits described above are embedded within floodplain deposits (M2c), the surface of which forms the lowest elevation parts of the cross-section of Figure 3.5. Unit M2c comprises fine and medium sand identified in tubes 3 and 4 of Core 1 at Trench HWK6 site, fining upward as observed in the clay-silt mixtures with thin sandy deposits, in seismic CPT1 and at Trench HWK4a where they were exposed. The soil profile at Trench HWK4a consisted of: a topsoil (0- 30 cm depth); a strongly gleyed loamy silt layer (30 to 48 cm depth); a peat layer (48 to 70 cm depth); and bluish-grey clean very fine (liquefiable) sand at the bottom, down to 3.40 m a.s.l.; (Figure A 14 in Villamor et al., 2014).

3.3.2.4 Macrounit 3 (M3) – pre-channel sand

Macrounit 3 is characterized by sandy sediment identified in the SBT columns of the seismic CPTs that currently lies at an elevation below sea level. No core reached this depth, therefore it was not possible to investigate further differences in grain size.

3.3.2.5 Clay layer (M4) – pre-channel clay

Unit M4 is interpreted as a thick clay layer on the basis of the SBT from the seismic CPT data. The top of the layer shows little relief, being located at 8 m depth under the crevasse splay and 7 m depth under the floodplain (Figure 3.5). The thickness of this layer was constant along the whole transect. Unit M4 was tentatively interpreted as Christchurch Formation estuarine and swamp sediments.

3.3.2.6 Sandy to Gravel unit (M5)

Unit M5 is the deepest unit revealed by the SBT columns. Because of the scope of this research, the sCPT were all stopped once the first gravel surface was reached and thus the thickness of this unit is a minimum. Unit M5 was identified as the Halkett Member of the Springston Formation in the Canterbury Plain (first gravel formation below the Canterbury plains in this region).

3.3.3 Age of the sedimentary sequence

The age of the crevasse splay was interpreted from the age of trees (some in growth position) rooted or embedded in the soil unit 6bA buried by the crevasse splay. (refer to Figures 3.5 and 3.6 for locations of all radiocarbon samples for the Hardwick site, and to table S1 in the electronic supplement for a complete list of sample ages) These are: a large piece of wood, buried and in growth position within unit 6bA, yielding an age of 641±20 ^{14}C y B.P. (AD 1311-1404; sample HWK T6-C10); a piece of wood rooted in growth position in 6bA and extended into 5Cg yielding an age of 721±18 ^{14}C y B.P. (AD 1282-1383; sample HWK T6-C12); and a piece of wood from a tree in horizontal position rooted within the buried soil unit of 6bA yielding an age of 641±19 ^{14}C y B.P. (AD 1314-1404; sample HWK T6-C14). These ages are corroborated by: 1) the age of clods of peat found at the base of the crevasse splay in unit 5Cg with an age of 668±18 ^{14}C y B.P. (AD 1300-1395; sample HWK T6-C7), that most likely are remnants of vegetation from the buried surface; and 2) the much older age of sediment belonging to the stratigraphic unit below the crevasse splay (M2b and in particular the soil unit 6bA, see below).

The minimum age of the top unit M2a is inferred from plant fragments retrieved from soil unit 7bOh1 at Trench HWK5, which yielded the age of 628±18 ^{14}C y B.P. (AD 1318-1405;

sample HWK T5-C1, Figure 3.6 and more details in Villamor 2016;2014). This is essentially identical to the age of the base of the crevasse splay, section 3.3.2.1).

The paleosoil unit 6bA is at least as old as the charcoal piece with an age of 2004±18 ^{14}C y B.P. (48BC-AD109; sample HWK T6-C5) found within it. A minimum age for the buried soil unit 6bA comes from the age of the trees growing on it and can be identified at 641±19 ^{14}C y B.P (AD 1314-1404; sample HWK T6-C14). This means that the buried soil on top of the stratigraphic unit M2b had been forming for at least 1300 years.

The oldest age found within M2b, obtained from a sedge and grass fragment was 2932±20 ^{14}C y B.P (BC 1195-976; sample HWK6-C1-T2-S1, Figure 3.6) at ~2.6 m a.s.l. in Trench HWK6. The base of unit M2b is at least 0.5 m deeper than this sample, and thus must be older.

The age of unit M2c is inferred from: a small piece of wood in a buried forest layer at ~3.14 m a.s.l. collected from Trench HWK4a, which yielded an age of 4695± 24 ^{14}C y B.P. (3516-3197 BC, sample HWKT4a-C2, Figure 3.5); and a charcoal fragment from a peat layer at ~ 2 m a.s.l., in the core at Trench HWK6, which yielded an age of 4807±27 ^{14}C y B.P (3638 to 3381 BC; sample HWK6-C1-T3-C). The observation of such an old age characterizing the core sediment ~2 m a.s.l. beneath Trench HWK6 corroborates that the sediment beneath unit M2b is the same sediment as that exposed at Trench HWK4a, and that M2c was eroded by the river activity at Trench HKW6 site. As a consequence, it is suggested that those two ages represent the same geomorphic surface with nearly 1 m of difference in elevation, reflecting the relief at the time. The initiation of deposition of M2c must be older than 3638 to 3381 BC as the base of M2c is at least two meters deeper than the radiocarbon sample. The deposition of M2c must have finished sometime after BC 3838-3381 and before BC 1195-976.

In summary, the old meander channel crossing the Hardwick property (unit M2b) was active and deposited sandy sediment for up to c. 3000 years, starting sometime between 3516-3197 BC (youngest age found in M2c) and 1195-976 BC (oldest age of M2b) and ending sometime prior to 48BC-AD109 (oldest age of paleosoil unit 6bA, the soil developing on M2b when the river abandoned the channel). The channel was then abandoned by the main flow of the river and channel fill sediment was deposited in it (M2a). At HWK6 Trench site, M2b was exposed and soil formed on it between 48 BC-AD 109 up to at least AD 1314-1404 (nearly 1300 years). A peaty clay unit (7bOh1) on top of M2a at Trench HWK5 was dated to AD 1318-1405 (from Oxcal analysis by Villamor et al., 2016). The consistency in dating suggests that soil units 6bA in unit M2b and the soil unit 7bOh1 in unit M2a can be considered the same soil stratigraphic unit, cutting across both M2a and M2b. Both sites were subsequently buried by the crevasse splay at c. AD 1300-1400.

3.3.4 Identifying the liquefaction source layer

This section describes the approach taken to identify the liquefaction source layer and its depositional setting in two steps: visual inspection of cores, and grain size correlation between sediment retrieved in cores and ejecta, at each trench site.

3.3.4.1 Visual inspection of cores

Visual inspection of cores revealed soft sediment deformation in the channel-fill sands of unit M2b at ~ 3.7 m a.s.l. (core 1 of Trench HWK5). A sandy injection (sill) within a clay unit was present at 1.88 m depth. This inference was based on an analogous sill exposed at the bottom of the Trench HWK5 (Figure 3.10). Clay rip-up clasts were found at ~ 2.20 m a.s.l. embedded in a fine sand unit with silty- sand laminations at the base (Figure 3.9). Although the isolated presence of rip up clasts and sill- like injections do not necessarily indicate liquefaction processes triggered by an earthquake, the extensive liquefaction features characterizing the

study area and exposed in Trench HWK 5 (Figure 3.10) leads to the conclusion that the soft sediment deformation observed in the core of Trench HWK5 may be related to the same liquefaction event. Therefore, the layer between 2 and 2.50 m a.s.l. beneath Trench HWK5 may be the source layer for surface ejecta.

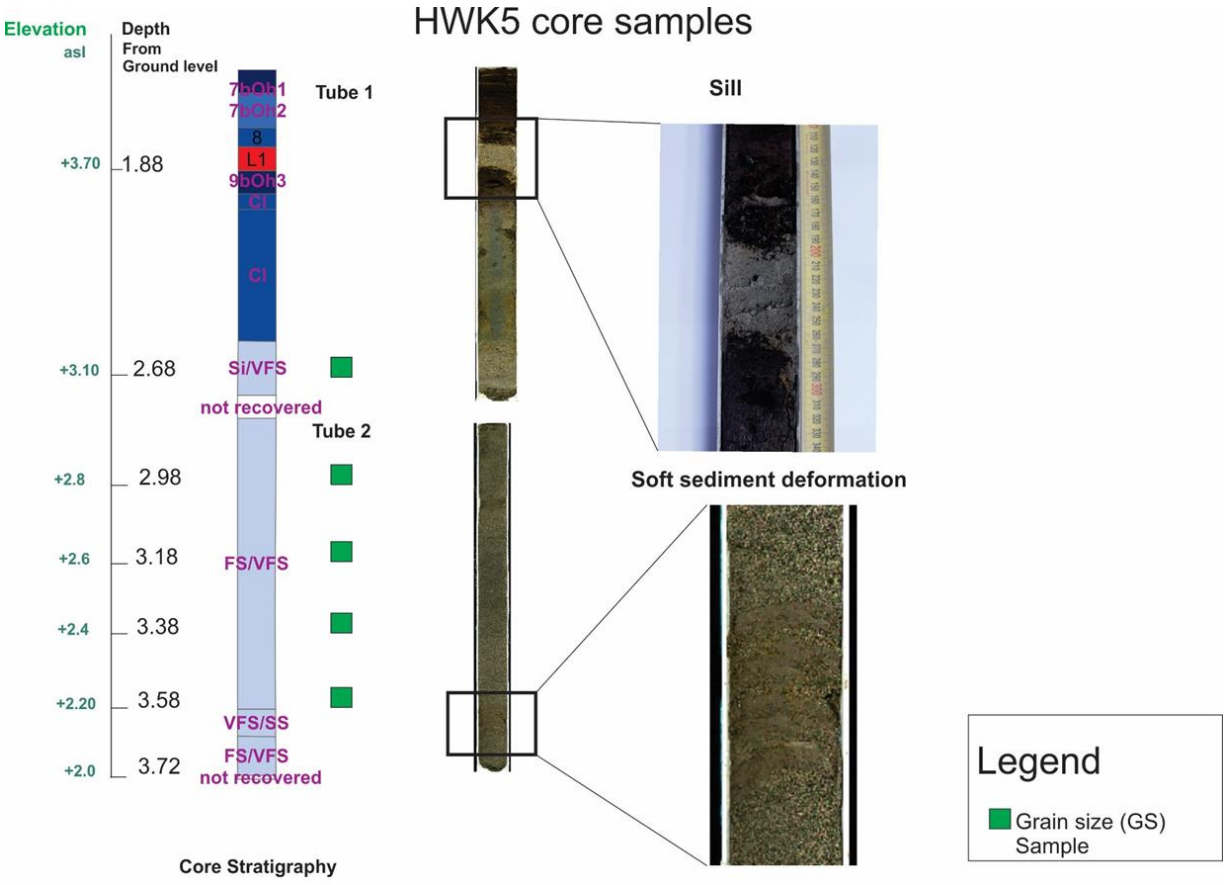

Figure 3. 9 High resolution photography from the core scanner and stratigraphy of the first and second sections of HWK5 core. Note sill injection and soft sediment deformation in parts of the cores. Top most unit names are from trench descriptions (Figure 3.8). Cl, clay; Si, silt; VFS, very fine sand; SS, silty sand, FS, fine sand. Sediment core down to 2.5 m depth (from ground level) is unit M2a in text and down to 3.72 m is unit M2b in text.

3.3.4.2. Grain size correlation at Trench HWK5

Thirteen grain size samples were collected from Trench HWK5. On the west wall, eight samples of liquefied sediment (GS1, GS2, GS3, GS4, GS5, GS6, GS7, GS8) were collected from a surface ejection vent area, and vertically along a dike at different depths. Five more samples were collected on the east wall (GS100, 101, 102, 103, 105) (Figures 3.10 and 3.11) from different surficial sand blow units. Five samples were collected from the cores at different depths (depth in parenthesis): T5C1T180 (2.68 m), T5C1T220 (2.98 m), T5C1T240 (3.18 m), T5C1T260 (3.38 m), T5C1T280 (3.58 m).

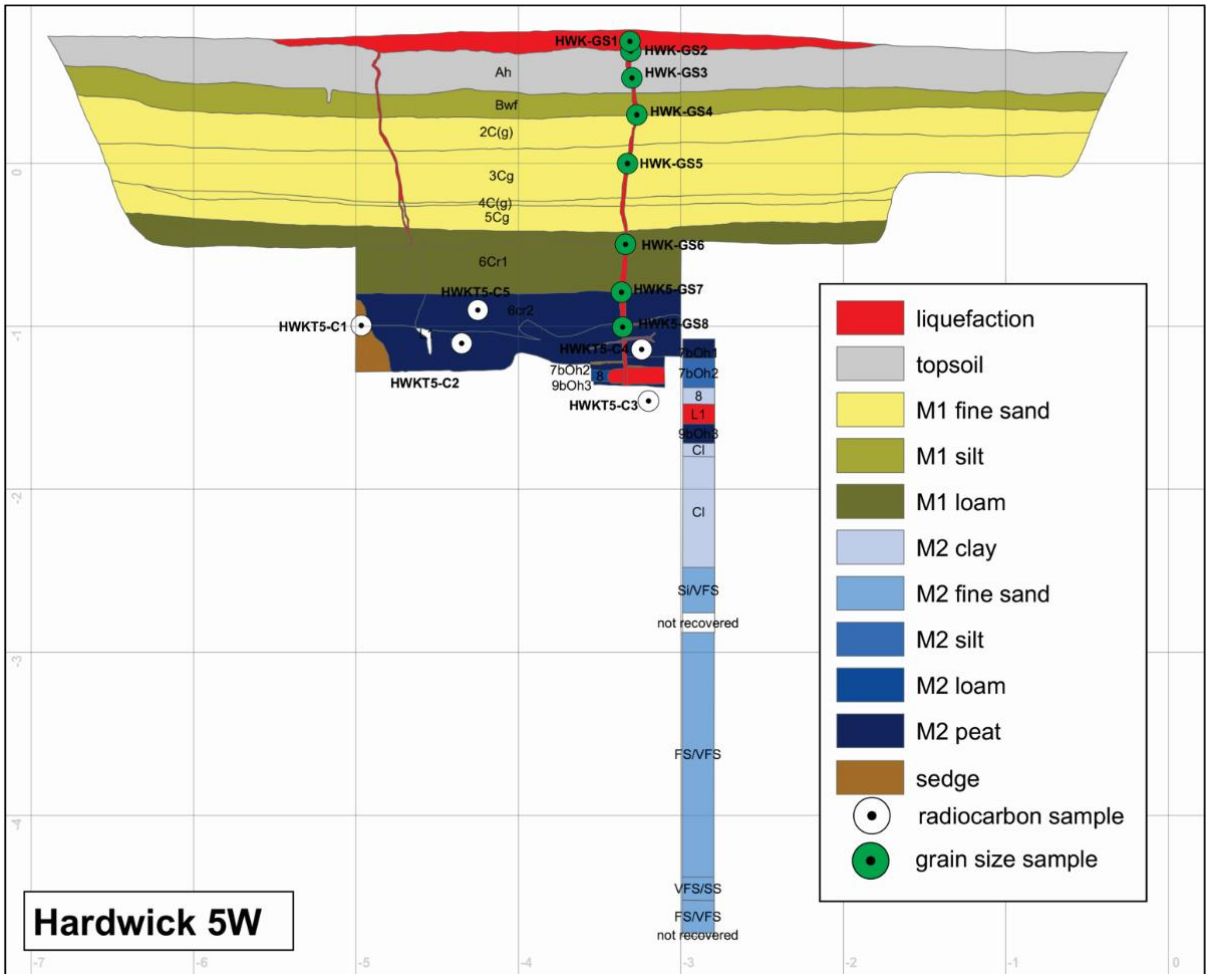

Figure 3. 10 Log of Trench and Core at HWK5, west wall from Villamor et al.,(2016; 2014). M1 (fine sand, silt and loam) in this figure corresponds to the crevasse splay of Figure 3.5 and 3.6 and M2 (all sub-units) corresponds to M2a in text (channel fill deposit). Note also location of grain size samples taken along the dike (GS3, GS4, GS5, GS6, GS7, GS8) and the sand blows (GS1 and GS2).Red colour is liquefied sand (dikes, sills, and sand blows).

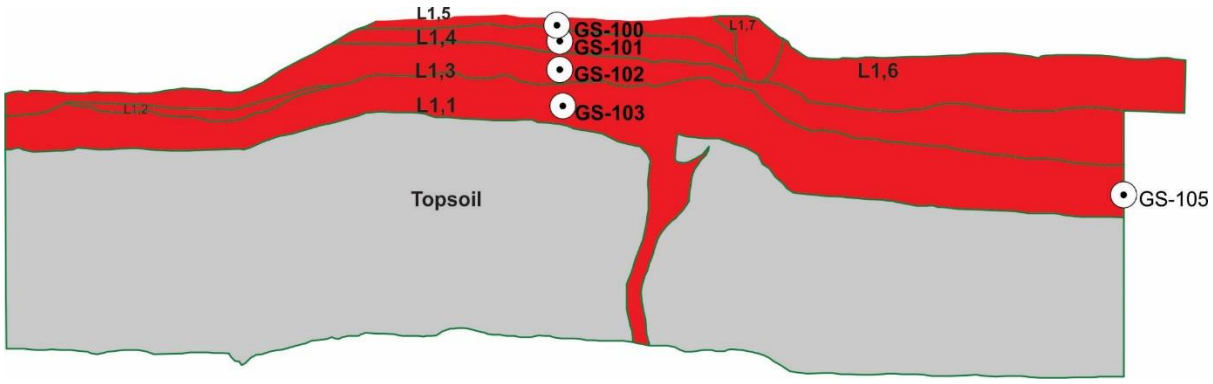

Figure 3. 11 Grain size samples from Trench HWK5, East wall. Grey is the 2010 topsoil unit and red is the liquefied sand (dike and sand blow). The samples were taken from different sand blow units recognized in the field as different liquefaction events or pulses with an event: GS-100 from unit L1,5 (0-2 cm depth); GS-101 from unit L1,4 (3-6 cm depth); GS-102 from unit L1,3 (3-6 cm depth); GS-103 from unit L1,1 (10-13 cm depth); and GS-105 from unit L1,1 but from a more distant location to the vent that sample GS-103 (50-60 cm)

Figure 3.12 shows examples of grain size distribution curves of a sample collected from the sand blow at Trench HWK5 and of a sample collected from the core retrieved at the same trench site. River sediment generally displays a poorly sorted, and thus multimodal (also called multigaussian) grain size distribution curve (see methods section). From the samples analysed, the multimodal grain size distributions were often characterised by abundant modes in the coarser fractions (e.g. fine sand modes) and fewer (less significant) modes in the finer fractions (e.g. clay and silt or coarse silt) – see for example Fig. 3.12a. In contrast, a silty sand (Fig. 3.12b) had more significant modes in the fine fractions but was still dominated by large modes in the coarse fraction. Clean sandy sediment will have cumulative curves similar to Tsuchida's (1970) sand curves (Figure 3.12 c), whereas silty mixtures are likely to have cumulative curves dissimilar from Tsuchida's (1970) curves, crossing liquefaction-soil-behaviour boundaries towards the finest range of grain size (Figure 3.12 d). These characteristics are relevant to the interpretation below.

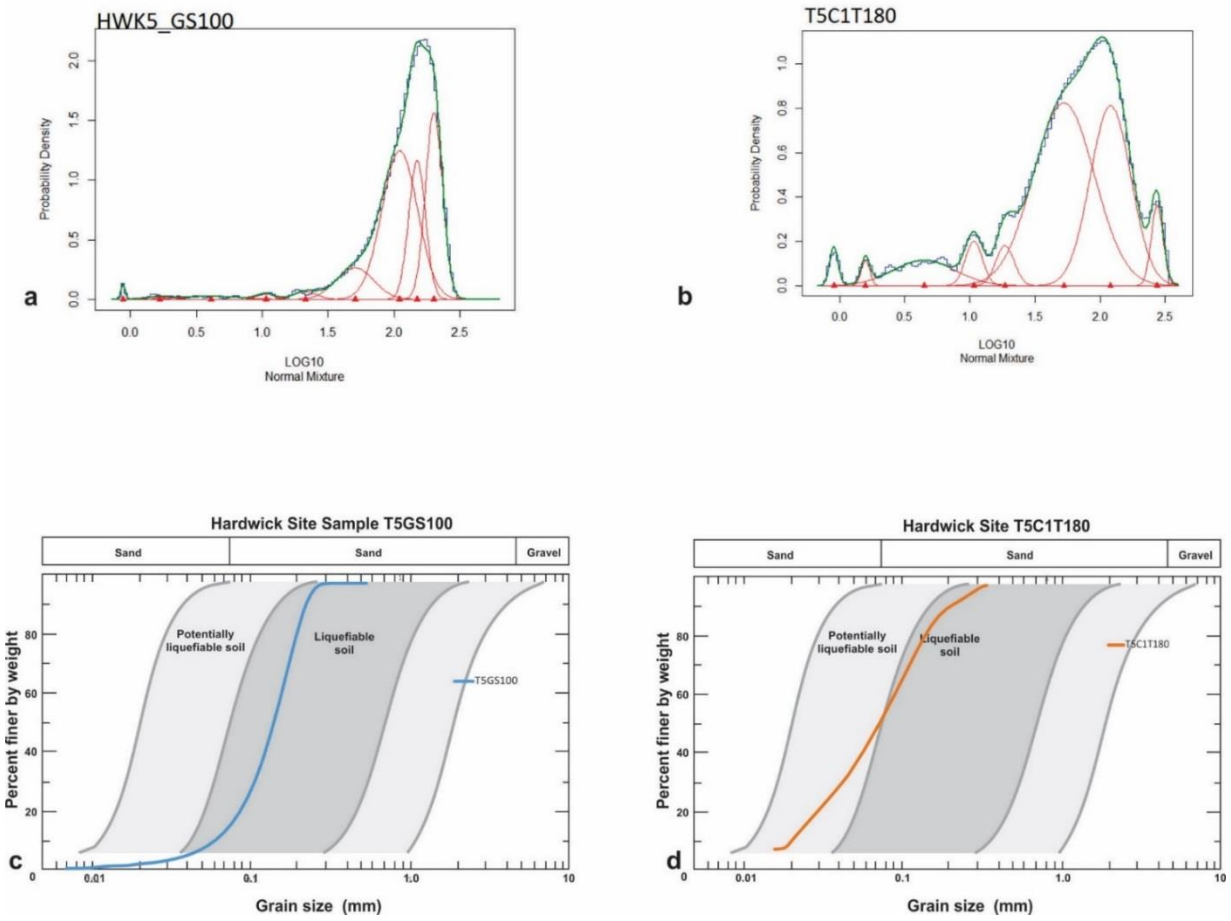

Figure 3. 12 Panels a and b are probability density functions of the mixdist analysis of a better sorted clean sandy sediment vs multimodal poorly sorted grain size distribution at the Hardwick site. Panels c and d are cumulative distribution curves with Tsuchida's (1970) liquefiable soil boundaries. Panels a and c illustrate grain size samples taken from a sand blow unit at Trench HWK5; note the high peak in the fine sand range and the good fit of the cumulative curve to Tsuchida's (1970) liquefiable sediment boundaries. Panels b and d represent a grain size sample collected from a core retrieved at HWK5 at nearly 2.68 m depth. The core sample was characterized by a mixture of silty sand; note the peaks also in the clay and silt range (from 0.0 to 1.0 of the log 10 scale). As a consequence, the corresponding cumulative curve (panel d) crosses the boundaries of the Tsuchida's (1970) liquefiable range.

Figure 3.13 shows results of cumulative grain size distribution curves from Trench HWK5 east and west walls, and from the core. The samples from the east wall, collected from a different part of the sand blow, are sandier and they all fall in Tsuchida's (1970) liquefiable soil area (Figure 3.13 a). In contrast, the samples from the west wall and the core appear less homogeneous and are characterized by a mixture of silty sands (Figure 3.13 b and c). The latter curves cross Tsuchida's (1970) soil boundaries and partially fall in the liquefiable area (for its sandier fraction), although its finer fraction does not.

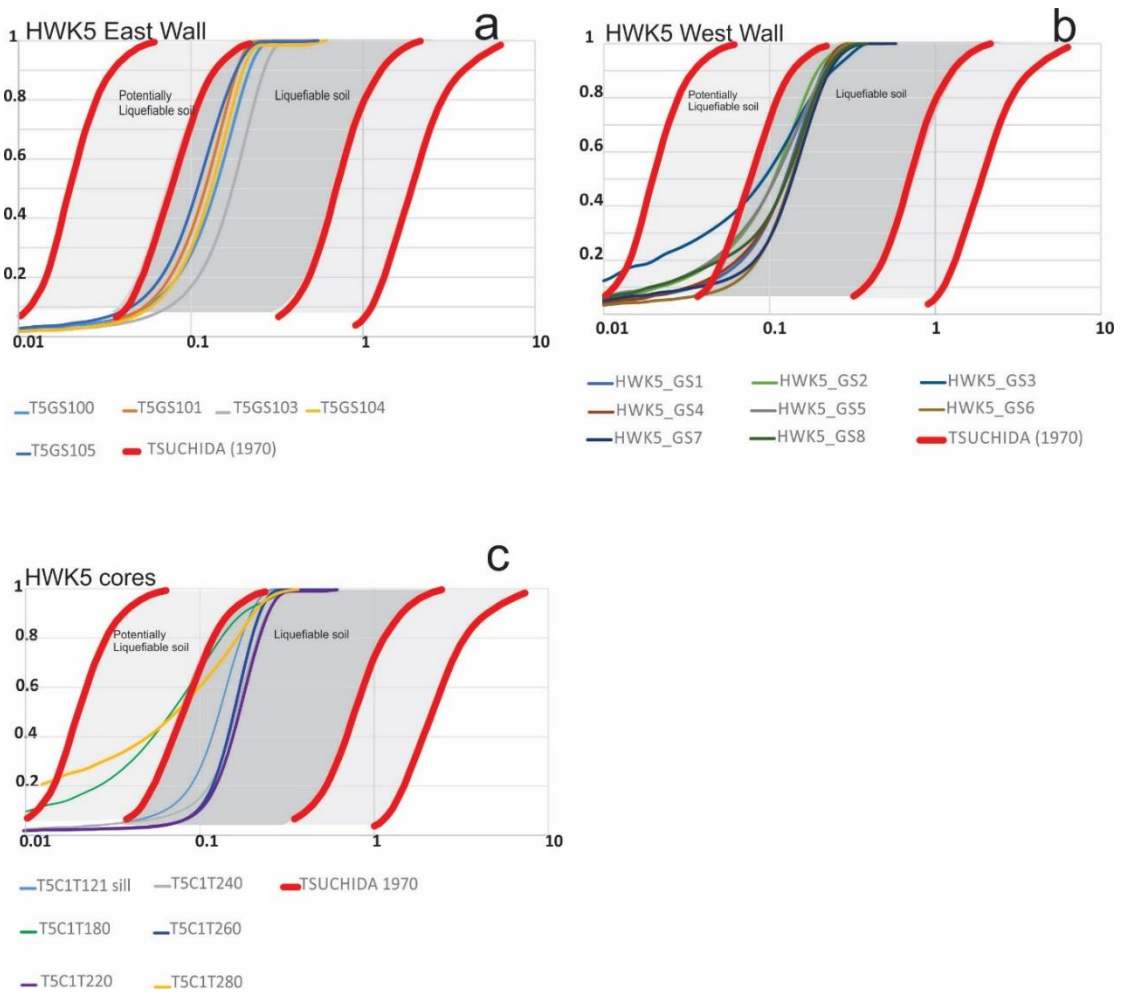

Figure 3. 13 Cumulative grain size distribution curves of samples at Trench HWK5 site with Tsuchida's (1970) liquefiable soil boundaries. a) Samples from the sand blow on the east wall. b) Samples from the west wall. HWK5 GS1 is from the sand blow, and all the other samples are from different depths of the dike. c) Sediment samples from the core at HWKT5 Trench site.

From the comparison of Tsuchida's (1970) cumulative curves at Trench HWK5, it is clear that the sand blow grain size samples are better sorted and they all fall in Tsuchida's (1970) liquefiable range, while dike samples belong only partially to the liquefiable range defined by Tsuchida's (1970) cumulative curves. However, both represent liquefied sands. The similarity of all the grain size samples from the east wall of the trench, which were taken in different sand blow units, suggest the ejecta probably had the same source and underwent similar

sorting processes during emplacement. All core sediment would appear only potentially liquefiable.

3.3.4.3 Mixdist Analysis

The second step of the grain size analysis involved matching the subpopulation modes from the cores with the modes of surface ejecta as a means of identifying the source of the ejecta (see methods section for details). Results of the similarity metric (S) classification are showed in Table 3.1.

TABLE 3. 1 Visual correlation at site HWK5 between core samples and dike and sand blows samples from the west and east walls

Cores \ Trenches			West Wall Trench HWK5								East Wall Trench HWK5				
			GS1	GS2	GS3	GS4	GS5	GS6	GS7	GS8	GS 100	GS 101	GS102	GS103	GS105
CORE SAMPLE (depth in -m)	Unit M2a	T5C1T180 (2.68 g.l.; 3.1 a.sl.)	0.6	0.8	0.8	0.5	0.8	0.8	0.5	0.8	0.8	0.6	0.4	0.5	0.4
	Unit M2b	T5C1T220 (2.98 g.l.; 2.8 m a.s.l.)	0.5	0.5	0.5	0	0.5	0.25	0	0.75	0.5	0.5	0.5	0.25	0.25
		T5C1T240 (3.18 g.l.; 2.6 a.s.l.)	0.9	0.8	0.8	0.9	0.6	0.9	0.6	0.5	0.8	0.9	0.8	0.8	0.6
		T5C1T260 (3.38 g.l.; 2.4 a.s.l.)	0.5	0.25	0.5	1	0.5	0.25	0.75	0.5	0.75	0.5	0.5	0.5	0.5
		T5C1T280 (3.58 g.l.; 2.20 a.s.l.)	0.9	0.9	1	0.6	0.5	0.8	0.5	0.8	0.5	0.6	0.6	0.6	0.6

Red= high value of S (0.8 to 1); yellow= S value from 0.8 to 0.4; green= low value of S from 0.4 to 0; g.l = ground level; a.s.l= above sea level

A higher S value occurred in samples T5C1T180, T5C1T240, T5C1T280 at 2.68, 3.18 and 3.58 m depth from the ground (3.1, 2.6, 2.4 m a.s.l. in Figure 3.5), respectively, and they all occurred in Unit M2b. Furthermore, sample T5C1T280 was selected very close to the core portion in which there were rip up clasts, further supporting the inference that M2b is likely

to be the source of ejecta at the Hardwick site, in the vicinity of Trench HWK5. Figure 3.14 summarizes evidence to identify the layer that liquefied and supplied ejecta at Trench HWK5.

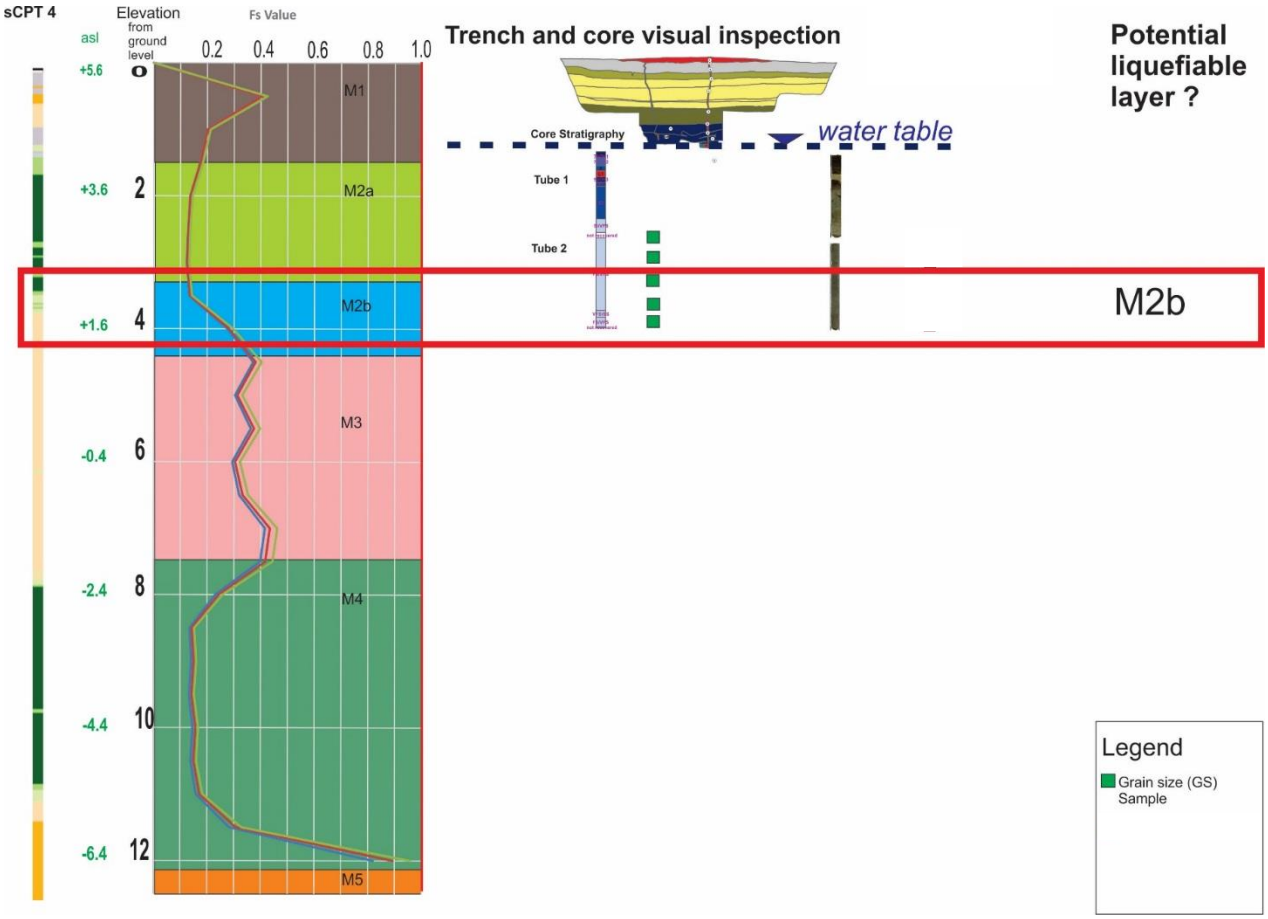

Figure 3. 14 Synoptic diagram presenting different types of evidence for identifying the liquefiable layer at Trench HWK5 (the red box). The tests used at this site are seismic CPT, paleoseismic trench, core, grain size analysis. See text for details of evidence for liquefaction from different techniques. See Figures 3.5 and 3.6 for the legend of the stratigraphic units.

3.3.4.5 Grain size correlation at Trench HWK6

In Trench HWK6, samples from paleo- (HWK GS1 and GS2) and modern liquefaction features (HWK GS3 and 4) were collected. Grain size samples were collected along the cores every 20 cm. Locations of grain size samples and detailed core descriptions can be found in Villamor et al., (2014). The cumulative diagrams (Figure 3.15) showed that both modern and paleoliquefaction samples fall in the liquefiable range. However, the samples collected from the cores have a higher variability (Figure 3.15 a). The first two sections of Core 1 HWK6, between ~2.5 and 3.9 m a.s.l. were characterized by an alternation of laminated silt and very

fine sand, resembling point bar deposits. They fall in Tsuchida's (1970) "potentially liquefiable area". The third and fourth sections of Core 1 HWK6, between ~ 0.4 and 2.1 m a.s.l. comprised massive, fine and medium, clean sand. The latter sand occurred within Tsuchida's (1970) "liquefiable soil range".

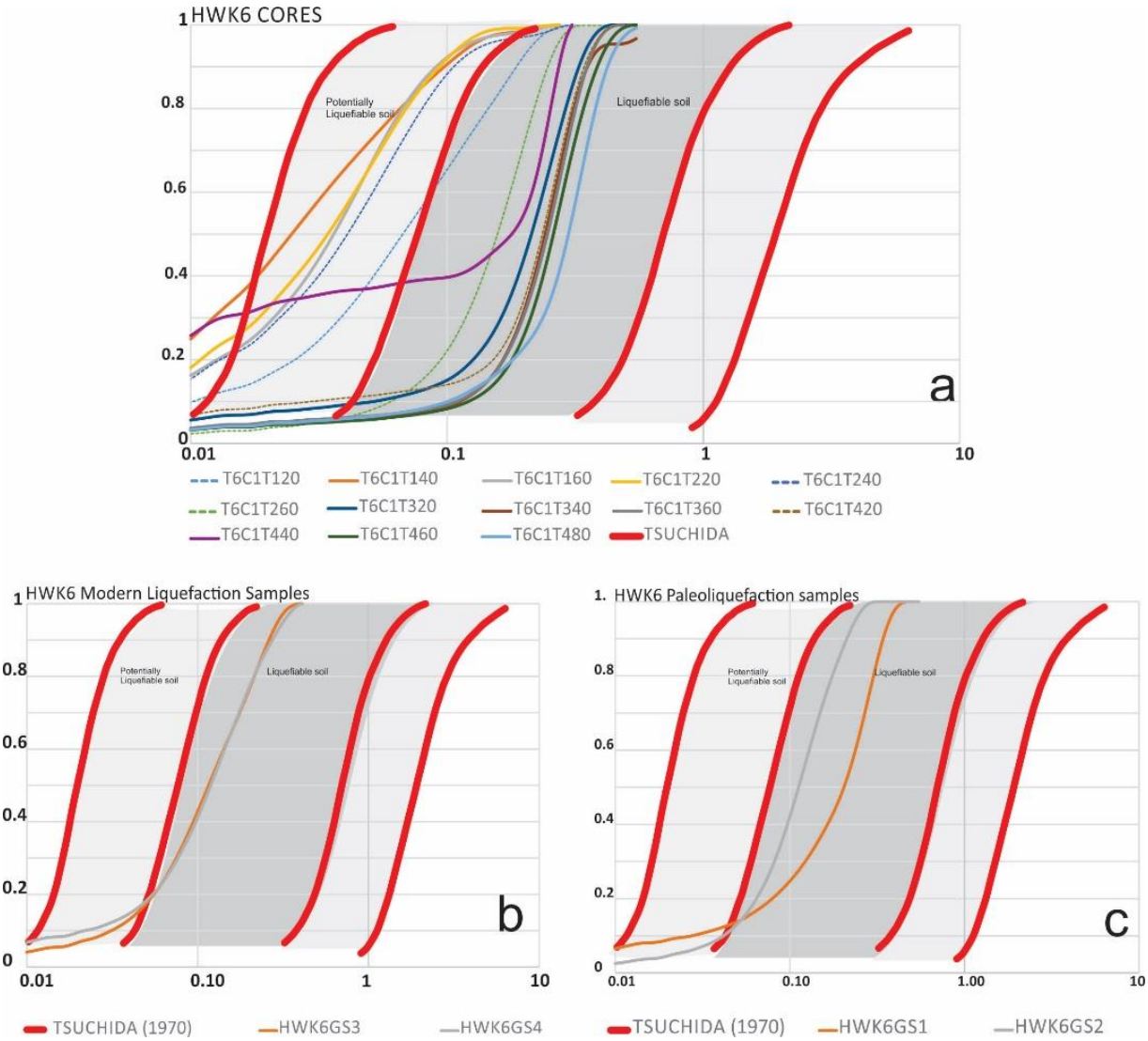

Figure 3. 15 Cumulative grain size distribution curves of samples at Trench HWK6 site with Tsuchida's (1970) liquefiable soil boundaries. a) Cumulative curves for grain size samples from cores. b) Cumulative curves for modern liquefaction samples (HWKGS3 is a modern dike, HWK6GS4 is a modern sand blow). c) Cumulative curves for paleoliquefaction samples (HWKGS1 and HWKGS2 are samples from a paleodike on the trench floor, see Villamor et al., 2016 for paleodike description).

Table 3.2 shows the grain size subpopulation similarity metric (S) of the samples collected in Trench HWK6. The modern liquefaction samples (GS3 and GS4) at HWK6 matched best with

samples from 3.9 to 4.8 m depth from g.l[6]., which corresponds to unit M2c (Pre-channel sands). The paleo liquefaction sample (GS1) also had a strong similarity to core sediments between 3.9 and 4.8 m depth from g.l. However, paleoliquefaction sample GS2 did not show a consistent S value with any area of the cores apart from at 1.9 and 4.4 m depth from g.l. No high S value was found with the samples collected in core 2 at HWK6, except for the modern liquefaction samples and a core sample at 1.51 m depth from g.l. (Table 3.3). From Figs 3.5 and 3.6, it appears that this core, which extended to only 3.0 m depth from g.l., did not reach the liquefiable layers beneath Trench HWK6.

TABLE 3. 2 Visual correlation at site HWK6 between samples from Core 1 and modern and old liquefaction features from the East wall of Trench HWK6.

Cores \ Trench			GS1 Paleodike (on the floor)	GS2 Paleo dike	GS3 Modern dike	GS4 Modern sand blow
CORES SAMPLES (depth –m-)	Unit M2b	T6C1T120 1.7 m g.l; 3.8 m a.s.l.	0.3	0.6	0.6	0.6
		T6C1T140 1.9 m g.l.; 3.6 m a.s.l.	0.3	0.8	0.3	0.4
		T6C1T160 2.1 m g.l.; 3.4 m a.s.l.	0.1	0.6	0.6	0.6
		T6C1T220 2.6 m g.l.; 2.95 m a.s.l.	0.6	0.6	0.5	0.3
		T6C1T240 2.8 m g.l.; 2.75 m a.s.l.	0.4	0.3	0.6	0.3
		T6C1T260 3.0 m g.l.; 2.55 m a.s.l.	0.6	0.3	0.3	0.3
		T6C1T320	0.6	0.3	0.6	0.4

[6] g.l. is an abbreviation for ground level.

CORES SAMPLES (depth –m-)		3.5 m g.l.; 2.1 m a.s.l				
	Unit M2c	T6C1T340 3.7 m g.l.; 1.9 m a.s.l.	0.4	0.3	0.5	0.4
		T6C1T360 3.9 m g.l.; 1.7 m a.s.l.	0.9	0.2	0.4	0.9
		T6C1T420 4.4 m g.l.; 1.25 m a.s.l.	0.6	0.7	0.6	0.8
		T6C1T440 4.6 m g.l.; 1.05 m a.s.l.	0.7	0.4	0.6	0.7
		T6C1T460 4.8 m g.l.; 0.95 m a.s.l.	0.7	0.4	0.6	0.6
		T6C1T480 5.0 m g.l.; 0.75 m a.s.l.	0.4	0.3	0.5	0.5

Red= high value of S (0.8 to 1); yellow= S value from 0.8 to 0.4; green= low value of S from 0.4 to 0; g.l = ground level; a.s.l= above sea level

TABLE 3. 3 Visual correlation at site HWK6 between samples from Core 2 and modern and paleo liquefaction features from the East wall of Trench HWK6.

Cores \ Trench			GS1 Paleodike (on the floor)	GS2 Paleodike	GS3 Modern Dike	GS4 Modern sand blow
CORE SAMPLES (Depth m)	Unit M2b	T6C2T120 1.51g.l.; 3.69 a.s.l.	0.3	0.6	0.8	0.8
		T6C2T140 1.71g.l.; 3.49 a.s.l.	0.3	0.4	0.5	0.5
		T6C2T160 1.91g.l.; 3.29 a.s.l.	0.4	0.6	0.5	0.6
		T6C2T180 2.11g.l.; 3.09 a.s.l.	0	0	0.1	0.1
		T6C2T220 2.41 g.l.; 2.79 a.s.l.	0.4	0.3	0.6	0.5
		T6C2T240 2.61g.l.; 2.59 a.s.l.	0	0.1	0	0.1
		T6C2T260	0.1	0.4	0.25	0.4

		2.81 g.l.; 2.39 a.s.l.				
		T6C2T280 3.01 g.l.; 2.19 a.s.l.	0.1	0.22	0.5	0.5

The grain size analysis by mixdist for Trench HWK6 is not as robust as for samples collected at Trench HWK5 (Table 3.1). However, in general terms it supports the inference that Unit M2c (floodplain deposits) between 0.5 and 2.20 m a.s.l. is the likely source layer for ejecta at Trench HWK6 and not the overlying unit M2b (point bar deposits).

3.3.5 Factor of Safety analysis

Detailed analysis of the seismic CPT results can be found in Appendix A1 electronic support of this Chapter. The Factor of Safety (FS) diagrams (Figure 3.16) revealed that all the sites selected for sCPT at the Hardwick site were likely to have experienced liquefaction during the three major earthquakes. Most of the sCPT profiles show FS < 1 for all depths, except for sCPT1 and sCPT3 profiles where FS > 1 between 10 - 12 m and 12 - 14 m depth, respectively. A FS > 1 occurs where the penetrometer encounters gravel, which is not commonly liquefiable because of the coarser size of the sediment and the higher permeability, which do not allow the build-up of a pore water pressure sufficient to trigger liquefaction. The sCPT results indicate that a gravel occurs between 9 and 12 m depth beneath the Halswell floodplain at the site.

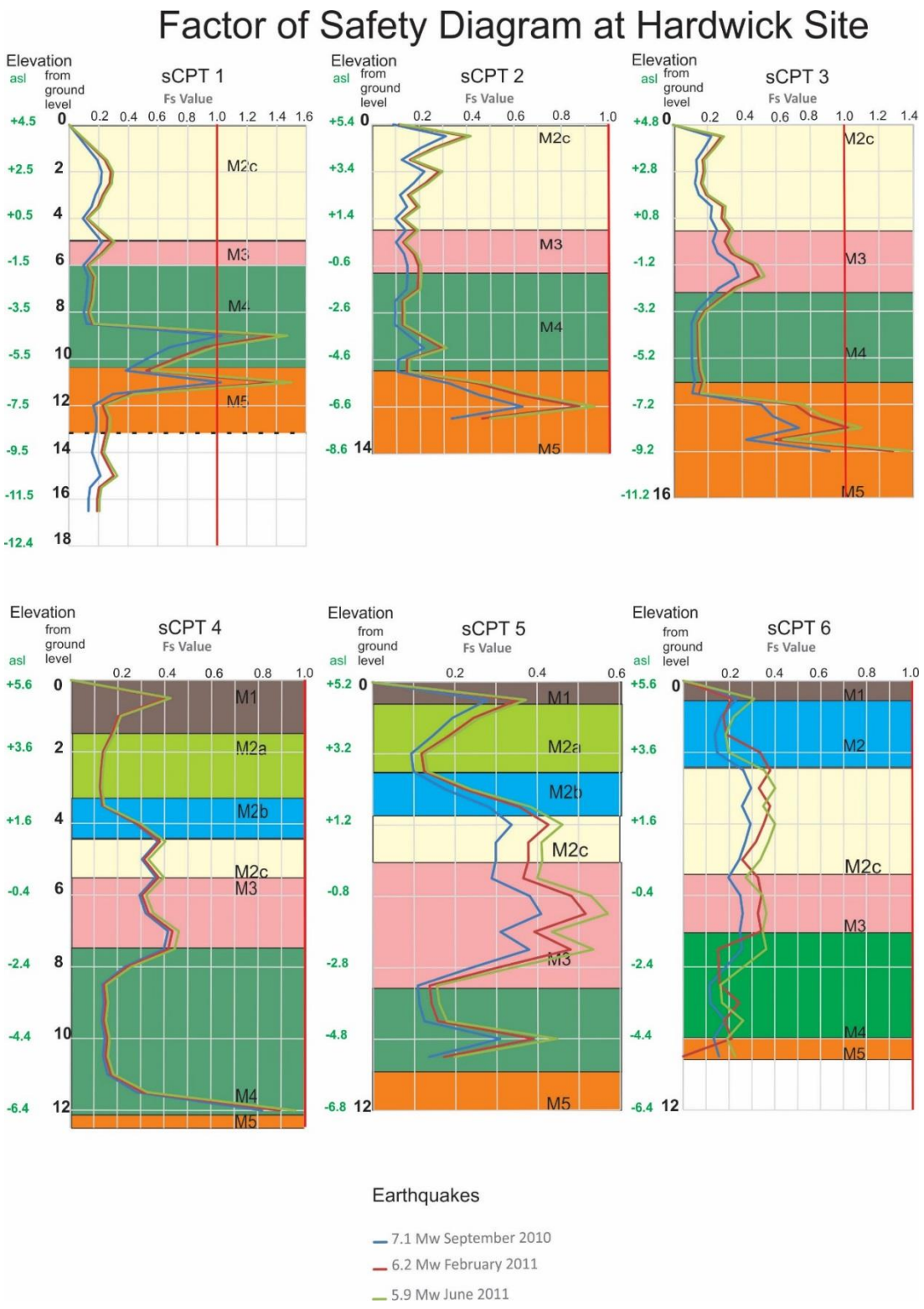

Figure 3. 16 Factor of Safety Analysis at Hardwick site. Note the FS is less than 1 across most of the profile analysed. FS >1 only occurs at sCPT 1 and 3 between 9 and 12 m depth (from ground level) due to the gravel encountered. The stratigraphic units identified at Hardwick site (M1 to M5; Figure 3.5) are superimposed on the sCPT results.

At Trench HWK5, sCPTs 4 and 5 (Figure 3.16) show the lowest FS (0.1) for layers M2a and b. Coincidence with other lines of evidence suggests unit M2b is the likely ejecta source despite FS < 1 in layers below. It is possible that the liquefaction susceptibility of the liquefied layer has changed after liquefying (that is always an intrinsic problem of CPT analysis after the event); however, these results suggest that the layer that liquefied in 2010-2011 was still highly liquefiable in 2015 when CPT data were obtained.

Seismic CPT 3, 2 and 1 were located in the floodplain, where there was no surface manifestation of subsurface liquefaction, to study the stratigraphic differences among the landforms with and without surface ejecta. The results of the FS computation revealed that the floodplain is also likely to experience liquefaction (FS<1) with some layers having FS < 0.1, a similar susceptibility to those found in M2b within the meander channel. The lack of expression of surface manifestation of liquefaction must relate to other conditions that do not allow the liquefied sediment to surface. Drained conditions are highly unlikely based on the soil characteristics (Villamor et al., 2016)

3.4 The Marchand Site

3.4. 1 Geomorphic association

At the Marchand site, Villamor et al., (2016; 2014) suggested that sand blows had a strong spatial association with two subtle ridges on the inside bend of the Halswell River floodplain (Figure 3.17). The detailed geomorphic map shown in Figure 3.17 suggests that the two ridges could correspond to different depositional settings. The northern (outer) ridge, named B0 bar, and the southern (inner) ridge, B1 bar, were each severely affected by liquefaction, B1 more so. From the aerial photos (Almond et al., 2010b) it is obvious that the ejecta on the outer ridge have an olive-brown colour, whereas the ejecta on the inner ridge are grey (Figure 3.17 b).

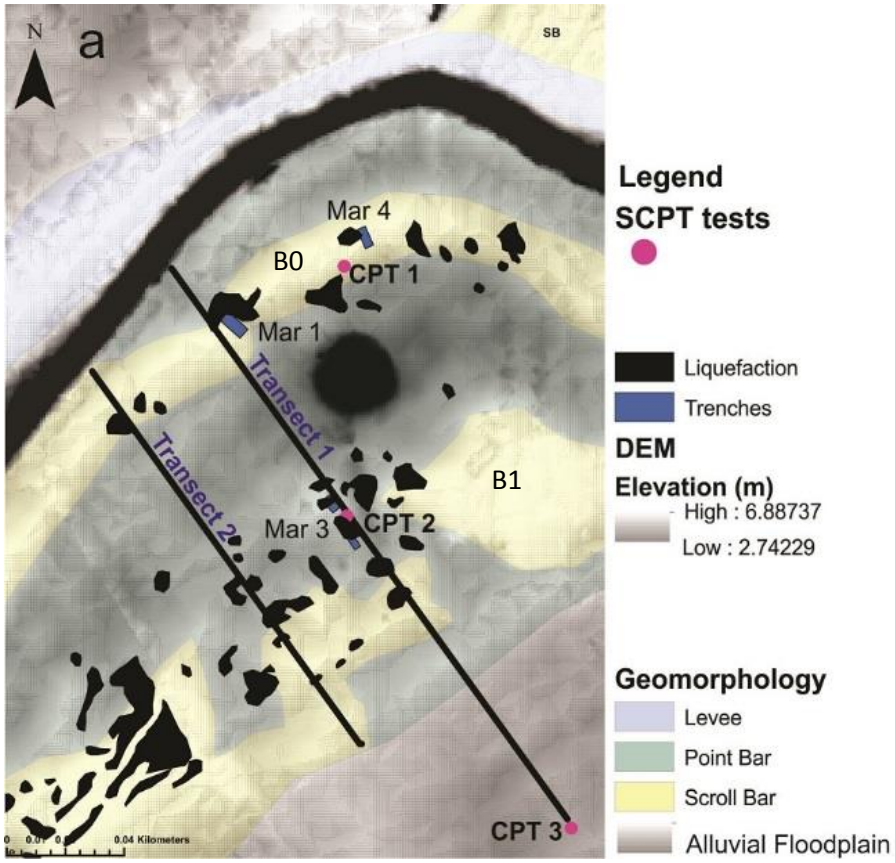

Figure 3. 17 Marchand site a) Geomorphic map and CES Liquefaction surface manifestation (in black) at the Marchand site (Halswell River, Greenpark, 24 km southwest of Christchurch). Liquefaction surface manifestation occurs along two scroll bars (higher elevation areas mapped in yellow and labelled B0 and B1). Also note more substantial liquefaction affecting B1 bar. Black lines are location of stratigraphic transects. Also, note location of trenches and sCPTs; b) Aerial photos of the Marchand site taken after the September 2010 earthquake. These aerial photos show the difference in colour of the ejecta on B0 (olive-brown) and B1 (grey).

3.4.2 Sediment architecture

At the Marchand site, two topographic cross sections were built perpendicular to the Halswell River (Transect 1 is 230 m long; Transect 2 is 160 m long; Figure 3.17) in order to map the stratigraphy and support identification of source layers for surface ejecta. On both transects the higher topographic areas correspond with the two bars, whereas the swales and the floodplain occupied the lower elevation areas (~ 5.4 m a.s.l.).

Transect 1 crosses B0 bar at Trench Mar 1[7] (and associated Core 1 Mar 1) and B1 bar at Trench Mar 3 (and associated Core 1 Mar 3). The transect ends at sCPT3 (Figure 3.17 and 3.18).

[7] For abbreviations the trenches at Marchand site are called Trench Mar 1= Trench Marchand 1; Trench Mar 2= Trench Marchand 2; Trench Mar 3= Trench Marchand 3

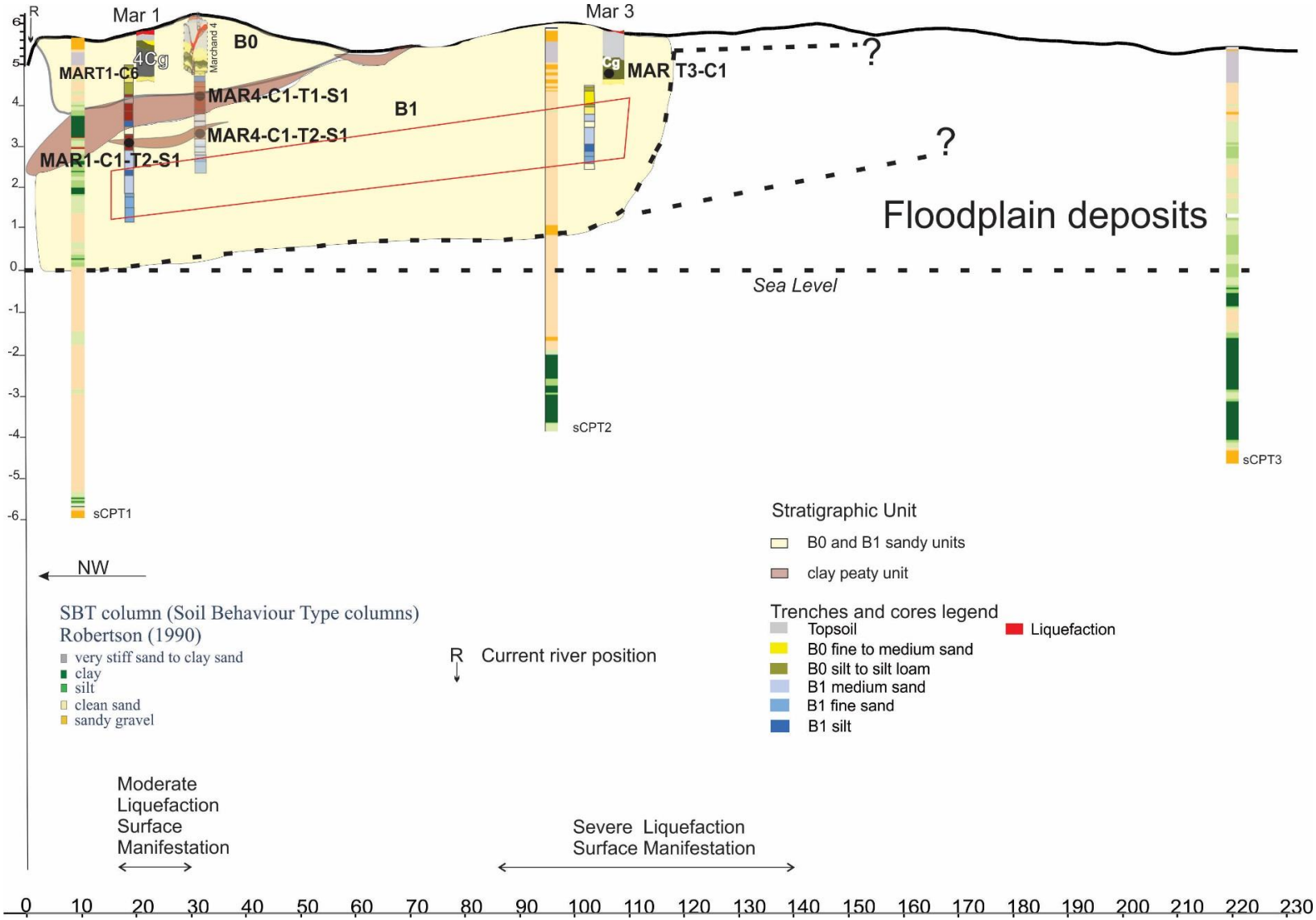

Figure 3. 18 Stratigraphic cross-section along Transect 1 at the Marchand site including trenches Marchand (Mar for abbreviation in the text) 1 and 3, cores and sCPT stratigraphy. Trench Mar 4 is projected along the transect but it is not physically on the transect line. The red frame highlights the possible ejecta source layer. More details on the identification of the source layer are explained in the text. Note on this transect the dated radiocarbon samples are noted, for details see Appendix 1. Elevation in m on the vertical axis and Distance in m on the horizontal axis

Seismic CPT1 has been projected onto Transect 1 but is located ~40 meters north-eastward on the point bar. Seismic CPT2 is physically located along Transect 1 (Figure 3.17). Trench Mar 4 is also projected onto Transect 1 as it was excavated nearly 50 m north-eastward of Transect 1 and, within the same point bar (Figure 3.17). Trench Mar 4 has a similar stratigraphy to Trench Mar 1, hence it makes a contribution in defining the stratigraphy beneath B0 bar. One (1.5 GHz) GPR profile was surveyed along Transect 1 (Figure 3.19).

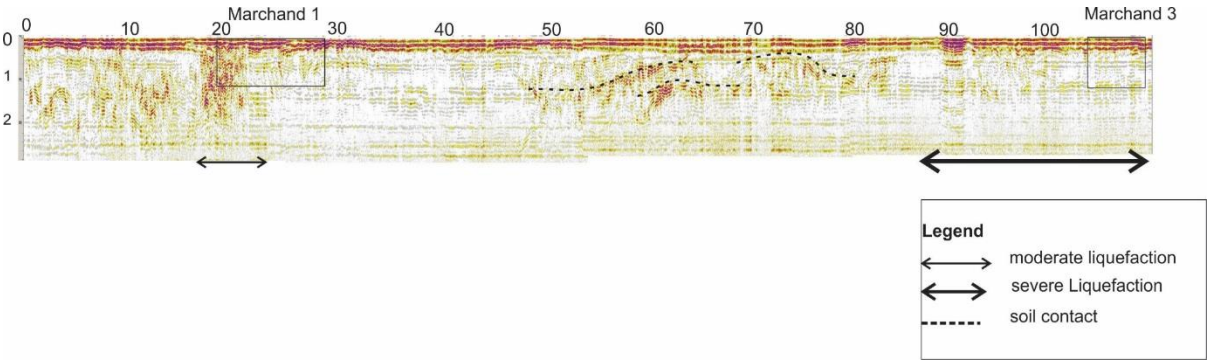

Figure 3. 19 GPR image along Transect 1 at the Marchand site with 1.5GHz GPR Antenna. Maximum resolved depth shown on image is 2 m. Note disturbed reflectors at areas where liquefaction was identified at the surface; however, not all liquefaction disturbance can be clearly seen in the radar-gram. In this radar-gram it is also possible to identify an en-enchelon structure that likely resembles the point bar stratigraphy. Horizontal and vertical scales are in metres.

Transect 2 (Figure 3.20) was oriented parallel to, but south of, Transect 1 and also crossed both ridges. The stratigraphic cross-section along Transect 2 was inferred from nine auger holes (Almond et al., 2010a) and a GPR profile at 1.5 GHz (Figure 3.20). Villamor et al. (2014) sedimentary units have been refined here and renamed according to the B0 and B1 terminology.

In general, the stratigraphy of a point bar is characterized by a coarser sandy deposit occurring at the base of the bar, while overlying (cross) stratified sand and silt distinguish the different steps of river migration or lateral point bar accretion (Chapter 1, Figures 1.9 and 1.10). The uppermost unit includes very fine sediment such as silt, loamy silt and clay deposited as part of a vertical accretion.

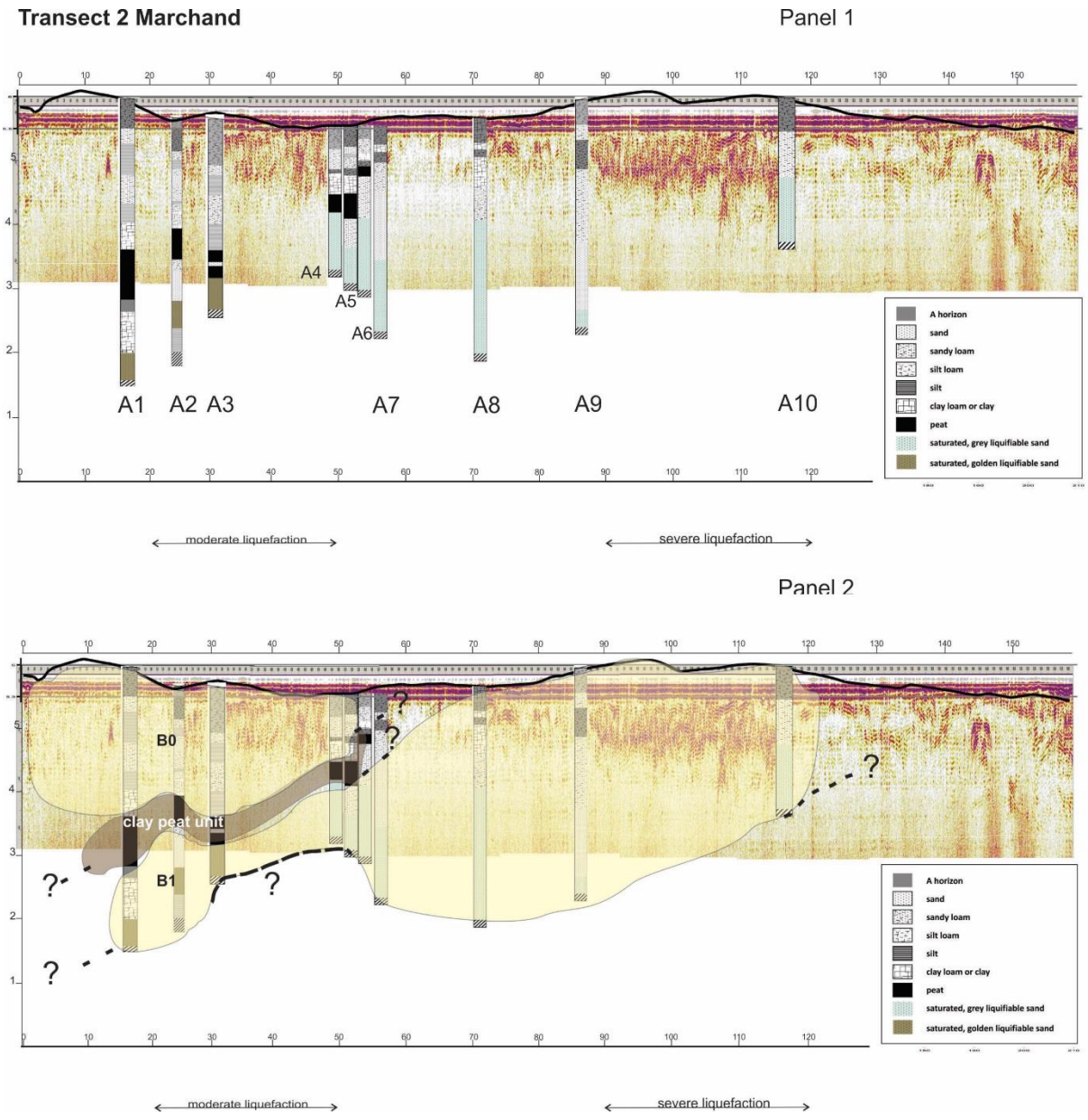

Figure 3. 20 Transect 2 at Marchand site. Panel 1 shows GPR image (1.5GHz GPR) antenna overlain by stratigraphy from auger hole (A1 to A10) data by Almond et al (2010a), Panel 2 shows interpretation of units B0, B1 clay peat unit and B1 sandy component unit. Depths measurements are expressed in elevation above sea level. Note that radar gram has not been corrected for topography. Depth in meters on the vertical axis and Distance in meters on the horizontal axis.

Unit B1 represents the oldest deposit at the site in the area of surface ejecta. It comprises clean sands forming (scroll) bar B1, most distant from the river, and underlies bar B0. In Transects 1 and 2, unit B1 fines in the south-east, but plunges beneath B0 in the northwest, being separated by a buried soil horizon of the peaty clay unit. Beneath the buried peay clay unit the sands of B1 are stained olive-brown, and these sands were also observed in the ejecta

between 15-30 m and 20-50 m along Transects 1 and 2, respectively, and at Trenches Mar 1 and Mar 4.

Unit B0 is represented by the clean sand unit in sCPT1 and very fine sandy beds in Trench Mar1 and Core 1. In the auger holes of Transect 2, B0 includes sandy loams, silty loams and silts. Where exposure permits, it appears that B0 contains a greater proportion of fines than the older B1.

A close look at Transects 1 and 2 shows that sand blows were larger along the wider point bar B1. This could have been caused by a larger volume of liquefiable and water-saturated sand within unit B1. Figure 3.18 shows that the ridge seems to be located over a thicker section of unit B1 (6 m thickness of water saturated sand), while the point bar (B0) has ~ 1 m thickness of the B0 unit and another 1-2 m of water saturated sand belonging to B1.

3.4.3 Age of the sedimentary sequence

Unit B1 is undated, although it must predate the buried peaty clay unit that overlies it. Plant material at the base of the peaty clay unit beneath Trench Mar 4 (3.06 m below the surface, and close to the top of B1) yielded an age of 1918±20 ^{14}C y B.P. (AD 73-206; sample MAR4 C1-T2-S1) (Figure 3.18). Plant material from the top of the clay peat unit (1.77 m below the surface) was dated at 709±19 ^{14}C y B.P. (AD 1286-1386, sample MAR4 C1-T1-S1) (Figure 3.18).

Together the ages define a period from AD 73 to AD 1400 (at the outer limit) when the river was absent from this site and a soil formed with only minor accumulation of clay overbank sediment. Unit B0 must be younger although ages from detrital organics within it yielded ages that were older then AD 1400. A lump of sediment with embedded fragments of charcoal, from unit 4Cg ~1.30 m deep on the east wall of Trench Mar 1 gave an age of 861±18 ^{14}C y B.P. (AD 1187-1268; sample MAR T1-C6), while a piece of wood (at 2.9 m below the surface)

yielded an age of 1009±18 ^{14}C y B.P. (AD 1024-1148; sample MAR1-C1-T2-S1), Figure 3.18. The age reversals created by these two samples are reconciled in terms of erosion and reworking of wood and organics from the underlying peaty clay unit into unit B0. The ages afforded by the two samples in unit B0 are bracketed by the period in which the peaty clay unit formed, corroborating the interpretation of reworking.

3.4.4 Characterizing the ejecta source layer at Trench Mar 1 and Mar 4

The grain size correlation of Trenches Mar 1 and Mar 4 is presented together as they both sit on B0 bar (Figure 3.17 a) and have similar stratigraphy.

3.4.4.1 Grain size correlation at Trench Mar 1

At Trench Mar 1, five grain size samples were collected from the sand blow on the northeast wall of the trench (Figure 3.21a), namely MAR T1 GS1, MAR T1 GS2, MAR T1 GS3, MAR T1 GS4, MAR T1 GS5. Twelve samples were collected at different depths from the sandy portion (B0 and B1, see Figure 3.18) of Core 1 at Trench Mar 1 (M1C1T120, M1C1T140, M1C1T160, M1C1T260, M1C1T320, M1C1T340, M1C1T360, M1C1T370, M1C1T420, M1C1T440, M1C1T460, M1C1T480).

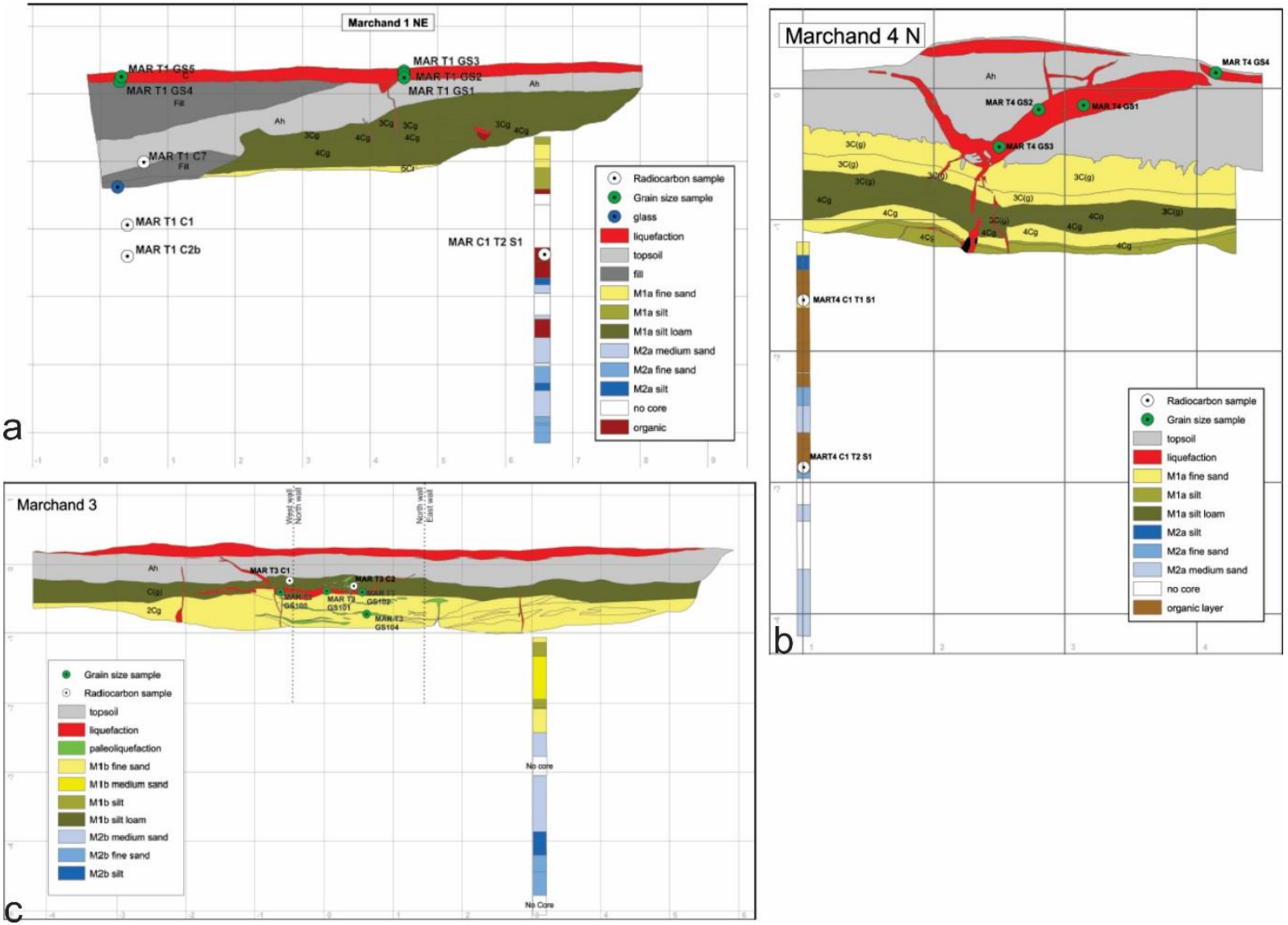

Figure 3. 21 Detail of Trenches and cores retrieved at Marchand site from Villamor et al., 2016. a) Trench Marchand 1, north east wall; b) Trench Marchand 4, north wall c) Trench Marchand 3. Unit M1a fine sand, silt and silt loam of Trenches Mar 1 and 4 correspond to Unit B0 of the text. Unit M1b fine sand, silt and silt loam of Trench Marchand 3 correspond to Unit B0 in the text. Note the location of the grain size samples in each trench.

Figure 3.22 (a and b) shows the cumulative frequency curves of grain size analysis at Trench Mar 1 for samples collected from the core sections and from the stacked sand blows, respectively. As seen at the Hardwick site, the samples from sand blows appear to be sandier and better sorted and most of them fall into the Tsuchida's liquefiable soil area of the grain-size distribution diagram. However, most of the core samples are characterized by a mixture of sand and silt and cross Tsuchida's soil boundaries.

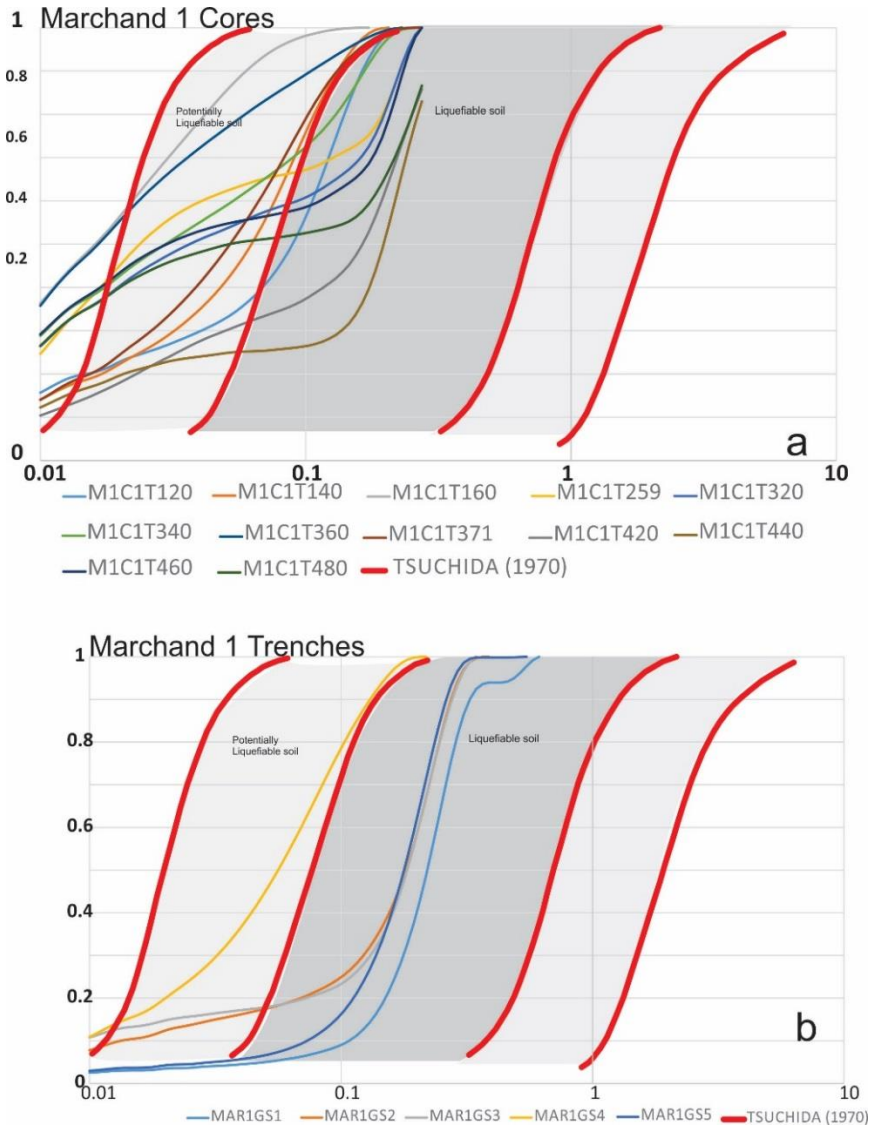

Figure 3. 22 Cumulative grain size distribution curves of samples at Trench Mar 1 site with the Tsuchida's (1970) liquefiable soil boundaries. a) Curves from core samples; b) Curves from samples collected at different depths within the sand blow in the trench. Sample locations in Figure 3.21.

Table 3.4 summarizes the similarity metric at Trench Mar 1.

TABLE 3. 4 Visual correlation at site Trench Mar 1 between samples from the Core and modern liquefaction features.

Cores \ Trench			MAR T1 GS1	MAR T1 GS2	MAR T1 GS3	MAR T1 GS4	MAR T1 GS5
CORE SAMPLES (DEPTH-m)	Unit B0	M1C1T120 1.03g.l.; 4.77 a.s.l.	0.2	0.4	0.4	0.6	0.2
		M1C1T140 1.23g.l.; 4.57 a.s.l.	0.1	0.8	0.6	0.4	0
		M1C1T160 1.43g.l.; 4.37 a.s.l.	0.2	0.5	0.2	0.4	0.1
	Unit B1	M1C1T260 2.22g.l.; 3.58 a.s.l.	0.2	0.8	0.4	0.4	0.2
		M1C1T320 2.83g.l.; 2.97 a.s.l.	0.2	0.8	0.6	0.8	0.2
		M1C1T340 3.03g.l.; 2.77 a.s.l.	0.2	0.6	0.6	0.6	0.1
		M1C1T360 3.23 g.l.; 2.57 a.s.l.	0.2	0.5	0.6	0.7	0.1
		M1C1T370 3.34g.l.; 2.35 a.s.l.	0.2	0.6	0.3	0.7	0.1
		M1C1T420 3.83 g.l.; 2.15 a.s.l.	0.2	0.5	0.4	0.3	0.2
		M1C1T440 4.03 g.l.; 1.77 a.s.l.	0.2	0.8	0.4	0.7	0.1
		M1C1T460 4.23 g.l.; 1.57 a.s.l.	0.25	0.8	0.6	0.7	0.1
		M1C1T480	0	0.6	0.6	0.6	0.2

		4.43 g.l.; 1.37 a.s.l.					

Red= high value of S (0.8 to 1); yellow= S value from 0.8 to 0.4; green= low value of S from 0.4 to 0; g.l = ground level; a.s.l= above sea level Samples M1C1T420 through to M1C1T480 fall into the saturated golden liquefiable sand identified in Panel 2 of Figure 3.20.

3.4.4.2 Grain size correlation at Trench Mar 4

At Trench Mar 4, four grain size samples were collected in different portions of a sand dike intruding a blister feature (Villamor et al, 2014, 2016) on the north wall (MAR T4 GS1, MAR T4 GS2, MAR T4 GS3; Figure 3.21b), and from the related sand blow, MAR T4 GS4. From Core 1 of Trench Mar 4, eight grain size samples were collected from the sandy units at different depths (M4C1T120, M4C1T122, M4C1T140, M4C1T220, M4C1T240, M4C1T260, M4C1T320, M4C1T340).

Figure 3.23 illustrates the cumulative curves of Trench Mar 4 of samples collected from the cores (Figure 3.23a) and in the trenches (Figure 3.23b) with Tsuchida's (1970) liquefiable soil boundaries. In both sets of samples (ejecta and core), cumulative curves had distinct fine tails, reflecting a relatively high component of silt and clay. Thus, the cumulative curves do not fully fall within Tsuchida (1970) liquefiable soil area but they cross the boundaries and are skewed towards the fines, with the sand blow samples fitting somewhat better to Tsuchida (1970) liquefiable soil area than the core samples.

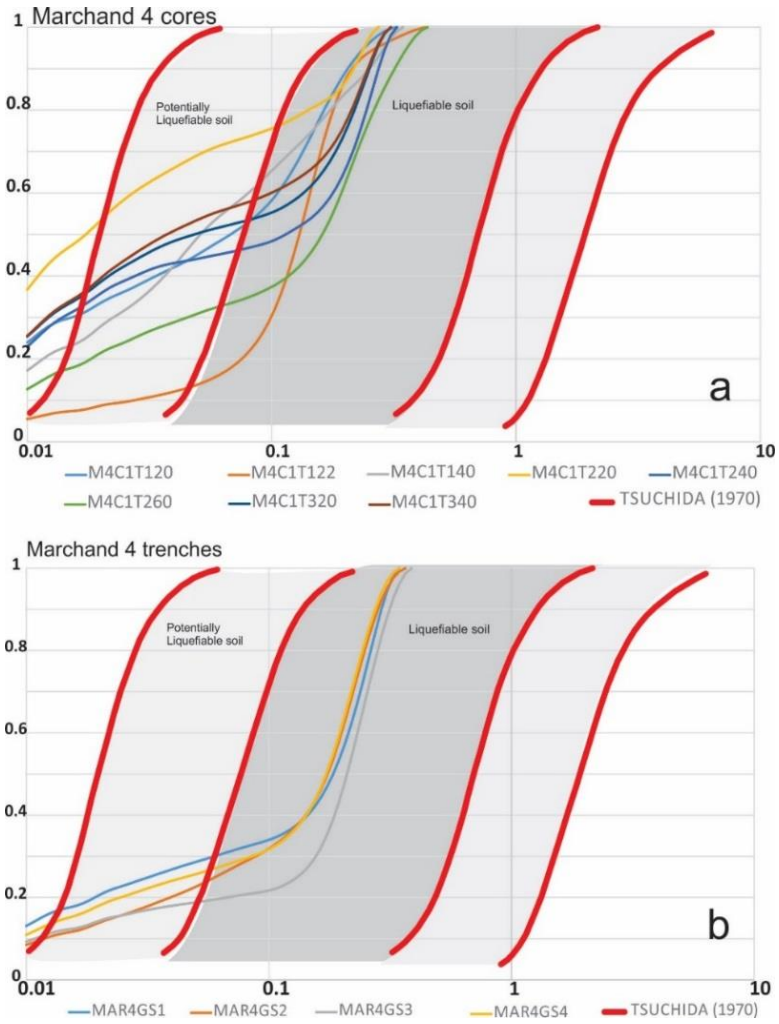

Figure 3. 23 Cumulative grain size distribution curves at Trench Mar 4 with Tsuchida (1970) liquefiable soil boundaries. a) Curves for samples collected from the core sediment. b) Curves for samples collected from trenches; MAR4GS1, MAR4GS2, MAR4GS3 are samples from a dike, and MAR4GS4 is a sample from a sand blow. Sample locations are shown in Figure 3.21.

Table 3.5 displays the correlation between sediment samples taken from the sand dike at Trench Mar 4 (clearly injected by olive- brown sand, Villamor et al., 2016; 2014) and Core 1.

TABLE 3. 5 Visual correlation at site Trench Mar 4 between samples from the Core and modern liquefaction features.

Cores \ Trench			MART4GS1 (dike- blister)	MART4GS2 (dike- blister)	MART4GS3 (dike-blister)	MART4GS4 (sand blow)
CORE SAMPLES (Depth-m)	Unit B0	M4C1T120 1.53g.l.; 4.67 a.s.l.	0.3	0.8	0.8	0.8
		M4C1T122 1.55g.l.; 4.65 a.s.l.	0.1	0.2	0	0
		M4C1T140 1.73g.l.; 4.47 a.s.l.	0.4	0.6	0.8	0.7
	Unit B1	M4C1T220 2.53g.l.; 3.67 a.s.l.	0.3	0.7	0.6	0.7
		M4C1T240 2.73g.l.; 3.47 a.s.l.	0.4	0.4	0.8	0.7
		M4C1T260 2.93g.l.; 3.27 a.s.l.	0.4	0.4	0.3	0.4
		M4C1T320 3.53g.l.; 2.67 a.s.l.	0.4	0.8	0.8	0.9
		M4C1T340 3.73g.l.; 2.47 a.s.l.	0.4	0.9	0.8	0.9

Red= high value of S (0.8 to 1); yellow= S value from 0.8 to 0.4; green= low value of S from 0.4 to 0; g.l = ground level; a.s.l= above sea level Samples M4C1T320 and M4C1T340 belong to the saturated golden liquefiable sand identified by Almond et al 2010 and pictures in Panel 2 of Figure 3.20.

3.4.4.3 Characteristics of the ejecta source layer at bar B0

Multiple core samples at Trench Mar 1 and Mar 4 show high similarity to many of the ejecta samples. However, at bar B0 the distinctive colour of the ejecta (Fig 3.17b) allows the source sediment to be identified with high confidence. Olive-brown sands in unit B1 closely matching the colour of the ejecta occur immediately beneath the buried clay peaty unit at Trenches Mar1 (between ~ 2.15 and 1.37 m a.s.l.) and Trench Mar4 (between 2.67 and 2.47 m a.s.l.) and in augers A1, A2 and A3 of Transect 2. The olive-brown colour is most likely a redox phenomenon related to the demand for an electron

acceptor other than O, Fe^{3+} being one, during anaerobic decomposition of the peat. Subsequent re-oxidation of Fe^{2+} to Fe^{3+} in oxygenated waters in the sand below would provide the Fe oxide grain coatings to give the olive brown colour.

Despite the olive-brown sand having contributed to the surface ejecta, none of the samples taken from it (M1C1T440, M1C1T460 at Trench MAR1, or M4C1T240, M4C1T320, M4C1T340 at Trench MAR4) match well with the liquefiable soil field of Tsuchida's (1970). Like most of the core samples, a significant fine-textured tail overlaps the liquefiable, potentially liquefiable and sometimes even the non-liquefiable fields.

Samples taken from the sand blow at Trench MAR1 and from the dike at Trench MAR4 (Fig. 3.24) are much better sorted, having an attenuated fine tail, and match well with Tsuchida's liquefiable soil field (Figs 3.22 and 3.23). The comparison of the source sediment with ejecta is clear evidence of the sorting process occurring during liquefaction, fluid flow and ejection. Variability of sorting within the sand blow at Trench MAR1 is evident and appears to relate, at least partially, to depth in the sand blow: deeper (earlier vented) samples tend to be less well sorted (samples MAR 1GS2 and MAR1GS4) whereas later-ejected samples (Fig. 3.24) are better sorted (MAR1GS1 and MAR1GS5). In contrast to the sand blow samples at Trench MAR1, all the four samples from the dike in Trench MAR4 retain a fine tail, suggesting much of the sorting may occur during surface deposition of ejecta.

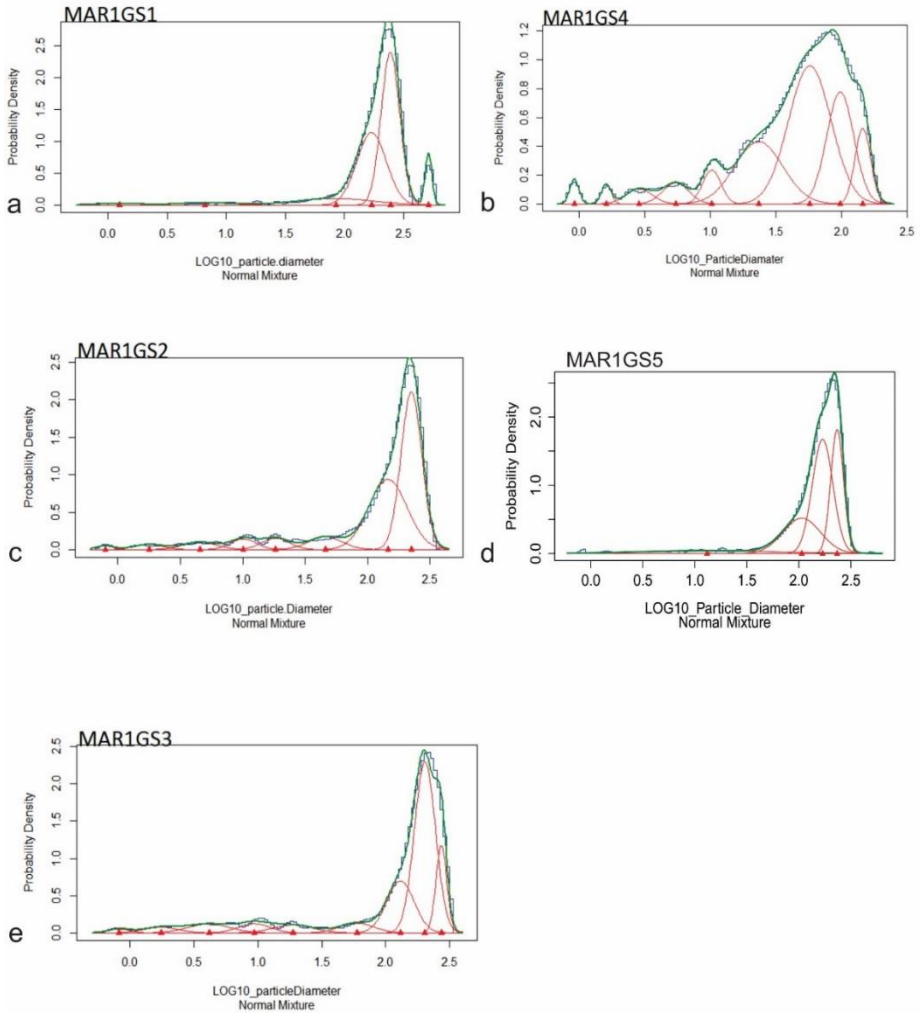

Figure 3. 24 Probability density functions for grain size distribution of samples collected at Trench Mar 1 from different portions of the sand blow Sample locations in Figure 3.21. Panels a and b from the base of the sand blow, panels d, and e from the top of the blow, and panel c from the middle of the blow.

The certainty of identifying the source sediment for the ejecta at bar B0 also provides an opportunity to evaluate the efficacy of the grain-size based similarity metric for tracing the source. At Trench MAR1 there is a high similarity between the more poorly sorted ejecta samples (MAR T1 GS2 and GS4) and the subsurface olive-brown source sediment (M1C1T440, M1C1T460), but poor matching where the ejecta are well sorted (MAR T1 GS1, GS3 and GS5). At Trench MAR4, all but one of the grain size samples taken from the dike or blow at this site matched well with the subsurface olive-brown source layer. The exception was a dike sample (MAR T4 GS1).

It is important to note that the similarity metric identified other candidates for the source layer at both trenches. The sample M1C1T320 in unit B1 at 2.83 m depth matched well with two ejecta samples, and it too had an olive colour, so may well be a contributor. A sample from a grey sand at 2.22 m depth (M1C1T260) matched one of the ejecta samples, but any contribution of this layer (18 cm thick) must have been relatively minor considering the colour contrast. At Trench MAR4 a grey layer immediately above the olive-brown sand and a couple (M4C1T120 and M4C1T140) of thin (~10 cm) grey sand or silty sand layers in B0 deposits also show a good match.

3.4.4.4 Grain size correlation at Trench Mar 3

At Trench Mar 3 on bar B1, five grain size samples were collected from the dikes and sills in the west and north walls of the Trench (Figure 3.21 c M3GS100, M3GS101, M3GS104, M3GS200, M3GS201). Six samples were collected from the sandy unit in Core 1 of Trench Mar 3 (M3C1T120, M3C1T140, M3C1T160, M3C1T180, M3C1T220, M3C1T280).

Figure 3.25 shows the cumulative curves of samples collected from the cores and the trench, with Tsuchida's (1970) soil boundaries for comparison. A similar pattern emerges to other sites: most samples collected from the core do not fit well within the liquefiable soil range because of their fine tail, whereas samples from sills and dikes do.

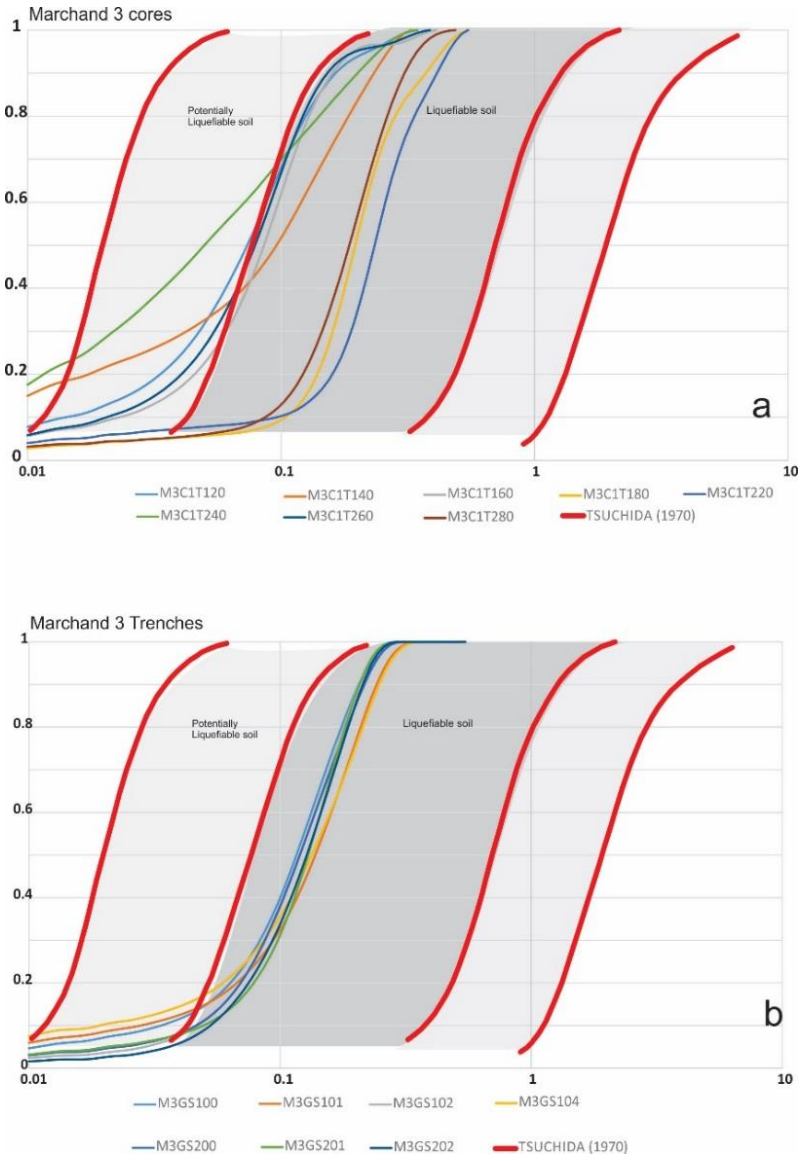

Figure 3. 25 Cumulative grain size distribution curves at Trench Mar 3 in comparison with Tsuchida's (1970) liquefiable soil boundaries; a) Curves from core samples; b) Curves from dikes and sills in Trench Mar 3.

The comparison between the cumulative curves of cores and trench samples with Tsuchida's soil boundaries (Figure 3.25) suggests that samples M3C1T180, M3C1T220, and M3C1T280 may be the ejecta source layer. These samples fall within unit B1 beneath Trench Mar 3.

The mixdist analysis at Trench Mar 3 was also inconclusive (Table 3.6). Some samples from the cores did not show strong similarity to the ejecta samples. Furthermore, the buried peat and the distinctive olive-brown sand beneath were absent (Fig 3.20) beneath bar B1, and all ejecta were grey (Fig. 3.17b). Accordingly, it was impossible to unequivocally identify the source layer as at bar B0, although the candidate appears to be a layer at 1.60 m depth in unit B1.

TABLE 3. 6 Visual correlation at Trench Mar 3 between samples from the Core and modern liquefaction features.

Trenches / Cores		M3GS100 Modern sill	M3GS101 Modern sill	M3GS102 Modern sill	M3GS104 Paleodike	M3GS200 Sand blow	M3GS201 Sand blow
CORE SAMPLES (Depth-m) Unit B1	M3C1T120 1.20g.l.; 4.6 a.s.l.	0.25	0.6	0.4	0.6	0.5	0.6
	M3C1T140 1.40g.l.; 4.4 a.s.l.	0.55	0.4	0.4	0.4	0.4	0.6
	M3C1T160 1.60g.l.;4.2 a.s.l.	0.5	0.5	0.5	0.6	0.7	0.7

Red= high value of S (0.8 to 1); yellow= moderate degree of similarity metric 0.8 to 0.4); green= low value of S from 0.4 to 0; g.l = ground level; a.s.l= above sea level

3.4.5 Factor of Safety analysis

The Factor of Safety analysis shown in Figure 3.26 revealed that all the sites selected for sCPT at the Marchand site were likely to experience liquefaction since FS was < 1 across all the profiles. This is a very similar result to the Hardwick site. However, sCPT3 was placed on a site with no surface expression of liquefaction (Figure 3.17- see sCPT 3), and differs substantially from sCPT1 and 2 where ejecta were present. Seismic CPT3 is characterized by much thinner layers of sand, and more and thicker layers of silt and clay. It is likely this stratigraphy prevented the build-up of high pore water pressure (less volume of sand), limiting the amount of liquefaction within the deposit and/or the amount of liquefied sediment that could have reached the surface.

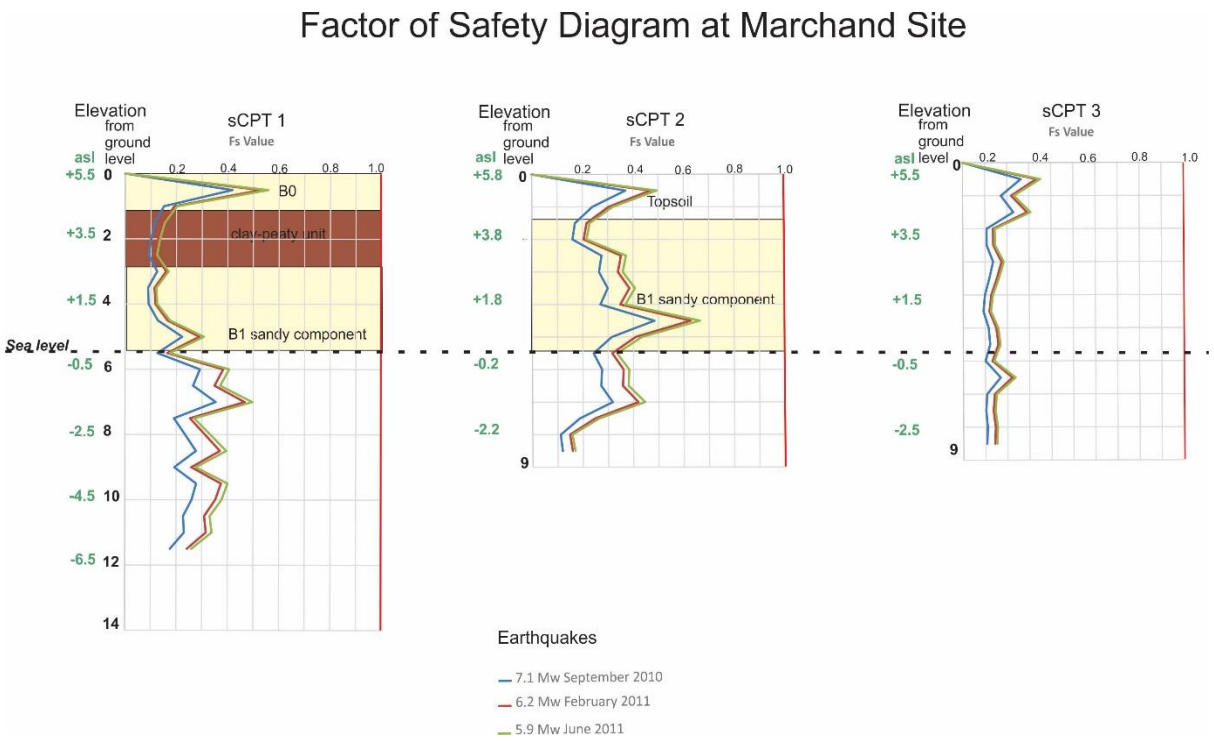

Figure 3. 26 Factor of Safety Analysis at the Marchand Site. The FS is less than 1 for all depths of sCPTs. This means that the Marchand site the Riccarton gravel was not hit during the sCPT investigations, hence it lies deeper than 12 m (from ground level) at this site.

3.5 DISCUSSION

3.5.1 Geological context

The complex alluvial system associated with the Halswell River evident from the LIDAR-based DEM is attributed to a higher energy river, the Waimakariri River, which flowed into the Halswell River in the late Holocene (Chapter 2 of this dissertation and references Brown et al., 1988; Cox and Mead, 1963). The chronostratigraphy of the Waimakariri/Halswell River is not the focus of this dissertation, however the analysis of the two study sites Hardwick and Marchand provided new insights into the stratigraphy of the area and the depositional setting of the Halswell River.

At the Hardwick site, the stratigraphy suggests that a floodplain of the Waimakariri River, that was at least 5500 years old (older than BC 3638-3381 - M2c unit), was incised by a meandering river prior to BC 1195-976. During this period, the river deposited fine and very fine sandy sediment (M2b). The meander loop that crossed the Hardwick site was later abandoned and very fine clay-silty clay sediment was deposited (M2a) in an oxbow lake to 600 or 550 years ago (AD 1318-1405). Subsequently (at AD 1314-1405), a temporary reactivation of the channel produced flooding and a crevasse splay deposit partially buried the paleochannel.

While at the Hardwick site the paleosoil unit 6bA was being formed (top of stratigraphic unit M2b, paleochannel floor deposit) between BC 48 -AD109 and AD 1314-1404 (Figure 3.6), at the Marchand site, the B1 peaty clay unit was forming over a similar time interval (about 1300 years) between AD 73-206 and AD 1286-1386. After the formation of the peaty clay unit, new sandy sediment was deposited on top, forming Unit B0 at Marchand, sometime after AD 1286-1386. At the Hardwick site, formation of the crevasse splay is tightly constrained to AD 1300-1395, and this may also be the timing of initiation of B0 deposition. Simultaneous phases of river activity and stability would not be surprising given the proximity of the two sites.

In summary, the age information suggests that at both sites the landscape was stable for about 1300 years (6bA unit at Hardwick site and B1 clay peaty unit at Marchand). These dates match with former

studies conducted on the Waimakariri River and its paleochannels (Basher et al., 1988; Cox and Mead, 1963; Johnston, 1958). The study presented here corroborates that the Waimakariri River stopped flowing into the Greenpark area prior to ~ 600-650 years ago, while avulsing north of Christchurch (current river position). However, there was a temporary reactivation of the former channels of the river only 600 years ago when the crevasse splay was deposited at the Hardwick site and when B0 formed at the Marchand site. The results here presented are consistent with an unpublished age (Johnston, 1958) from charcoal from *Podocarpus Totara* at Islington ~ AD 1265 (Sample 416/JNZ, In Table VI of Johnston, 1958) calibrated by Calib 7.1 online (Stuiver et al., 2017). The latter age was consistent with the soil unit (6bA) forming on top of the paleochannel (at Trench HWK6) and also helped constrain a temporary reactivation of the former Waimakariri channel in Selwyn soil age (~650 years ago). Taken together, the two sites at Greenpark indicate that floodplain accretion and the corresponding soil formation started in Templeton soil age group time (3000-6000 years B.P.). Channel infilling occurred in Waimakariri soil age group time (2400-700 years B.P.), although channel initiation appeared to predate the lower constraint (Figure 3.6, sample HWK6 C1-T3-C). The reactivation of the channel took place after a period of quiescence and soil formation at about 600 years B.P. which is the age of initiation of Selwyn deposition according to Basher et al. (1988b).

Unit M3 was identified as sandy deposits recognized only in the SBT columns of the seismic CPT tests, below modern sea level. The origin of these deposits is unknown. A diatom sample was analysed but no diagnostic assemblage was found (Ursula Cochran pers. comm.). Beneath M3, extensive fine grained sediment deposits, possibly attributed to estuarine sediment of the Christchurch Formation were deposited (M4), underlain by gravel (M5). Unit M5 reaches > 3 m of thickness at sCPT1 (~ -6 and – 9 m a.s.l.). Evidence of gravel deposits of similar thickness to M5 identified in this study were also recorded in two ECan (Environment Canterbury) boreholes (Mc Lauchlan, 2012). The latter identified a sandy gravel unit between -11 and -15 m a.s.l., and between -6 and -14 m a.s.l., respectively, in the vicinity of the Hardwick property. The gravel in unit M5 is tentatively attributed to the Springston

Formation (Chapter 2), Halkett Member. The Burnham structural contour map (Begg et al., 2015) (Figure 3.27) supports this finding, and shows that in the Halswell area, the Burnham Formation, (Riccarton Gravel ~ 18-25 ka Basher et al., 1988; Brown et al., 1988) is located at least -18 m below sea level. Considering an average elevation at the Hardwick and Marchand sites of ~ +5 m a.s.l., this means that the Burnham Formation is located at least -23 m below the ground in the Halswell Floodplain, while the seismic CPT tests undertaken at Hardwick and Marchand reached at most 15 m depth below the ground at sCPT 1. As a consequence but tentatively, the gravel reached in the sCPT (labelled as M5) at the Hardwick site (between -4 and -9 m a.s.l., Figure 3.5) was considered a fluvial member of the Springston Formation (at most ~14 ka old, Brown and Weeber, 1992), graded to a lower sea level, with estuarine sediment (M4) of the Christchurch Formation above representing deposition at the post glacial sea level rise culmination.

3.5.2 Characterization of surface manifestation of liquefaction and sedimentary architecture

Based on geomorphic mapping, sedimentary architecture and grain size analysis, two layers, units M2c and M2b, at Hardwick site liquefied and produced ejecta during the 2010-2011 earthquakes. Unit M2c occurs at 5 metres depth (Core 1 of Trench HWK6; Figures 3.5 and 3.6) and represents medium to fine sandy floodplain deposits. Unit M2b (between +3.1 and +1.9 m a.s.l.) represents channel deposits of the Waimakariri River. The detailed geomorphic map showed that sand blows were mainly associated with a paleochannel hosting M2b and its related point-bar sediment.

At the Marchand site a distinctive ejecta colour on the inner scroll bar (B0) allowed the source to be identified with high confidence. The layer that liquefied and produced ejecta is predominantly identified in unit B1 but it is not possible to rule out a sandy component from unit B0. The olive-brown sand coming from B1 unit liquefied (at ~ 4 m depth, Figure 3.18) and produced ejecta in spatial coincidence of Trenches Mar 1 and 4, while the grey sand in B1 (from nearly 1.60 m depth or more) liquefied in coincidence of Trench Mar 3. At the Marchand site surface manifestation of liquefaction

occurred predominantly along the ridges. The swale between bars B0 and B1 experienced little sediment ejection, as did floodplain areas far from the point bar.

Tuttle and Barstow (1996) documented that dikes originating in fluvial channel floor deposits were guided up-section along the inclined base of the overlying channel fill deposit of the St. Francis Basin in the New Madrid Seismic Zone. In particular, the authors showed that the feeder dikes seemed to form an en-echelon pattern subparallel to the margins of the channel-fill deposit. An analogue of this process could potentially be happening along the margins of the paleomeander at Hardwick site, where paleo point bars are located (Trench HWK6), and at the Marchand site, which is dominated by point bar sedimentation. Several other studies have documented a spatial association of point bars with liquefaction ejecta globally (Alessio et al., 2013; Civico et al., 2015; De Martini et al., 2015; Holzer et al., 2010; Tuttle, 2001a).

Subtle shaking amplification occurring along the point bar ridges at the Marchand site but also at Trench HWK6 may have enhanced the localization of ejecta along the point bar ridges (Anggraeni, 2010; Celebi, 1985; Lee et al., 2009). Micro-lateral spreading (subtle spreading) may occur along the bar ridges and produce cracking that can facilitate venting of water and entrained sand on the surface, forming sand blows. Also at the Marchand site, the nearby modern channel of the Halswell River provides a free face and topographic driving force for lateral spreading towards the river (Tonkin and Taylor, 2015). It is possible that the small graben structure described by Villamor et al. (2016) for Trench MAR4 is a consequence of lateral spreading, as that trench is close to the river free face.

The pattern of ejecta at the Hardwick site had a geospatial association with the crevasse splay that covers part of the channel and the inner part of the meander in the northern section of the paleo-channel. However, only few and isolated sand blows occurred along the meander paleochannel where the crevasse splay was absent (Villamor et al., 2016) in the southern section of the meander, west and south of the Hardwick site (Figure 3.3A). Villamor et al.'s

conclusion, supported by the findings here, suggested that the crevasse splay did not provide the ejecta source sediment but it had some other indirect control on the ejection of liquefied sediment.

The crevasse splay (M1) and the channel fill deposit (M2a) could have provided a thicker and more impermeable crust (Obermeier, 1996; 2005), which enhanced the pore water pressure build-up during the shaking. Alternatively, the higher elevation of the crevasse splay may have modulated earthquake-related shear stresses (Martel, 2016; Moon et al., 2017 and Chapter 7), which enhanced surface cracking and the likelihood sand dikes would propagate through the overburden to the surface.

In summary, this study suggests that the point-bar geometry of the Halswell River and the paleochannel shape, which may drive ground failure, together with the strength and thickness of relatively impermeable layers above the sandy lenses, have led to the formation of sand blows above the point bar but not in the floodplain far from the channel or in the swales.

3.5.3 Grain size distribution of liquefiable sand and seismic CPT

The grain size distribution curve of dikes and sand blows showed that there are differences in sorting and in the grain size characteristics of the different liquefaction features. Sand blows are better sorted and tend to fit well within Tsuchida's (1970) liquefiable soil thresholds.

The sand blows are the result of liquefied sediment travelling upward through the soil profile and venting at the surface. Several processes contribute to sorting of the sand in sand blows. Once the sediment is ejected it tends to be deposited in a volcano like shape . This peculiar shape will cause coarser sediment (fine or medium sand) to drop out of the flow closer to the vent while finer sediment (very fine sand) will be carried further. Fine grained sediment from the original liquefied sediment is washed away with the water, although some is often deposited as lenses of silt or silty clay on top of the sand blow (Quigley et al., 2013) during the final phases of venting, when excess pore pressure is low. After deposition the ejecta is exposed to weathering effects (aeolian and rain splash). As a consequence, sediment deposited in the uppermost section of the sand blow will be affected by a sorting process influenced by wash of fine sediment during the ejection and by aeolian winnowing. Samples from the sand blow trenched at Trench Mar 1 are a good example of variable levels of sorting within a sand blow (Table 3.4 and Figures 3.21 a and 3.22).

Sand dikes are characterized by a mixture of sand and silt as shown in the multimodal distribution curve of the mixdist analysis. In general, the cumulative curves of dikes do not fit well with Tsuchida's (1970) liquefiable soil thresholds, but they have better correspondence with the potential source sediment. Within a dike, sorting occurs to some extent as shown by observations of a variety of sediment sizes deposited in different sections of a dike (see also Figure 6.7, Chapter 6). However, the sorting is not as pronounced as for the sand blows.

Grain size and location (depth) of source layer are useful information to improve the accuracy of the back-calculated earthquake magnitude from liquefaction distribution and ejecta characteristics (Obermeier, 1998; Olson et al., 2005a; 2005b; Papathanassiou et al., 2005; Pirrotta et al., 2007; Tuttle and Hartleb, 2012a). The findings here so far suggest that the composition of samples from the dikes and from the proximal part of the sand blow are better candidates to represent the composition of the source layer, and this should be accounted for when aiming to identify the source layer at a site.

For instance, at Trench HWK5 there was a strong similarity between samples T5C1T240, T5C1T280 of the core (at ~2.2 -2.6 m a.s.l.) and the grain size samples from the dike in the west wall at Trench HWK5 (Table 3.1). There was also a strong similarity with the grain size samples taken from the sand blow vent area (HWK5GS1 and HWK5GS2, Figure 3.10). The comparison showed that in the vent area, the ejecta is better sorted than the source layer and the bottom of the dike, but here it still retains the finer portion from the source layer. Ejecta transported further is sorted during transport and deposition and subsequently by subaerial processes if close to the surface of the blow.

A general observation from the grain size analyses of liquefied sand is that only the samples that may have undergone sorting fit Tsuchida's (1970) liquefiable soil thresholds. This poses the question whether Tsuchida's thresholds are biased towards sampling of sand blows and thus the cumulative curves expressed in that study are not fully representative of the characteristics of all liquefiable sediment. Tsuchida's (1970) soil curve boundaries are derived from sediment that had experienced liquefaction in previous Japanese earthquakes (Koester and Tsuchida, 1989), and thus the samples were probably sorted relative to their source. Incontrovertible evidence of the limitations of Tsuchida's classification came from the analysis

of the source layer at bar B0 at the Marchand site. Here, subsurface sands linked to the surface ejecta by colour criteria had poor correspondence with Tsuchida's liquefiable soil field.

At Trench HWK6, the mixdist analysis showed there was a strong similarity between the modern liquefaction samples and core samples from unit M2c, but not for the paleoliquefaction samples. This may be caused by many factors such as: i) the sand that liquefied at the time of the paleo earthquake lay deeper than the sand that liquefied during the CES; ii) the sand of the paleoliquefaction feature was the same but the weathering of the sediment has changed its characteristics (higher content of very fine sediment, e.g. clay and fine silt); or iii) there were not enough grain size samples collected at the surface (either modern or old) to establish a robust comparison.

3.5.4 Efficacy of seismic CPT in predicting liquefaction surface manifestation

Based on CPT results in areas with and without sand blows the factor of safety (FS) showed that all the layers except for peaty clay and gravelly-sandy layers are susceptible to liquefaction (FS < 1). For instance, the FS computed at sCPT1 (Figure 3.5) at the Hardwick site showed that all the layers are susceptible to liquefaction (FS<1) with the exception of the first gravel encountered between 10 and 12 m depth below g.l. (Halkett Gravel, see section 3.5.1). However, no surface manifestation of liquefaction was observed at this site. The grain size analysis reported in this chapter showed that across most of the Halswell floodplain the sediment was characterized by very fine sand /fine sand. However, liquefaction ejecta were only centred on some specific geomorphic features. In some cases, blisters were produced (Trench Mar 4) or sub-horizontal injections (Trench Mar 3), which can only be discovered by excavating trenches. The formation of features such as blisters and/or sub-horizontal

injections is potentially one of the reasons why most of the floodplain far from the Halswell paleochannel and point bar deposits did not show liquefaction ejecta at the surface, although the sand texture was potentially liquefiable and could have in fact liquefied (Villamor et al., 2014).

Results so far suggest that the interpretation of CPT datasets for paleoliquefaction investigations need to be supported by a stratigraphic study and by a geomorphic analysis to assess the highest likelihood of liquefaction susceptibility and to evaluate why specific landforms are more prone to ground failure and the formation of sand blows.

3.6 CONCLUSION

Detailed site investigations of liquefaction associated with the 2010-2011 Canterbury Earthquake Sequence (CES) in the alluvial setting of the Christchurch region has been documented, integrating geospatial, stratigraphic and geotechnical analysis.

At the two study sites, sand that likely liquefied during the Canterbury earthquakes underlies much of the alluvial floodplain but it predominantly vented along the margin of an abandoned channel, filled with channel floor sandy deposits, and by a crevasse splay forming higher topography. Paleochannel floor sands and point bar deposits were the most susceptible to venting of sediment, owing to their fine and very fine sandy sediment and position below the water table. Possible reasons for this are: subtle seismic wave amplification; micro-lateral spreading that creates cracks as paths for ejection; sediment architecture with lens shapes that guide the sand flow towards higher points. This means that, at alluvial sites, the distribution of sand blows is influenced by sedimentological (e.g., sediment types with loose packing arrangement and high void ratio are highly susceptible), stratigraphic (e.g. the presence of a relatively impermeable capping layer can promote development of a higher

pore-water pressure in underlying sand and the 3D shape of units can influence fluidization, ground failure, and dike formation) and hydrological conditions (e.g. sediment must be saturated to liquefy, so the depth of the water table and influence of aquifers and rivers on the water table is important) as well as by topography (e.g. it may amplify ground motion and drive ground failure). The topographic control on the surface manifestation of liquefaction will be further investigated in Chapter 7 of this thesis.

The Factor of Safety (FS) calculated from seismic CPT indicates that sediment susceptible to liquefaction, and that likely liquefied during the Canterbury earthquakes, is broadly distributed at both study sites even in areas where no liquefaction features or sand blows formed at the surface. Finding out what will liquefy and produce ejecta and what will not for areas that traditionally do not show surface manifestation (e.g. flood plains) is difficult. However, the analysis undertaken here of the local stratigraphy at the two sites where sand blows did not form reveals that geomorphic analysis can substantially assist geotechnical analysis by identifying areas that are likely to experience liquefaction surface manifestation.

With regards to the efficacy of the techniques used to investigate liquefaction in the alluvial setting for this study:

- the 2-dimensional high resolution GPR (400 to 1500Hz) is an important tool for detecting changes in sediment geophysical properties (e.g. organic content) and for defining stratigraphic units within 2 m of the ground surface.
- Deconvolving grain size distribution into component sediment populations is a valuable tool to assess the sorting of the vented sediment and to identify the source layer for ejecta.

- Tsuchida's (1970) liquefiable soil cumulative curve thresholds have to be used with care when assessing if deeper sediment types (e.g. retrieved from cores) are liquefiable, as that compilation of data is biased towards sand blows that may have undergone substantial sorting and may not fully resemble the grain size characteristics of the original source. In this study, the sediment that liquefied had a larger component of fine grained material than liquefiable sediment as defined by Tsuchida (1970).
- The Factor of Safety analysis in sCPT is a valuable and affordable technique to estimate the liquefaction susceptibility of sediment. However, seismic CPT analyses need to be supported by geomorphic and sedimentological site investigation to clarify which landform is likely to experience liquefaction ejecta and which layer will act as a source for ejecta. The knowledge of where liquefaction will occur is important in order to guide future paleoseismic studies, but also in relation to the impact of liquefaction and ground failure on infrastructure such as buildings, roads and bridges.
- With regard to the importance of better identification of the liquefaction source layer, more paleoseismic studies need to address this point by testing the mixdist R-package and the similarity metric technique used here. A good delineation of the potential liquefaction source layer is useful for improving some of the parameters used in the relationships for back-calculating earthquake magnitude.

Chapter 4

LIQUEFACTION INVESTIGATION IN THE COASTAL DUNE SETTING OF CANTERBURY

4.1 INTRODUCTION

The coastal dune system of Christchurch, along with the alluvial setting, was very susceptible to liquefaction during the 2010-2011 Canterbury Earthquake Sequence (CES). Alluvial, deltaic and coastal dune systems have been worldwide recognized for several decades as liquefaction prone settings (e.g. Amick et al., 1990; Holzer et al., 2010; Holzer, 1998; Tinsley et al., 1998; Tuttle, 1999; Youd and Hoose, 1977; Youd and Perkins, 1978; Ziony, 1985). The CES studies (Almond et al., 2012; Bastin et al., 2015; Quigley et al., 2013; Villamor et al., 2016; 2014) together with studies from other recent liquefaction events (Alessio et al., 2013; Civico et al., 2015; De Martini et al., 2015; Fontana et al., 2015) have focussed on the alluvial setting. Liquefaction features in the coastal setting of Christchurch have not been the object of detailed research to date.

The modern coastal environment of Christchurch is characterized by dunes, estuaries, lagoons and swamps that have occupied the Christchurch area for at most 10,000 years since post glacial sea level rise (Brown and Weeber, 1992). The present sea level was established around 6000-6500 years ago and coastal progradation began soon after that (Brown and Weeber, 1992). Coastal dunes are present at the modern coast, as well as older ones at Burwood, Richmond, Avonside and Linwood suburbs, areas that are up to 6 km from the present day coast (Brown and Weeber, 1992) (Figure 5.1).

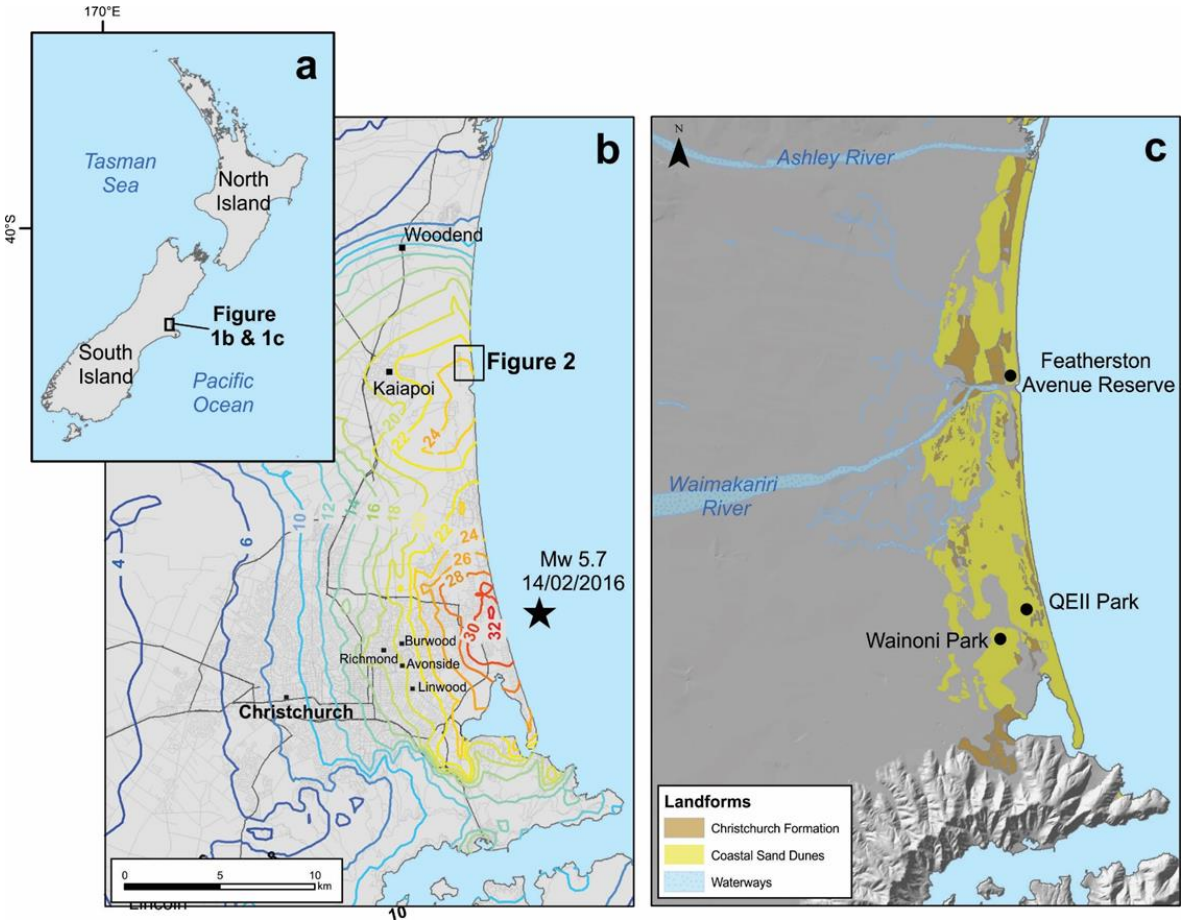

Figure 4. 1 a) General location of study sites; b) Location of Valentine's Day Earthquake (2016) main shock and recorded PGA levels across the Canterbury Plains. Location of main townships and Christchurch's suburbs more affected by liquefaction effects during the CES and during the Valentine's Earthquake; c) Geomorphology of the coastal fringe of the Canterbury Plains. Location of the coastal study sites investigated during liquefaction field campaigns between January 2015 and February 2016.

Kirk (1987) considered that most of the sand for the progradation process at Pegasus Bay derived from sand accumulated south of Banks Peninsula, during postglacial sea level rise, and then this sand was reworked shoreward (Brown and Weeber, 1992). Today this reworking and progradation is no longer occurring; the coastline has reached an equilibrium and most of the sand is supplied by the Waimakariri River. Other studies (Blake, 1964, 1968; Herzer, 1981; Reed, 1951) corroborated that the Waimakariri River catchment is the main source of sand of the present day sea floor and coastal dunes in Pegasus Bay. The dunes are sourced from greywacke and argillite with also contribution from igneous rocks of Banks Peninsula (Brown and Weeber, 1992).

Blake (1964) identified three dune systems north of Christchurch (North Canterbury region): i) dunes forming the present beach yielding an age of 600 years; ii) the Kairaki dune complex, developed between Waimakariri and Ashley Rivers, and returning an age of less than 2000 years B.P.; and iii) Waikuku dune complex, furthest landward yielding an age of 5000-6000 years B.P.. These three systems are more clearly distinguishable north of the Waimakariri River. To the south of the Waimakariri River, the dunes coalesce, which impedes a similar classification to that of Blake (1964). Schulmeister and Kirk (1996) revised Blake's (1964) dune classification based on the chronology of the coastal dune system near Leithfield, established by thermoluminescence and ^{14}C dating techniques (Shulmeister and Kirk, 1993, 1996, 1997). Schulmeister and Kirk (1996) discovered that the dune system of North Canterbury can be classified into five distinct chronological events that correspond to five episodes of geomorphic evolution of the coastal plain. The later system proposed by Shulmeister and Kirk (1996) includes 1) coastal dune systems (0.5 ± 0.0 ka), which correlate with Blake's (1964) dune system that forms the present beach; 2) Ashworth Beach ridge (between 1.0 and 3.0 ± 0.6 ka), which equates to Blake's (1964) Kairaki dune complex; 3) Main Road ridge dune (2.6 ± 0.4 ka) formerly classified as Kairaki; 4) Marine Cliff dune system (6.0 ± 0.5 ka); and 5) Boyds Beach dune system (between 7.3 ± 1.6 ka and 9.2 ± 1.6 ka) corresponding to Blake's (1964) Waikuku Dune complex (see Figure 1 of Shulmeister and Kirk, 1993; Shulmeister and Kirk, 1996).

The study sites analysed in this chapter are Wainoni and QEII Parks in Christchurch City, and Featherston Avenue Reserve, the latter between Kaiapoi and Pegasus Bay (about 25 km North of Christchurch) (Figure 4.1b &1c). Wainoni and QEII Parks are located on the dunes of the Christchurch urban area (Christchurch Formation, Brown and Weeber, 1992), and it is unclear how they fit into the classifications defined above, although they are mapped as Kairaki soil family (Sandy Raw Soils, Hewitt, 2010) according to S-MAP (LCR, 2016). Featherston Avenue Reserve dune belongs to the Kairaki group, (Blake, 1964) and soils are mapped as Kairaki and Burwood families (LCR, 2016), the latter being a Mottled Sandy Recent Soil.

Wainoni and QEII parks were affected by liquefaction caused by the M6.3 February, the M6.4 June, and the M6.0 December 2011 earthquakes; whereas Featherston Avenue site was affected also by two more events: the M7.2 September 2010 (Darfield) earthquake (see location of the CES earthquakes in Figure 1 of Bannister and Gledhill, 2012) and the recent M5.9 Valentine's Day Earthquake (14th February 2016, Figure 5.1b). Fieldwork was undertaken in two separate campaigns. Trenches excavated at Wainoni and QEII parks were investigated in January 2015 and cores were obtained in February 2016. Featherston Avenue Reserve site was fully investigated in February 2016.

The aim of this chapter is to investigate surface and subsurface manifestations of liquefaction in the coastal dune system and their relations with landform and the subsurface environment.

In order to achieve this aim three objectives are established:

1) Determine potential spatial correlation between the patterns of liquefaction surface manifestation and geomorphic elements of the dunes system;
2) Define the sedimentary architecture of the dune setting and identify sediment susceptible to liquefaction, which may have acted as the source layer;
3) Integrate results to explain why liquefaction is associated with certain elements of a coastal dune system .

4.2 METHODS

Objective 1 was achieved with detailed liquefaction mapping as well as mapping of the geomorphology of the dune systems at the study sites. Objectives 2 and3 were achieved by using Ground Penetrating Radar Surveys, paleosesimic trenches, coring (piston and vibracores), and micromorphological analysis. For the latter technique, methods are described in Chapter 6 of this thesis.

4.2.1 Detailed mapping

A detailed liquefaction map of the study areas was created for each of the three sites, Wainoni, QEII Parks and Featherston Avenue Reserve. Post-Earthquake (February 2011) aerial photos were used to map the CES liquefaction features, no longer visible at the surface. The post- February 2011 earthquake photos, having a resolution of 0.4 m per pixel, were downloaded from the LINZ portal (LINZ, 2011) .

4.2.2 Ground penetrating radar

At our study site two types of GPR survey were undertaken: 2D and 3D, firstly to identify the most prominent near-surface anomalies caused by the CES liquefaction events; and secondly to be able to appropriately locate the trenches.

Ground penetrating radar (GPR) surveys were carried out using a GSSI SIR-3000 system with 400MHz antennae and 1.5 GHz antenna. In this area, the 400 MHz antenna can image the soil anomalies as deep as 3 m, whereas the 1.5 GHz antenna can image subsurface anomalies down to 1.5 or 2 m at most. A combination of Differential GPS, digital survey wheel and survey tapes were used for positional control. Measurements were recorded at 24-bit resolution and a sampling density of 100 scans per metre. A close line spacing of 0.5 m was used to ensure high resolution of the 3D images. GPR data were processed in RADAN 6.6 software. Processing involved bandpass HP/LP filtering, predictive deconvolution, stacking, gain adjustments and background removal (Data acquisition and processing were provided by Scantec Ltd).

The 2D ground penetrating radar survey was carried out prior to the January 2015 field campaign, between December 2014 and January 2015, on the selected study sites. Three 3D GPR was only used for targeting specific liquefaction features. A grid (3 m by 3 m or 2 m by 2 m, in line with the size of the liquefaction feature,) was set up on each targeted sand blow. The grid was subsequently transferred to the trenches to ensure a common coordinate system. The grid allowed subsurface anomalies along two orthogonal directions to be recorded. The 3D GPR produced an image of a block of sediment from which horizontal slices at various depths from the ground (in m, e.g. 0.25, 0.50, 0.75, 1.0, 1.25, 1.5, 2.0) were selected.

4.2.3 Paleoseismic trenches

Ten paleoseismic trenches were excavated in total at the three sites. The trenches were between 3 and 5 m long, 1.20 wide, and between 1.30 and 1.50 m depth. Trenches were sited based on aerial photo review and GPR survey results.

For details on the soil units exposed in the trenches the reader can refer to the Soil Description, Appendix A4. The soil stratigraphy in the trenches was described according to standard soil and sedimentological protocols (Clayden and Hewitt, 1994; Schoeneberger et al., 2012) .

4.2.4 Coring

Piston and vibracores are useful to investigate the stratigraphy in the subsurface and expose liquefaction features or soft sediment deformation deeper than those exposed in the trenches.

The clean sand of the coastal sediment caused problems for extruding cores from the core barrel. As a consequence, the piston core system was modified. A disposable PVC barrel of 50 mm internal diameter was used to retrieve the sediment; the barrel was cut longwise to allow the sediment to be exposed and described in the sedimentology laboratory.

The stratigraphy in the cores was described using the same methods for soil description mentioned above. A detailed description of piston and vibracores with high definition pictures is presented in the Core Description Appendix A5.

4.2.5 Grain size analysis

Seventy six grain size samples were collected in total from the paleoseismic trenches in order to assess the depositional setting of the coastal sediment that experienced liquefaction. The samples were analysed using a micrometrics Saturn Digisizer II 5205 at Canterbury University, which uses the light scattering analysis technique to improve the resolution and accuracy of the particle size analysis.

Cumulative size distribution curves from our study samples were compared with Tsuchida's (1970) soil behaviour curve boundaries to recognize whether the sediment exposed in the trenches at the three sites were *liquefiable* or *potentially liquefiable*.

A more detailed statistical grain size analysis was undertaken using the software Gradistat (Blott and Pye, 2001). Gradistat provides a classification of the samples, computing the main statistics such as mean, mode, sorting, skewness, and also provides a graphical classification. An example of Gradistat output is shown in Figure 4.2. The reader can refer to Gradistat grain size analysis, to read the statistics details for each sample from trenches and cores.

SAMPLE STATISTICS

SAMPLE IDENTITY: **38-PBT1GS1** ANALYST & DATE: mgb, 05/06/2016

SAMPLE TYPE: Unimodal, Moderately Sorted TEXTURAL GROUP: Sand

SEDIMENT NAME: Moderately Sorted Fine Sand

	μm	ϕ
MODE 1:	217.6	2.201
MODE 2:		
MODE 3:		
D_{10}:	68.22	1.926
MEDIAN or D_{50}:	191.7	2.383
D_{90}:	263.1	3.874
(D_{90} / D_{10}):	3.857	2.011
(D_{90} - D_{10}):	194.9	1.948
(D_{75} / D_{25}):	1.588	1.316
(D_{75} - D_{25}):	85.62	0.667

GRAIN SIZE DISTRIBUTION

GRAVEL: 0.0%	COARSE SAND: 0.0%
SAND: 90.8%	MEDIUM SAND: 15.3%
MUD: 9.2%	FINE SAND: 65.7%
	V FINE SAND: 9.8%
V COARSE GRAVEL: 0.0%	V COARSE SILT: 3.9%
COARSE GRAVEL: 0.0%	COARSE SILT: 2.1%
MEDIUM GRAVEL: 0.0%	MEDIUM SILT: 1.4%
FINE GRAVEL: 0.0%	FINE SILT: 0.7%
V FINE GRAVEL: 0.0%	V FINE SILT: 0.4%
V COARSE SAND: 0.0%	CLAY: 0.8%

	METHOD OF MOMENTS			FOLK & WARD METHOD		
	Arithmetic	Geometric	Logarithmic	Geometric	Logarithmic	Description
	μm	μm	ϕ	μm	ϕ	
MEAN ($\bar{x}$)	180.8	150.7	2.730	172.8	2.533	Fine Sand
SORTING (σ):	71.61	2.300	1.202	1.741	0.800	Moderately Sorted
SKEWNESS (Sk):	-0.673	-3.304	3.304	-0.522	0.522	Very Fine Skewed
KURTOSIS (K):	3.100	16.46	16.46	2.027	2.027	Very Leptokurtic

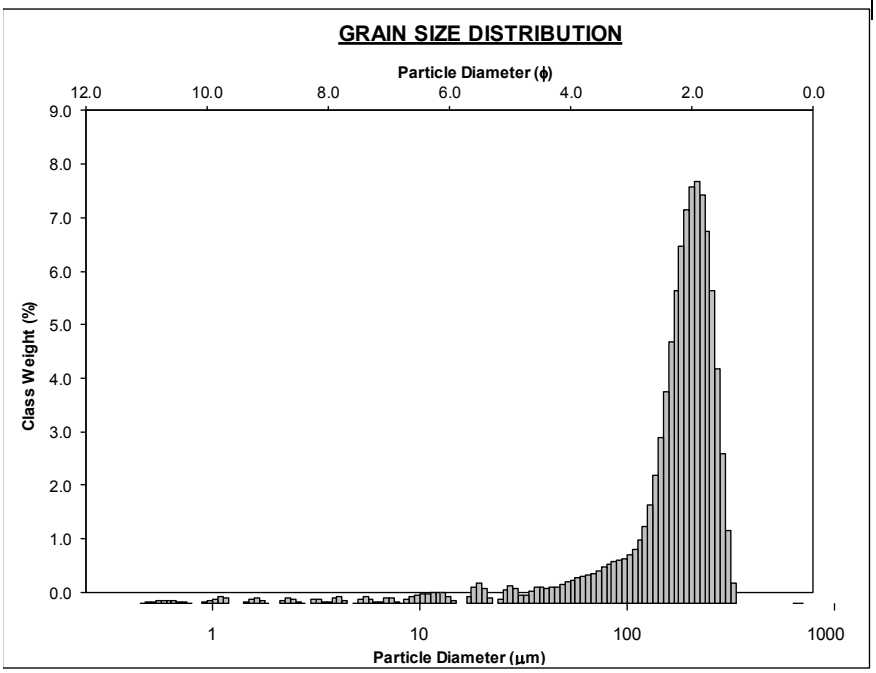

Figure 4. 2 Example of Gradistat output in Gradistat grain size analysis.

4.2.6 Radiocarbon Dating

Radiocarbon dating was used to assess absolute ages of the sediments. The samples were sent to the Rafter Radiocarbon Laboratory, GNS Science. The southern Hemisphere calibration curve SHcal13 (Hogg et al., 2013) was used to convert ages to calendar years. The complete list of the submitted samples is in Appendix A2.

4.3 RESULTS

4.3.1 Broad spatial analysis of sites affected by liquefaction in the Canterbury Plains

The broad physiography of the coastal fringe of the Canterbury Plains is shown in Figure 4.1. The dunes interfinger with the low-lying alluvial deposits formed by the Waimakariri and the Avon Rivers. At Wainoni and QEII Parks the original coastal dune geomorphology is not obvious since they have been flattened for urbanization. At Featherston Avenue Reserve, the original geomorphology is preserved: closer inspection reveals the site is located on an interdune deposit, which grades into estuarine – fluvial sediment.

The liquefaction features in the coastal dunes do not follow an obvious lineament as documented in the alluvial setting (Almond et al., 2012; Villamor et al., 2016; 2014, Chapter 2 of this thesis). At Wainoni and QEII Parks the liquefaction sand blows formed subrounded, spherical to prismoidal shapes (Powers, 1953) arranged without any obvious pattern (Figure 4.3 and 4.4). At these two parks, the sand blows comprised 10% and 13.2% of the area for Wainoni and QEII Parks, respectively. At Featherston Avenue Reserve, where the natural topography is preserved, the liquefaction features had a similar form but occurred preferentially along the lower elevation area of the interdune deposits (Figure 4.5) and represented approximately the 6% of the reserve area. No liquefaction manifestation was observed along the dune ridges.

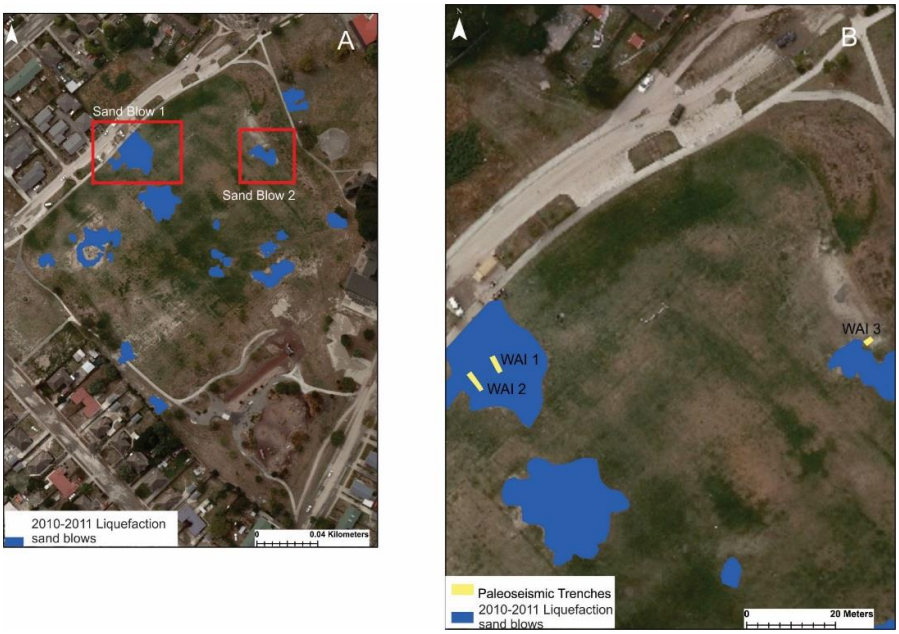

Figure 4. 3 Wainoni Park liquefaction mapping A) Sand Blows targeted for the 3D GPR survey and trenching as a result of the 2D GPR survey; B) Trench locations on the targeted sand blow, Trenches WAI 1 and WAI2 on Sand Blow 1 and Trench WAI3 on Sand Blow 2. Aerial photos from LINZ portal (LINZ, 2011).

Figure 4. 4 QEII liquefaction mapping A) Sand blows targeted for the 3D GPR survey and trenching as a result of the 2D GPR survey; B) Trench locations on the targeted sand blow, QEII Trench 1 on sand blow A and QEII Trench 2 and Pit on Sand blow B. Please note the Pit QEII will be not described in this dissertation. Aerial photos from LINZ portal (LINZ, 2011).

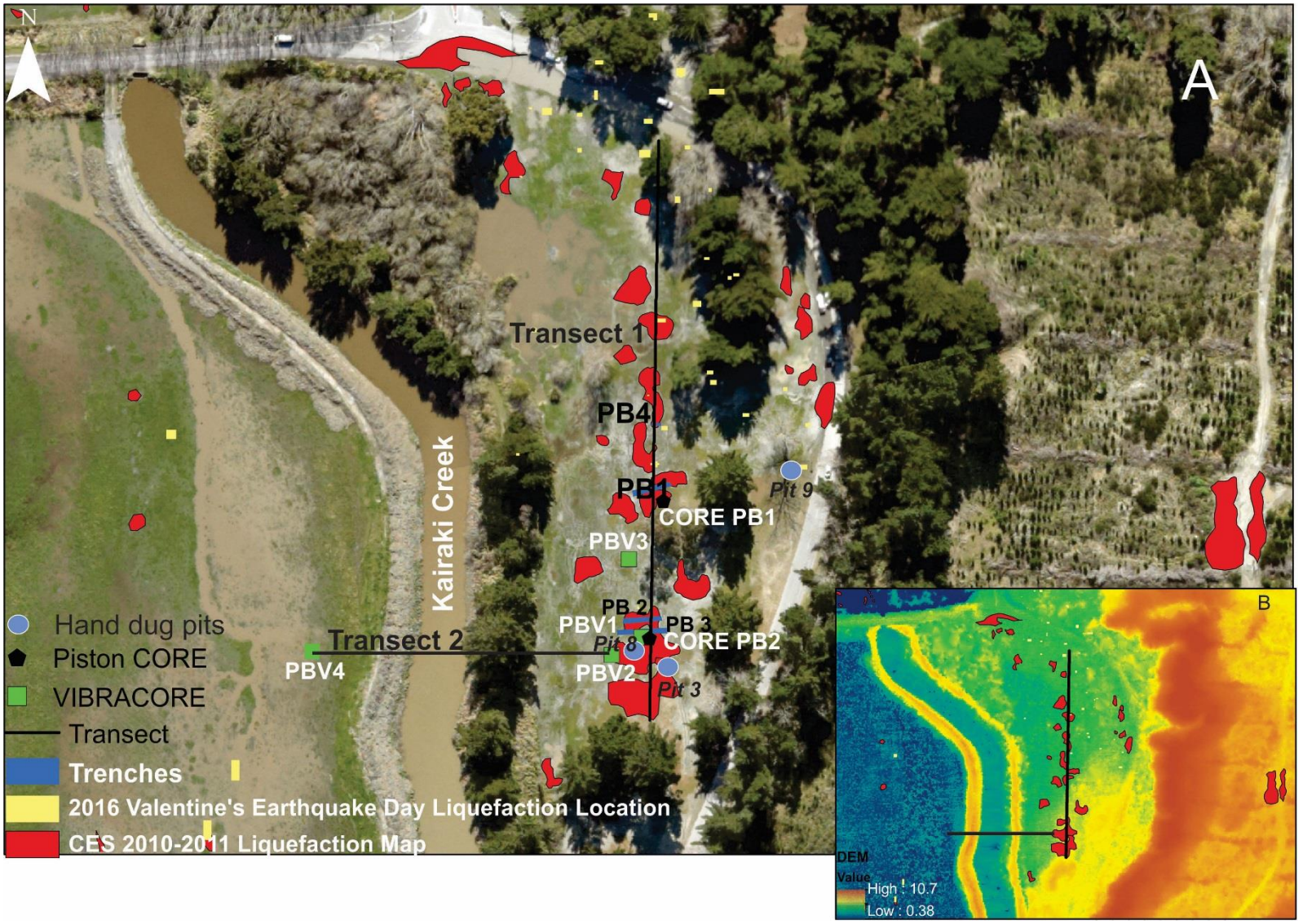

Figure 4. 5 Featherston Avenue Reserve Liquefaction Map A) Liquefaction map showing the trenches, the piston cores, the vibracores and the transect for the cross section analysis; B) DEM showing the liquefaction map and the transect, note the liquefaction sand blows are concentrated mainly in the lower elevation area of the interdune deposit. The hand dug pits are described in the Soil Pits appendix A8.

4.3.2 Liquefaction Investigation at Wainoni Park

4.3.2.1 GPR investigation

The 400 GHz 2D GPR at Sand Blow 1 revealed subsurface anomalies within 1 to 2 m depth (Figure 4.6) and between 1.5 and 3.8 m distance along the line. By interpreting the preliminary results gained from the 2D GPR survey it was possible to identify the precise location of several subsurface anomalies corresponding with sand blows mapped at the surface.

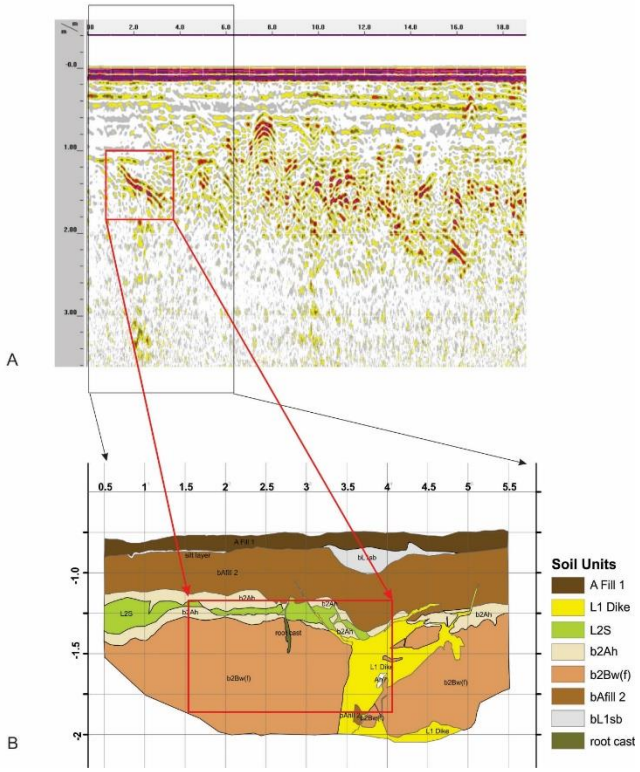

Figure 4. 6 2D GPR line for Sand Blow 1 at Wainoni Park. 2D GPR Line on Sand Blow 1, black frame highlights the trench dug on Sand Blow 1; the red frame targets the main anomaly (possibly a dike features). The GPR anomaly are coloured in red. For more details on the stratigraphy of Trench WAI 1 the reader can refer to Figure 4.10

The 3D GPR identified anomalies at 0.25 m depth (Figure 4.7).

Figure 4. 7 3D GPR line at 0.25 m depth on Sand Blow1.

At Sand Blow 2 the anomalies were localized between 76 and 86 m distance along the line and within 2 m from the surface. The same anomalies appeared in the 1.5 MHz survey but between 0.15 and 0.75 m depth (Figure 4.8). This anomaly was targeted to run the 3D GPR survey (Figure 4.9). Trench locations and orientations were informed by the GPR surveys. At Wainoni Park and also at QEII Park the area available for excavation was restricted by City Council conditions.

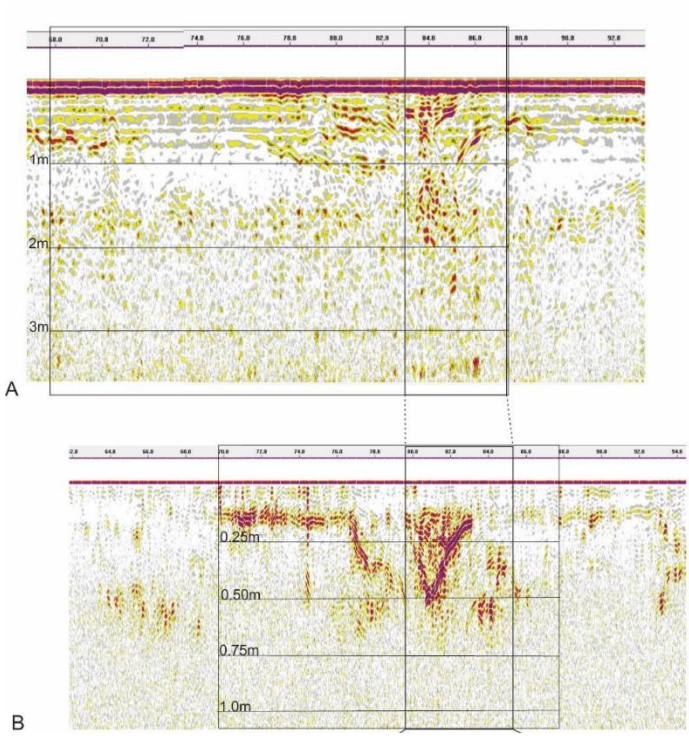

Figure 4. 8 2D GPR lines for Sand Blow 2 at Trench WAI 3. Screenshots A and B show the same subsurface anomaly observed close to Sand blow 2, where the Trench WAI 3 was excavated. However, it was not possible to identify a clear matching between the GPR anomalies and the trench stratigraphy, since Trench WAI 3 was excavated to the GPR line survey (Figure 5.2). The GPR anomalies are coloured in red.

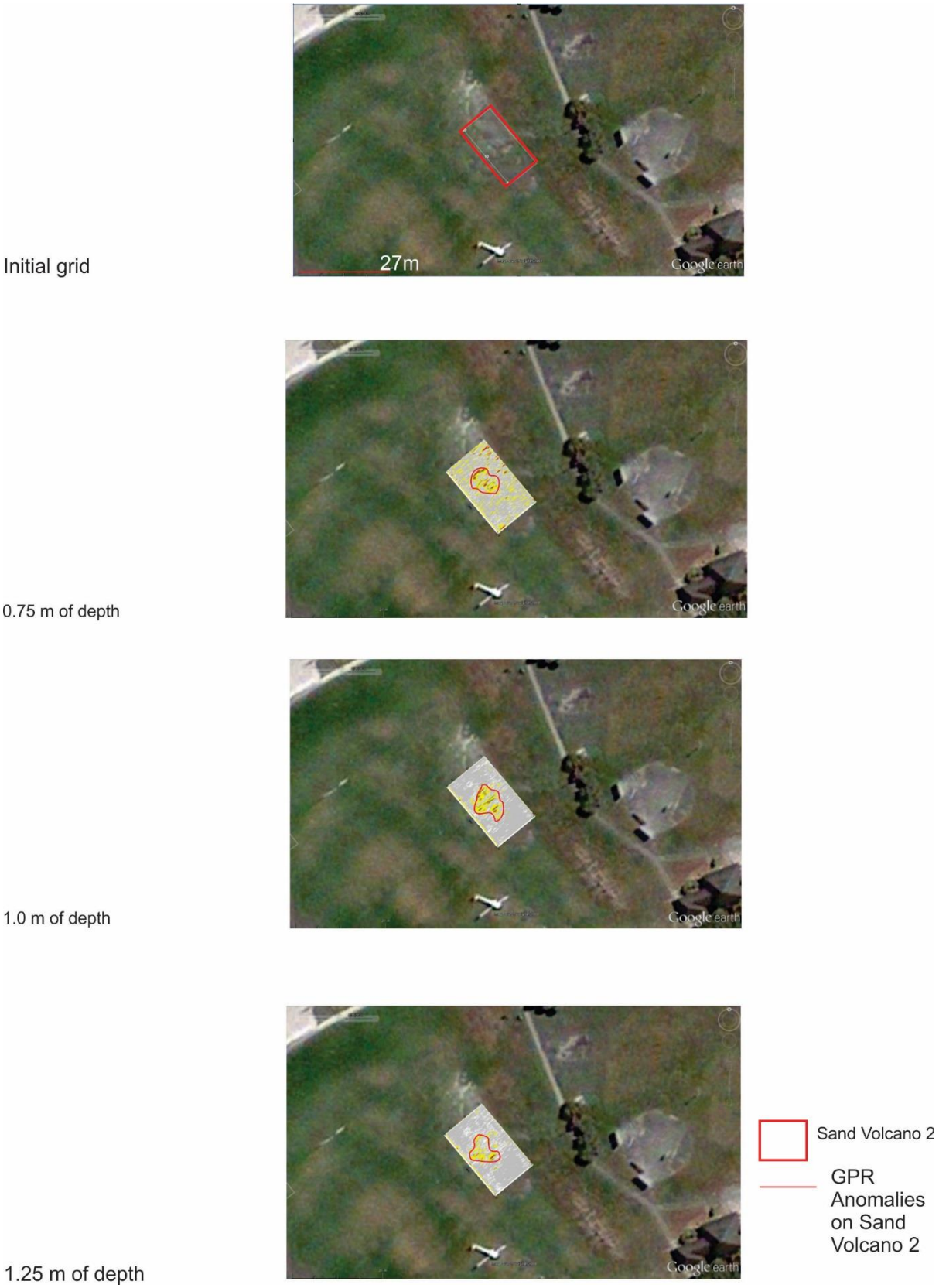

Figure 4. 9 Sand Blow 2 at Wainoni Park, 3D GPR anomalies noticed between 0.75 m and 1.25 m depth

4.3.2.2 Trench WAI 1

Trench WAI 1 (Figure 4.3) was 5 m wide and 1.30 m deep. The NE and SW walls were logged and photographed in detail (Figure 4.10 and 4.11). The soil units were described (Soil Description Appendix A4) and samples of liquefied sand were collected for grain size analysis. Trench WAI 1 was characterized by a post- CES organic-rich anthropogenic fill (unit A Fill1; it is identified as man-made fill hereafter) of nearly 15 cm thickness overlying a CES liquefaction sand blow (unit bL1sb –buried L1 sand blow-). The latter was a grey, very fine sand including many rip-up clasts. Unit bL1sb overlies a pre-CES fill (unit bAfill2). Both fills (pre- and post-earthquakes, bAfill2 and A Fill 1, respectively) had a very hard consistency and stiffness, were organic rich and had common greywacke gravels. The pre earthquake fill (bAfill2) was on top of the natural dune topsoil mapped as Kairaki soil family (LCR, 2016) present in this area (unit b2Ah). The b2Ah soil horizon was characterized by weak consistency and sandy texture with few roots, and it overlies a sandy weathered B horizon (unit b2Bw(f)) with loose to weak consistency.

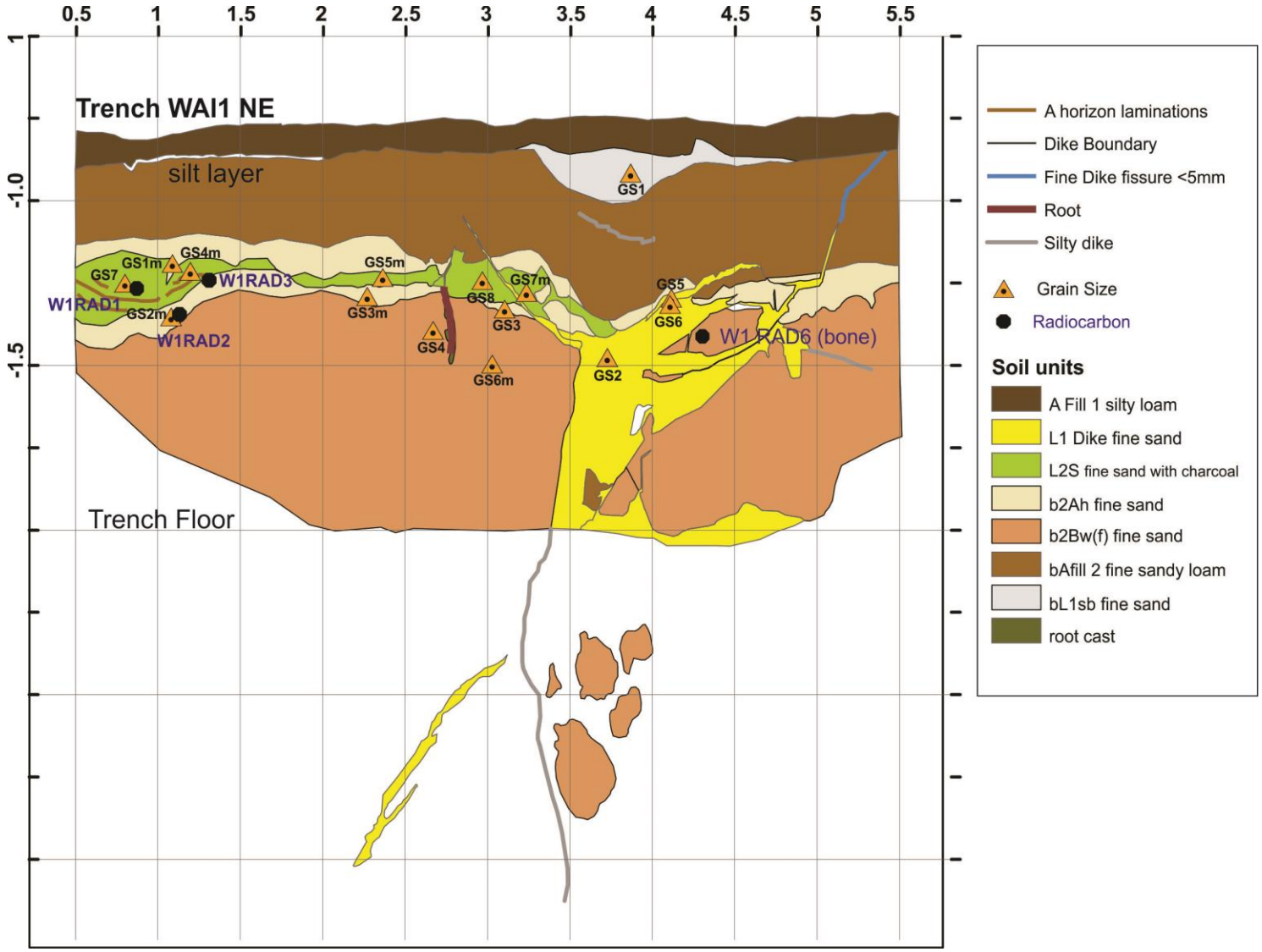

Figure 4. 10 Trench Wainoni 1 north east wall

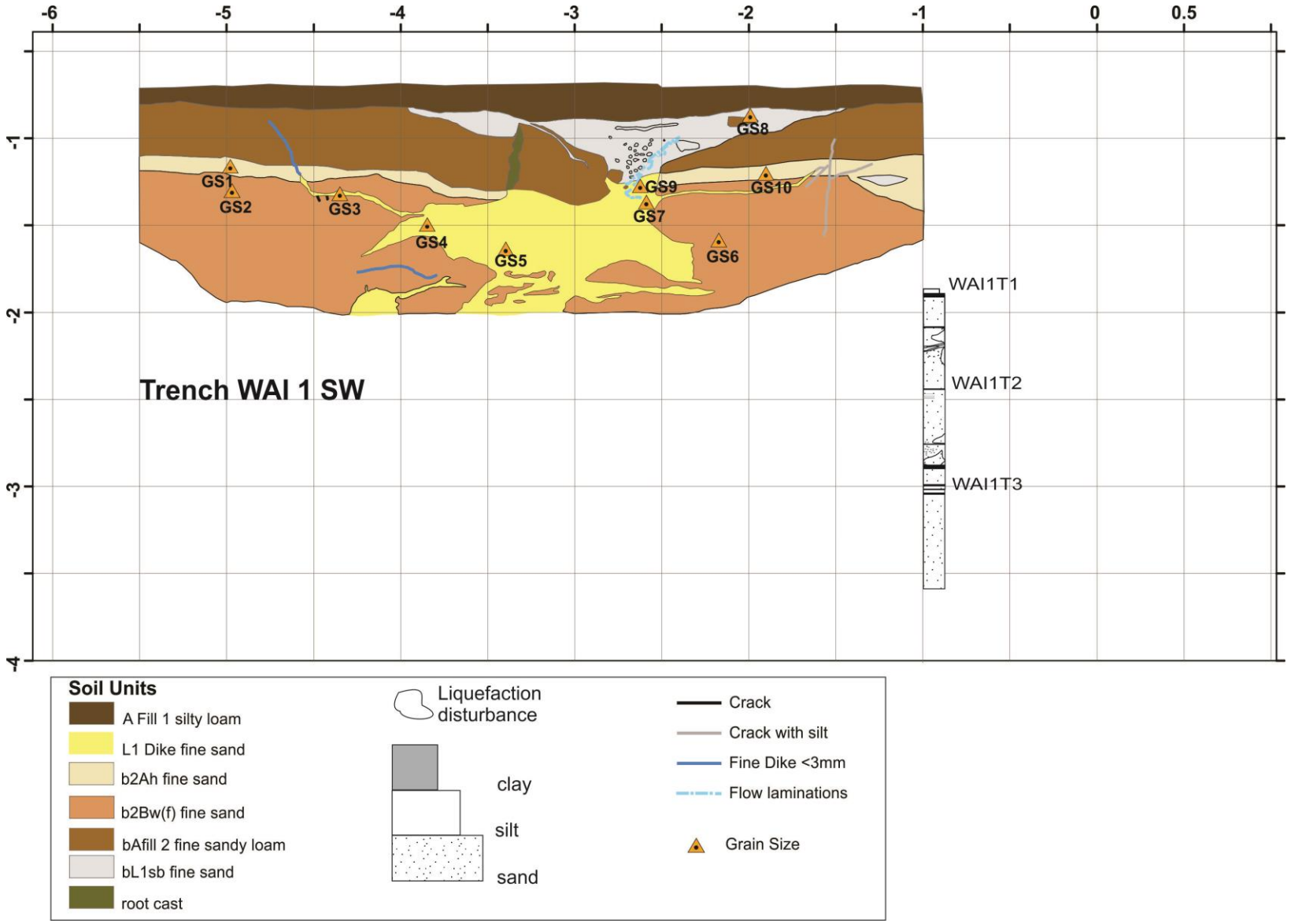

Figure 4. 11 Trench WAI 1 south west wall and corresponding core retrieved at Wainoni Park from 1.25 to 3.59 m depth, for more details on the core descriptions see Core Description Appendix A5.

On the north east wall of the trench, a potential paleoliquefaction layer (Unit L2S) was identified as injection (a sill) because it split the buried A horizon (unit b2Ah) into two layers (Figure 5.15). It was characterized by a very fine sand texture, massive structure, with few charcoal fragments and rip up clasts. A sandy dike (L1 Dike) of nearly 1.0 m width was exposed in the trench. The b2Ah layer was split by L1 [8]Dike. Many rip up clasts were observed in the dike.

4.3.2.3 Core at Trench WAI 1

At Wainoni Park one piston core was retrieved at Trench WAI 1 site, at a starting depth of 1.25 m, down to 3.59 m below the ground. The sediment retrieved in core WAI 1 was dark olive colour to grey colour, very fine and fine sand. Evidence of modern liquefaction features, in the form of fine sandy dikes, was observed at ~2.75 m depth Core Description Appendix A5.

4.3.2.4 Sediment ages at Trench WAI1

Three samples for radiocarbon dating were submitted from Trench WAI 1: W1RAD1, W1RAD2, WAI1RAD3, and one bone sample W1RAD6 (Figure 4.10). Sample W1RAD1 was a charcoal fragment from unit L2S (suspected paleoliquefaction feature), and it gave an age of 221 ^{14}C y B.P. (AD 1730-1803). Samples W1RAD2 and 3 were charcoals collected from the buried A horizon (b2Ah). Sample W1RAD2 yielded an age beyond radiocarbon dating threshold (>49000 BP). Sample W1RAD3 yielded the age of 201 ^{14}C y B.P. (AD 1722-1811). Sample W1RAD6 was a bone fragment, found in the b2Bw(f) horizon disrupted by L1 Dike, and it yielded a younger age of 126 ^{14}C y B.P. (AD 1808-1950).

4.3.2.5 Trench WAI 2

Trench WAI2 was parallel to Trench WAI1 about 1 m to the west, and targeted the same sand blow (Sand Blow 1). The *in situ* soil profile was very similar to Trench WAI 1. At this trench the north east wall and the floor were logged and photographed in detail (Figure 4.12). On the north-east wall a fine sandy sill of convex upward shape (unit L1 dike/sill) was exposed at 0.75 m depth. On the floor of this trench a dark grey, sandy sub-rounded feature of 0.63 by 0.73 m was exposed, which was interpreted

[8] In this dissertation the modern liquefaction will be named as L1 and the paleoliquefaction will be labelled as L2.

to be a plan section through a similar but deeper sill. The sill breached the floor of the trench in the oxidised b2Bw(f) horizon (buried twice B horizon), along with other modern sandy dikes.

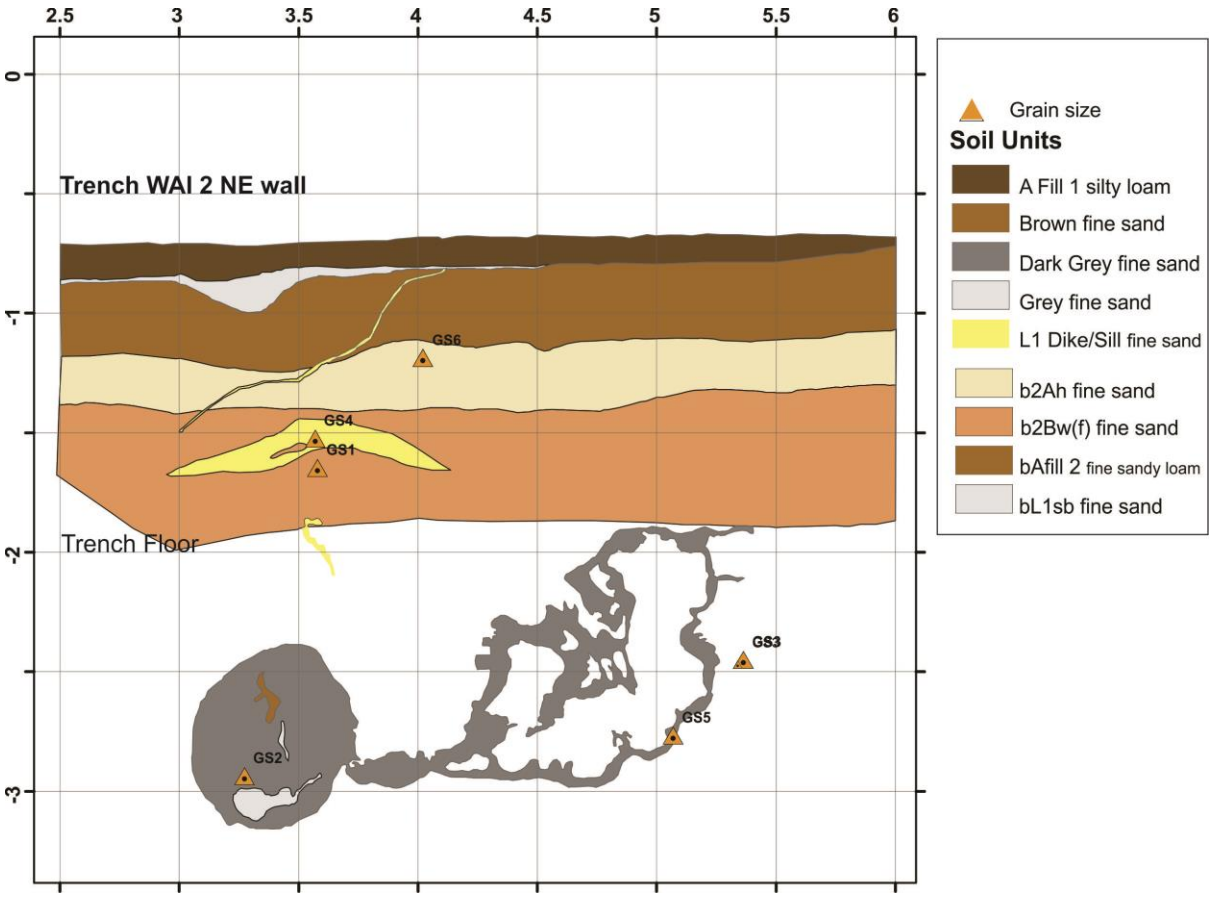

Figure 4. 12 Trench WAI 2 north east wall and floor.

4.3.2.6 Trench WAI 3

Trench WAI 3 was 1.32 m deep and nearly 2.5 m long. Both east and west walls were logged and photographed in detail (Figure 4.13 and 4.14).

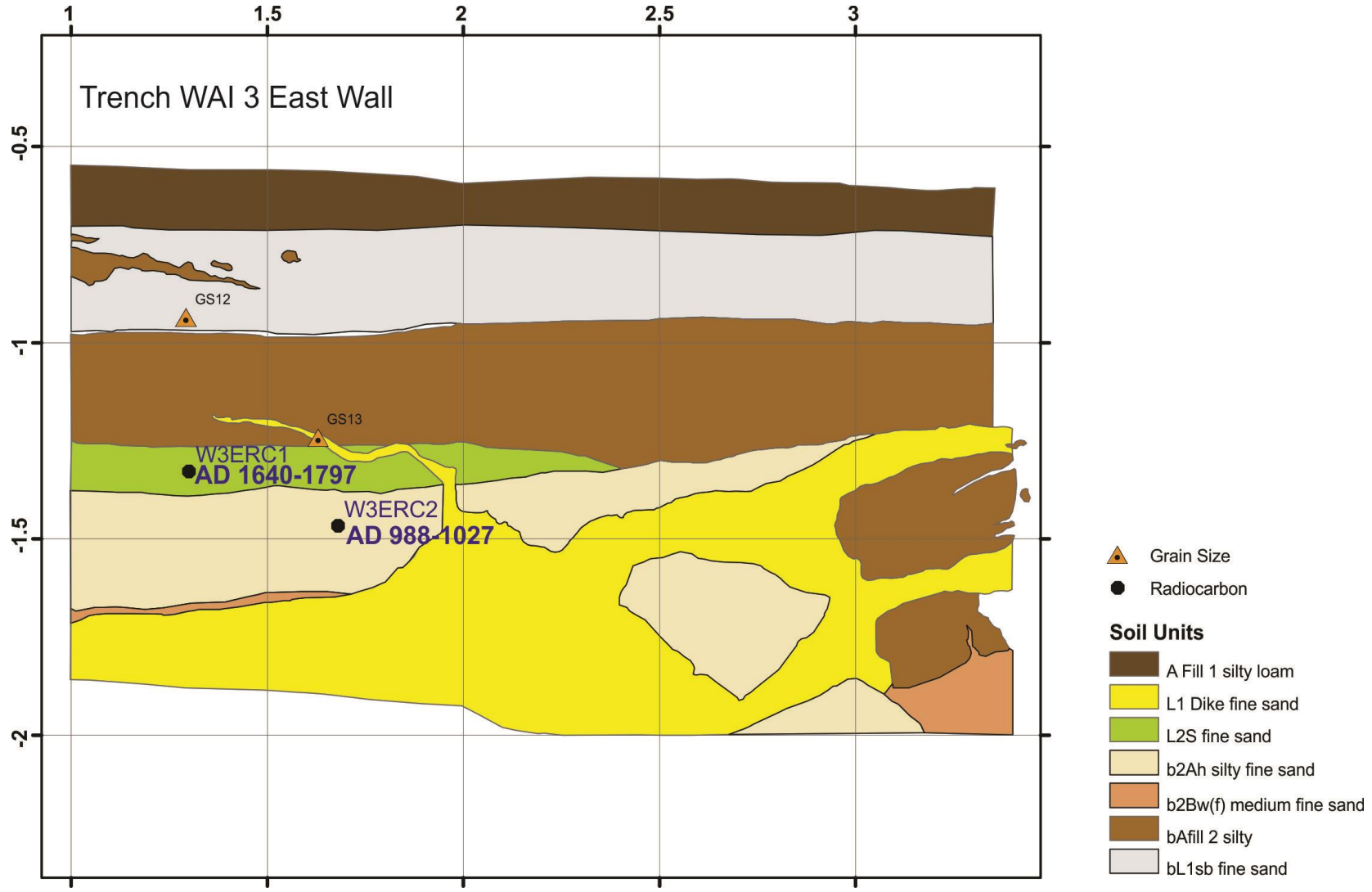

Figure 4.13 Wainoni 3 east wall.

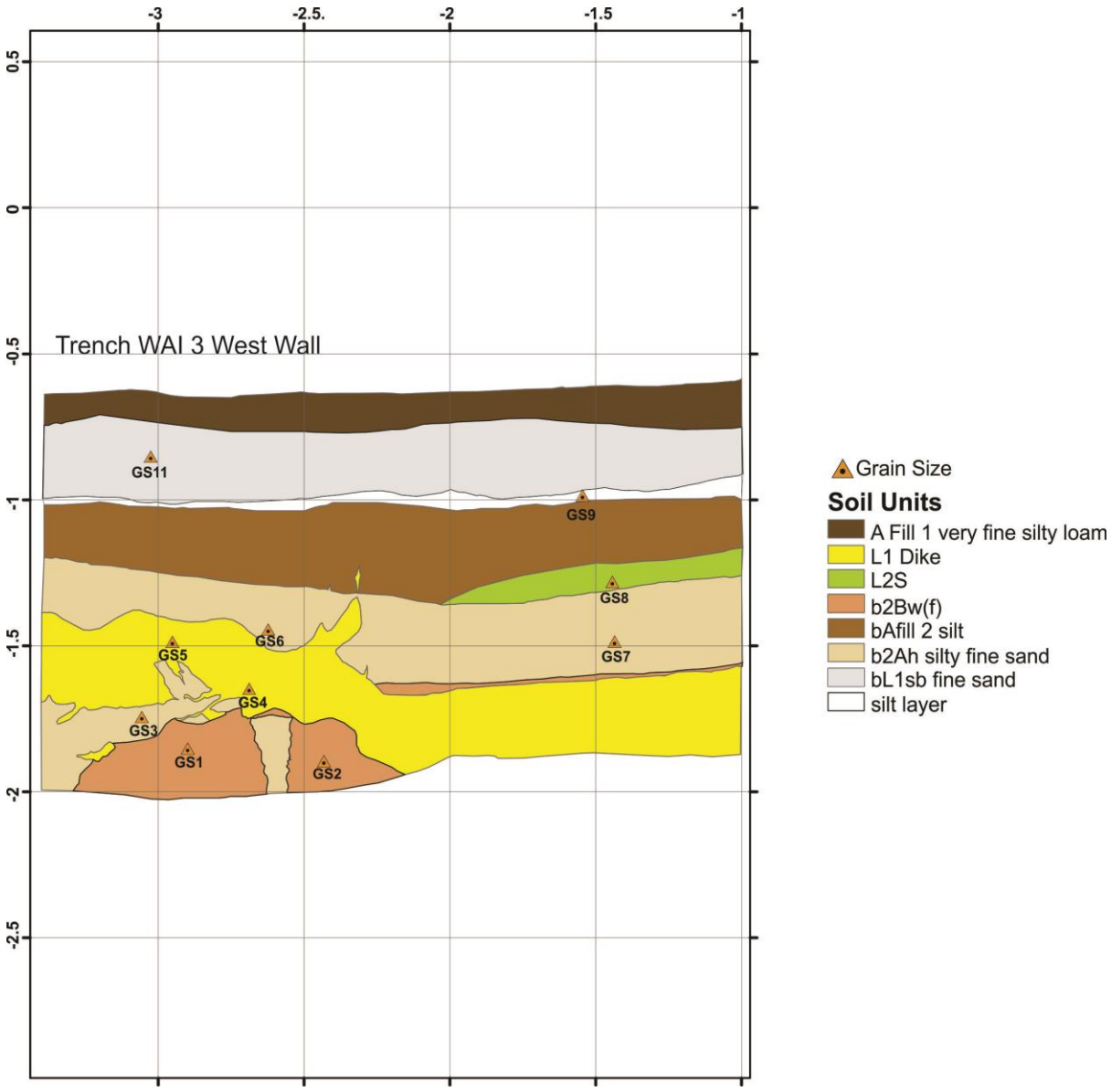

Figure 4.14 Wainoni 3 west wall.

This trench exposed a post-CES fill (unit A Fill 1) overlaying a 0.26 m-thick unit (bL1sb - buried L1 sand blow) distinguished by a white silt lamina on the bottom contact, more obvious on the west wall (Figure 4.14). Unit bL1sb overlay an organic-rich pre-CES fill (bAfill2) of stiff consistency, which in turn overlies unit L2S. Unit L2S represents a suspected paleoliquefaction deposit and it was identified as a compact and weathered (2.5Y3/2 colour) sandy layer sitting on top of unit b2Ah (buried A horizon). Unit b2Ah (from 0.11 to 0.15 m thickness) is the original loamy sand topsoil, which has been disrupted by the liquefaction injection (Unit L1 Dike). Some b2Bw(f) horizon (buried twice B horizon) fragments were exposed in one corner of the trench. The b2Bw(f) horizon is a medium to fine sand with mottles,

worm burrowed near its upper contact. The increased thickness of the buried A horizon (b2Ah) at this trench relative to those at sand blow 1 may be due to its situation in a former interdune depression.

4.3.2.7 Sediment ages at Trench WAI3

Two samples for radiocarbon dating were submitted from Trench WAI 3: W3ERC1, W3ERC2 (Figure 4.13). Sample W3ERC1 was charcoal from a sand-rich paleoliquefaction layer on the east wall (unit L2S), which yielded an age of 263 BP ± 20 ^{14}C y B.P. (AD 1640-1674). Sample W3E-RC2 was a bulk sediment sample from unit b2Ah and it yielded the age of 1079 ^{14}C y B.P. (AD 988-1027).

4.3.2.8 Summary of Trenches at Wainoni Park

The three trenches revealed a similar soil stratigraphy, namely a soil with a thin A horizon and an olive or olive brown B horizon buried by a pre- and post CES anthropogenic fill. Sediment types making up the soil and those retrieved from cores extending below the soil had grain size distributions characteristic of aeolian (dune) sand, and liquefiable sediment. The morphology of the soil is indicative of a generally well drained condition, suggesting the source of the liquefiable sediment is likely to be from below 1.5 m depth. At least two generations of liquefaction features could be identified: the younger from the CES (L1), including sand blows buried by the most recent fill, thick dikes and sills, and the older a weathered sandy sill and potentially a sand blow (L2).

4.3.3 Liquefaction Investigation at QEII Park

4.3.3.1 GPR investigation at QEII Park

At QEII park we targeted Sand Blow A and Sand Blow B (Figure 3 A). At Sand Blow A the 2D 400 MHz GPR survey showed a soil anomaly between 1.0 and 1.5 m depth between 94 and 102 m distance along the line (Figure 4.15). The 3D GPR illustrated an anomaly in the soil profile between 0.25 and 0.75 m depth (Figure 4.16). QEII Trench 1 was dug on this subsurface anomaly.

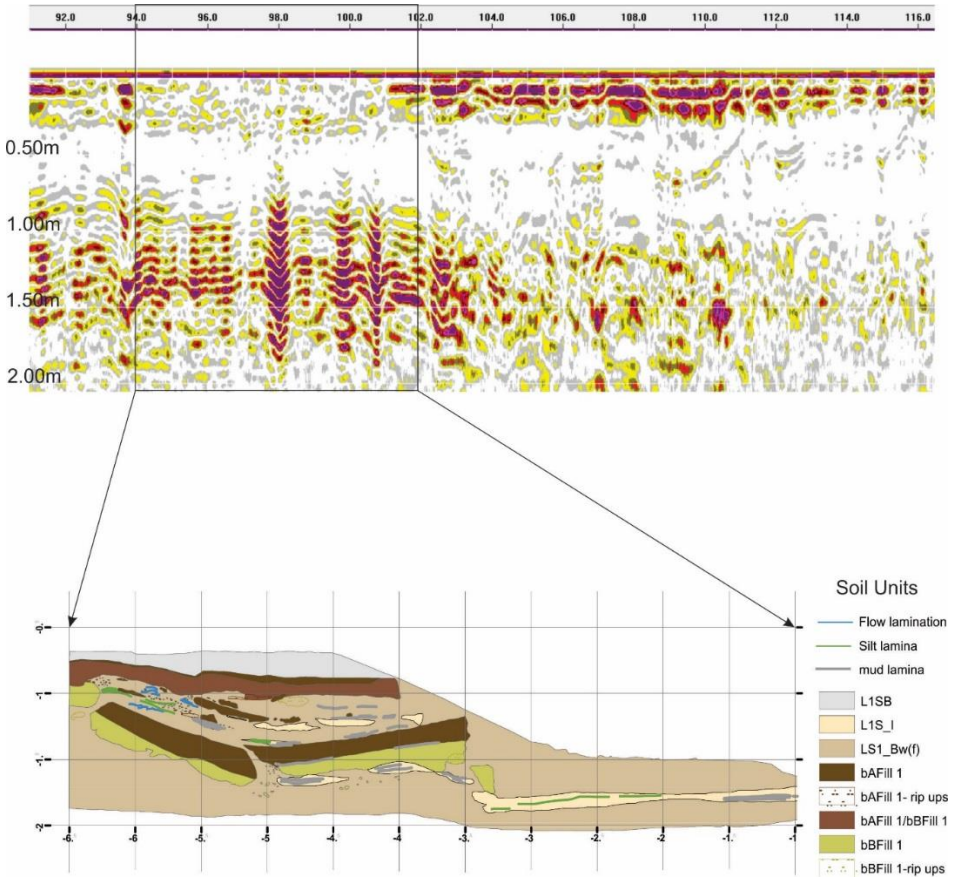

Figure 4. 15 2D GPR line Analysis at QEII Trench 1. The black frame highlights the trench position. The strong reflectance appeared to be between 1 and 1.50 m depth, and can be attributable to a rich organic layer interlayered with a sandy one. However the strong reflectance showed in this 2D line does not clearly match the stratigraphy exposed in the trench. For more details on the stratigraphy of QEII Trench 1 the reader can refer to Figure 4.18.

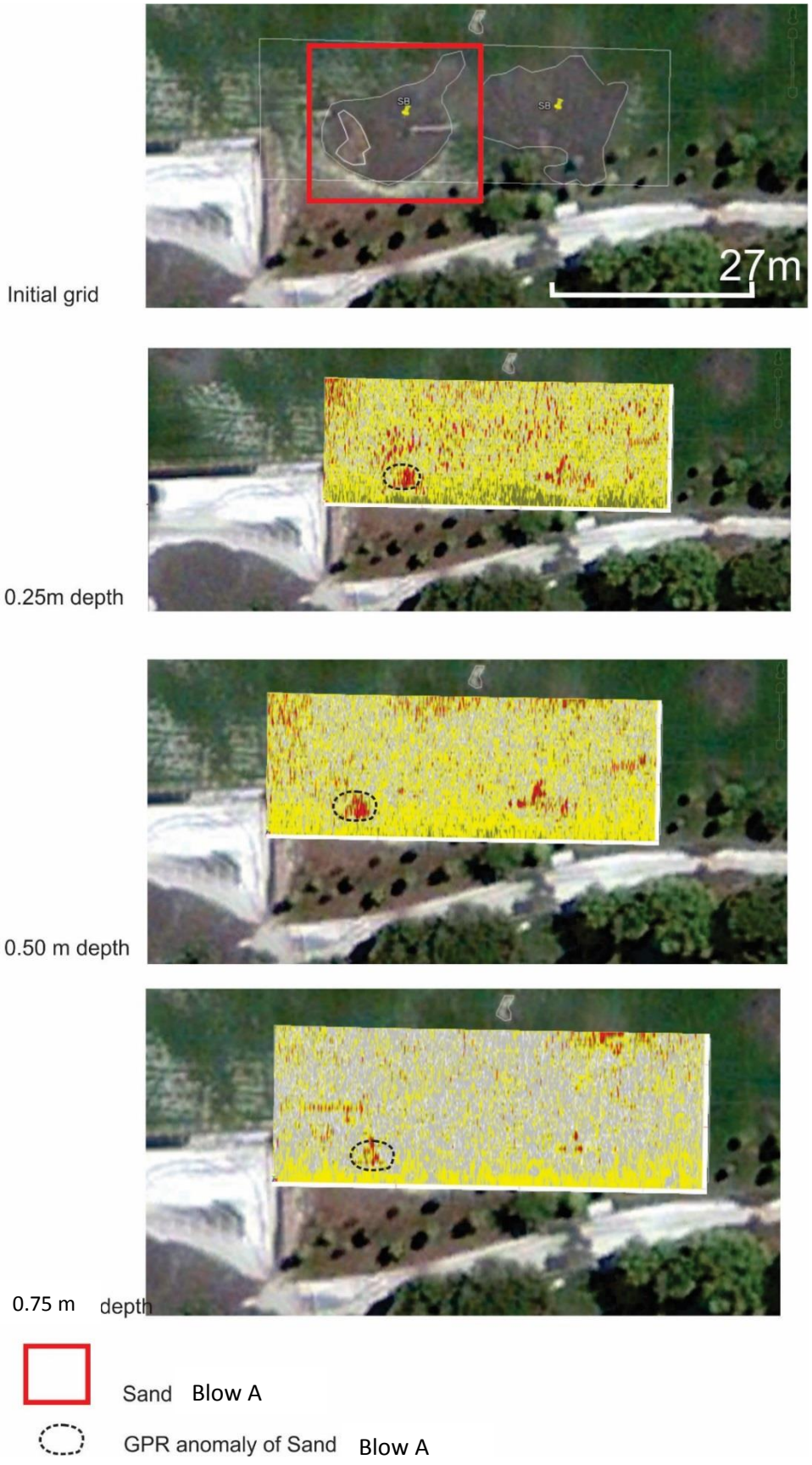

Figure 4. 16 GPR Analysis on Sand Blow A. The GPR anomaly appeared to be observed at 0.25, 0.50, 0.75 m depth.On the right hand side of the GPR image another anomaly is coloured in red and this is associated with the sand blow located on the right hand side of the picture.

At Sand Blow B, the 2D GPR showed a strong subsurface anomaly between 1 and 1.5 m depth (Figure 4.17). The 3D GPR line showed a strong reflectance recorded between 0.75 and 1.25 m depth (Figure 4.17). QEII Trench 2 was dug the subsurface anomaly highlighted by the 3D GPR. A small pit was also excavated parallel to QEII Trench 2 on the same targeted Sand Blow B. Because park services ran close to Trench 2, it was not possible to dig out a bigger trench (Figure 4.3 A and B).

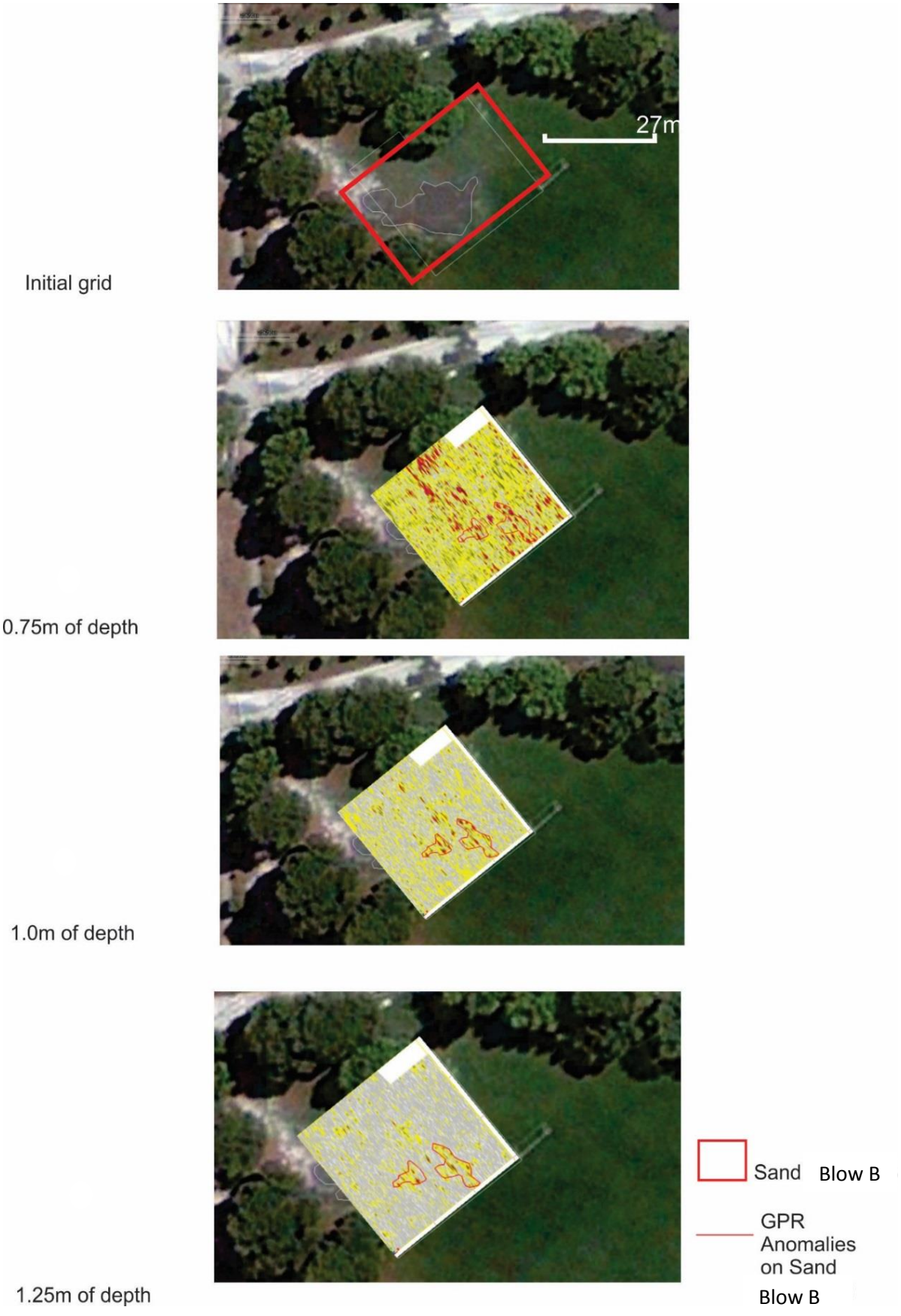

Figure 4. 17 3D GPR anomalies on Sand Blow B. The subsurface anomaly was observed between 0.75 and 1.25 m depth.

4.3.3.2 QEII Trench 1

QEII Trench 1 was 1.18 m deep and nearly 6.5 m long. The north and south wall were logged and photographed in detail (Figures 4.18 and 4.19).

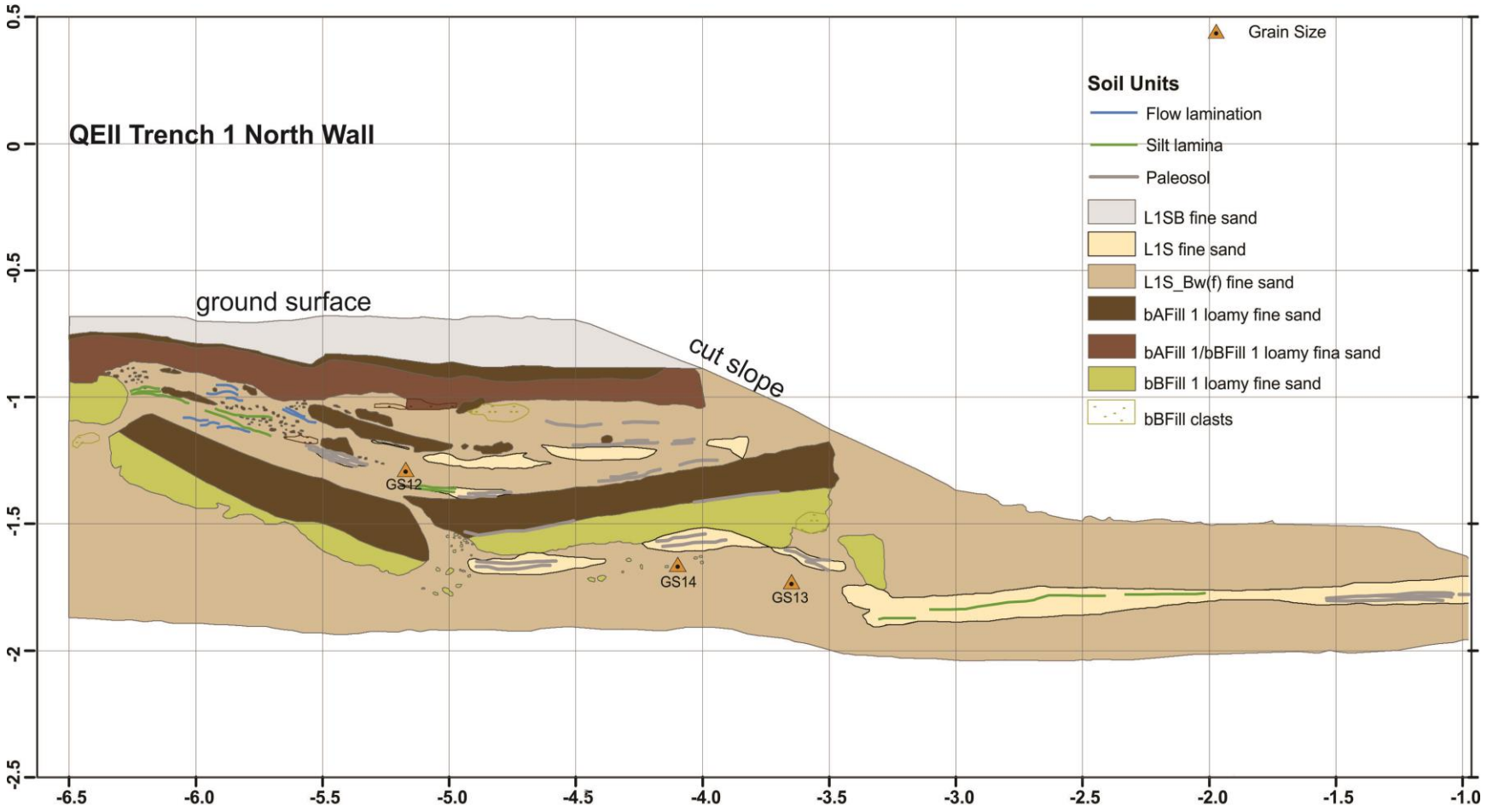

Figure 4.18 QEII Trench 1 north wall

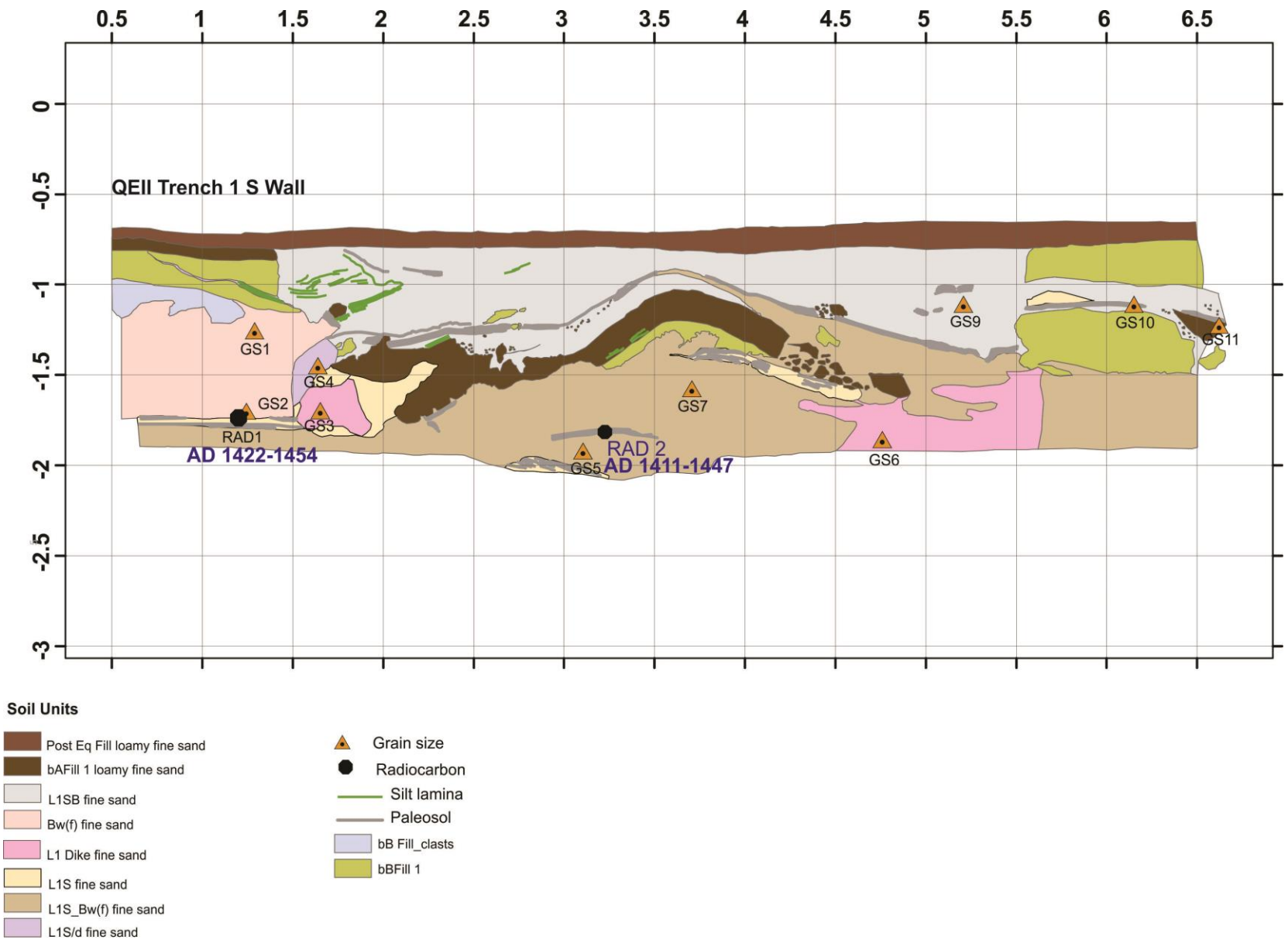

Figure 4.19 QEII Trench 1 south wall

A 0.25 m thick unit L1SB (L1 Sand Blow) occupied the profile of the trench, overlying a pre CES- fill, which was composed of two fill units: unit bAFill 1 (more organic) and bBFill1 (less organic and more weathered). The north wall exposed a combined form of the two fills called unit bAFill 1/bBFill 1. The pre CES fill was buried by a post-CES fill but only on the south wall of the trench (unit Post Eq Fill in Figure 4.19). The sand blow (L1SB) contained many brown rip up clasts from the pre CES fill (unit bBFill clasts). The pre CES fill was broken in many parts and injected by liquefied sand coming from the underlying fine sand LS1_Bw(f) horizon, that is the liquefied form of the Bw(f) horizon (brownish-grey colour). Unit L1 Dike was a nearly 1 m-wide dike exposed on the south wall of QEII Trench 1 (Figure 4.19). Unit L1 Dike presented a bluish-grey very fine sand, in contrast to the liquefied sand from the B horizon. Many scattered fragments of the same bluish-grey very fine sand, but richer in organic matter, were found in many parts of QEII Trench 1, and this layer was called "paleosol" (Figure 4.18 and 4.19). Units L1S ,L1S/d or L1S_Bw(f) are both liquefied sands from the Bw(f) horizon but recognized in the field as different because of their dissimilar content of fines and/or organic matter.

4.3.3.3 Sediment ages at QEII Trench 1

Two samples for radiocarbon dating were submitted from QEII Trench 1 south wall (Figure 4.19): RAD 1 and RAD2 from the fragments of the mud lamina layer.These afforded ages of 504 ^{14}C y B.P. (AD 1422-1454) and 530 ^{14}C y B.P. (AD 1411-1447), respectively.

4.3.3.4 QEII Trench 2

Trench QEII 2 was 3.5 m wide and 1.5 m deep, the north and south wall of which were logged and photographed in detail (Figures 4.20-4.21). This trench was characterized by a pre CES fill (composed by two fill units: unit bAFill 1 and bBFill1), and a post-CES fill (unit Post Eq Fill) (see Appendix A4, electronic supplement for details) overlying a sandy sill (Unit L2) characterized by many organic lenses. The complex and disrupted sandy layer exposed in the trench was fed by a dike breaching through a buried A horizon (unit b2Ah). The latter was notable for a collapse feature. Unit bCg represented the sandy gleyed parent material underlying unit b2Ah.

The dike in Unit L2, close to the collapse feature exposed in the original wall, was initially misinterpreted as a surface crack or fissure caused by the depression of unit b2Ah, then filled by aeolian sand. The three dimensional characteristics of this feature were examined by excavating back into the wall and logging its geometry in exposures 0.18, 0.20, 0.39 and 0.45 m into the face (Figure 4.21). The diagram illustrated that the “crack” merged with the sandy sill within unit b2Ah, suggesting that it was in fact a dike (see log at 20 cm in Figure 4.21). The dike fed a sill, which injected and split unit b2Ah, forming many A horizon lenses. The collapse portion of unit b2Ah was then filled up with sand, as shown on the left-hand of Figures 4.20 and 4.21 A,B,C,D.

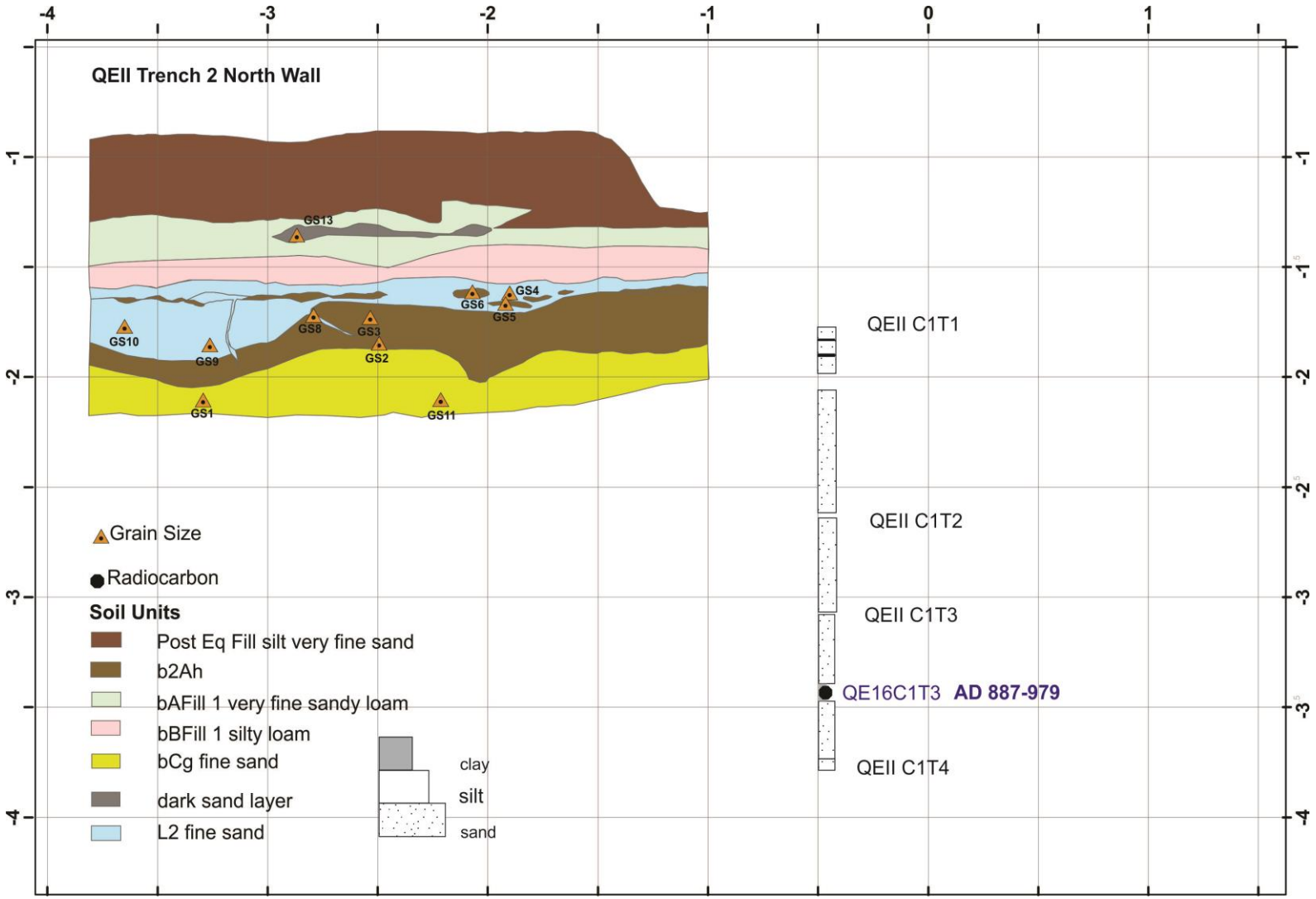

Figure 4. 20 QEII Trench 2 north wall and corresponding core retrieved at QEII park between 1 and 3.45 m depth.

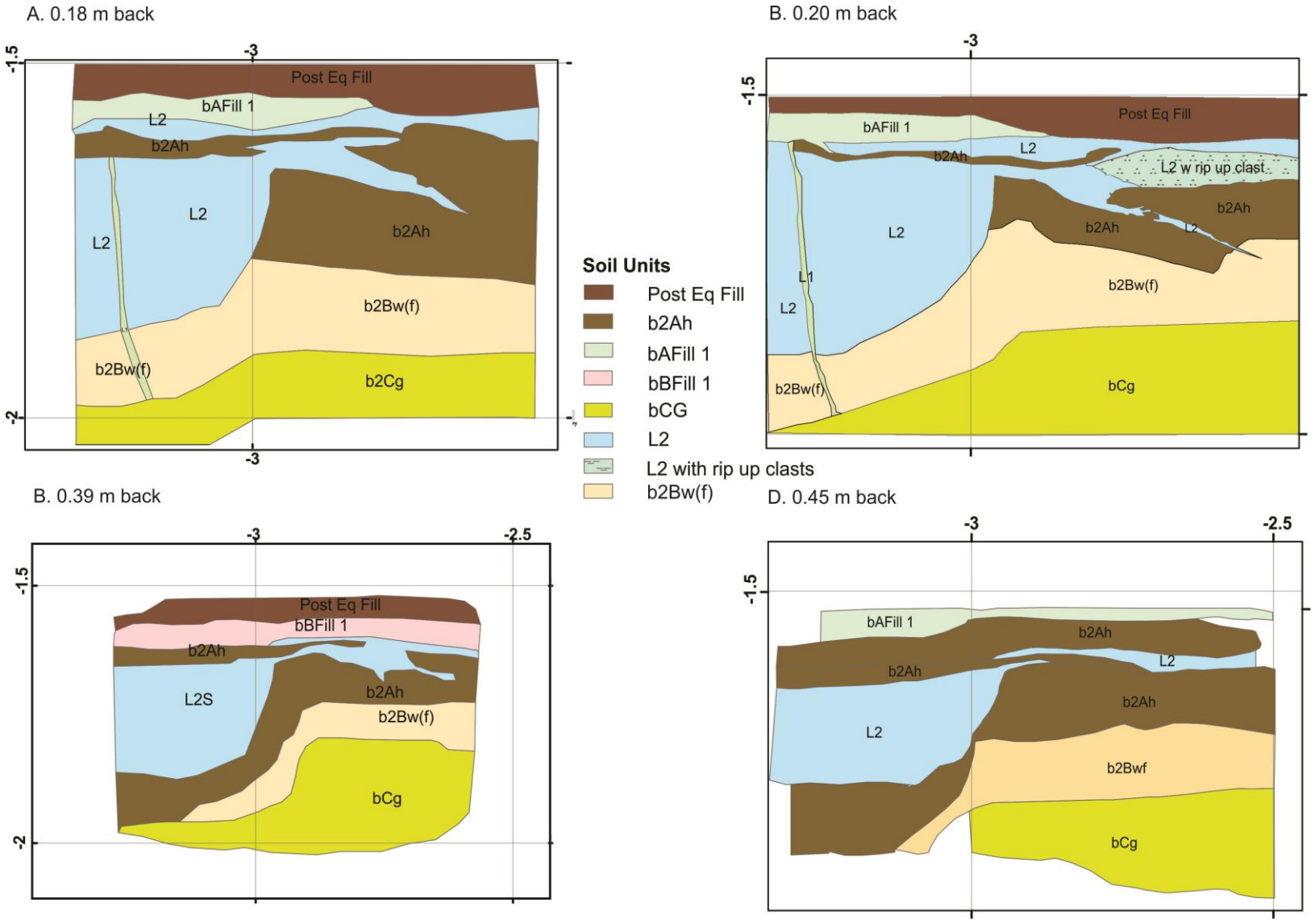

Figure 4. 21 QEII Trench 2 north wall details of the dike of unit L2 excavated back into the wall and logged at A 0.18m; B. 0.20 m; C. 0.39 m; D. 0.45 m, see more details in the text.

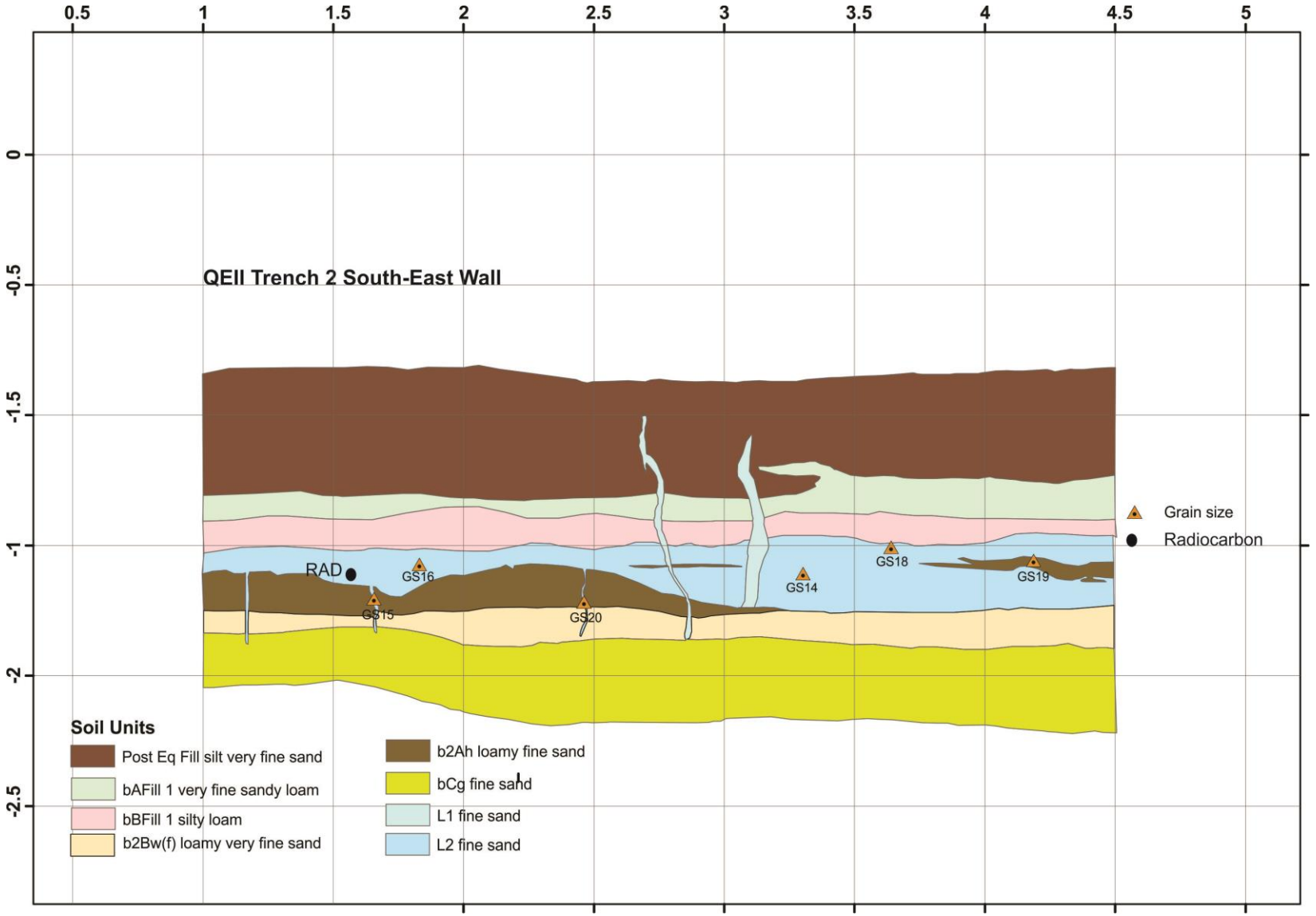

Figure 4. 22 QEII Trench 2 south east wall.

4.3.3.5 Core at QEII Trench 2

At QEII Park a piston core was retrieved at QEII Trench 2 site from 1.0 to 3.45 m below the ground. The whole core was dominantly sand (Figure 4.20 and Appendix A5). The only obvious liquefaction feature observed was a thin (3 mm) whitish silt injection at 1.96 m depth.

4.3.3.6 Sediment ages at QEII Trench 2

One sample from QEII Trench 2 (RAD, in Figure 4.22 from L2 unit) and one sample at 3.17 m depth in the core (QE16C1T3, Figure 4.20) were submitted for radiocarbon analysis. The radiocarbon sample collected from QEII Trench 2 yielded a modern age, which was rejected for the interpretation of this trench stratigraphy. The radiocarbon sample collected from the core yielded an age of 1176 ^{14}C y B.P (AD 887-979).

4.3.3.7 Summary of Trenches at QEII Park

The soil stratigraphy at the two trenches dug at QEII Park were similar and characterized by a very thick compound anthropogenic fill unit. The in situ A horizon was not exposed at Trench QEII 1 which presented instead a loamy very fine sand Bw and fine sand Cu(g) horizons. Trench QEII 1 was characterized by a thick buried A horizon with reddish mottles. The sediment in the trench was coastal sand dune sediment, well sorted, with a massive structure. One generation of liquefaction was exposed at QEII Trench 1 and potentially two generations of liquefaction were discovered at QEII Trench 2. The latter was supported by micromorphology analysis (see Chapter 6 of this dissertation for more details). The sediment characterizing trench and core up to 3.64 m depth was aeolian sand, all liquefiable. The possible source of the liquefaction features was the Bw horizon of the trenches.

4.3.4 Liquefaction investigation at Featherston Avenue Reserve

4.3.4.1 GPR investigation at Featherston Avenue Reserve

Featherston Avenue Reserve site was selected to provide an example of a greenfield area within the dune system with the original topography intact. The 2D GPR displayed a strong anomaly in the reflectance between 154 and 176 m distance along the transect line illustrated in Figure 4.23, caused by liquefaction features and tree roots. This anomaly (coloured in red) was targeted at two of the

trenches excavated (PB2 and PB3). The trenches excavated at Featherston Avenue Reserve are Trench PB1, PB2, PB3 and PB4 (see location on Figure 4.4). The latter was exposed after the Valentine's Day Earthquake and is fully discussed in Chapter 5. Trenches PB1, PB2 and PB3 are discussed next.

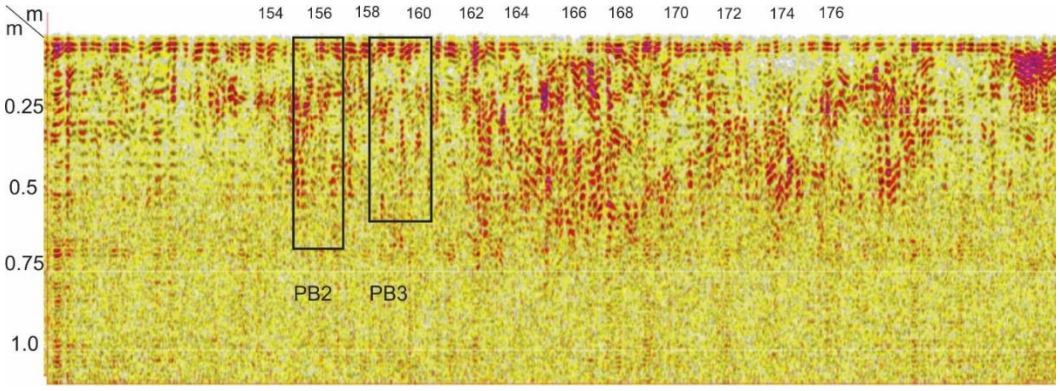

Figure 4. 23 Bidimensional GPR at Featherston Avenue Reserve with the location of trenches PB2 and PB3. The strong reflectance (coloured in red) between 162 and 176 m of lengths is not clearly attributed to liquefaction features but also the presence of tree roots. Overall, the GPR survey at Featherston avenue reserve was inconclusive.

4.3.4.2 Trench PB1

Trench PB1 was ~0.5 m deep and 11 m long. Because of the shallow water table rising within a few hours of excavation, the western portion of this trench collapsed and only the floor was logged and photographed in detail (Figure 5.10, Chapter 5). The floor of this trench exposed a complex circular fine sandy feature comprising three concentric layers (Figure 5.10). The inner circular shape with irregular boundary was a light grey fine sand (unit CES sand blow sediment); the surrounding layer was a brown-coloured organic layer (sandy loam; unit bAh 2010) with fragments of rotten roots; the outer layer was a gleyed fine sand with mottles (unit CES dike), with an irregular contact with the background sand and rotten roots.

4.3.4.2 Core at Trench PB1

Core PB1 was retrieved nearly 5 m south of Trench PB1 (Figure 4.4) from 0.20 m to 2.36 m below the surface Appendix A5 Core PB1 showed predominantly sandy sediment, with evidence of rip up clasts and thin olive brown sandy injections between 1.57 and 1.74 m from the ground (37 and 54 cm along tube 2 of this core). Between 1.9 m and 2.2 m depth the sandy unit alternates with grey clay and silty clay interlayers. Within this unit the contact between sand and clay layers was often abrupt and

irregular, suggesting that liquefaction and soft sediment deformation might have happened at nearly 2 m depth.

Vibracore PBV3 was retrieved at 15 m south of Trench PB1 (Figure 4.4) from 0.2 to 3 m below ground level (Appendix A5). The sediment recovered in Vibracore PBV3 were olive fine sand - sandy loam alternating with clay- clay loam. They were characterized by abundant organic material such as rotten twigs and leaves. In the sandy layer, there was evidence of many clay rip up clasts between 0.83 and 1.66 m below ground level.

4.3.4.3 Trench PB2

Trench PB2 (see location in Figure 4.5) was excavated across Sand Blow 2. It was 0.75 m deep and 8.5 m long. The south wall was entirely photographed and logged (Figure 4.24), while the north wall was photographed and logged only between 0 and 1.50 m of the grid (Figure 4.25).

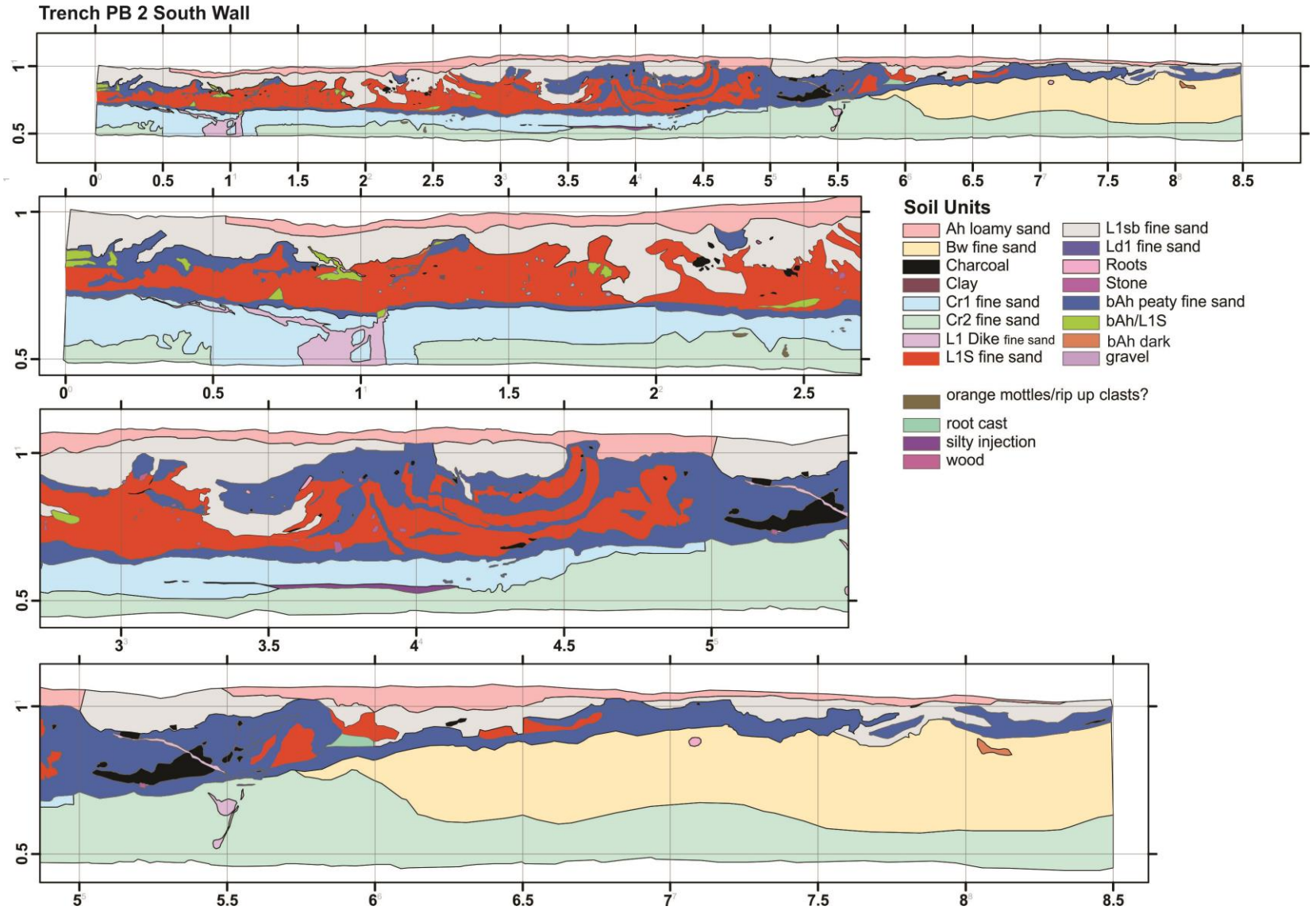

Figure 4. 24 Trench PB2 south wall. Note the pillow-like structures between 3 and 5 m distance along the trench.

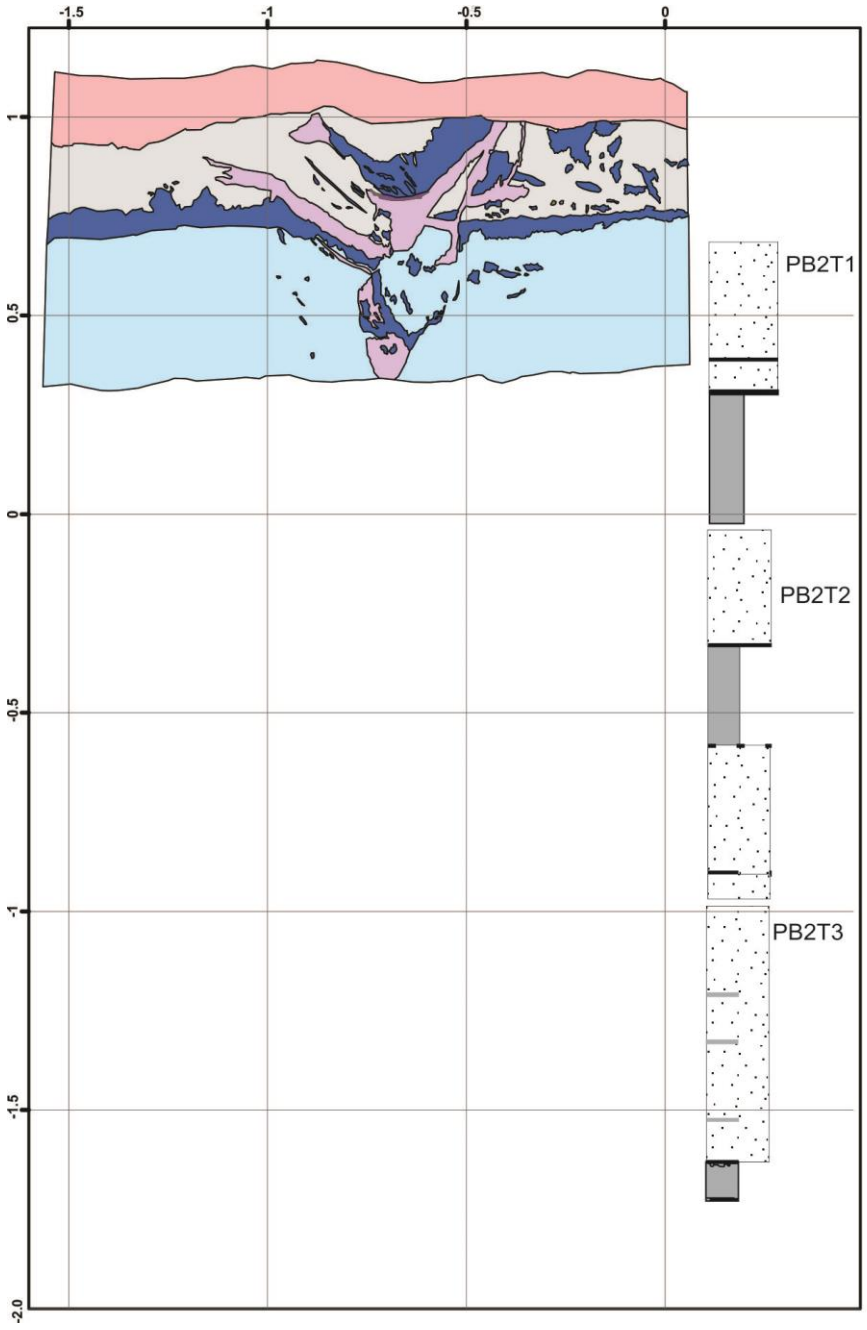

Trench PB 2 North Wall and Core PB2

Soil Unit

- Ah loamy sand
- Cr1 loose fine sand
- L1 Dike fine sand
- L1sb fine sand
- Rip up clasts
- bAh loamy fine sand
- silty injection

clay
silt
sand

Figure 4. 25 Trench PB2 logged portion of the north wall and corresponding core.

Unit Ah, a brownish black loamy sand topsoil with few roots sat on a grey, loose and CES sand blow (unit L1sb). Unit L1sb overlies the pre 2010-2011 topsoil, unit bAh, characterized by an olive and loose massive fine sand. Several phases of unit bAh were observed in this trench, based on the different content of sand or organic matter. Unit bAh-dark was identified as a variety of unit bAh with a higher content of organic matter, whereas unit bAh/L1S had a higher content of sand (see legend of Figure 4.24). The whole stratigraphy of Trench PB2 was heavily disrupted by unit L1S (sill), causing splitting of unit bAh (as well as bAh/L1s or bAh dark) and of the original depositional contact between the layers. Unit Bw was identified as the B soil horizon under the buried Ah horizon (bAh) and it was only observed between 6 and 8.5 m along the trench. Unit Bw was characterized by olive brown fine sand and massive structure. Two slightly different C horizons were identified, units Cr1 and Cr2. In some parts of the trench, this distinction was not possible (see Soil Description Appendix A4). The C horizon was a dark grey, loose fine sand and it hosted the CES dike features observed.

The most striking features at Trench PB2 were "pillow-like features" between 3 and 5 m along the south wall. These features appeared as an alternation of sand (unit L1S) and organic rich material (unit bAh) with common charcoal fragments contorted into a strong concave-upward forms. They were overlain by the CES sand blow (unit L1sb). These features were observed at this site for the first time as unique liquefaction features within the Canterbury coastal setting (Chapter 4 of this thesis).

The north wall of Trench PB2 (Figure 4.25) contained a bifurcating dike (unit L1 Dike) rooted in the Cr1 horizon and injecting into unit bAh. The injection of unit L1 Dike into unit bAh formed many bAh fragments which were dragged into unit L1sb, while some others sank into unit Cr1. Some rip up clasts coming from units not exposed on the wall of this trench were also observed.

4.3.4.4 Core at Trench PB2

Core PB2 was retrieved at nearly 10 m south of Trench PB2 (Figure 4.4) from 0.48 to 3.08 m below ground level (Core Description Appendix A5). The sediment retrieved were grey fine sand beds with root fragments, a massive structure and clay-loam rip up clast that alternated with grey massive clay and silt units. The clay/sand contacts at 2.05 m, 2.53 m, 2.73 m were abrupt, suggesting that the sand

units could have been injected into the clay. Along the bottom portion of the core (2.83 to 3.08 m depth), the clay layers were very disrupted (deformed) and small lenses of sand could be interpreted as being injected into the clay. The presence of rip up clasts and the soft sediment deformation in the core corroborated the idea of liquefaction or soft sediment deformation (SSD) (sensu Allen, 1982) occurring.

4.3.4.5 Trench PB3

Trench PB3 was 5.5 m long and between 0.37 and 0.43 m deep (Figure 4.26). This trench was also excavated on Sand Blow 2, parallel to trench PB2 and only 2 m away. It was excavated to shallower depth than PB2 to avoid the water table, and to facilitate collection of sediment and liquefaction features on the trench floor.The south wall and the trench's floor were logged and photographed in detail. The trench's floor log is not reported in this dissertation.

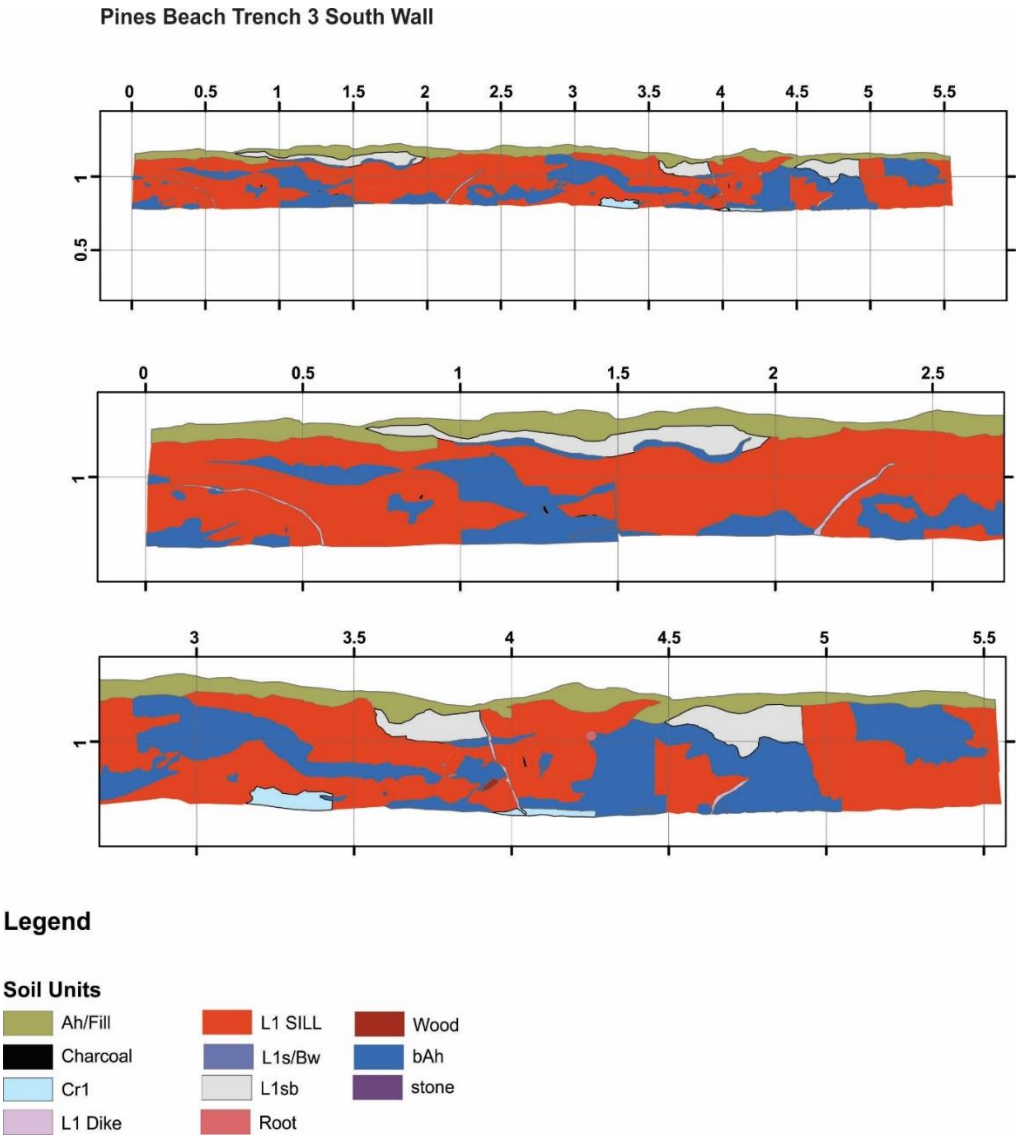

Figure 4.26Trench PB 3

The stratigraphy exposed at Trench PB3 was very similar to that of Trench PB2 (Figure 5.26).

4.3.4.6 Coring at Trench PB3

Two vibracores were retrieved close to the trench (Figure 4.4) (PBV1 and PBV2; Core Description Appendix A5 and in Vibrocore pictures of Vibrocore PBV1, PBV2, PBV3, PBV4) . Vibracore PBV1 was a trial and was only 1 m long. Vibracore PBV2, located at 12 m south of Trench PB3 on the toe of a dune, recovered sediment between ~0.2 m and ~3 m depth. It was characterized mainly by a massive greyish olive fine sand with roots. The clean sand unit graded into a sandy loam at 0.83 m depth. Then, at 2.0 m depth the sandy loam unit alternated with clay sediment and organic rich lenses, resembling rip up clast features.

4.3.4.7 Sediment age at Featherston Avenue Reserve

Two radiocarbon samples were submitted from PBV2 core at Featherston Avenue Reserve from rotten organic fragment covered by detritus at 0.82 and 1.42 m along the tube within a clay unit exposed in the core from 0.8 to 1.6 m along the tube. Both radiocarbon samples yielded overlapping ages of AD 1697-1950 and AD 1637-1797.

4.3.5 Grain size Analysis

All grain size samples collected from the three study sites demonstrated characteristics of unimodal well sorted sediment, typical of aeolian dune sediment (Ricci-Lucchi, 1980) with a percentage of sand >75% (Gradistat grain size analysis). All samples analysed from trenches and cores across all study sites fell into Tsuchida's (1970) "liquefiable soil" boundaries (see Figure 4.27 as an example and Figures 1 to 9 in Appendix, A7).

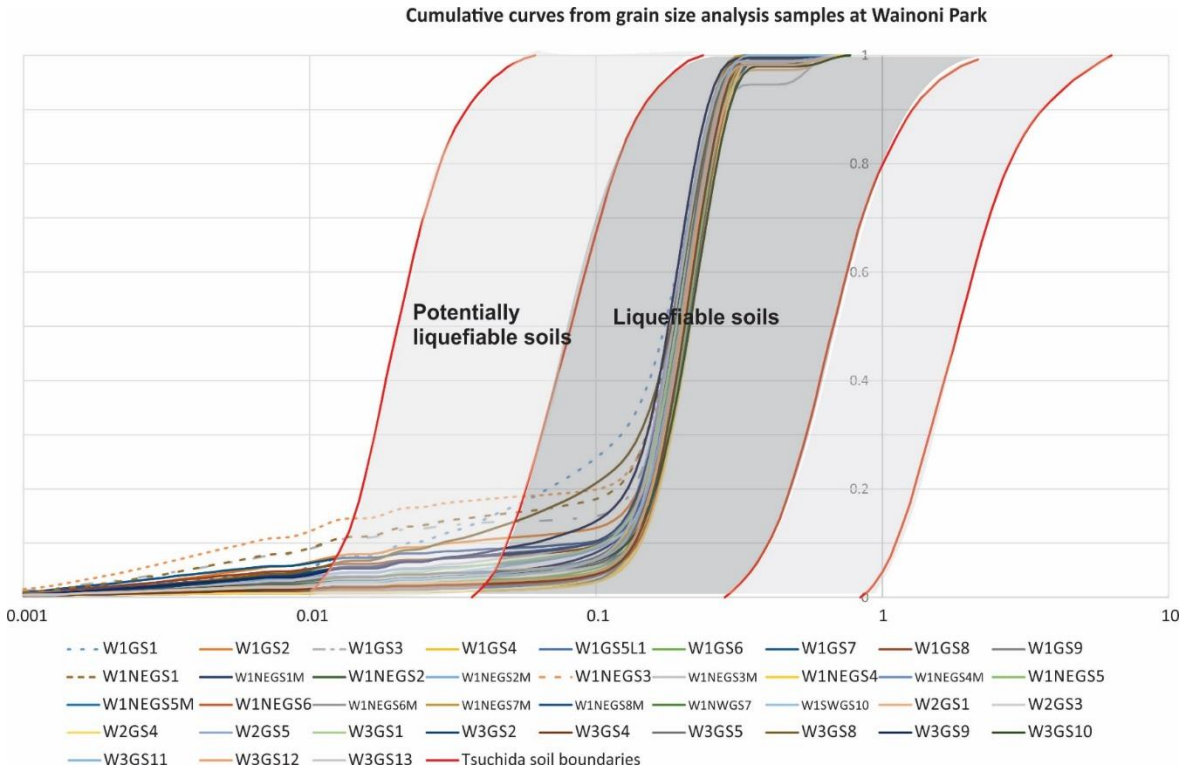

Figure 4. 27 Cumulative Curves for grain size samples collected from Trenches at Wainoni Park. All samples fell into the "liquefiable soils" area of Tsuchida's'(1970) soil diagram. Some samples (i.e. W1GS1 or W1GS3 or W1NEGS3) present a higher content of fines therefore their curve crosses the boundaries of Tsuchida's (1970) soil diagram. Note the samples here displayed are the same samples shown in the Trench log (Figure 5.15) but with the prefix "W1". Therefore sample GS1 of Figure 5.15 here becomes W1GS1 and so on.

This result reflects the environment of deposition of dune sand characterizing the three study sites, which produced clean fine sand highly predisposed to liquefaction. A few samples are characterized

by a multimodal grain size distribution, typical of alluvial sediment (see Chapter 3 of this thesis for more details): at Wainoni Park, Sample WAI1T2 -GS2-_50-52 was collected from a liquefaction feature in the core (LF3, at 2.75 m below the surface, Core Description A5), Figure 4.29; at QEII Park, two other samples collected from unit L1 Dike (samples QEIIT1S3 and QEIIT1S6 in polymodal grain size distribution of ejecta samples collected in the coastal environment) and labelled as GS3 and GS6 in the trench log in Figure 5.25) Figures 4.30 and 4.31; at Featherston Avenue Reserve sample PB1T3GS2, at 2.6 m depth Figure 4.31. This result suggests that on the dune system of Christchurch, liquefaction features were potentially sourced from aeolian but also alluvial sediment.

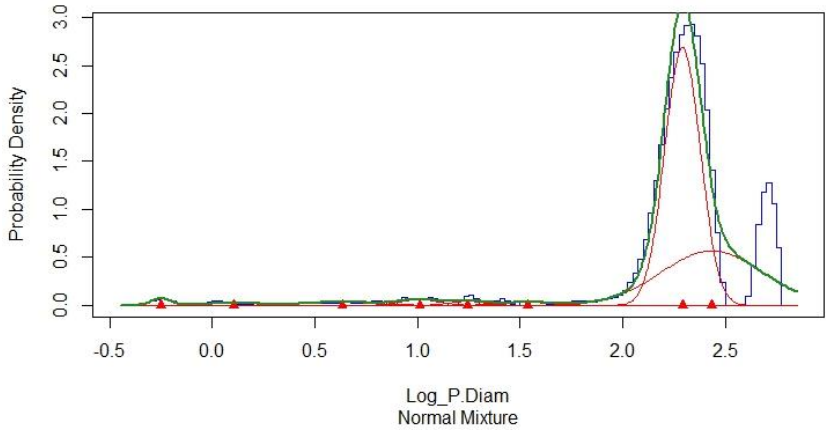

Figure 4. 28 WAIT2_GS2_50-52 sample showing a multigaussian distribution, typical of alluvial setting from a core sample at Wainoni site at 2.75 m depth, see Chapter 3 of this thesis for more details on the multimodal distribution characterizing the alluvial sediment.

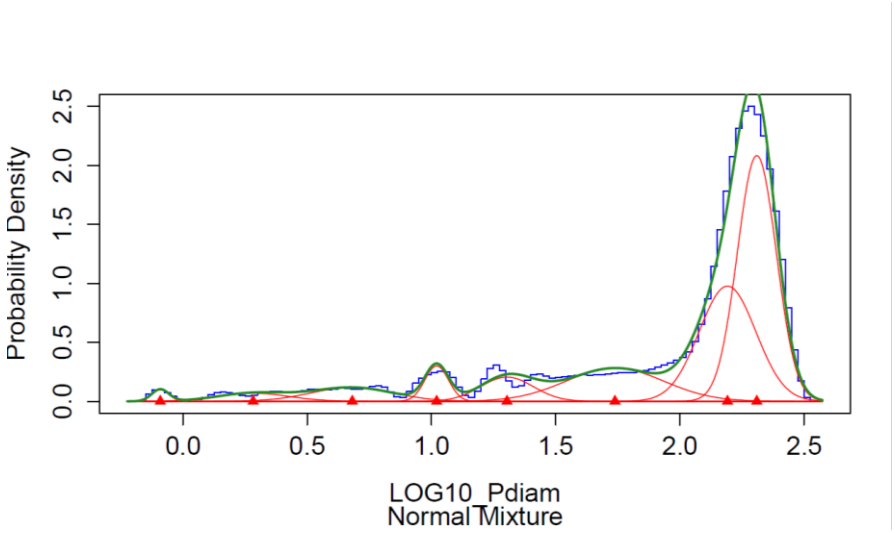

Figure 4. 29 Multigaussian grain size distribution of sample QEIIT1S3 (GS3 in the log of Figure 5.25) collected from a layer identified as liquefaction layer.

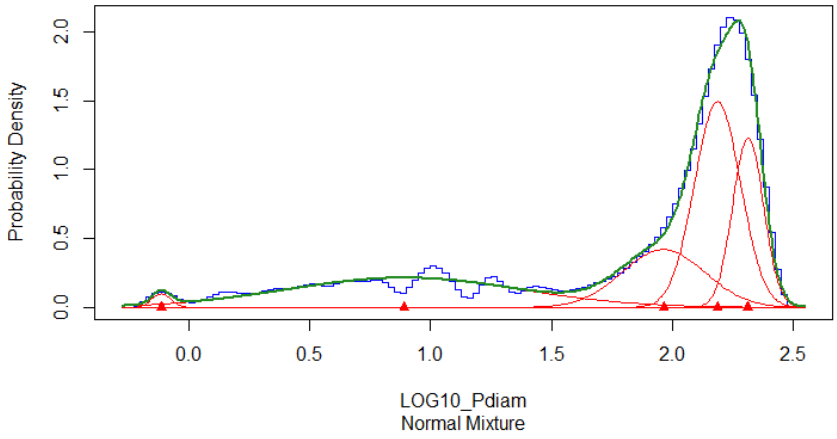

Figure 4. 30 Multigaussian grain size distribution of sample QEIIT1S6 (GS6 in the trench log of Figure 5.25).

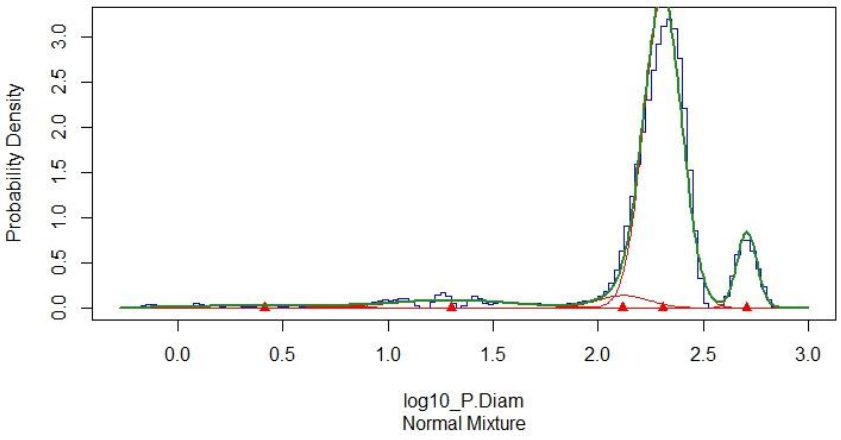

Figure 4. 31 Multigaussian Grain size distribution of sample PB1T3GS2 located at 2.6 m depth

4.3.6 Sedimentary architecture description at Featherston Avenue Reserve

Two transects, Transect 1 and Transect 2 (Figure 4.4), are used to characterize the general stratigraphic architecture at Featherston Avenue Reserve, as shown in Figures 4.32 and 4.33.

4.3.6.1 Transect 1

Transect 1 (Figure 4.32), 170 m long and oriented north-south, lay along the interdune swale and ranged in elevation between 1.4 m a.s.l. and a maximum of nearly 2 m a.s.l. Unit D represents a dune sand exposed in the trenches and the upper portion of all the cores. It is identified on the basis of the geomorphic characteristics and grain size analysis. Unit D overlies or is interfingered by a massive clay unit with some organic fragments, identified as a channel fill deposit and labelled as unit C. The inference that unit C is a channel fill is based on sediment characteristics and the proximity of Kairaki Creek. The low lying area now occupied by Kairaki Creek could represent a relict lagoon of the Waimakariri River (Shulmeister pers. comm). Unit C is found entirely above mean sea level and thins to the north, being last observed in core PBV3.

Below the modern sea level and underneath unit C, a transitional unit, unit T, was identified. Unit T has two slightly different facies: 1) an alternation of clean sand layers with clay layers; or 2) an alternation of clay layers with sandy clay or sandy clay loam (Core Description, Appendix 5). Unit T occupies a similar elevation range along the transect from about 0 m a.s.l. to -1 m a.s.l. . Below unit T, unit D, with grain size characteristics of dunes appears again.

There is no clear association of surface manifestation of liquefaction with geomorphic features or sedimentary units along this transect. Sand blows were apparently scattered randomly along the whole low lying-interdune area of Featherston Avenue Reserve.

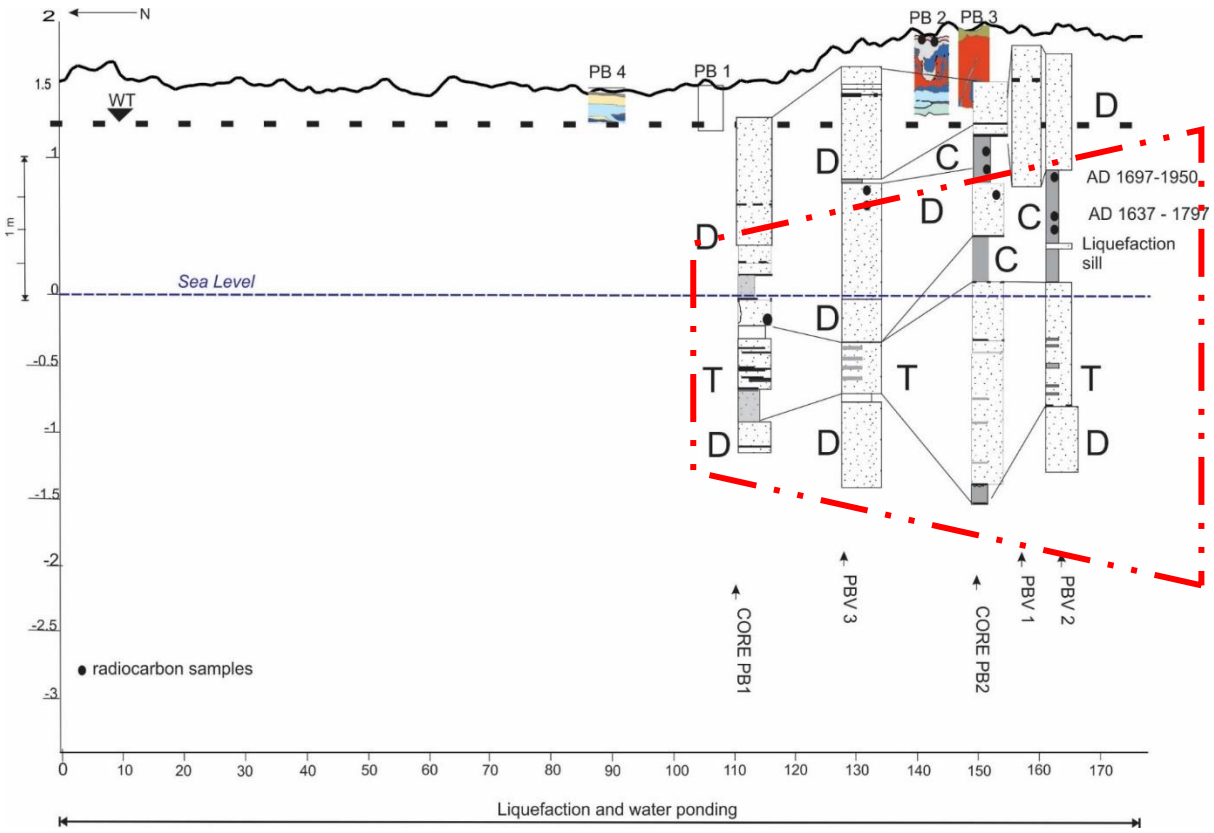

Figure 4. 6 Subsurface sedimentary architecture at Featherston Avenue Reserve site along Transect 1, the red frame highlights the potential liquefaction source layer, see text for more details. Please note, not all the radiocarbon samples collected have been submitted for dating within the scope of this thesis.

4.3.6.2 Transect 2

Transect 2 (Figure 4.33) was aligned west to east from Vibracore PBV2 to PBV4 (for description of Vibracore PBV4 see Appendix A5) to study the stratigraphic changes from the dunes toward the floodplain/estuary system of Kairaki Creek. The higher elevation area to the east corresponds to the dune toe (~2.0 m a.s.l.), the low elevation area in the west, to the floodplain/estuary, and the two highpoints midway, to manmade river stopbanks.

Unit D in the top of PBV2 pinches out to the west, between 88 and 92 m along the transect (Figure 4.33) while unit C thickens from occupying the height interval -0.2 to 0.7 m a.s.l. to - 2 to 0.7 m a.s.l. in PBV4. Unit T forms the base along the whole transect though its upper boundary declines from -0.8 m a.s.l. to -3 m a.s.l. from east to west.

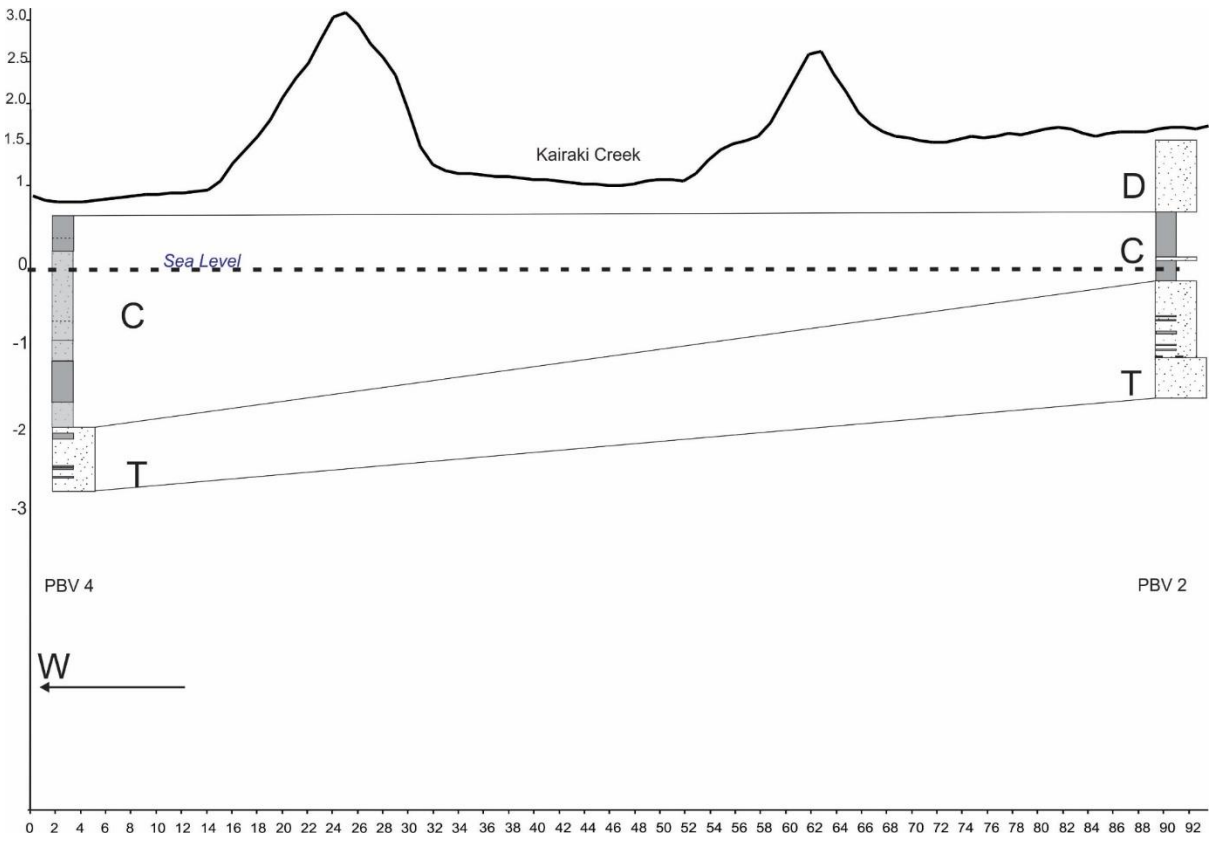

Figure 4. 7 Subsurface sedimentary architecture at Featherston Avenue Reserve site along Transect 2.

4.3.6.3 Summary of Trenches at Featherston Avenue Reserve

All trenches excavated at Featherston Avenue Reserve showed very similar soil stratigraphy, characterized by a very thin brown post CES A horizon and a Bw horizon heavily disrupted by CES liquefaction. The sediment exposed in the trenches is well sorted sandy sediment of aeolian origin. However, the sediment retrieved in the core revealed the presence of other sedimentary units such as a channel fill unit and a transitional unit (as a mixture of dune and channel sediment). The liquefaction source layer was exposed in the trenches in most cases as Bw horizon disturbing and deforming the pre CES A horizon. No paleoliquefaction features were easily recognizable at this site

4.4 DISCUSSION

The liquefaction investigation in the coastal fringe of the Christchurch region presented in this chapter brought to light important aspects of the sedimentary evolution of the dune field of the north Canterbury region, and, more importantly, its liquefaction susceptibility.

4.4.1 Style of liquefaction features at the surface

The liquefaction sand blows in the coastal setting resulted in a rounded or sub-rounded shape (commonly 1 m in diameter, but often more) that are randomly scattered in the dune fields, with particular concentration along the interdune field deposits. This result differs from the alluvial environment where liquefaction features often coalesced to form lineations corresponding with paleochannel margins or scroll bars (Chapter 1 of this Thesis, and Almond et al., 2012; Bastin et al., 2015; Tuttle, 2001a; Tuttle et al., 2017 ; Villamor et al., 2016; 2014).

4.4.2 Main liquefaction features observed in the coastal system of Christchurch

4.4.2.1 Near surface liquefaction

In the coastal fringe of Christchurch, sand blows, dikes and sills analogous to the liquefaction features exposed in the alluvial setting were observed. The dikes revealed in the coastal dune system of Christchurch are wider than those observed in the alluvial setting. For example, Wainoni and QEII Parks exposed dikes up to 1 m wide, while in the alluvial setting (Chapter 3 of this thesis, and Villamor et al 2014, 2016) the dikes were up to few cm wide only. However, new liquefaction features were also revealed, such as collapse systems, A horizon splitting, and “pillow-like structures”. The tendency for liquefiable source layers to be close to the surface (<1.3 m depth in all study sites) was also a feature of the coastal zone. This arises as a result of the ubiquity of liquefiable sediment deposited by aeolian saltation processes, and also the proximity of the water table to the surface in the lower part of the coastal plain where these sediment types and landforms occur.

4.4.2.2 A horizon splitting

In most of the trenches of the coastal setting disturbance was observed of the original organic-rich surface (A) horizons of the sandy soils of the coastal area (e.g. bAh2010 at Featherston Reserve) by both CES and past liquefaction events. The disrupted A horizons displayed many discrete organic-rich lenses, and appeared disintegrated horizontally and sometimes vertically (Figure 5.8).

It is hypothesized that deformation of the A horizon is a multi-step process which involves:

(1) injection of low angle dikes and sills, which dislocates or "delaminates" that horizon (Figure 5.8 b);

(2) further intrusion or injection of fluidised sand (sand dikes and sills) into the soil produces inflation, fragmentation and disintegration of the A horizon (Figure 5.8 c);

(3) evacuation of fluidised sediment from close to the surface, and sometimes immediately beneath the A horizon, causes collapse of parts of that horizon, which causes overthickening of sand blows in the surface depressions created.

Other examples of A horizon splitting were observed at all the trenches investigated. For example, between vertical lines 0.5 and 4 on the north-east wall of Trench WAI 1, a sandy paleoliquefaction sill (L2S) is injected into a buried A horizon (b2Ah), splitting the soil (Figure 4.15). In QEII Trench 1, large sections of the A horizon seem to be floating in a massive liquefaction sand (Figure 4.23 and 4.24). Other examples of A horizon splitting features were exposed in the hand dug pits nearby the trenches at Featherston Avenue Reserve (see logs of the pits in the Soil Pits Appendix, A8).

In general, A horizon splitting seems to create a complexity of the (soil) stratigraphy that could be difficult to interpret after the event. In particular, A horizon splitting may be misinterpreted when strong weathering starts obscuring the textural and chemical differences between the injected sand and the in situ soil (e.g., old paleo-liquefaction) or when the injection occurs at the base of the Ah. The organic-rich surface (A) horizons of the aeolian sandy soils of the coastal area appear to be particularly prone to disruption or splitting caused by high pressure liquefied sediment and fluid-drag stresses during injection of liquefied sediment. This is because A horizons are developed on well sorted aeolian sand in which poorly structured or structureless soil horizons develop. Low clay content, poor structure and low cohesion predispose the soil to parting and rupture (see Chapter 5 of this thesis for more details).

4.4.2.3 "Pillow-like" and collapse features

At Featherston Avenue Reserve, the disrupted buried A horizon remnants formed concave-upwards crescentic forms, delineated by weathered sand (Fig. 5.11), that were called "pillow-like" features. Physically, they resembled pillow structures, i.e., soft sediment deformation (SSD) features characteristic of lacustrine sediment (sensu Anketell et al., 1970; Seilacher, 1969). However, in lacustrine environments, the pillow structures are triggered by an inverse density gradient (denser layer over a less dense layer see for references Alfaro et al., 1999; 2001 ; 2010; Moretti et al., 1999; 2002; Moretti and Sabato, 2007) not observed at Featherston Avenue Reserve: A horizons are low density surface horizons with no high density overburden. Therefore, the mode of formation of "pillow-like" features exposed in the coastal system of Christchurch posited here is different from the above literature and is described as follows: 1) liquefaction of soil layers close to the surface such as B or C horizons injects and splits the former topsoil forming two (or more) A horizon layers, or produces several lenses of A horizons separated by liquefied sand (Figure 5.12b, of chapter 4); 2) evacuation of sediment from the shallow subsoil causes subsidence and surface depressions (Fig. 5.12 b); 3) subvertical water-escape features (Figure 5.12 c) form to carry the sediment upward and allow the high porewater pressure to be vented (Figure 5.12 c); 4) sand blow material and surface organics/debris flow into surface depressions, increasing stratigraphic complexity (Figure 5.12 of Chapter 5). In this scenario, the concave-up crescentic forms are result of the subsurface collapse shown in Figure 5.11.

Collapse features observed in the coastal setting of Christchurch also resembled, in plain view, a sand blow discovered by Amick et al. (1990) in the coastal setting of the East of United States. The latter features were named craters and resulted from an explosive ejection of sediment resulting from liquefaction. However, our experience during the Valentine's Day Earthquake showed that the sand blows were not induced by an explosive event (Chapter 5). Moreover, eye-witness reports from residents of the Featherston Avenue Reserve make no mention of explosive ejection of material in any of the liquefaction-inducing main shocks of the CES.

Pillow-like features are therefore considered as type of collapse feature, which are likely to form when the water table is close to, or at, the ground surface and the sediment is fully saturated. These features have possibly been formed during the September 2010 Earthquake when the early spring water table was very close to the surface.

The collapse features are formed as a result of the evacuation of fluidised subsurface sediment to the ground surface, and to the formation of a void into which the overlying material collapsed (Chapter 5). In some cases the collapse is also followed by deposition of liquefied material on top of it. This latter was observed, for example, at QEII Trench 1 south wall and at QEII Trench 2 Figures 4.19 and 4.21, respectively). Often the collapse feature is observed in conjunction with A horizon splitting features.

At Trench PB1, another example of a 2010-2011 collapse feature was observed. Prior to 14th February, a circular feature in the floor of Trench PB1 (c. ~ 0.5 m) was interpreted as a conduit through which liquefied sand vented during a paleoliquefaction event (Figure 5.10). Based on lessons learned from the Valentine's Day liquefaction features (Figures 5.5, 5.6), this feature is now considered to be a plan-section of a collapse feature. The central sandy core was interpreted as CES sand blow material that flowed into a subsided topsoil (see Appendix 3). The olive green-coded ring (unit bAh 2010) surrounding the central sandy core represents the subsided 2010 A soil horizon. Outside the olive-green ring, a blue-coded thinner ring of sand is probably a later dike of the CES exploiting the weakness at the boundary between the distorted A and C horizons (Chapter 5). In cross-section, the buried A horizon would delineate the upwardly concave crescentic forms described as 'pillow-like features'.

4.4.3 Surface manifestation and Landforms

The surface manifestation of liquefaction in the coastal fringe of Christchurch region appeared to occur in spatial coincidence with the interdune depression, where the water table was shallower. At Wainoni and QEII Parks there is no clear geomorphic expression of the dune field because these sites are located in the Christchurch urban area, and their original topography was modified. However, the natural geomorphology of Featherston Avenue Reserve site is well preserved. The latter site is located

in an interdune depression and a clearer association between liquefaction ejecta and geomorphic features was observed. The nearby region was characterized by dune ridges that had none or very rare surface manifestation of liquefaction (Figure 4.4). The high susceptibility of Featherston Avenue site is caused by the shallower water table, induced by the proximity to the sea, and to Kairaki creek. It is clear that the sites with surface manifestation of liquefaction had highly susceptible layers within 0.5 m of the surface. However, as previously addressed it is not ruled out that other subsurface beds may have liquefied but the liquefied sand did not reach the surface, as shown by liquefaction features and soft sediment deformation observed in the vibracores and piston cores retrieved at this site, or by the soil pits.

4.4.4 Source layer of the 2010-2011 liquefaction

Information on the potential liquefaction source layer is inferred from the grain size analysis and evidence for liquefaction features in trenches and cores. The analysis with Gradistat (in Gradistat grain size analysis), permitted quantification of the main grain size properties of the stratigraphy explored: grain size distribution, mean, sorting, skewness, kurtosis.

Comparison of the cumulative curves with the Tsuchida's (1970) highlighted that all the sediment (both trenches and core sediment) at the three sites investigated fell into the "liquefiable soil" area. At all sites the dune sand was the primary source layer of liquefaction sand. However, at the three sites there was also evidence of a second potential liquefaction source layer. At Wainoni Park there was evidence of injection of alluvial sediment within the core at ~ 2.75 m depth from the ground (or ~+ 3.0 m a.s.l.), from grain size samples WAIT2_GS2_50-52 (Figure 4.28). The source layers of coastal and alluvial origin could have liquefied during the same event or in two different liquefaction events. At Wainoni Park, the water table was between 1.30 and 1.50 m depth during auger investigation in the summer period (before the 2015 February trenching campaign), suggesting that during dry periods the deeper layers (alluvial origin) may be an important source. Also, Wainoni Park did not liquefy during the September 2010 earthquake (local reports and CGD0200, 2013) when it is reasonable to assume higher water table conditions, but it did liquefy during the three major earthquakes in 2011

(February eartquake, June and December earthquakes CGD0200, 2013). As a consequence, the modern liquefaction features sourced from alluvial sediment (at least at 2.75 m from the ground or deeper than this) could have been caused during any of the three 2011 liquefaction events, whereas the modern liquefaction features formed from aeolian sediment were likely to result from the June or December events when the water table was higher, reflecting winter or early summer conditions.

At QEII Park the visual inspection of cores and trenches, and grain size analysis of the 2.45 m core of QEII Park confirmed the presence of aeolian sediment down to ~3.5 m depth (Figure 4.25). Therefore the liquefaction source layer at this site is only characterized by aeolian sediment.

At Featherston Avenue Reserve, the high liquefaction susceptibility and the shallow water table meant that a source layer was exposed in the trenches. The grain size analysis confirmed the field stratigraphic interpretation showing that, like Wainoni and QEII Parks, all the samples analysed (collected from trenches and cores) fell into the liquefiable soil area of Tsuchida's (1970), (Appendix A7). The detailed analysis of the soft sediment deformation observed in the cores revealed also that sand liquefied i) between 1.9 and 2.3 m depth in PB1T3; ii) potentially in the whole core sections of PB2T2 and PB2T3; and iii) between 2.33 and 3.08 m depth and in PBV2 (see red dashed frame in Figure 4.32) but it did not reach the surface. The presence of clay rip-up clasts in the ancillary hand-dug soil pits confirms also that liquefaction occurred at depth but did not come to the surface, as most of the soil pits were dug in areas not affected by sand blows (see the soil pits profile in the Soil Pits Appendix, A8).

4.4.5 Example of subsurface architecture of the costal environment of Christchurch

Information from trenches and cores at Wainoni and QEII Parks brought to light that coastal sediment occurs to at least 4 m depth and that alluvial sediment is found below the coastal sediment at varying depths.

At Featherston Avenue Reserve it was possible to investigate the subsurface architecture by interpreting the stratigraphy along two orthogonal transects. The sediment from the surface (~1.2-1.5 m a.s.l.) to 3 m depth (-1.5 a.s.l., Figure 4.32) is of aeolian origin with a well sorted, unimodal grain size distribution Gradistat grain size analysis. The sedimentary architecture at this site also shows interactions of coastal and alluvial processes as for the coastal study sites of the Christchurch Formation (Brown and Weeber, 1992). The location of the study site is likely to correspond with the location of an old Waimakariri River channel that may have become a lagoon, and finally the channel of the tidal Kairaki Creek. Once the channel was abandoned, it became filled with clay deposits (clay plug or unit C in Figure 4.32). Old river channels near the coast can turn into swamps or lagoons (Ricci-Lucchi, 1980) and can have their beds located below the modern sea level, at a time of marine regression. Due to the proximity to the coast, the old Waimakariri channel would have been separated by a spit from the sea with a dune complex on it (unit D in Figure 4.32). As a consequence, the presence of dune sediment below sea level may be explained with the migration of the dune set into the channel (Shulmeister pers. comm). Such a scenario is consistent with the alternating clay- sandy clay and sandy clay loam textures of unit T. However this hypothesis warrants further investigation to better define the dynamics of the dune migration and to constrain the age of their migration.

4.4.6 Dune ages and paleoliquefaction features in the coastal setting

The dunes ages in Christchurch's coastal fringe can be better constrained as an outcome of the radiocarbon assays performed in this study. At Wainoni Park, a potential minimum dunes age is afforded by sample W3ERC2 (Trench WAI 3) embedded in the b2Ah horizon at ~1.5 m depth of AD 988-1027. In a complementary manner, at QEII Park a maximum dune age is established by samples RAD 1 and RAD 2 (from the disrupted "mud lamina" layer of QEII Trench 1, at ~ 1.20 m depth) of

AD 1422-1454 and AD 1411-1447, respectively. Another dune age was provided from a charcoal in the retrieved core sediment at QEII Park at ~ 3.5 m depth (Figure 4.20) of AD 887-979. The latter age is consistent with the dune's age retrieved at Wainoni Park.

The age from the core at QEII Park revealed that the 'mud lamina layer' containing the two charcoal samples dated (AD 1422-1454 and AD 1411-1447) is an in situ layer, disrupted by the liquefaction of the Bw horizon. The age of the two samples dated within the mud lamina layer are ~ 600 years younger the charcoal embedded in the core sediment at ~ 3.5 m depth. Therefore the mud lamina layer and the sandy sheets including it must be younger than the sediment retrieved in the core. In conclusion at QEII Park the sand dunes started to form at least 1000 years ago and were still forming ~ 600 years ago in their upper part.

Considering that QEII Park is higher in elevation (~7 m a.s.l.) but closer to the coastline, whereas Wainoni Park is located at ~4 m a.s.l. and more inland, it is possible to consider the ages retrieved at QEII Park as being closer to the minimum (latest) age of the Christchurch Formation dunes. This means that the dune field of the Christchurch Formation investigated at Wainoni and QEII Parks were deposited between 1000 (AD 988-1027 and AD 887-979) and sometime after 500 years ago (AD 1422-1454 and AD 1411-1447) with deposition likely ceasing earlier at Wainoni Park.

The only satisfactory dating of the sand sheets at Featherston Avenue Reserve yielded an age of AD 1697-1950 (from sample PBV2_84 sample located at 1.70 m depth from the ground level, ~0.8 m a.s.l., Figure 5.32), and an age of AD 1637-1797 (from PBV2_124 sample located at ~1.90 m depth from the ground level, ~0.5 m a.s.l.). The dune fields at Featherston Avenue Reserve are lower in elevation (~2 m a.s.l.) and very close to the coastline and it is expected they are younger than the dunes at Wainoni and QEII Parks.

According to the most recent chronology work on dune sediment of the north Canterbury Plains (Shulmeister and Kirk, 1996), the ages of the dune system dated in this chapter have a reasonable

correspondence to the Ashworths Beach Dune Ridge (1.0 ± 0.6 ka) and to the coastal Dune ridge (0.5±0.0 ka, from (Shulmeister and Kirk, 1996).

4.4.7 Paleoliquefaction features at Wainoni Park

In Trench WAI 1 the sandy unit within the buried A horizon (unit L2S) was interpreted as a paleo liquefaction sill (between 0.5 and 4 m on the north east wall; Figure 4.15). The stratigraphic position of unit L2S (splitting the A horizon, b2Ah unit), and its obvious weathering were the main reasons for recognizing this unit as a paleoliquefaction feature (Figure 4.15).

There were no samples to date the sediment above and/or below the paleoliquefaction feature and thus only a maximum age can be estimated based on two pieces of charcoal carried within the liquefaction material. Samples W1RAD1 and W1RAD3 yielded ages of AD 1657-1803 and 1663-1950, respectively. Combining these two samples' calibrated age probability density functions in Oxcal (Ramsey, 2008, 2009), the 95% confidence interval limits the maximum age to AD 1666-1803. These dates are close to other paleoliquefaction investigations reported by Bastin (2015; 2016) which documented paleoliquefaction ages between 1321 and 1960 in a site along the Avon River in Christchurch. The potential paleoearthquake source of the paleoliquefaction features observed at Wainoni study site is not investigated in this dissertation.

At Trench WAI 3 a wedge-like sandy unit (Unit L2S Figures 4.17 and 4.18) was interpreted as a possible paleoliquefaction sand blow. This unit has a stratigraphic position on top of a buried A horizon and below an anthropogenic fill. Unit L2S was characterized by sandier texture in comparison to the thick buried organic topsoil below it, and its texture was very different to the anthropogenic fill. The trench did not expose a feeder dike for this unit and thus the interpretation is only tentative. The two radiocarbon samples collected from the east wall at WAI 3 yielded ages of AD 1640-1797 from unit L2S and of AD 988-1027 from the b2Ah horizon, both establishing maximum ages for the putative sand blow. The minimum maximum age is consistent with the age of the paleoliquefaction features dated at Trench WAI 1, suggesting that this layer could have been part of the same paleoliquefaction event.

4.4.8 Paleoliquefaction features at QEII Park

The weathered dike and the corresponding sill on the north wall of QEII Trench 2 was the only occurrence of a paleoliquefaction feature at QEII Park. The micromorphological analysis (Chapter 6 of this dissertation) was able to ascertain that this layer was a paleoliquefaction unit, by investigating the degree of weathering and other features of the soil fabric (Sample 716 of Chapter 6). A modern liquefaction fabric is loose and single grain with none or very few pedofeatures (silt and clay coating, organic fragments, excrements). The dike on the north wall of QEII Trench 2 was characterized by high abundance of soil pedofeatures and bridged fabric yet featured grain fabrics consistent with emplacement by liquefaction processes. For details on the micromorphology technique and on QEII Trench 2 liquefaction features fabric the reader is referred to Chapter 6. Unfortunately, it was not possible to date this paleodike as no datable material was found to constrain its age.

No paleoliquefaction features were exposed at Featherston Avenue Reserve,despite the site having conditions highly susceptible to liquefy during even relatively low intensity shaking. The near surface liquefaction and the extreme disturbance of the soil profile that results from each liquefaction event conspire against preservation of a history of past events (Chapter 5)

4.5 CONCLUSION

Liquefaction features at three sites of the coastal setting of Christchurch have been documented: Wainoni and QEII Parks in the urban area of Christchurch and Featherston Avenue Reserve in the north Canterbury region. In the coastal dune setting, liquefaction features are more associated with interdune deposits, which may be underlain by alluvial sediment (as shown by the Transect 1 and 2 at Featherston Avenue Reserve site). Sand blows are large and occur in isolation, in contrast to the linear trends of sand blows in alluvial environments. The liquefaction source layer is the dune sediment itself, supplemented by minor alluvial sediment sourced from depth. Liquefaction subsurface features observed in the coastal setting are mainly a consequence of near surface liquefaction, and they are: A horizon splitting, collapse features, and pillow-like structures. Other features observed are also common to the alluvial setting such as sand blows and sub-vertical dikes. Surface liquefaction features observed in the coastal setting are characterized by a rounded or subrounded shape and are larger than those observed in the alluvial sites (Chapter 3 of this thesis) with dikes up to 1.0 m, and sand blows greater than 1 m diameter, except for alluvial sites with liquefaction in association with lateral spreading. Near surface liquefaction can strongly disrupt the original stratigraphy making the sedimentary and liquefaction history interpretation difficult.

A maximum age for paleoliquefaction features is only inferred at Wainoni Park (AD 1666-1803). In contrast, the micromorphology analysis ascertained the presence of paleoliquefaction features also at QEII Park, but no age constraints were found satisfactory at this site. At Featherston Avenue Reserve the overprinting of multiple liquefaction generations, due to the high liquefaction susceptibility at this site resulted in particularly challenging identification of past liquefaction events. This is common problem in areas were the liquefaction source is immediately below the ground surface.

Regarding pros and cons of each technique tested during the liquefaction investigation in the coastal setting, it is possible to conclude that:

- After six years from the major earthquakes causing liquefactions, CES-related liquefaction ejecta was not well preserved. Thus the 3D GPR enhanced the effectiveness of our trenching campaign, since it accurately localized the liquefaction features at depth by the subsurface anomalies they created. The 2D GPR survey results were not always effective as they did not clearly reflect the stratigraphy exposed in the trenches on occasions.

- In the coastal dune setting the paleoseismic trenches had to be very shallow because of the shallow water table. They were more susceptible to collapse because of the lack of cohesive material and shallow water table. However, very relevant information was extracted from them. In addition, analysis of hand-dug pits in proximity of the trenches was a useful exercise to understand the stratigraphic variations that were not exposed in the trenches.

- The high susceptibility to liquefaction that characterizes the coastal setting prevents this setting from recording evidence of paleoliquefaction in its stratigraphy. Therefore, in contrast to the alluvial setting, the coastal setting is not the best depositional setting to look for paleoliquefaction features.

The compounded methodology for investigating liquefaction and paleoliquefaction identified by Villamor (2014, 2016) is here applied to the coastal setting with satisfactory results. The liquefaction investigation in the coastal setting of Christchurch here presented can be considered as a pioneering but still reconnaissance study. More studies are needed to corroborate the liquefaction susceptibility of the dune fields in the Canterbury Plains and elsewhere and, as a consequence of this, the variability of some specific coastal liquefaction features (e.g. A horizon splitting, collapses and pillow-like structures) in relation to dune age and degree of weathering.

Chapter 5
WHEN THE EARTH BLISTERS: EXPLORING RECURRENT LIQUEFACTION FEATURES IN THE COASTAL SYSTEM OF CHRISTCHURCH, NEW ZEALAND

Giona Bucci, M.; Almond, P.; Villamor, P.; Ries, W.; Smith, C.; Tuttle, M;

Paper accepted for publication in the Terra Nova Journal 2017 on 14th March 2017

ABSTRACT

The 14th February, or Valentine's Day, 2016 earthquake located offshore of Christchurch produced a new generation of liquefaction in the coastal environment of Christchurch, an environment of recurrent liquefaction during the 2010-2011 Canterbury Earthquake Sequence. The Valentine's Day earthquake occurred while trenches were open at a site in the coastal environment for studying the 2010-2011 liquefaction features. Observations in the 2016 trenches provided insights into the formation of a suite of surface and subsurface liquefaction characteristic of the dune deposits related to the persistent shallow water table, well sorted sand within the liquefiable layer and the soil above. Given these conducive conditions, there is a high potential that all earthquakes capable of inducing liquefaction may have been recorded during the dune formation of Christchurch. However, overprinting of subsequent generations of liquefaction features may be common and present challenges in unravelling the event history.

5.1 Introduction and geological context

The Mw 5.7, 14th February 2016 (Valentine's Day) earthquake, centred ~15 km offshore of Christchurch city (Figure 5.1), occurred during a field campaign aimed at studying liquefaction features in the coastal dune environment resulting from the 2010-2011 Canterbury earthquake sequence (CES) (Figures 5.1 and 5.2) (Bannister and Gledhill, 2012). Our study site at Featherston Avenue Reserve, near Kaiapoi (Figure 1), suffered liquefaction during each of the larger earthquakes of the CES (September 2010, February 2011, June and December 2011 quakes) (Bannister and Gledhill, 2012; Brackley et al., 2012; Townsend et al., 2016), and reports from local residents) and again during the Valentine's Day Earthquake (Kaiser et al., 2016) (Figure 5.3). Featherston Avenue Reserve is located

on the landward margin of the coastal dune field near Kaiapoi and adjacent to Kairaki creek (Figures 5.1, 5.2 and 5.3). At this site, the water table is very shallow (0.6-0.7 m depth from the surface) and during wet winters the sediment and soil are fully saturated.

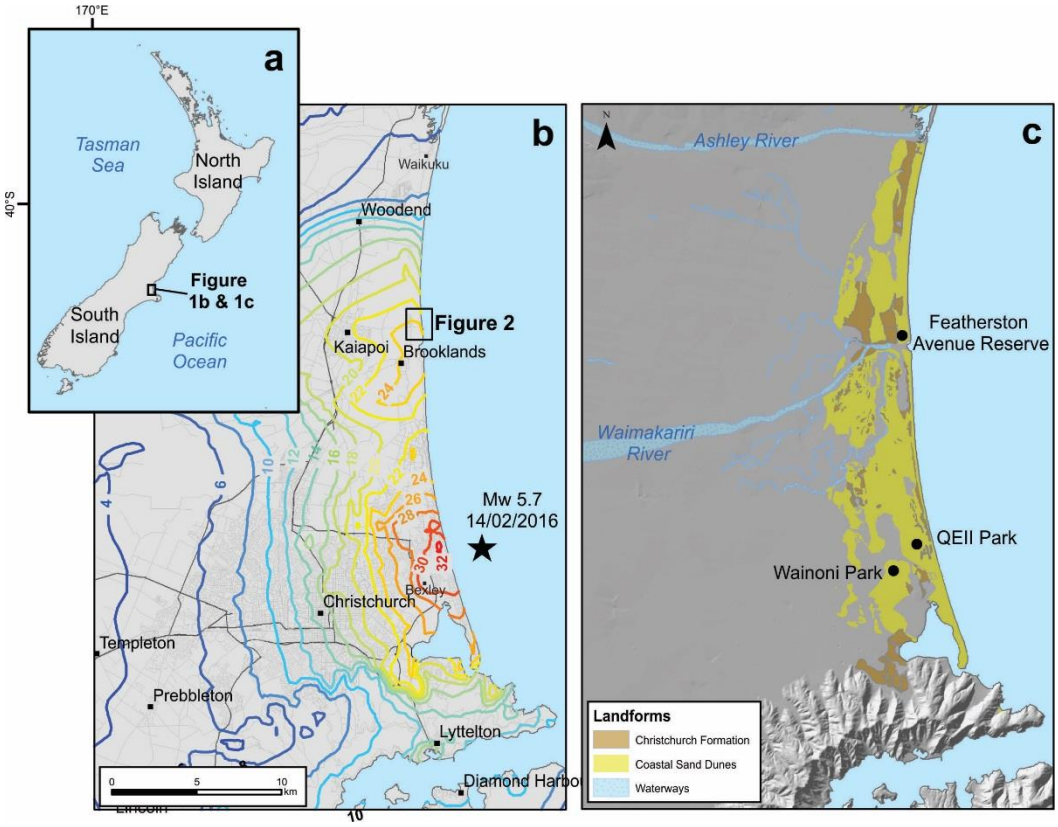

Figure 5. 1 a) General location of study sites; b) Location of Valentine's Day Earthquake (2016) main shock and recorded PGA levels across the Canterbury Plains. Location of main townships; c) Geomorphology of the coastal fringe of the Canterbury Plains. Location of the coastal study sites investigated during liquefaction field campaigns between January 2015 and February 2016.

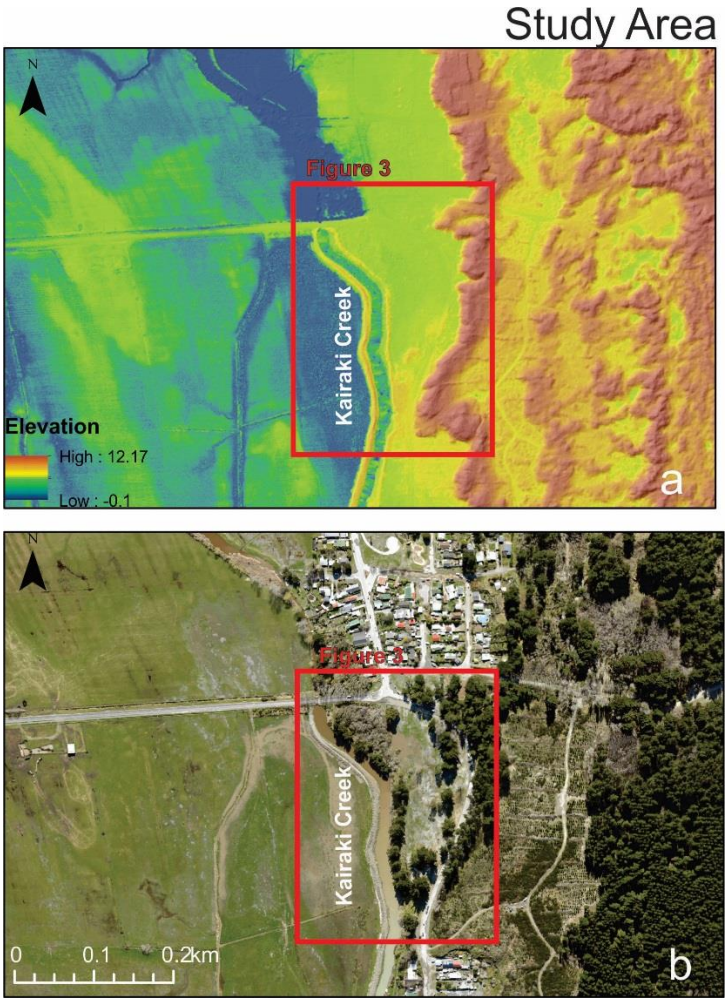

Figure 5. 2 a) DEM of the Coastal site at Featherston Avenue. Featherston Avenue Reserve study area is highlighted by the red frame; b) Aerial imagery of Featherston Avenue Reserve study area after the September 2010 Earthquake showing liquefaction features in the study area and in the adjacent low laying area close to the Kairaki Creek.

For several decades, alluvial, deltaic and coastal dune systems have been recognized worldwide as liquefaction prone settings (Alfaro et al., 1999; Amick et al., 1990; Holzer et al., 2010; Moretti, 2000; 2002; Tinsley et al., 1998; Tuttle, 1999; Youd and Hoose, 1977; Youd and Perkins, 1978) . The CES studies (Almond et al., 2012; Bastin et al., 2015; Quigley et al., 2013; Tuttle et al., 2017 ; Villamor et al., 2016; 2014), together with studies from other recent liquefaction events (Alessio et al., 2013; Civico et al., 2015; De Martini et al., 2015; Fontana et al., 2015), have focussed on the alluvial setting. However, liquefaction features in the coastal setting of the Canterbury Plains have not been the subject of detailed study.

A post-earthquake survey following the Valentine's Day Earthquake documented liquefaction along the coastal fringe of Christchurch, Figure 5.1 b, (Kaiser, et al 2016). Investigation of the pristine features of the 14th February 2016 event provided us with insights into the morphology, stratigraphy and genesis of surface and subsurface liquefaction features in the coastal environment.

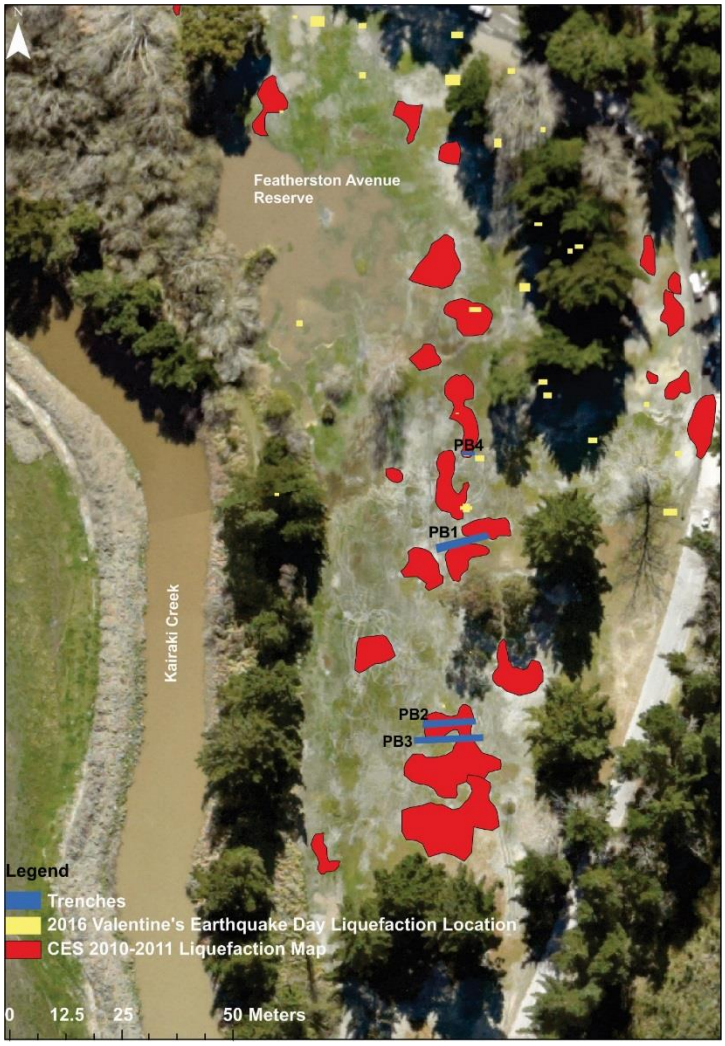

Figure 4. 3 Map of the liquefaction surface manifestation at Featherston Avenue Reserve caused by the 2010-2011 Earthquake sequence and by the 2016 February event. Location of paleoseismic trenches excavated before (PB1, PB2 and PB3 trenches) and after (PB4 trench) the Valentine's Day Earthquake.

In this study, we describe liquefaction effects in the coastal dune setting at Featherston Avenue Reserve (Figures 5.2 and 5.3). This serendipitous event enabled us to: 1) better understand the 2010-2011 liquefaction features observed during previous field campaigns in coastal suburbs of Christchurch city (Wainoni and QEII Parks, Christchurch City- Figure 5. 1c; trenching study undertaken

in January 2015, not reported here) and at Featherston Avenue Reserve site (trenching study undertaken between 1st and 12th February 2016, prior to the Valentine's Day Earthquake); 2) document the different types of surface manifestation of liquefaction in the coastal setting; 3) analyse the complexity of a dune soil profile affected by liquefaction soon after the event and several years later; and 4) confirm that coastal dune deposits are highly susceptible to liquefaction.

5.2 Methods

We documented liquefaction surface manifestation three hours after the Valentine's Day Earthquake event. This involved photographing, locating (hand-held GPS), and characterising (length, width, thickness, colour and texture) each feature. Data were then compiled into a geospatial database.

After the Valentine's Day earthquake, we excavated an exploratory trench (PB4 trench; Figures 5.3 and 5.5) at Featherston Avenue Reserve, across a compound liquefaction feature that contained a blister -similar to those documented by Villamor et al., (2016; 2014)-, a fissure (3.5 m length), a collapse structure, and sand blows (Figure 5.4). The presence of a shallow water table did not allow us to dig below 0.25-0.30 m depth. This trench added to the three previous trenches (PB1, PB2 and PB3, Figure 5.3) we had excavated between 1 and 12th February to study CES-related liquefaction features.

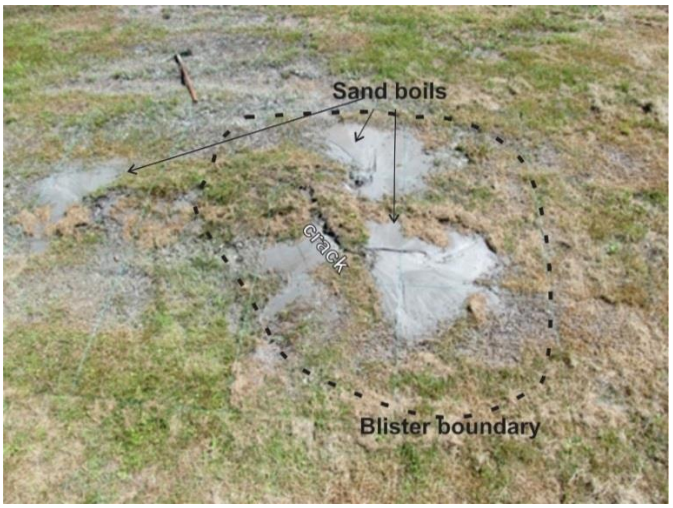

Figure 5. 4 Blister and related sand blows caused by the Valentine's Day Earthquake at Featherston Avenue Reserve site, (photo taken on 15th February 2016).

In all trenches, we mapped the strata and liquefaction features using grids of about 0.25 m^2 or less both on the floor and on the walls. For sedimentary and soil units descriptions, we used standard methods (Clayden and Hewitt, 1994; Schoeneberger et al., 2012) .

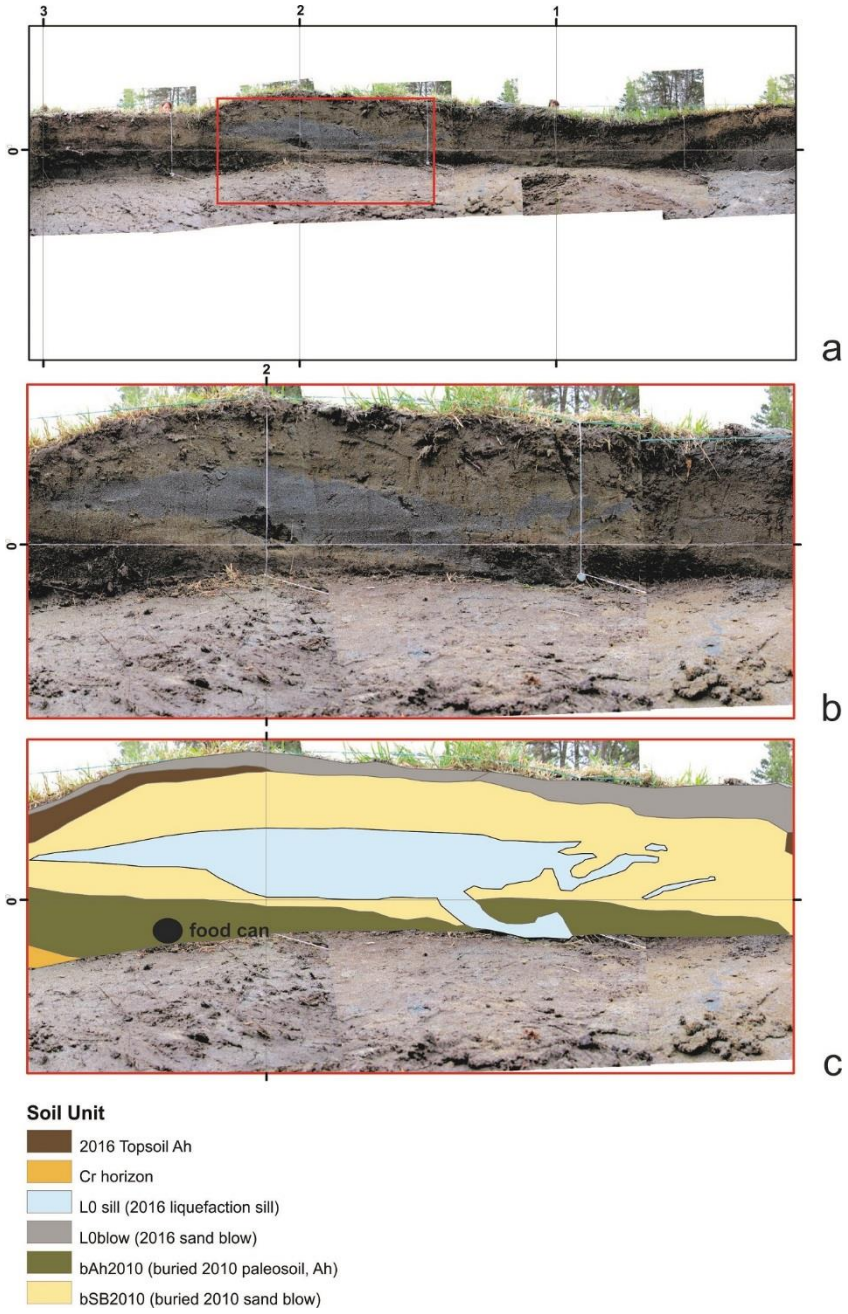

Figure 5. 5 Trench PB4, north wall (liquefaction during Valentine's Day Earthquake). A blister formed as a sill was injected into a CES sand blow. The CES sand blow was dated based on the location of a food can with a 2010 expiry date found in the buried 2010-2011 A horizon (unit bAh2010), for more details see Appendix A3 Figure1. Location of the food can projected on trench wall. The trench was only ~25 cm deep because the water table was very shallow soon after the earthquake. The spacing of the grid lines is 0.5m as showed in Figure 4.

5.2.1 Valentine' s Day liquefaction features at Featherston Avenue Reserve site

The top layer in the PB4 trench walls was the 14th February sand blow (unit L0blow in Fig. 5.5). Below unit L0blow, a thin topsoil (labelled as unit 2016 Topsoil Ah in Fig. 5.5) had developed above olive-brown sand (unit bSB2010) that buried a paleo-topsoil (unit bAh2010) in which we found a food can *in situ* with a 2010 expiry date (Data Supplement Figure 5.1). The food can confirmed the interpretation of units bSB2010 and bAh2010 as post-CES. The Valentine's Day earthquake liquefaction formed grey, sandy dikes and sills (unit L0 sill) that partially intruded the CES sand blow (unit bSB2010).

The features exposed in the trench and at the ground surface are exemplars of three phenomena that appear to be common in the surface manifestation of liquefaction in a coastal setting: Blister-collapse systems, A-horizon splitting, and rapid chemical weathering.

5.3.1.1 Blister-collapse system

We described the Blister-collapse system (Figure 5.6) as a compound feature characterized by a surface protrusion (blister, see convex shape of the ground surface above unit L0 sill in Trench PB4; Figure 5.5b and c; Figure 5.6) and an adjacent collapse feature (see the surface concavity to the right of vertical grid 1 m on Figure 5.5a, and Figure 5.6). Blisters were often associated with collapse features, thus we name them here blister-collapse features (Figure 5.6).

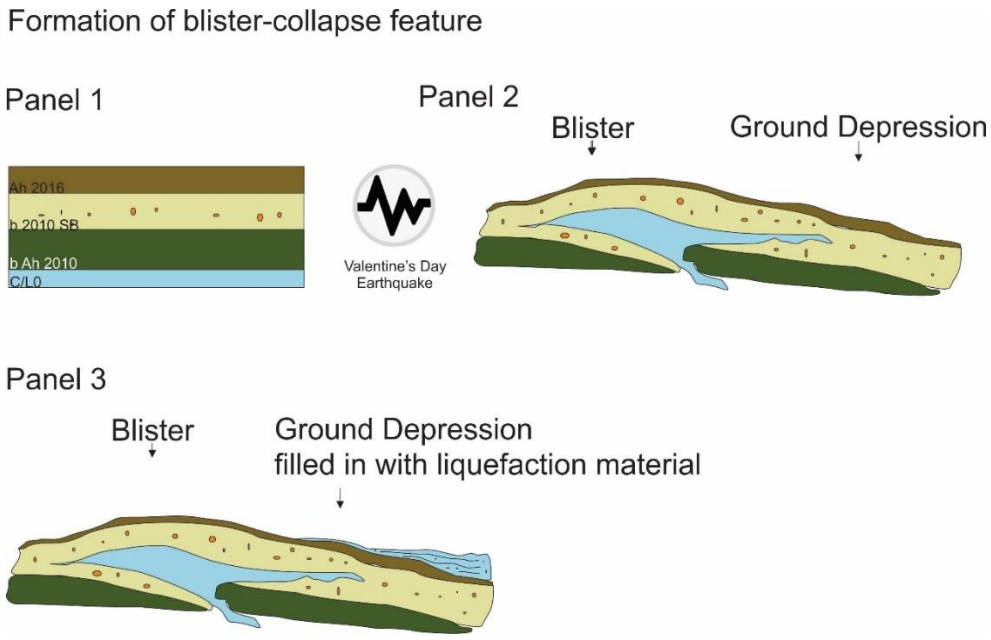

Figure 4. 6 Formation of the blister-collapse system in PB4 a) Soil profile of the coastal sand dune at Trench PB4. Note that the sandy layer b2010SB is a 2010 Sand blow covered by 2016 A horizon (Ah 2016 unit), and on top of a buried 2010 A horizon (bAh2010); b) As a consequence of the Valentine's Day Earthquake: the C horizon liquefies and injects a sill into the 2010 sand blow (unit b2010SB). The new injection inflates the subsurface producing a blister. Next to the blister, ground subsidence occurs due to the evacuation of water and sandy sediment during the liquefaction process; c) The liquefied sediment extrudes at the surface (ejected through dikes not visible in this figure) and flows into the ground depression.

Blisters were described for the first time in an alluvial setting by Villamor et al., (2016; 2014), where they were not as common as what was observed in the coastal setting. For example, in Featherston Avenue Reserve and in the wider Christchurch coastal fringe numerous blisters appear as a consequence of the the Valentine's Day Earthquake.

We hypothesized that the collapse feature adjacent to the blister formed as result of the evacuation of fluidised subsurface sediment to the ground surface and the formation of a void into which the

overlying material collapsed. We probed beneath the water table and confirmed the existence of a void. The PB4 trench floor intersected the base of the collapse, revealing a semirounded structure of the near-surface A/C horizon (Fig. 5.7). The semirounded shape was delineated by silt lenses and by the weathered olive yellow sand of the CES sand blow (unit bSB2010, Data Supplement Figure 5.2).

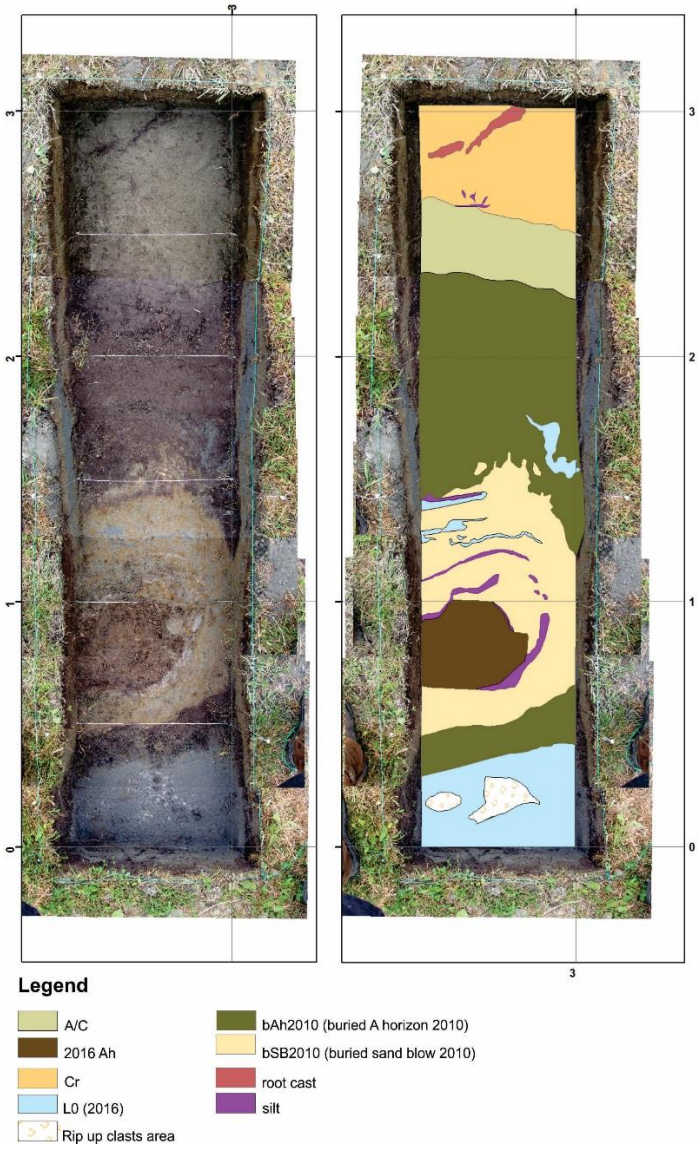

Figure 4. 7 Collapse feature as exposed on the floor of Trench PB4. Note the 2016 A horizon (2016 Ah unit) showing a rounded shape and surrounded by a silt layer (in purple colour). The silt layer is a typical feature of the post liquefaction process during which fine sediment settles out, as a consequence of the decrease in pore water pressure. The circular A horizon (2016 Ah unit) was surrounded by another circular exposure of yellow weathered sand representing the collapsed 2010-2011 sand blow (bSB2010 unit). Within the yellow weathered sand blow there is again evidence of the new Valentine's Day liquefaction injections appearing as gray fine sand (L0). In this case, the colour pattern was very important to help distinguishing the new event (non- weathered and blueish colour) from the old one (yellow and weathered). Unit bAh 2010 represents the buried 2010 topsoil; unit Cr is the sandy parent material of the coastal dune soils, and the A/C soil layer represents transitional horizon between the bAh2010 and the Cr horizon.

5.3.1.2 A-horizon disruption

In the trenches, we observed disturbance of the original organic-rich surface (A) horizons of the sandy soils of the coastal area (e.g. bAh2010). The A horizons displayed many discrete organic-rich lenses, and appeared disintegrated horizontally and sometimes vertically (Figure 5.8).

We hypothesized that deformation of the A horizon was a multi-step process as follows:

(1) injection of low angle dikes and sills into the A horizon, which dislocates or "delaminates" that horizon (Figure 5.8, b);

(2) further intrusion or injection of fluidised sand (sand dikes and sills) into the soil produces inflation, fragmentation and disintegration of the A horizon (Figure 5.8, c);

(3) fluidised sand (sand dikes) breaks through the entire thickness of the A horizon to form many closely spaced vents at the ground surface, carrying A horizon rip-up clasts into the matrix of the sand blow (Figure 5.9).

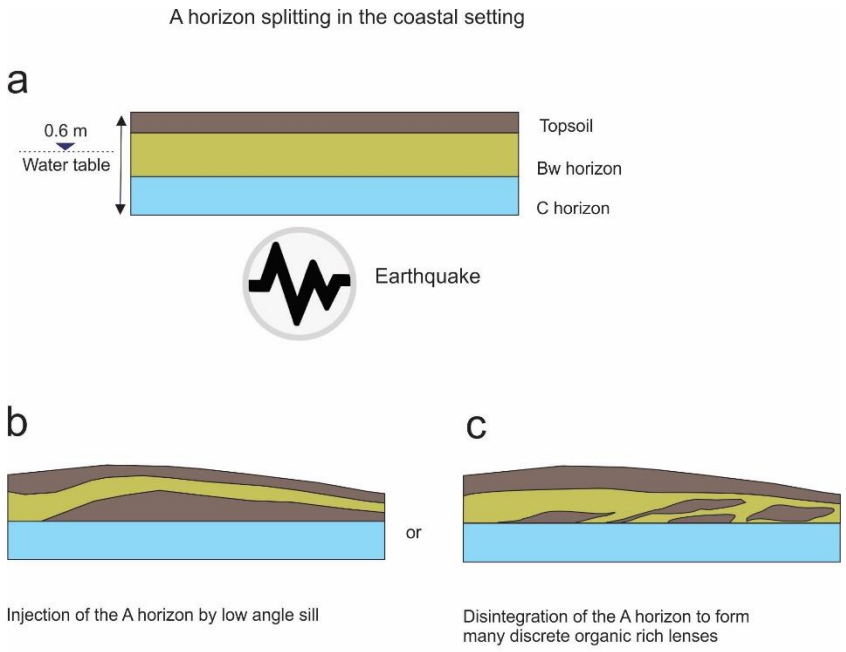

Figure 4. 8 A horizon disruption; a) soil profile before the earthquake; b) the liquefaction splits apart the A horizon; c) the liquefaction injection splits apart and further delaminates the A horizon forming disconnected lenses of A horizon material. The black arrow indicates the flow direction of the liquefaction material.

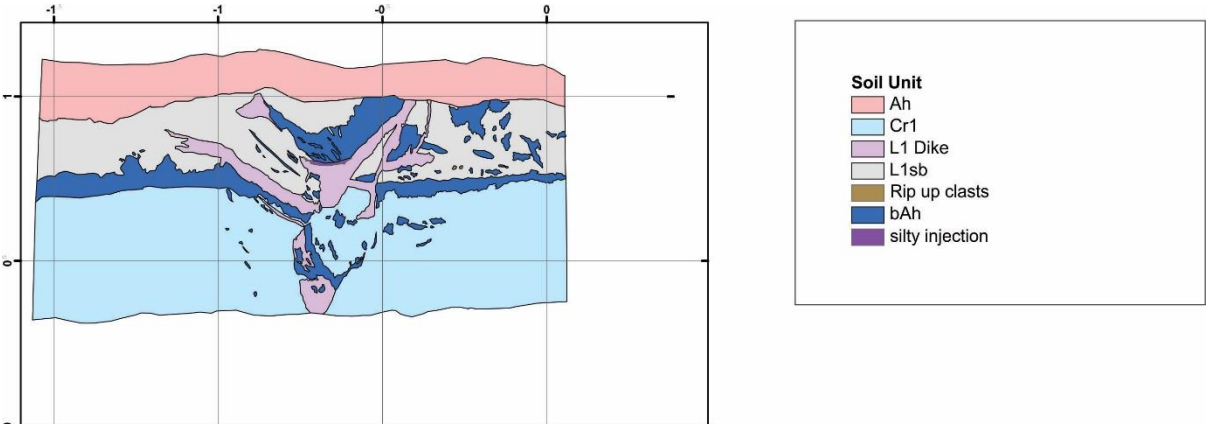

Figure 5. 9 9Example of A horizon splitting producing numerous rip-up clasts from the buried A horizon (bAh; dark blue colour) within a 2010 sand blow (unit L1sb; gray colour) in Trench PB2 (north wall).

5.3.1.3 Rapid weathering

We observed that at Featherston Avenue Reserve six years after the 2010-2011 liquefaction events, the sand comprising the sand blow, sills and dikes have weathered to a pale yellow (5Y 5/2) with or without ferruginous redox mottles. The vented sand appears to be particularly prone to chemical "ripening", which occurs when it is brought from the anoxic zone beneath the water table to the aerated zone above the water table (Lafrenz et al., 2013; Pons and Zonneveld, 1965; Vermeulen et al., 2003).

We interpret that the chemical "ripening" process was accentuated at our site by the very shallow water table and its seasonal fluctuation. In contrast, liquefaction features related to the CES studied in a fluvial setting (inspected between 2012-2013), remained grey in colour (Villamor et al. 2016). The rapid oxidation of the sediment caused us to initially misinterpret the CES-related liquefaction sediment as much older.

5.3.2 2010-2011 liquefaction at Featheston Avenue Reserve site

The three pre-Valentine's Day Earthquake (1st to 12th February 2016), paleoseismic trenches (Fig 5.3) were located where sand blows formed during the 2010-2011 earthquakes. Before seeing the effects of the Valentine's Day earthquake, the structures exposed in the trenches were difficult to interpret. For instance prior to 14th February, we interpreted a circular feature in the floor of Trench PB1 as a

large (c. ~ 0.5 m) conduit through which liquefied sand vented during a paleoliquefaction event (Figure 5.10). Based on lessons learned from the Valentine ’s Day liquefaction features (Figures 5.5, 5.6), we now consider this to be a cross-section of a collapse feature. We interpret the central sandy core as sand blow material that flowed into a subsided topsoil (see Appendix 3 Figure 5.3). The olive green ring (unit bAh 2010) surrounding the central sandy core represents the subsided 2010 A soil horizon. Outside the brown ring, a blue thinner grey ring of sand is probably a later dike of the CES exploiting the weakness at the boundary between the distorted A and BC horizons.

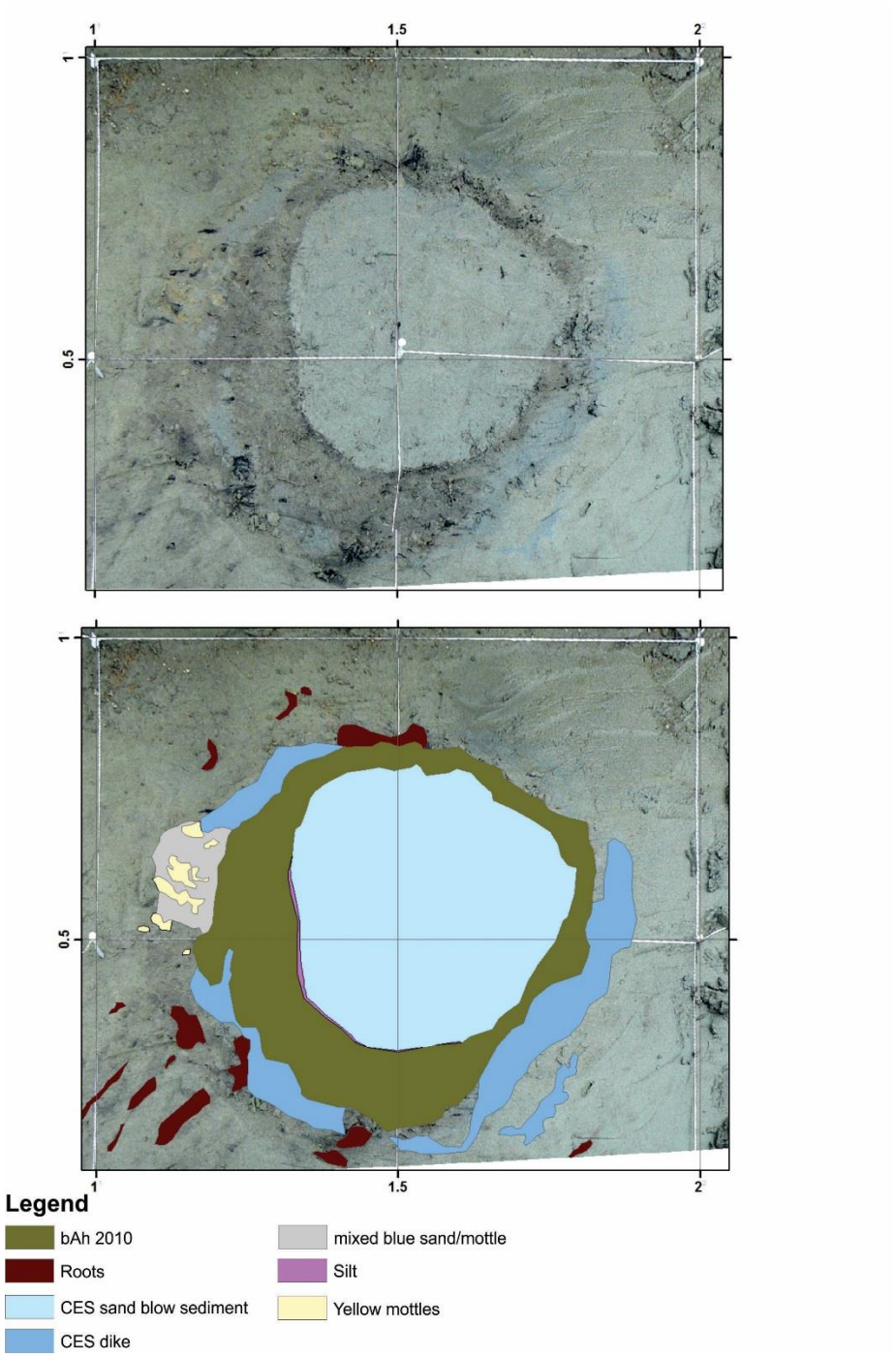

Figure 4. 10 Collapse Feature at PB1. The sandy core (unit CES sand blow, light blue colour in trench log) represents the sand blow material that flowed into a convex cavity in the ground. The dark olive green ring is the pre- CES topsoil (unit bAh 2010). The dark blue-grey sandy feature outside the pre-CES topsoil is a later CES dike of the CES that exploited weakness planes around the collapse feature.

Before the Valentine's earthquake, the complex stratigraphy and the strong weathering led us to infer multiple liquefaction events including effects of the CES and prior events. However, our re-evaluation of the rate of weathering (faster than we initially expected) suggests that the features exposed prior

to the 14th February formed as recently as the 2010-2011 CES events (with no need to infer a greater antiquity). Furthermore, the presence of multiple A horizon remnants does not necessarily suggest multiple liquefaction events (although we don't rule it out) because the process of A horizon splitting can produce a complex geometry during just one liquefaction event.

The buried A horizon remnants formed concave-upwards crescentic forms, delineated by weathered sand (Fig. 5.11), that we will call "pillow-like" features. Physically, they resembled pillow structures, i.e., soft sediment deformation (SSD) features characteristic of lacustrine sediment (sensu Anketell et al., 1970; Seilacher, 1969). In lacustrine environments, the pillow structures are triggered by an inverse density gradient (Alfaro et al., 1999; Alfaro et al., 2001 ; Alfaro et al., 2010; Moretti, 2000; Moretti et al., 2002; Moretti and Sabato, 2007) not observed at our study site. Therefore, our interpretation of their formation for the coastal setting is different from the above literature and is described as follows: 1) liquefaction of soil layers close to the surface such as B or C horizons injects and splits the former topsoil forming two (or more) A horizon layers, or produces several lenses of A horizons separated by liquefied sand (Figure 5.12.b); 2) evacuation of sediment from the shallow subsoil causes subsidence and surface depressions (Fig 5.12.b); 3) subvertical water-escape features (Figure 5.12.c) form to carry the sediment upward and allow the high porewater pressure to be vented (Figure 5.12.c); 4) sand blow material and surface organics/debris flow into surface depressions, increasing stratigraphic complexity (Figure 5.12.d). In this scenario, the concave-up crescentic forms are result of the subsurface collapse shown in Figure 5.12.

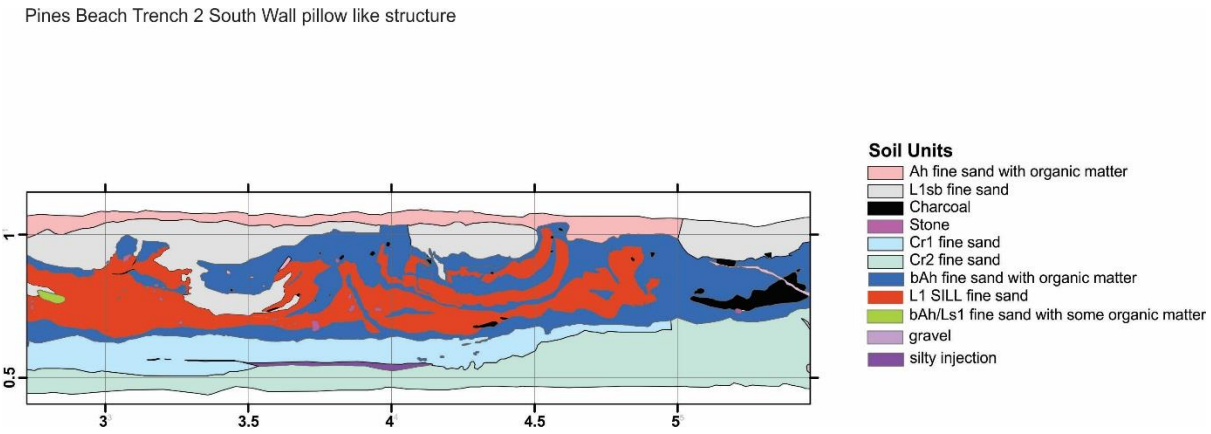

Figure 5. 11 Pillow-like features observed at Trench PB2. These features are caused by the low cohesion of the coastal sandy dune soils together with a shallow water table (close to the surface), which allow multiple, closely spaced vents acting as conduits for shallow liquefied sediment. Ejection of this sediment result in closely spaced depressions sited above subsurface collapses. Surface ejecta produce broad composite sand blows without significant sediment thickness. Splitting of the topsoil below the sand blows during liquefaction produces layering that also delineates depressions, adding to the complexity of the liquefaction induced sediment deformation (See Diagram in Figure 13 for detailed explanation). Sand blows are only thick where ejecta flow into the surface depressions. Because these peculiar pillow-like features are likely to be formed when the water table is at the surface, we interpret that they formed during the early spring September 2010 earthquake (higher water table).

Collapse features observed in the coastal setting of Christchurch also resembled in plan view, a sand blow discovered by Amick et al. (1990) in the coastal setting of the East of United States. The latter features were named craters and resulted from an explosive ejection of sediment resulting from liquefaction. However, our experience during the Valentine's Day Earthquake showed that the sand blows were not induced by an explosive event.

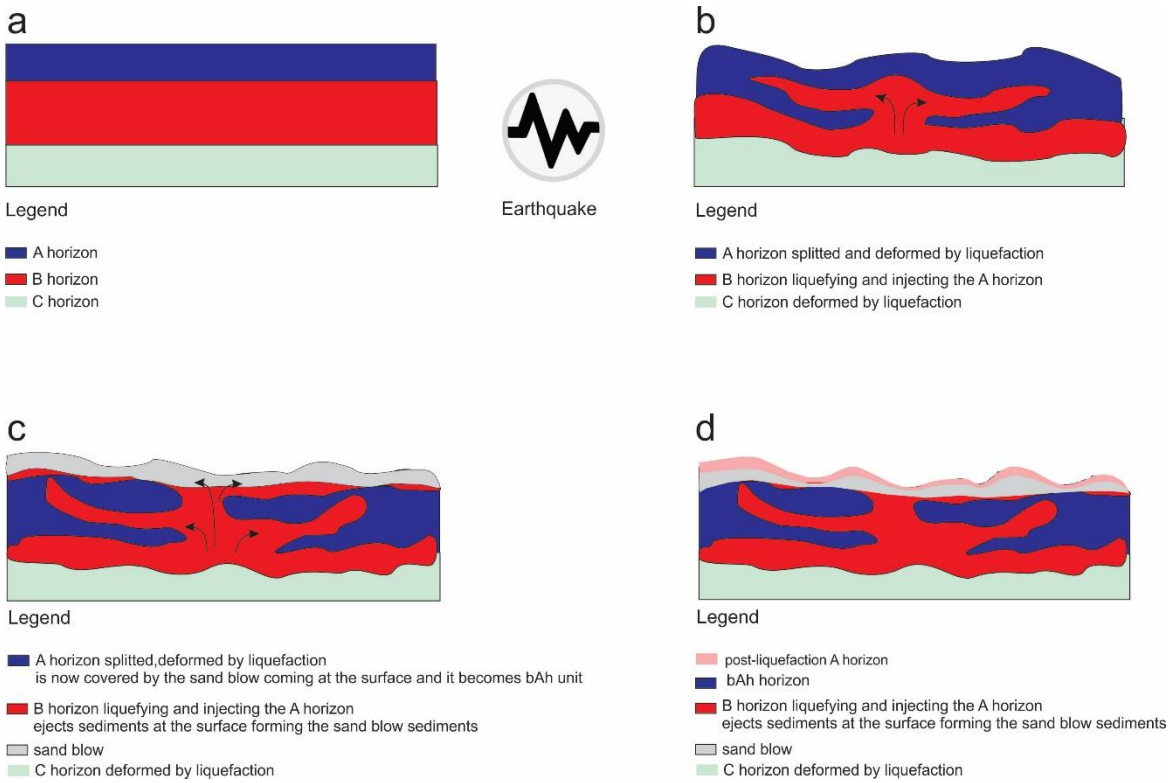

Figure 5. 12 Simplified diagram of pillow-like structures occurred at Trench PB 2; a) Soil profile of coastal sand dune before the earthquake; b) The B horizon liquefies and water and sediment travel upwards disrupting the overlying stratigraphy (Ah) through dikes and soil splitting. Also the mobilization of water and sediment induces subsidence of the ground surface; c) the liquefied material is vented at the surface and it starts to flow into the subsided areas, covering the topsoil. The original topsoil becomes a buried topsoil (bAh); d) Several months after the liquefaction new topsoil starts to form, which can modify the stratigraphy and features of the most recent sand blows.

5.3.3 Characteristics of the costal dune setting implicit in the style of liquefaction features

The nature of the sandy surface soil horizons and the shallow groundwater table (fluctuations from ground surface to less than 1 m deep) in the sand dune environment influence the response to liquefaction, as well as the high susceptibility to liquefaction in coastal settings. The coastal soils are weak (low cohesion) owing to the low clay and silt content and rarity of roots, which allows the soil to separate and fragment in ways not commonly seen in the finer textured and more cohesive soils of the alluvial environment. As a result, A horizon rip-ups are more abundant and A-horizon splitting more severe than in alluvial environment. Collapses develop where the low cohesion subsurface horizons drop or flow into an accommodation space formed by the evacuation of sediment.

In contrast to the dune setting, liquefaction in the alluvial environment produced mostly sand blows, dikes and sills in the finer and layered sediments (Bastin et al., (2015), Quigley et al.,(2013), Villamor et al., (2016; 2014)). Common to both settings, although apparently less abundant in the alluvial

environment (Villamor et al*.,* 2016, 2014), blisters form where a dense network of fine (grass) roots reinforce the surface soil (A) horizon.

While the coastal setting provides heightened opportunity for finding paleoliquefaction features, its susceptibility to liquefaction also means that the likelihood of overprinting by successive events is high. Therefore, sites should be sought where sand blows may be buried and preserved ideally forming an event stratigraphy. For example, the M 6.9 Cheviot earthquake of 1901 caused liquefaction in nearby Kaiapoi (~4.5 km west of Featherston Avenue Reserve) (Berrill et al., 1994; Wotherspoon et al., 2012) and almost certainly induced liquefaction at the Featherston Avenue Reserve, though did not necessarily at the same locations as our trenches. However, we could distinguish no unequivocal evidence of it amongst the complex stratigraphy. Furthermore, the rapid oxidation of sediments (confirmed in this study) limits our ability to discriminate on the basis of weathering characteristics.

5.4 CONCLUSIONS

Investigation of liquefaction features that formed during the 2016 Valentine's Day earthquake improved our understanding of complex liquefaction features that had formed during the 2010-2011 Canterbury earthquakes. The investigation was conducted at Featherston Avenue Reserve, Christchurch, in the interdune swales and low-lying fringe of the coastal sand dune belts. Features that formed during the Valentine's Day earthquake, include blisters, collapse structures, A horizon splitting, and rapid oxidation of vented sediment. These features are distinctive from those that form in the alluvial setting because of the lack of fines (silt and clay) in the dune sand and the persistent shallow water table. These characteristics make this type of coastal dune environment highly susceptible to liquefaction and thus a prime target for paleoliquefaction studies. However, the high susceptibility of the coastal sediment to liquefaction may lead to overprinting of liquefaction features by subsequent events. The latter effect will make discrimination between paleoliquefaction events especially challenging.

ACKNOWLEDGEMENTS

We thank Dan Cameron from the Waimakariri City Council for land access. This study is funded by the New Zealand Natural Hazards Research Platform and GNS Science Strategic Science Investment Funds.

Chapter 6
MICROMORPHOLOGICAL ANALYSIS OF LIQUEFACTION FEATURES IN ALLUVIAL AND COASTAL ENVIRONMENTS OF CHRISTCHURCH, NEW ZEALAND

6.1 Introduction

Liquefaction is one of the most important off-fault markers of the presence of past earthquakes in low lying areas where there are water saturated Holocene sediments. Liquefaction during the 2010-2011 Canterbury Earthquake Sequence (CES) provided new opportunities for studying this phenomenon. For example, a detailed study of the sedimentary architecture associated with surface ejecta was undertaken and presented in the first chapters of this thesis, in the alluvial and coastal settings, in order to better understand 1) the characteristics of the liquefaction hosting sediment, 2) the depositional setting of the liquefaction source layer and 3) the geomorphic correlation with the liquefaction surface manifestation (Chapters 3 and 5). One of the main results of this study is that liquefaction features are not always associated with a clear dike. For example, in the coastal setting and when the water table is close to the surface, processes such as A horizon splitting (Chapters 4 and 5) are caused by liquefaction but are not necessarily associated with presence of dikes, as known in the alluvial setting (Chapter 3). Therefore, new ways to identify the presence of paleoliquefaction are needed.

Paleoliquefaction studies are particularly important to assess the recurrence of strong ground shaking in areas where the faults are hidden and on-fault studies are not possible, such as New Madrid Seismic Zone (USA) (Csontos and Van Arsdale, 2008; Tuttle and Hartleb, 2012a). The identification of a sedimentary unit as representing a paleoliquefaction event in exploratory trenches or natural exposures is critical to assess the presence of past strong ground shaking.

Modern and paleoliquefaction features include sand blows, rip up clasts, dikes, and sills (see the Literature Review in Chapter 1 for a summary) but also blisters, A horizon splitting and soil deformations (see Chapters 3, 4 and 5 of this thesis). Commonly, identification of paleoliquefaction features relies heavily on the analysis of the geometric relationships, at outcrop scale, between natural

soil horizons or depositional layering (bedding/lamination) and the features produced by liquefaction. In particular, finding dikes connecting with units suspected of being sand blows or sills is traditionally considered a *sine qua non* requirement to confirm the presence of paleoliquefaction (Tuttle, 1999). Liquefaction features are either syn- or post- pedogenic phenomena depending on whether they are paleo or contemporary features, respectively, and hence their degree of weathering is often less than that of the hosting soil. Such weathering contrasts are corroborating evidence in support of stratigraphic inferences. Furthermore, weathering contrasts, including differences in oxidation, grain coating, and development of redoximorphic features, can be used to discriminate contemporary features from paleoliquefaction, or one generation of paleoliquefaction from another (Bastin et al., 2015; 2016; Tuttle et al., 2017 ; Villamor et al., 2016).

By chance, dikes feeding liquefaction features, sills or sand blows may not be intersected by the trenches, in which case confirmation of a liquefaction event remains equivocal. On the other hand, where multiple generations of paleoliquefaction features are evident, weathering contrasts at the outcrop scale may not have sufficient resolution to discriminate them temporally. It is common for weathering features to develop rapidly during the initial phase of pedogenesis and then to evolve at slower rates (Birkeland, 1999); hence, resolution of age differences declines with feature age such that unequivocal distinction between paleo-liquefaction features of different age may become problematic. For example, it is possible to easily identify the difference between a modern liquefaction of ~5 years and a paleoliquefaction of ~500 years old, but it becomes more difficult to properly identify the differences between a paleoliquefaction feature of 500 years and 800 years old.

This chapter explores the opportunity offered by micromorphology to characterise 1) microscopic sediment fabric features diagnostic of sediment emplacement by liquefaction; and 2) weathering features evident at this resolution that could be used to discriminate between different generations of liquefaction features.

Sediment or soil micromorphology involves the microscopic characterisation of sediment and soil fabric features (Brewer and Sleeman, 1960). Soil thin section analysis has been used in a wide variety of pedological and sedimentological studies to elucidate aspects of pedogenesis, deposition, post depositional disturbance and diagenesis (Phillips, 2006; 2013; Van der Meer et al., 2009; 2011). Only recently, micromorphology has been used in paleoseismic analysis. For example, Vanneste (2008) used the thin sections collected from two paleoseismic trenches along the active Geleen Fault segment in the Roer Valley Graben,Belgium, to prove the presence of a colluvial wedge caused by an old fault rupture. Vanneste's (2008) application made clear how thin section analysis can provide evidence of soft sediment deformation, sediment microfaulting and microfolding typical of low to moderate earthquake zones, with none or very small geomorphic evidence of past earthquakes. However, to date, earthquake induced liquefaction features have not been studied at the micro scale.

The approach used in this application of micromorphology is, firstly, to explore modern unequivocal liquefaction features related to the CES (Canterbury Earthquake Sequence) to characterise their sedimentary fabric. And secondly, to compare the micromorphology of modern with unequivocal paleoliquefaction features to define the more subtle microscopic scale weathering and pedofeatures that may be useful in distinguishing paleoliquefaction features from contemporary liquefaction features, or multiple generations of paleoliquefaction features. The aim is to define a set of characteristics that can be used in future micromorphological studies of paleoliquefaction to resolve sequences and timings of events.

6.2 Geological setting and field relationships

The 2010-2011 CES began with the Mw 7.1 Darfield earthquake on 4 September 2010. This event was caused by an unknown, blind fault near Darfield with a hypocentre located at depth of 10 km. During the 2010 event the fault ruptured the surface along several traces including the Greendale fault (Basher et al., 2011; Cubrinovski et al., 2010; Quigley et al., 2012; Van Dissen et al., 2011). Liquefaction affected residential houses near waterways, wetlands throughout the Christchurch city and the town of Kaiapoi as well as rural areas near streams and former channels of the Waimakariri River. (Almond

et al., 2012; Brackley et al., 2012; CGD0200, 2013; Orense et al., 2011; Townsend et al., 2016; Villamor et al., 2016). The sequence continued in a series of aftershocks through 2010 and early 2011 (Bannister and Gledhill, 2012). A significant event occurred on 13 June 2011 causing liquefaction and damage in the eastern suburbs, while further events of Mw 5.8 and Mw 5.9 occurred offshore from Christchurch in December 2011. The most devastating aftershock, the Mw 6.2 Christchurch earthquake of 22 February 2011, caused 185 fatalities, damaging landslides and rock falls in the hills, and extensive liquefaction throughout the city (Bannister and Gledhill, 2012).

As a precursor of the present project, multiple trenches were excavated on properties near Greenpark, close to Lincoln, in a green fields area near the Halswell River (Almond et al., 2012; Villamor et al., 2016; 2014) (Figures 3.3). Landforms are all of fluvial origin and are related to transport and deposition of sediment on the floodplain of the Halswell River or to a former distributory of the Waimakariri River (Brown et al., 1988). In a later campaign, trenches were excavated in the coastal environment where landforms included dunes, interdune swales, sand plains and swamps. Trenches provided vertical and horizontal exposure of subsurface stratigraphy, which included liquefaction and paleoliquefaction injection features and cross-sections of remnants of CES sand blows and blisters at the land surface (Tuttle et al., 2017 ; Villamor et al., 2016; 2014).

6.3 Sample Location

6.3.1 Alluvial paleoseismic trenches

In the alluvial setting, trenches were excavated and sampled at the Hardwick property, located on the Halswell River floodplain, Greenpark area, ~28 km south west of Christchurch (Figure 3.3 in Chapter 3).

The Halswell alluvial floodplain lies on the Yaldhurst surface, characterized by Waimakariri age (700-2400 years old) and Selwyn age (less than 300 years old) soils. In particular the soil at the study site is a Recent Gley soil of the Taitapu soil series (LCR, 2016). For more details on the geomorphic surfaces and soil types of the Halswell floodplain, refer to Chapter 2 and 3.

Two trenches were selected for thin section analysis: Trench HWK 3 and Trench HWK 6. Trench HWK3 was excavated on top of a crevasse splay (Figure 1S[9]) and the stratigraphy exposed was characterized by a collapse crater feature (Villamor et al., 2014) formed a few weeks after the liquefaction events (C. Hardwick pers. comm.). Three thin section samples were collected: Sample 689 was collected from a sand blow; samples 695 and 680 were collected from a liquefaction sill.

Trench HWK6 was the longest trench dug at the Hardwick site (up to 24m) and it exposed both modern and paleoliquefaction features (Figure 2S). Trench HWK6 revealed crevasse splay deposits (M1 unit) sitting atop a channel fill deposit occupying a Waimakariri River paleochannel (M2 unit) (Figure 2S) (for a detailed stratigraphic description and interpretation of Trench HWK6 refer to Villamor 2014, 2016). Two thin section samples were collected at Trench HWK6. Sample 676 was collected from the modern dike observed on the east wall (Figure 3S, samples 678 and 675 are not analysed in this study) and sample 674 was collected from a paleoliquefaction feature observed on the floor (Figure 4S) (Almond et al., 2012; Villamor et al., 2016; Villamor et al., 2014). Five oriented thin section samples (689, 695, 680, 676, 674) were collected from the alluvial environment.

6.3.2 Coastal paleoseismic trenches

The field campaign in the coastal environment involved three different sites: Wainoni and QEII parks on the dunes in the Christchurch urban area, and at Featherston Avenue Reserve in the Pines Beach area (~25 km north of Christchurch Figure 4.1, Chapter 4). The thin section samples were collected from paleoseismic trenches dug at Wainoni and QEII Parks. The sediment forming the dunes of the coastal system of Christchurch has been dated between 500-1000 years ago (see Chapter 4 for more details). The soils of the dunes at Wainoni and QEII Parks are Kairaki and Waikuku soils, belonging to the Recent and Brown soil orders respectively (Hewitt, 2010).

The samples at Wainoni Park were collected from Trenches WAI 2 (Figure 5S) and WAI 3 (Figure 6S). Trench WAI 2 was characterized by a sill of concave shape exposed at 0.75 m depth on the north-east

[9] S Figures in Appendix A9

wall. Also a dark grey sandy circular feature of 63 by 73 cm was exposed on the floor of this trench. Sample 706 was collected from the exposed modern liquefaction dike.

Trench WAI 3 revealed a very thick sand blow (26 cm) with many rip up clasts from the pre CES-anthropogenic fill with a clay texture and stiff consistency. The pre-earthquake fill sits on top of the original loamy sand topsoil (11 and 15 cm thick) disrupted by liquefaction injection. Some Bw horizon fragments were exposed only on the left hand corner of Trench WAI 3 (Figure 6S A). Sample 709 was collected from the sand blow on the west wall (Figure 6S B).

The samples at QEII were collected from QEII Trench 1 and QEII Trench 2. QEII Trench 1 (Figure 7S) cut across a 25 cm thick sand blow with many brown clay rip up clasts coming from an underlying pre-earthquake surface fill. The pre-earthquake fill was broken in many parts and injected by liquefied sand coming from the underlying Bw horizon. A 1 m-wide dike was exposed on the south wall of QEII Trench 1, characterized by a greyish-blue- very fine silty sand. Fragments of the same (organic rich) blue grey very fine silty sand were observed in other parts of the trench as rip up clasts within the Bw horizon (paleosollayer in the legend of Figure 7S). At QEII Trench 1, sample 711 was collected from the Bw(f) horizon injected by the “mud lamina” layer (Figure 7S).

QEII Trench 2 was characterized by very thick and complex layers of fill overlying a sandy sheet containing many organic lenses (Figure 8S). The latter was fed by a dike breaching a collapsed buried A horizon, above which the sand pooled (left hand side Figure 8S). The buried A horizon is underlain by the sandy gleyed parent material.

Samples 715 and 716 were collected from the north wall of QEII Trench 2 from the dike and the sill respectively (Figure 8S) with the aim of understanding the genesis of the sandy sill exposed in QEII Trench 2. Samples 717 and 719 were collected from the south-east wall of QEII Trench 2 (Figure 9S) to investigate the origin of the parallel dike-like features exposed on the south east wall (Sample 717) and to study the hosting sediment (Sample 719). Seven oriented thin section samples (706, 709, 711, 715, 716, 717, 719) were collected from the dune deposits.

6.4 METHODS: Micromorphology

The methods used for collecting and processing the thin sections are standard methods for thin section analysis (Fitzpatrick, 1984; MacLeod, 2008; Moran et al., 1989; Murphy, 1986). Kubiena tins (70 x 50 x 30 mm) (Figure 10S) were emplaced into the sediment on a horizontally or vertically excavated surface along the features of the trench walls that were targeted for this study. The samples were processed in the thin section laboratory at Lincoln University. First, the samples were dried by replacing the soil water using the acetone vapour replacement technique (MacLeod, 2008). As these samples were unconsolidated loose sand, the normal acetone replacement technique of immersion in liquid acetone would have resulted in sample destruction. The samples were retained within the Kubiena tins and were placed in a vacuum desiccator with a container of acetone. The desiccators were evacuated under pressure until the acetone boiled and filled the desiccators with acetone vapour. Due to the porous nature of the samples, the acetone vapour permeated the sample, replacing the soil water, which was collected at the base of the desiccator (Figure 10S b and c). A container of silica gel was also added at the bottom of the vacuum desiccator to facilitate drying (Figure 10S d). The acetone was changed every two or three days. A densimetric method developed by MacLeod (2008) was used to monitor water exchanged by the acetone. Once a sufficient quantity of water had been removed (see table in MacLeod, 2008), the samples were impregnated with resin in a vacuum chamber (Figure 10S), resin was cured (under vacuum) and then blocks were trimmed, sectioned, ground and then polished to produce the final thin section (Palmer et al., 2008). The samples presented in this study were processed into thin section slides at Stirling University. Each thin section was cut orthogonal and parallel to any deformation structures observed, producing thin sections of 35 µm of thickness. The overall sample preparation was 3-4 months. Microfabric analysis was performed using an Olympus BX53P microscope under plain and crossed polarised light.

The thin section samples were analysed to describe mineralogy, microstructure, related distribution, organic fragments, textural, and excremental features (Bullock et al., 1985; Stoops and Verpraskas, 2003). The mineralogy of the alluvial samples was analysed by using QEMSCAN, (Quantitative

Evaluation of Minerals by SCANning electron microscopy). This is a new cutting edge technique to create mineralogy maps from small specimens (Field and Atkins, 2012). The results from the QEMSCAN are presented in the QEMSCAN Appendix, A10. The detailed description of the alluvial samples is in the Appendix A11for the alluvial samples, and in Appendix A12 for the coastal samples.

6.5 RESULTS

6.5.1 Mineralogy

The mineralogy of the alluvial samples revealed by QEMSCAN was dominated by quartz and plagioclase feldspar, consistent with a sediment derivation from the Torlesse Supergroup of the Southern Alps (Brown and Weeber, 1992). For further details on the mineralogy refer to the Qemscan Appendix A10.

6.5.2 Microstructure

The thin section analysis of alluvial and coastal sediments highlighted three types of observed fabric:

1. Original soil fabric including rip up clast fabric
2. Modern liquefaction fabric (dikes, sills or sand blows);
3. Paleoliquefaction fabric.

6.5.2.1 Original soil fabric and rip up clast fabric

The alluvial soils are characterized by poorly sorted and compact sediment, very packed grain structure and high abundance of organic fragments and textural pedofeatures (silt and clay coating). Theundisturbed soil fabric remains visible in sample 676 (Figure 6.1-Soil matrix).

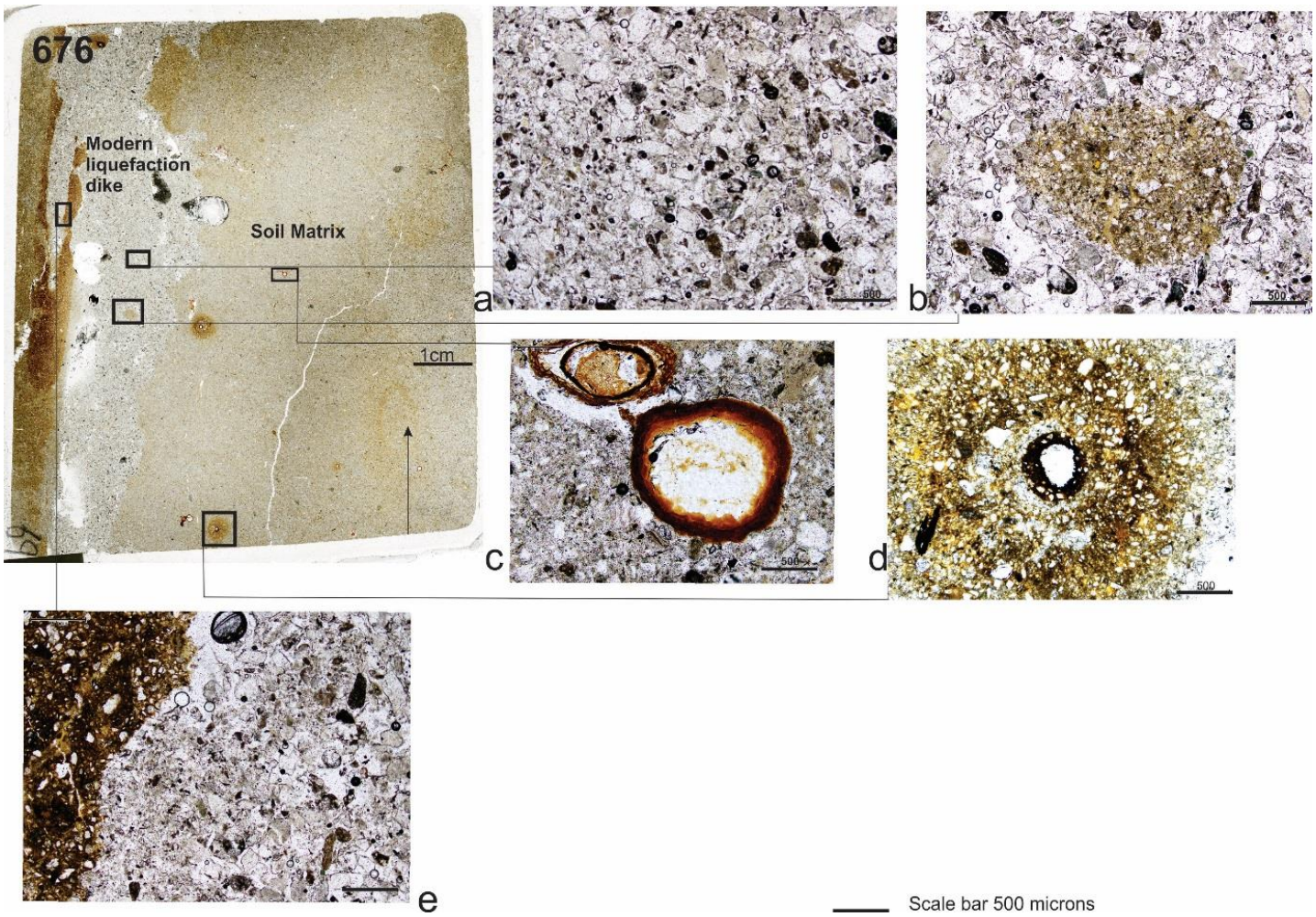

Figure 6. 1 Sample 676 modern liquefaction dike and original alluvial sediment microstructure a) the liquefaction dike is characterized by a single grain microstructure, locally bridged; b) rip up clast in the dike, note the grain size and micromass contrasts. The rip up clasts are characterized by close packed fabric, higher abundance of micromass (yellowish-brownish colour) compared to the surrounding single grain microstructure; c) Lignified parenchymatic plant residue of root in the soil matrix. This organic pedofeature is characterized by distinct cell walls, brown colour, loose but not complete internal coating developed in the fragment at the upper right hand side; d) concentric iron staining developed in the soil matrix. The first ring is a strongly iron impregnated nodule; e) detail on the porewater-induced- structure at the contact between soil matrix and liquefaction material. Note the increasing grain size from the dike edge toward the centre, more detail about this is shown in Figure 6.5 and Figure 6.7. Photos taken in plane polarized light.

In contrast, the coastal dune soils are characterized by well to moderately sorted sediments and by an intergrain-microaggregate or close packing microstructure, locally single grain (no fine material bounding the grains) or bridged (presence of fine material bridging the grains) (Figure 6.2). In the fabric of coastal dune sediments the abundance of the fine material bridging the grains can vary as a function of the soil horizon and of the weathering affecting the site (dune ridge or interdune deposit). Common and widespread mottles and textural pedofeatures differentiate a coastal mineral soil

horizon from a modern liquefaction fabric. The original coastal sediment microstructure is shown in sample 706 (Figure 6.2).

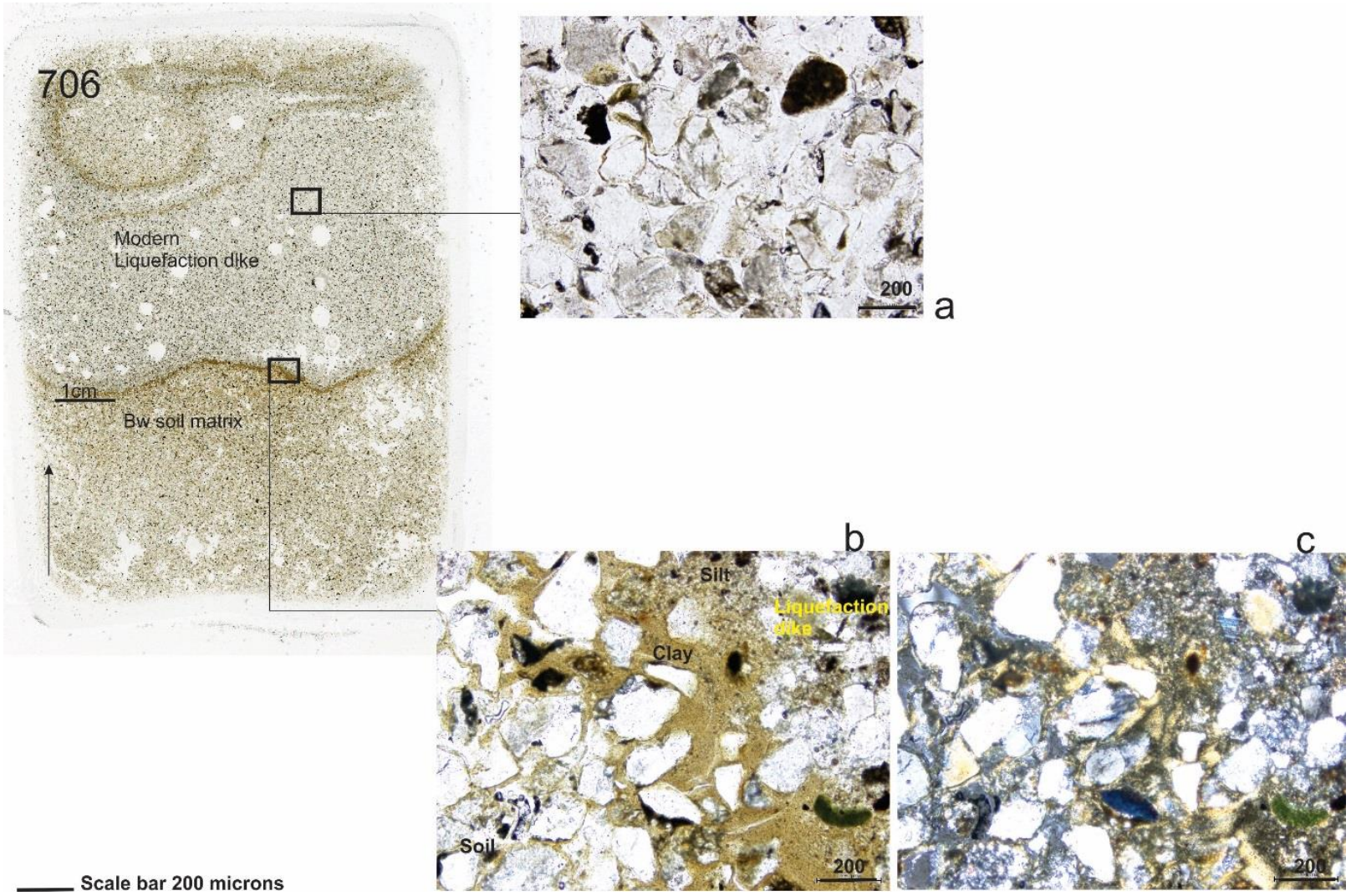

Figure 6. 2 Sample 706, modern liquefaction and original soil matrix in coastal sediment, transmitted light; a) single grain microstructure of the 2010-2011 modern dike; plain polarised light b) grain size gradient along the dike's edge from sand to silt and clay; plain polarised light b) and c) show how the clay matrix was deposited in the interstices of the sandy sediment. c) birefringence pattern of clay indicates one period of clay deposition; cross polarised light.

The difference in sorting and microstructure results from the depositional setting and the transportation medium. Alluvial sediments are naturally polymodal in grain size due to the different load that rivers can carry (Chapter 3 of this thesis Fontana et al., 2015; Haberlah and Mctainsh, 2011; Leys et al., 2005), while coastal dune sediments are characterized by a unimodal grain size distribution. The wind blows at a relatively steady velocity, transporting grains only up to a certain threshold. This results in coastal dune sediment being well sorted between fine and medium sand (Nichols, 2009). The micromorphology results are also corroborated by the grain size analysis (Chapter 3 and Chapter 5). This analysis showed that the alluvial sediment has characteristically a multigaussian (polymodal) grain size distribution, whereas the coastal sediments are better sorted and have a unimodal distribution (Chapters 4 and 5). Also the QEMSCAN analysis outlines at least seven grain size classes within the alluvial samples (Qemscan Appendix, A10).

Rip up clasts fabric

The rip up clasts are tiny fragments of *in situ* soil dragged from the liquefaction flow (see Figure 6.1 for example). Rip up clasts are distinguished from the liquefaction material by the different grain size, higher abundance of micromass, textural and organic pedofeatures (strong soil development), and sharp boundaries. These features make the rip up clasts easy to identify even in a thin section sample affected by soil development.

6.5.2.2 Modern liquefaction Fabric

The modern liquefaction fabric for alluvial and coastal dikes is characterized by single grain microstructure (grains loosely arranged with little or not fine material to provide aggregation, grain to grain contact is predominant) and lack of organic fragments and textural pedofeatures. Exemplars of the modern liquefaction dike fabric are samples 676 (Figure 6.1) and 706 (Figure 6.2) (dikes in the alluvial and coastal environment, respectively) and samples 680 and 711 (Figure 11S and 12S) (modern sand blows with rip up clasts in alluvial and coastal setting, respectively).

The liquefaction fabric of modern sand blows and modern dikes or sills have many similarities. Sample 680 (Figure 11S) is an example of modern liquefaction sediment deposited in a sill. The microfabric

and the pedofeatures observed in sample 680 are consistent with samples 676 and 706 (Figure 6.1 and 6.2): single grain microstructure, locally pellicular (grains almost completely surrounded by fine material which bridges the grains), with lack of textural pedofeatures and organic fragments and many rip up clasts. Sample 709 (Figure 13S) represents a modern liquefaction sand blow fabric. It is characterized by single grain microstructure, locally bridged (grains partially surrounded by fine material, forming bridging between the grains) with lack of textural and organic pedofeatures. A silty thin layer is often deposited at the outer edge of the sand blow, when the porewater pressure is reduced and also the finer grains of the liquefaction material are deposited (Figure 6S). The deposition of finer (silty) sediment at the outer edge of the sand blow can be considered an analogue feature to the finer sediment deposited along the dike's edge in sample 706 (Figure 6.2), and explained later in this chapter.

6.5.2.3 Paleoliquefaction fabric

The paleoliquefaction fabric is characterized by bridged microstructure, locally compact; including common to very common textural pedofeatures and organic fragments. The main differences between a modern liquefaction fabric and a paleoliquefaction fabric is the occurrence of weathering features in the latter. However, the rate of weathering characterizing a paleoliquefaction feature is always little in comparison to the weathering affecting the hosting soil An obvious example of paleoliquefaction thin sections fabric is shown in Sample 674 in the alluvial setting (Figure 6.3) (Tuttle et al., 2017 ; Villamor et al., 2016; 2014).

A summary of the undisturbed soil, modern liquefaction and paleoliquefaction fabric is provided in Table 6.1 and 6.2 for alluvial and coastal environment respectively.

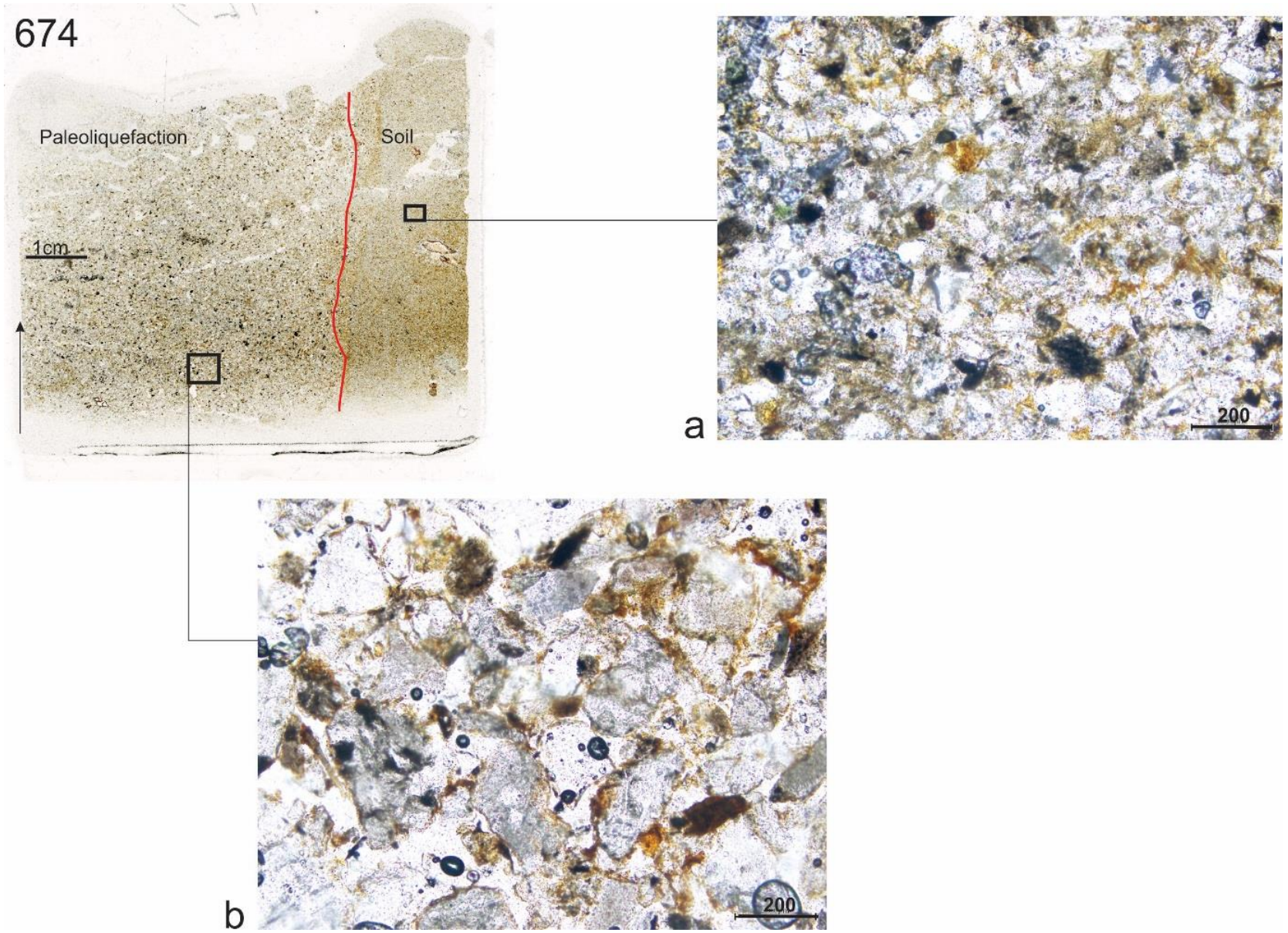

Figure 6. 3 Sample 674, comparison between paleoliquefaction fabric and soil matrix in the alluvial setting. a) very compact microstructure from the soil matrix, note the presence of micromass bridging the grains; b) paleoliquefaction sample showing bridged to compact microstructure. Scale bars in microns. Photos taken in plane polarized light.

TABLE 6. 1 Summary of the in situ soil and liquefaction fabric investigated in the alluvial setting of the Canterbury Plains. terminology follows Bullock et al (1985) and Stoops (2003).

Feature/ Alluvial Environment	Micro-structure	Voids	Related Distribution (microfabric)	Textural pedofeatures	Organic and excremental Pedofeatures	b-fabric
Modern Liquefaction	Single grain	Simple packing voids	Monic to enaulic	none	none	none
Paleoliquefaction	Bridged to compact micro-structure	Chambers and planar voids	Monic to enaulic	From few to common: infilling of voids, dense and complete, common coating, silt capping	Organic: few to common: lignified parenchymatic plant residue of root, charcoal fragment, residue of fungus sclerotium Excrement: ellipsoids, egg shaped, likely origin is oribatid mites, orange brown and coalesced. Ellipsoid excrement brown dark brown: coalesced and dense but few are disjoined.	Common, speckled b-fabric
Soil/ Rip up clasts	From compact microstructures to chamber or prismatic structure	Chambers and planar voids	Chitonic to porphyric	From common to very common: infilling of planar voids, dense and complete, common coating, silt capping, iron staining, ferruginous dense and concentric nodule coating, coating of planar voids, crack infilling, coating and capping with iron staining.	Organic: common to very common: lignified parenchymatic plant residue of root, charcoal fragment, residue of fungus sclerotium	speckled b-fabric

TABLE 6. 2 Summary of the in situ soil and liquefaction fabric investigated in the coastal setting of the Canterbury Plains. terminology follows Bullock et al (1985) and Stoops (2003).

Feature/ Coastal Environment	**Microstructure**	**Voids**	**Related Distribution (microfabric)**	**Textural pedofeatures**	**Organic and excremental Pedofeatures**	**b-fabric**
Modern Liquefaction	Single grain mictrostructure	Simple packing voids	Gefuric, sediment very well sorted	none	none	none
A horizon Soil/ Rip up clasts	Compact and very compact grain structure		Porphyric related distribution	Common: silt coating and void coatings	Common: Lignified parenchymatic tissue of plant residual and charcoals. Ellipsoid excrement brown-dark brown they look coalescent and dense but few of them are disjoined	Common speckled b-fabric
Bw(f) horizon	Single grain microstructure, locally bridged	Single packing voids, common chambers	Chitonic	Silt coating and mottles	No organic components and no excremental pedofeatures observed	Common speckled b-fabric

A summary of the liquefaction, paleoliquefaction and original soil matrix microstructure investigated in the alluvial and coastal setting, according to the weathering intensity is shown in Figure 6.4.

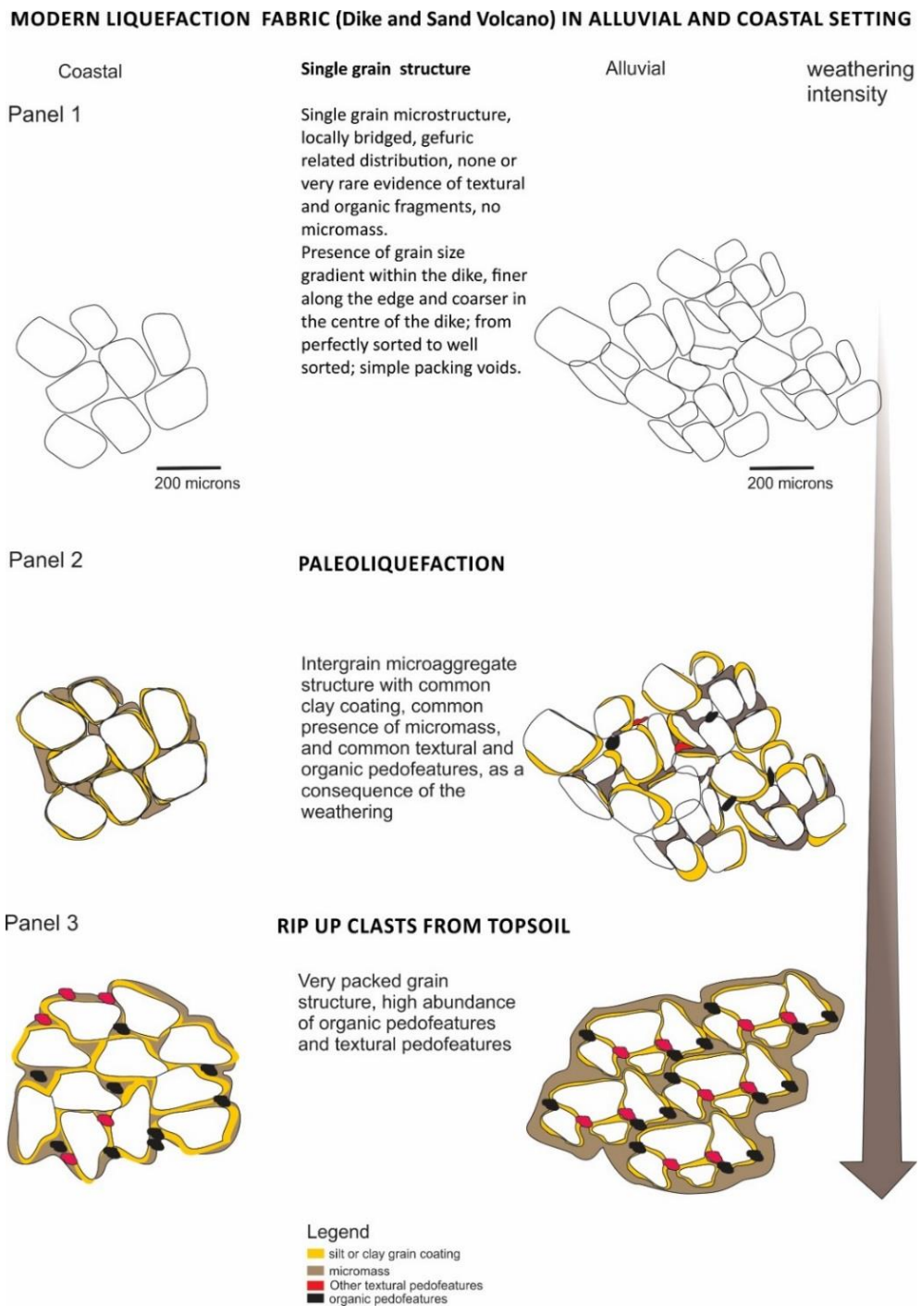

Figure 6. 4 Summary of the different fabrics analysed in the alluvial and coastal setting, in relation to the weathering occurring in the sediment. Panel 1 shows the single grain microstructure typical of a modern liquefaction deposit; Panel 2 shows the paleoliquefaction fabric characterized by a higher abundance of micromass and an increasing number of textural and organic pedofeatures, in contrast with the modern liquefaction fabric; Panel 3 illustrates the close packed microstructure characterizing the soil hosting liquefaction features or the topsoil rip up clasts often identified in the modern liquefaction sediment. There are no differences in fabric between the two settings. Legend: in yellow is highlighted the silt and clay coating, in brown the micromass, in red organic and excremental pedofeatures, in black charcoal (Glossary from Bullock et al., 1985).

6.6 DISCUSSION

Cyclic stress loading causes a sudden increase of pore water pressure in water saturated and unconsolidated sediment that liquefy. The increase in pore water pressure breaks the inter-particle (effective) stress forces, which bond the grains together (effective stress Terzaghi et al., 1996), turning the sediment from a solid state into a liquid-like state (liquefaction sediment). The excess porewater pressure is then vented when the water and entrained sediment travel upward and are ejected at the surface, forming dikes or sills within the soil profile, and sand blows at the surface. The effective stress is also rebuilt once the sediment is deposited.

As a consequence of mobilisation induced by liquefaction, the fabric of sediment that has experienced recent liquefaction (samples 676, 706 Figures 6.1 and 6.2) resembles that of sediment recently deposited by a water flow, and which has not been subjected to chemical weathering processes. As a consequence, modern liquefaction features are characterized by water escape structures (*sensu* Van der Meer and Menzies, 2011).

For example, sample 706 is characterized by a particle size gradient from sand to silt and clay, closely compacted at the outer edge of the dike (Figure 6.5 a).

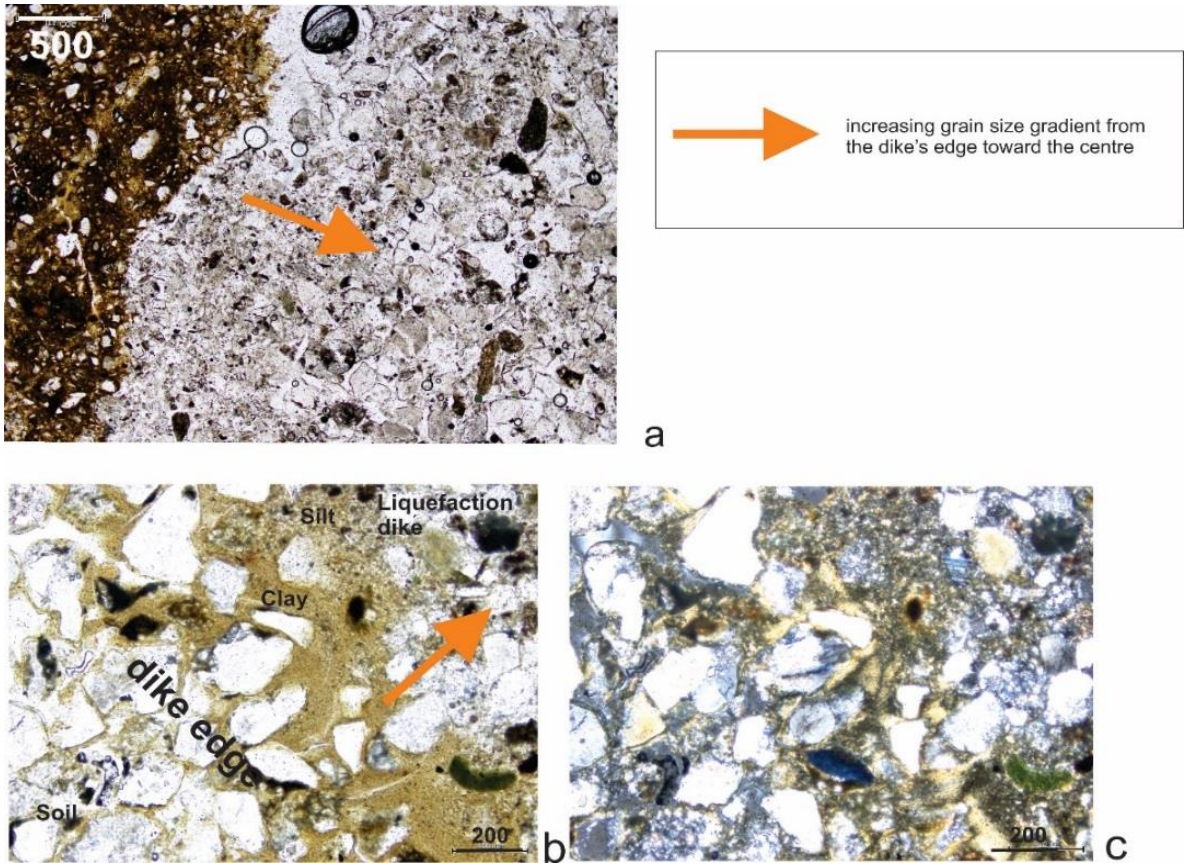

Figure 6. 5 Grain size gradient examples from the dike's edge toward the centre; a) Sample 676, alluvial modern liquefaction dike, note the finer sand and silt deposited along the dike's edge while the coarser sand occupies the centre of the dike; b) and c) show a detail from sample 706 of the grain size gradient from the dike's edge toward the centre of the dike in plain light (b) and in cross polarized light (c). Note clay and silt are lined up along the dikes' edge while the sand occupied the main body of the dike. More details are shown in Figure 6.6 and in the diagram of Figure 6.7. Scale bars in microns. Photos taken in plane polarized light.

A closer observation of this feature revealed that the clay matrix is only visible along the dike's edge as a brownish boundary draping the dike. It is assumed that the clay surrounding the coarser sandy sediments was deposited from the water flow within the dike toward the dike's edge where the flow velocity is lower, and once the hydrostatic pressure was reduced. The granostriated b-fabric of the clay indicates that anisotropic clay particles are orientated parallel to the sand grains, indicating that it is most likely the clay was deposited in one event. In summary, the sandy dike and the finer sediment (silt and clay) deposited along the dike's edge are part of the same liquefaction event but they mark different flow regimes during the liquefaction process (Figures 6.6). A schematic summary of the liquefaction-porewater-induced-structure in the thin sections is shown in Figure 6.7.

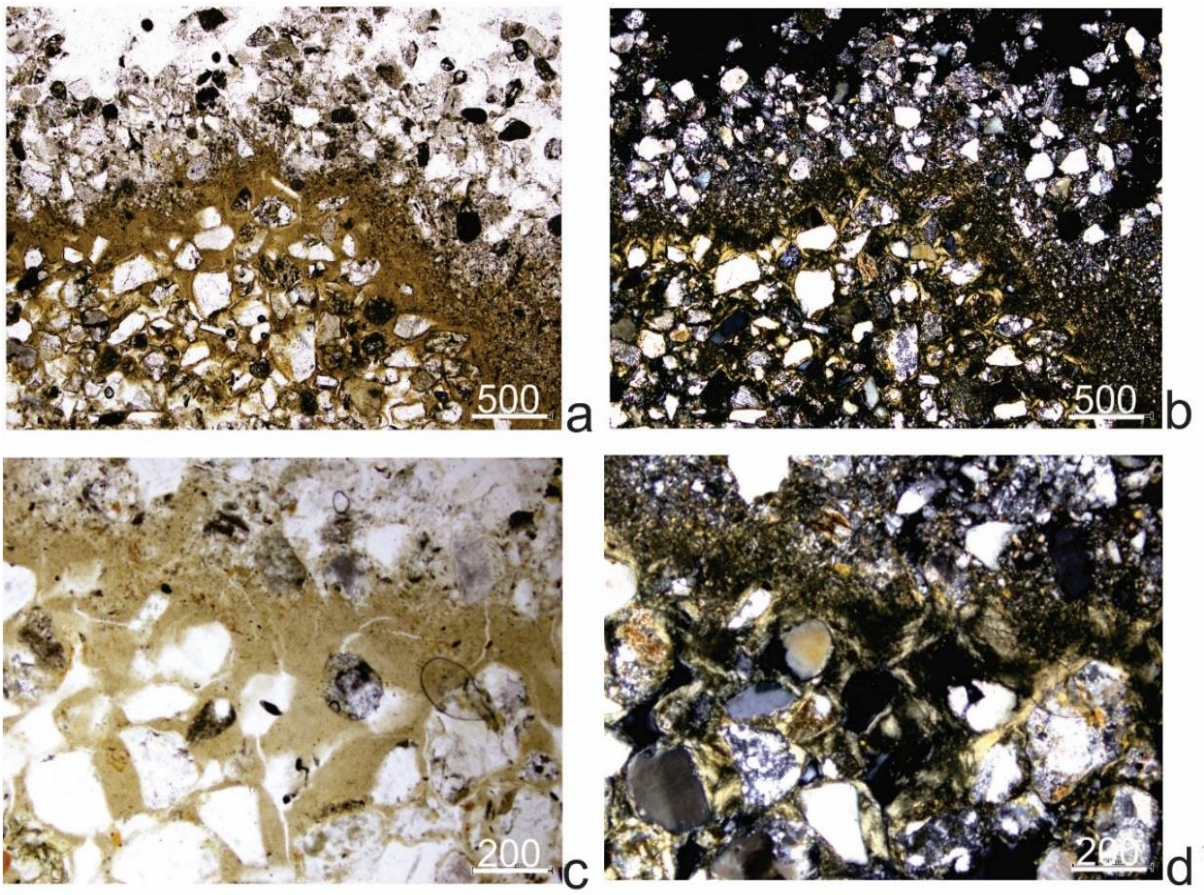

Figure 6. 6 Photo credits by Carol Smith. Details of the grain size gradient from the dike's edge toward the centre of sample 706, analysis of birefringence. Panels a, c, are pictures taken in plane light and panels b, d are cross polarized pictures. Scale bar in microns.

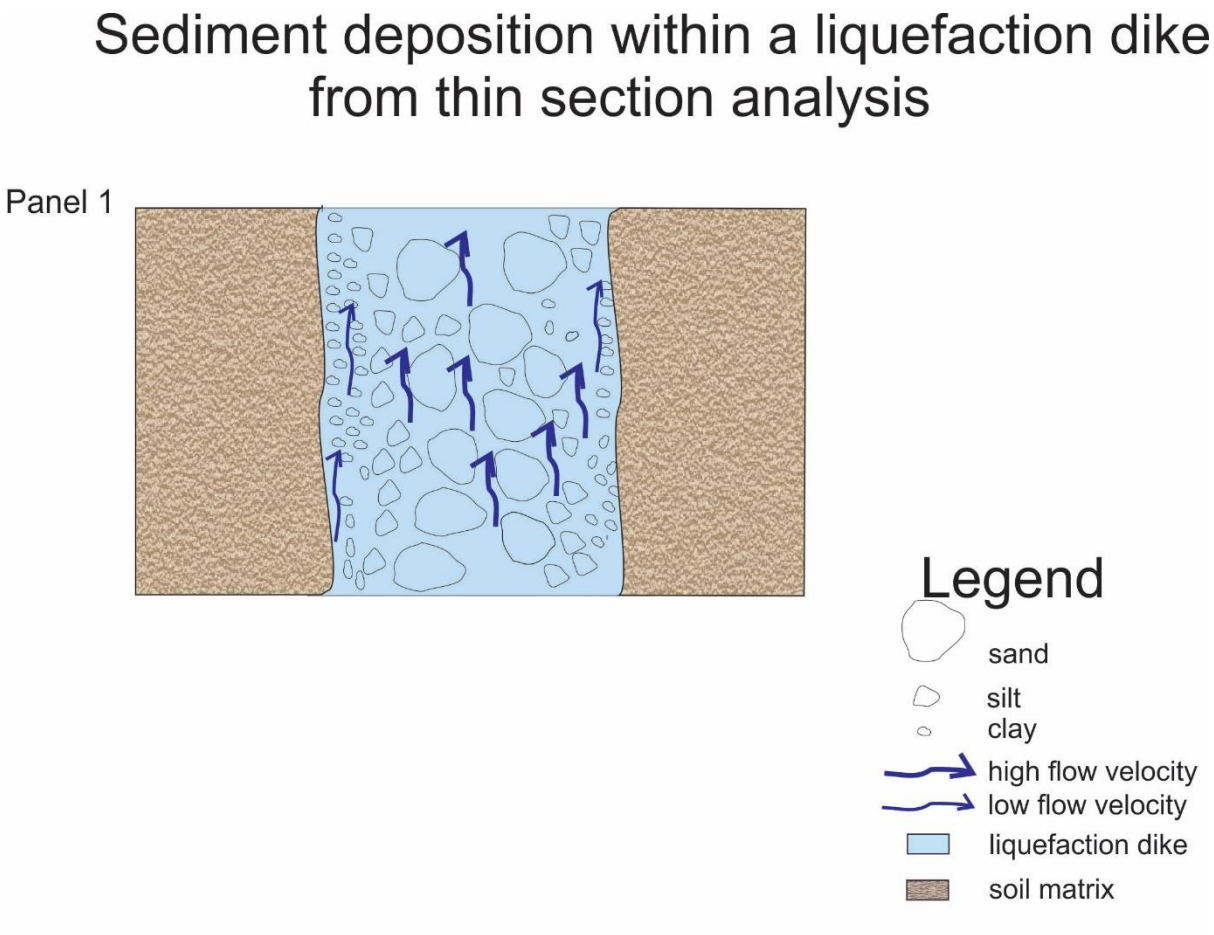

Figure 6. 7 Diagram of the liquefaction-induced pore-water structure. Panel 1. The liquefaction process starts, the porewater pressure is high, the liquefaction material comprises coarse and fine sediments. Panel 2 the liquefaction process is almost completed. At this stage the porewater pressure is lower and the coarser grains have been deposited. The finer (silt and clay) sediment gradually gets deposited once the porewater pressure is reduced and the liquefaction process ends.

The main distinction between paleoliquefaction and modern liquefaction features is the expression of weathering features such as the presence of micromass, and organic and textural pedofeatures, as showed in the unequivocal paleoliquefaction sample 674. The paleoliquefaction features observed in this study feature an age between AD 908 and AD 1336 (from Oxcal analysis performed by Villamor et al., 2016)

Sample 715 (Figure 6.8), for example, was not unequivocally identified as a paleoliquefaction samples at the outcrop scale, but the following characteristics as i) abundance of organic and textural concentration pedofeatures- in comparison to modern liquefaction fabric (e.g. Samples 676 and 706, Figures 6.1 and 6.2 respectively)- ii) presence of rip up clasts; and iii) oxidized dike boundaries induced by the weathering process, visible also at an outcrop scale, lead to convey this sample a paleoliquefaction sample. At QEII Trench 2, the lack of charcoal did not allow the sediment to be dated and it was not possible to identify the age of the paleoliquefaction features. Therefore, at this site, the micromorphology description was crucial to reveal the presence of paleoliquefaction.

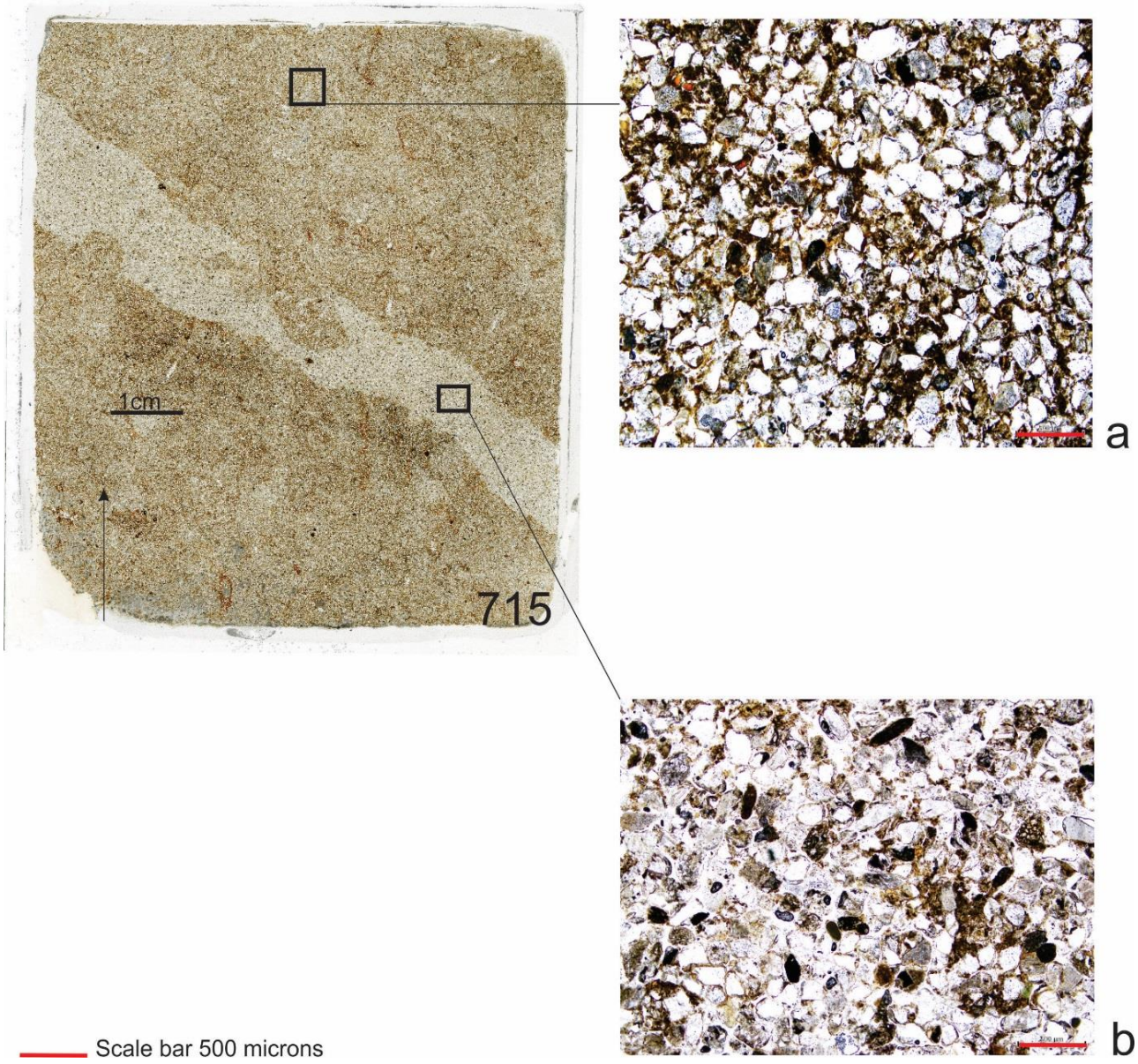

Figure 6. 8 Sample 715, comparison between soil matrix and paleoliquefaction dike microstructure in a coastal setting; a) very close packed microstructure from the buried topsoil, note the high abundance of micromass bridging the grains (from yellow brown to dark brownish colour); b) bridged microstructure, locally single grain or pellicular, note the soil micromass in the paleoliquefaction fabric is less abundant in comparison to the soil matrix. Photos taken in plane polarized light.

However, the evidence of oxidation along the dike's edge is not always indicative of paleoliquefaction features. Sample 717 (Figure 14S) on the south-east wall of QEII Trench 2 shows a single grain microfabric, a lack of micromass and textural or organic pedofeatures, depicting a modern liquefaction dike. However the edges of the dike in sample 717, and a small area at the base of the dike are iron stained. The formation of iron staining at the dike's edge is caused by redox reactions, the most important chemical weathering reactions occurring in water saturated soils. The sediment characterizing the liquefaction dike are water saturated owing to their depositional setting. Water saturated sediment is anaerobic and develops anaerobic microsites (Creeser et al., 1993), where there is absence or very low oxygen diffusion. When dikes intrude near surface sediment, for example A horizons, with a higher content of organic matters, the low availability of oxygen leads the anaerobic bacteria to use other elements like Iron in the form of Fe^{3+} as electron acceptors, reduced in the form of Fe^{2+} (Schaetzl and Thompson, 2015). Once the dike starts drying (this process can take weeks or months, according to the local fluctuations of the water table) the iron re-oxidizes again (Fe^{3+} + $3H_2O=Fe(OH)_3+3H^+$). Along the dike's edge, where the drying process is more intense, $Fe(OH)_3$ precipitates, producing the typical red colour characterizing the dike of Sample 717 (Figures 14S). Therefore, the strong iron staining occurring along the dike's edge is a further confirmation that water saturated sediment occupied the dike fracture, and that it was injected from depth.

The thin section methods for liquefaction and paleoliquefaction investigation documented in this study aid in assessing the morphogenesis of several liquefaction features not clearly interpreted during the field campaign. For instance, QEII Trench 2 exposed a dike-like feature in a buried A horizon, which linked to an overlying bed of sand with a wavy lower contact (Figure 8S). Uncertainty about the origin of the features arose from the observation of disrupted organic lenses in the sandy layer. Therefore, several backward cuts were made on the trench wall to better investigate the dike-like feature, and its link with the sand bed (Figure 5.26) in three dimensions. This feature was latterly interpreted as an example of A-horizon splitting (Chapter 4 and 5 of this thesis), a characteristic

liquefaction feature of the coastal dune setting. However, the micromorphological analysis was an essential corroborating evidence that the sand blow was emplaced by liquefaction processes.

Sample 716 (Figure 6.9) showed three different but coexisting fabrics i) liquefaction fabric: single grain with very few textural and organic pedofeatures; ii) paleoliquefaction fabric: bridged structure and increasing soil development; and iii) rip up clasts fabric: very close packing, strong soil development. The evidence of three different, but coexisting, fabrics revealed that sample 716 is characterized by a very heterogeneous microstructure and that it is not an undisturbed aeolian deposit. In particular, the evidence of rip up clasts as typical liquefaction features corroborated the assumption that the sandy sill- targeted by sample 716 was triggered by a liquefaction event, and likely by an old liquefaction event due to the soil development that characterizes the sample.

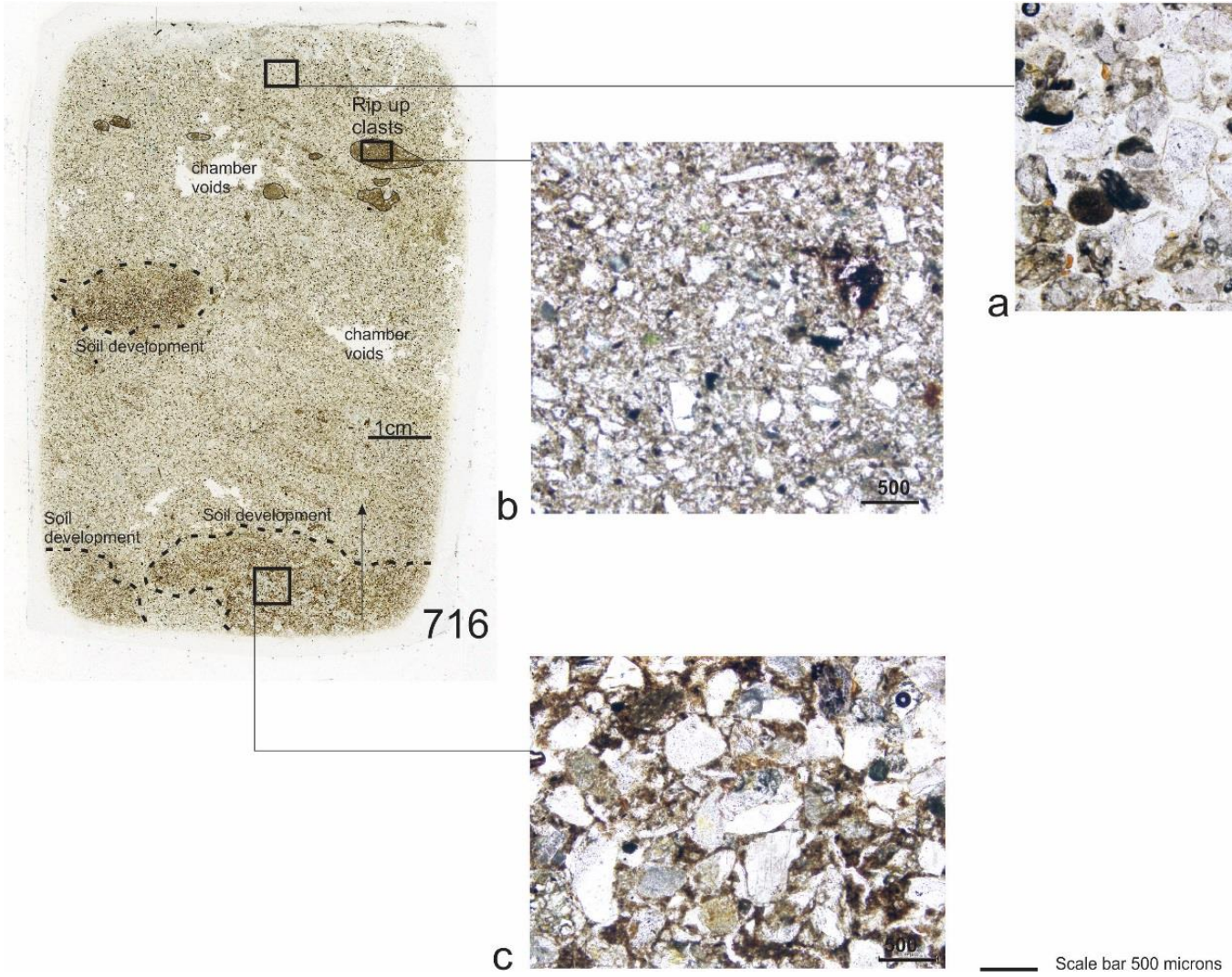

Figure 6. 9 Sample 716 description and interpretation; a) single grain microstructure from the paleo-sandy sill; b) c was characterized by three different types of microstructure: i) single grain (a), ii) close packed microstructure in the rip up clasts (b) and iii) bridged or intergrain microaggregate structure (c).

The rip up clasts were characterized by a very compact grain structure (b), porphyric related distribution and many textural concentration features. The rip up clasts were identified by their different colour from the micromass and sharp boundaries. c) The paleoliquefaction was characterized by a bridged or intergrain microaggregate microstructure (c). The related distribution varies from gefuric to enaulic; well sorted sediment locally poorly sorted; common presence of micromass. The presence of three different microstructures within the same stratigraphic layer revealed that this layer is not an aeolian sandy bed but a paleoliquefaction sill. Details on the stratigraphic evidence of the sandy sill are also explained in Chapter 5. Photos taken in plane polarized light.

6.7 CONCLUSION AND FUTURE WORKS

- The 2010-2011 Canterbury Earthquake Sequence (CES) was the first scenario that allowed micromorphological analysis of sedimentary fabrics of liquefaction injecta and ejecta.
- The soil thin section analysis was evaluated as a complementary technique to support outcrop scale interpretation in paleoliquefaction studies.
- The thin section analysis can differentiate multiple liquefaction generations based on the abundance of organic and textural pedofeatures.
- In order to accurately recognize the paleoliquefaction fabric, it is important to assess the fabric of the undisturbed soil matrix, as a calibration exercise which allows to compare the rate of textural and organic pedofeatures, along with the degree of sediment packing between soil and a recently deposited sediment (modern liquefaction).
- Apart from the original sediment sorting (alluvial sediment is polymodal, while coastal sediment is well sorted, unimodal) the alluvial and coastal sediments are characterized by similar liquefaction and paleoliquefaction fabrics. This result confirms that the liquefaction process occurs in a similar way in both environments, even though the liquefaction features exposed in alluvial and coastal environments can be characterized by important differences in features (see Chapter 3, 4 and 5 of this thesis).
- The thin section samples need to be calibrated in relation to the local weathering affecting the sediment. The weathering effect can be considered a sort of “background effect”, and when it is not properly recognized, it can cause misinterpretation of paleoliquefaction features.
- Regarding the thin section technique, the sampling and laboratory processing of soft sediment can be very complicated. The processing of unconsolidated samples is challenging and several samples have been destroyed during the sample collection and during the samples preparation.

Future work

With regard to future research it is suggested to apply the thin section analysis to the sediment retrieved in the core, in order to investigate the potential liquefaction source layer and study the type of soft sediment deformation occurring in the source layer, or in proximity of the source layer.

Due to the highly diagnostic features retained into the paleoliquefaction features, thin section analysis can also be applied to study sites that experienced multiple paleo liquefaction events in order to understand whether it is possible to distinguish different types of soil development in relation to different past liquefaction events (e.g. liquefaction features from New Madrid Seismic Zone).

Chapter 7
PRELIMINARY USE OF THE RANDOM FOREST CLASSIFICATION FOR MAPPING FUTURE LIQUEFACTION SURFACE MANIFESTATION

7.1 INTRODUCTION

Research of the liquefaction triggered by the 2010-2011 Canterbury Earthquake sequence (CES) has advanced the understanding of the phenomenon from geotechnical (Bray et al., 2014; Cubrinovski et al., 2011a; Cubrinovski et al., 2010; Cubrinovski et al., 2011b; Green et al., 2013; van Bellegooy et al., 2014), geological and sedimentological perspectives (Bastin et al., 2015; 2016; Quigley et al., 2013; Villamor et al., 2016; 2014). Furthermore, the availability of high quality imagery has supported intensive ground-based mapping efforts (Almond et al., 2010a; 2012; Brackley et al., 2012; Townsend et al., 2016) that together with high resolution pre- and post-CES LiDAR elevation data have greatly contributed to the understanding of the geomorphological controls on liquefaction surface manifestation (Almond et al., 2012; Bastin et al., 2015; Townsend et al., 2016; Villamor et al., 2016; 2014), and geomorphological responses to liquefaction (Hughes et al., 2015). In Chapter 2 of this thesis, liquefaction spatial databases (Brackley et al., 2012; Townsend et al., 2016) and a LiDAR-informed geomorphological map (Villamor et al., 2016; 2014) were combined to characterise landform susceptibility to liquefaction at a coarse scale. The derived understandings were then used to provide focus for detailed sedimentological and stratigraphic studies of the alluvial and coastal environments (Chapter 3 and 5 of this thesis). Landforms in the above analysis were delineated on the basis of morphology, topology and inferred genesis. However, to date, there has been no analysis of the fine scale relationships between liquefaction surface manifestation and terrain attributes derived from precise LiDAR-based elevation models. If quantifiable relationships exist, they would provide insights into local controls on ejection of liquefied sediment, and potentially a basis for predicting sites that may host paleoliquefaction phenomena.

Generally, liquefaction occurs in low lying areas of young Holocene sediment (<2000 years old) near waterways, where sandy or sandy silt sediment is water saturated, and near seismogenic sources that

can cause a ground shacking of PGA > 0.090 g (Bastin et al., 2015; Monaco et al., 2011; Quigley et al., 2013; Santucci de Magistris et al., 2013; Villamor et al., 2016). More specifically, (see Chapters 3, 4 and 5) liquefaction *surface manifestation* (ejecta) appear to be controlled by the local presence of (i) liquefiable sediment, (ii) a shallow water table (e.g. perched water table or confined and semiconfined aquifers) and (iii) by the existence of pathways (cracks or weaknesses) that the fluidised sediment can use to gain access to the surface.

Genetic landforms have specific morphological characteristics and are associated with characteristic sediment types (e.g. point bars or crevasse splays in a fluvial environment). Consequently, the liquefaction susceptibility of subsurface sediment, or the strength of surface crusts will be characterized by a specific geomorphology that may be identified by unique combinations of topographic attributes. Some studies also inferred that landforms' geometries determine surface gravitational stresses (Caputo, 2005), which may predispose certain parts of the land surface to tensional strain (via brittle failure and cracking) once a subsurface layer liquefies and loses shear strength. The latter is most strongly expressed in lateral spreading where free faces already exist, but is also hypothesised to occur where more gentle topographic variation prevails and not necessarily in proximity to free faces. In the particular case of lateral spreading, even a small gravitational component affects the loss in shear stress of the sediment prone to liquefy, facilitating the liquefaction of the material, and promoting the lateral spreading (Caputo, 2005; 2012). In other words, the landforms' geometry, inferred by microtopographic parameters plays a critical role in the liquefaction surface manifestation.

Accordingly, it is hypothesised that microtopographic parameters derived by LiDAR DEM have predicative power with respect to the location of liquefaction ejecta. The aim of this chapter is to assess whether it is possible to adopt a novel approach based on a Machine Learning scheme, in particular the Random Forest algorithm (Breiman, 2001, 2004), to objectively formalise the relationships between liquefaction ejecta presence or absence and microtopographic parameters. If

statistically significant relationships exist, the microtopographic parameters may provide a basis for better discriminating potential areas where liquefaction ejecta will occur under a given ground shaking in the future, or where paleoliquefaction may have occurred as a result of past earthquakes.

To achieve this aim the following objectives are established:

1) Understand the correlation between liquefaction manifestation and micro-topographic parameters. By using the CES liquefaction surface manifestation mapping in conjunction with a high resolution DEM derived from LIDAR, Machine Learning techniques are used to derive a new classification that links specific microtopographic parameters with liquefaction surface manifestation;

2) Understand whether the microtopographic parameters can accurately predict the liquefaction surface manifestation, and what is the sensitiveness of the classifier;

3) Apply the classification issued in a new area outside the Canterbury Region where there is no modern evidence of liquefaction features. The Manawatu River Basin was chosen as a target area to apply the algorithm. This area was selected because it has high liquefaction susceptibility (it has also historically liquefied, see Beetham et al., 2011) and has similar geomorphic expression to the machine learning CES training sites used.

7.2 LIQUEFACTION AND GEOMORPHIC BACKGROUND OF THE STUDY SITES

The selected CES sites to establish the correlation between liquefaction manifestation and micro-topographic parameters (training sites) were Hardwick and Marchand properties along the Halswell River (Greenpark, 28 km southwest from Christchurch). Both properties were severely affected by liquefaction during the major events (Mw 7.1 Darfield 2010 earthquake, Mw 6.2 Christchurch 2011, Mw 6.3 June and Mw 6.0 December 2011 earthquakes). Figure 7.1 shows the liquefaction maps and aerial photos (Almond et al., 2010b) at the two selected study sites, after the Darfield event. The detailed liquefaction mapping was undertaken using the resolution available from the aerial photos (Almond et al., 2010b).

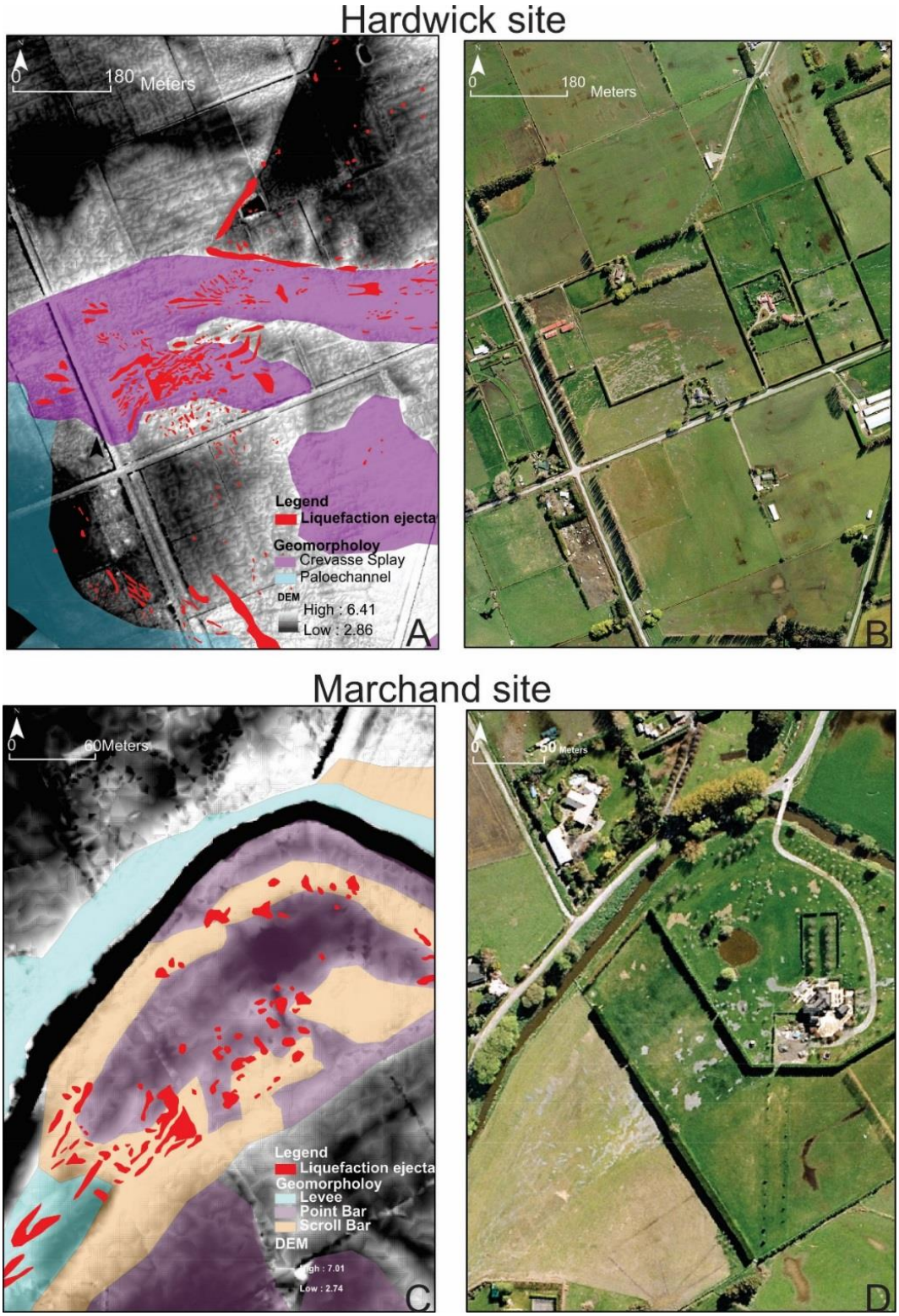

Figure 7. 1 Hardwick and Marchand sites selected as training sites for the Random Forest algorithm. A) Hardwick site geomorphic map and detailed liquefaction mapping; B) Hardwick site aerial photos after the Darfield Earthquake on September 2010 (Almond 2010b); C) Marchand site geomorphic map and detailed liquefaction mapping, D) Aerial photo of Marchand site after the liquefaction event of Darfield earthquake (September 2010).

At the Hardwick site, a crevasse splay sits atop an abandoned paleomeander of the Halswell River, probably formed when it was a distributary channel of the Waimakariri River (see Chapter 3 of this thesis). The crevasse splay partially covers the related point bars of the paleomeander (Figure 7.1 A). The detailed sedimentary architecture of the Hardwick site is explained in Chapter 3 of this thesis and by Villamor et al.,(2016; 2014). Ejecta comprised elongate composite sand blows aligned with paleocurrent direction centred on the crevasse splay and along the buried scroll bars on the south end of the paleochannel (Figure 7.1 A and B).

The Marchand site is on the inside of an active meander of the Halswell River, located 2 km north of the Hardwick site (Figure 7.1C and D). The Marchand site is mainly characterized by point bar deposits, the detailed stratigraphy and sedimentology of which is explained in Chapter 3. Ejecta form elongate features centred on and aligned with the scroll bar deposits (point bar ridges). In particular, the older wider (inner) bar was severely affected. This is possibly due to a thicker sandy layer constituting the potential liquefaction source layer (Chapter 3).

The new study site where the machine learning technique will be applied is a meander of the Manawatu River. The Manawatu River floodplain lies on the south west coast of the North Island, and it is part of the Plio-Pleistocene Wanganui Basin (Clement et al., 2010) (Figure 7.2). The geomorphology includes incised valleys, estuaries, a prograding coastal plain and transgressive dune field, all influenced by sea-level fluctuations (Clement et al., 2010). The physiography of the Manawatu River consists of Holocene levee systems and their associated deposits (S. Levick and J.G. Begg in Beetham et al., 2011). The active floodplain of the Manawatu River is characterised by relict sinuous alluvial channel forms of the late Holocene Manawatu River.

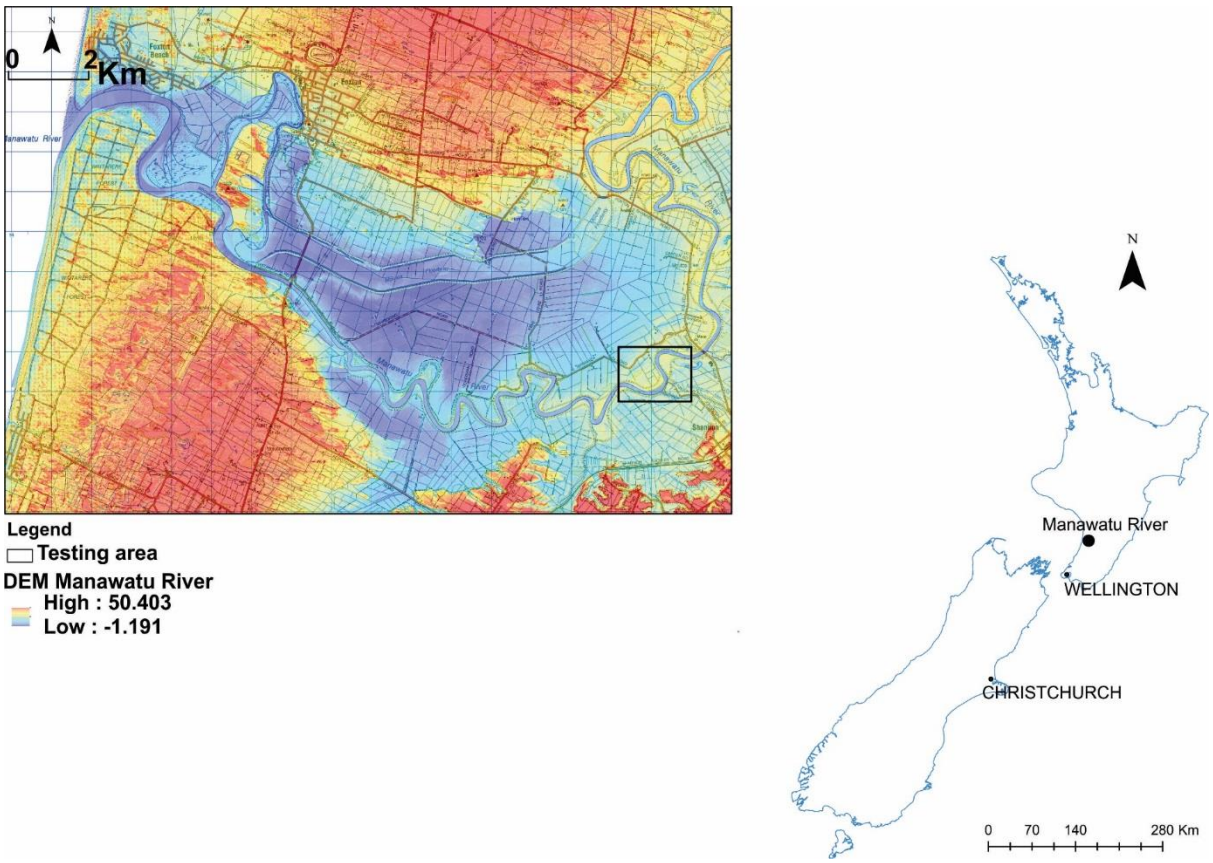

Figure 7.2 Geographic location of the Manawatu River basin targeted as liquefaction testing site of the Random Forest classifier application. The black square highlights the meander of the Manawatu basin area chosen to apply the classifier (Figures 7.9 to 7.13).

Previous liquefaction studies in the Manawatu region were undertaken to assess the liquefaction susceptibility of Palmerston North city (Beetham et al., 2011; Dellow et al., 1994; Tonkin and Taylor Ltd, 2014). Dellow's (1994) work used mainly geological and pedological information and only limited geotechnical information. A more recent GNS report (Beetham et al., 2011) included newer geologic maps (Begg and Johnston, 2000; Lee and Begg, 2000; Townsend et al., 2008), soil maps (Cowie and Kimpton, 1976), LIDAR analysis and drill-hole datasets, which enabled a more accurate understanding of the lithology, groundwater and mechanical properties of the layers.

Historic earthquakes in the Manawatu region are (from Beetham et al., 2011) the 1855 M8.2 Wairarapa earthquake (Downes, 1995), 1931 M7.9 Napier earthquake (Downes, 1995), 1934 M7.6 Pahiatua earthquake (Dellow et al., 1994; Downes, 1995), 1942 M7.2 Masterton I (Downes et al., 2001) and 1942 M7.0 Masterton II (Downes, 1995). However, only for the Pahiatua 1934 earthquake are

there reported liquefaction features such as sand blows, ground cracking and subsidence in the Foxton and Palmerston North area.

7.3 METHODS

7.3.1 Machine Learning theory and Random Forest technique

Machine learning is a set of data mining techniques used in discovering structural patterns within a dataset. In particular, machine learning is useful for datasets where non-linear relationships cannot be solved by using basic regression methods (Hastie et al., 2009 ; Witten et al., 2016).

One of the techniques that belong to the machine learning ensemble is Random Forest. The Random Forest grows many decision trees (see Section 7.3.2). After a large number of trees is generated, the most popular class is chosen by the algorithm (Breiman, 2001). This procedure was elaborated after many improvements in classification accuracy (Breiman, 1996; Breiman et al., 1984; Dietterich, 1998) and it has been demonstrated to be an effective tool for predictions[10] and an accurate classifier (Breiman, 2001) . A training dataset is used in the Random Forest procedure to enable the algorithm to learn the classification. Then a confusion matrix output provides an evaluation of how well the classifier has learnt and what will be the performance of the classifier on the testing dataset (see Section 7.3.4 for explanation). Once the model validation is carried out, the method is applied to a new area where its purpose is to predict certain behaviour (in this case surface manifestation of liquefaction).

7.3.2 Decision trees

A decision tree is a style of representation used in the Machine Learning Theory to show the outcome of the learning from a set of independent samples (Witten et al., 2016). Decision trees are characterized by nodes and leaves, where each node splits an attribute into two subsets (in the case of numerical classification). Decision trees can be very accurate for the data used to train the classifier but may perform less well on an independent dataset targeted as test data. This is because the set of

[10] In Theorem 1.2 explained in Breiman (2001) it is demonstrated that the Random Forests do not overfit as more trees are added, due to the Law of Large numbers.

predictors selected for the model works well in the training area but the learning cannot be generalized (Witten et al., 2016). Examples of decision trees are shown from Figures 7.4 to 7.6).

7.3.3 The testing and the training dataset

To test the success of the classification learning it is important to try out the classification on an independent set of data. The training dataset is not a good indicator of performance of the classifier. Further, the error rate on the training set is not likely to be a good indicator of future performance; any estimate of performance based on that data will be optimistic. The error rate on the training data is called the *re-substitution* error because it is calculated by resubstituting the training samples (rows of the testing dataset) into a classifier that was constructed from them. In order to predict the performance of a classifier on new data it is important to assess the error rate on a dataset that played no part in the formation of the classifier. This independent dataset is called the test data set (Witten et al., 2016). The output of the classification on the testing data set is an objective measure of how well the concept was learned and will measure the performance of the classifier. Both training and test sets need to be representative samples of the research question.

7.3.4 The credibility of the model

The basic performance of the model is evaluated by using the confusion matrix. The confusion matrix is a two by two-way table that contains the results of the classification. From the confusion matrix it is possible to derive other evaluators of the model like error-rate, accuracy, specificity, sensitivity and precision (see Appendix A13 for an example of confusion matrix). Since it is very difficult to construct a perfect classifier algorithm there will be differences between the observations and the expected predicted instances. The four outcomes then will be:

True positive (TP) - correct positive prediction;

False positive (FP) - incorrect positive prediction;

True negative (TN) - correct negative prediction;

False negative (FN) - incorrect negative prediction.

The classifier is expected to perform well in a testing area when the number of incorrect predictions is very low.

The ROC curve (receiver operating characteristics) is a graphical technique used for evaluating data mining, and derived from the confusion matrix outcomes. The ROC values (see Script Appendix A 13, for an example of ROC values) presents the performance of a classifier regardless of class distribution or error costs. So the higher the value of the ROC, the better a classification is expected to work.

7.3.5 Data

The data used in this study is obtained from the detailed digital elevation models (DEMs) for the three study sites (2 CES training and 1 application site in Manawatu region) and detailed maps of surface manifestation of liquefaction (Chapter 3). The relevant micro-topographic parameters for the analysis presented here were derived from the DEM and are: elevation, slope (measured in percent rise), profile and plan curvature (Figure 7.3), by using the Surface analysis toolset in ArcGIS 10.2 Spatial Analyst menu. These micro-topographic parameters are characterized by a relationship among themselves (the curvature is the second derivative of the surface) but also with the presence or absence of liquefaction; the latter extracted from the detailed liquefaction maps.

7.3.6 Data Resolution

At the Hardwick and Marchand sites a 1 m grid DEM derived from the 2008 Selwyn District Council (SDC) Lidar Survey was used for the detailed geomorphic mapping.

The initial 1 m pixel size DEM was resampled at 10, 15 and 20 m for computational efficiency reasons, while also providing opportunity to test model sensitivity to DEM resolution. Results will be shown for the sample sizes and they will be labelled, for example, HWK 10 m for the Hardwick site at a 10 m resolution, or MARCH 20 m for the Marchand site at a 20 m resolution.

7.3.7 Imbalanced datasets and the SMOTE technique

Although the two study sites suffered significant liquefaction effects, the liquefaction ejecta aerial extent was very limited in comparison to the whole selected study area. This means that the dataset for this study had a large number of pixels having the liquefaction attribute “NO” and very few pixels having the liquefaction attribute “YES”. As a consequence, the raster dataset was very imbalanced.

Three techniques are commonly used for solving unbalanced datasets: i) downsampling - the majority class is sampled to make their frequency closest to the rarest class; ii) up-sampling or over sampling -

the rarest class is re-sampled to increase the frequency up to a similar level of the majority class; iii) hybrid approaches or SMOTE, Synthetic Minority Over-Sampling Technique (Chawla et al., 2002). The SMOTE technique was adopted in this study, and it involves a combination of downsampling the majority class and over sampling the minority class, creating synthetic minority class samples (Chawla et al., 2002).

7.3.8 Analysis and Model Design

7.3.8.1 Training Stage

The Hardwick and Marchand sites were considered independent training datasets because of differences in geomorphology (Chapter 3 of this thesis and in Villamor et al., 2016; 2014). This methodology allowed a comparison of each attribute across the two training datasets and also revealed which parameter was more important in relation to the site- specific geomorphic features. The R script used is presented in the Script Appendix A 13.

7.3.8.2 Validation and application

The evaluation of the algorithm was undertaken by applying the classifier derived at the Marchand site to the Hardwick site and vice-versa, in order to estimate the performance of the classifier against the actual liquefaction surface manifestation mapped out after the 2010-2011 CES.

Then, the classifier was applied to a Manawatu River meander, which has similar geomorphic and geologic setting but with no modern evidence of liquefaction (Figure 7.2). The choice of the new area to apply the classifier needs to respect the topographic and geomorphic characteristics of the training site in order for the application to be reasonable and justifiable. As a consequence, the area of application of the classifier needs to be very similar in elevation and characterized by similar geomorphology to the two training study areas.

The meander chosen had an elevation between 0 and 8 m a.s.l., similar to Hardwick and Marchand training sites. The Marchand site classifier was chosen as the most appropriate algorithm because of close similarity of the landform elements between the sites. LiDAR data for the Manawatu region were collected between November 2005 and February 2006 by AAMHatch Pty Ltd and then processed by

GNS Science to create a DEM of 1 m resolution (for more details the reader can refer to Beetham et al., 2011).

7.4 RESULTS

7.4.1 Microtopographic characterisation of training sets

A preliminary microtopographic characterisation of the two training datasets (Hardwick and Marchand sites) may be obtained by plotting the cumulative frequency distributions of the microtopographic parameters chosen for this analysis (Figure 7.3).

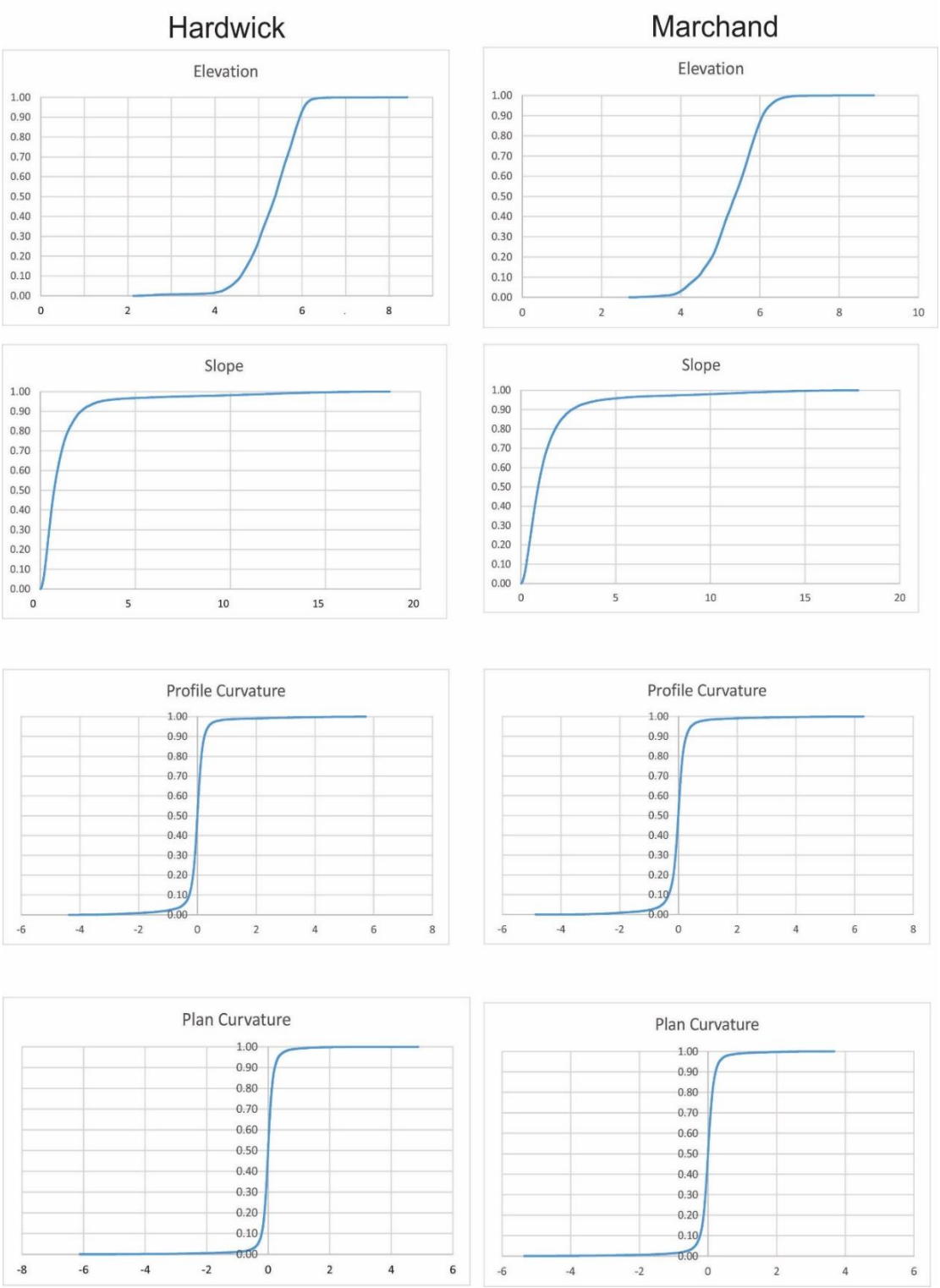

Figure 7. 3 Hypsometric Analysis of the Elevation and cumulative frequency distribution curve of the other micro-topographic parameters (Slope, Profile and Plan Curvatures) at the Hardwick and Marchand sites. Plan and Profile curvatures are calculated as second derivative of the surface. In particular profile curvature is parallel to the slope and indicates the rate of change of slope, while plan curvature is perpendicular to the direction of the maximum slope and relates to the convergence and divergence of flow across the surface (Buckley, 2010)

Most of the Hardwick and Marchand sites are characterized by an elevation between 4 and 6 m a.s.l.

(Figure 7.3 A and B). The Hardwick site features more areas with lower elevation (between 2 and 3 m

a.s.l.) than the Marchand site, while the Marchand site's curve display a slightly larger area with a higher elevation (between 7 and 9 m a.s.l.).

The Slope trend at both sites is very similar (Figure 7.3 C and D). Small differences of profile and planform curvature also occur between the two sites (Figure 7.3, E, F, G, H). In general, both Hardwick and Marchand sites are characterized by a positive profile curvature and by a negative plan curvature. This means that the training area depicts a gentle upwardly concave land surface dominated by convergent topography in plan (hollow or gully-like elements).

7.4.2 Correlation between microtopographic parameters and presence of liquefaction in the CES sites

The decision trees obtained using the Hardwick site as training dataset are shown in Figures 7.4 and 7.5; the decision trees issued using the Marchand site as training dataset are shown in Figures 7.6 and 7.7. Tables 1 and 2 below summarize the list of rules obtained with the Random Forest technique that identify presence of surface manifestation of liquefaction according to the microtopographic parameters used in the algorithm. Each row in Tables 7.1 and 7.2 is one of the positive leaves of the decision trees (highlighted by the red text in the trees of Figures 7.4 to 7.7), i.e. positive occurrence of ejecta. The microtopographic criteria are defined by the combination of threshold values at the nodes of the trees that determine a positive outcome.

Hardwick 10 m

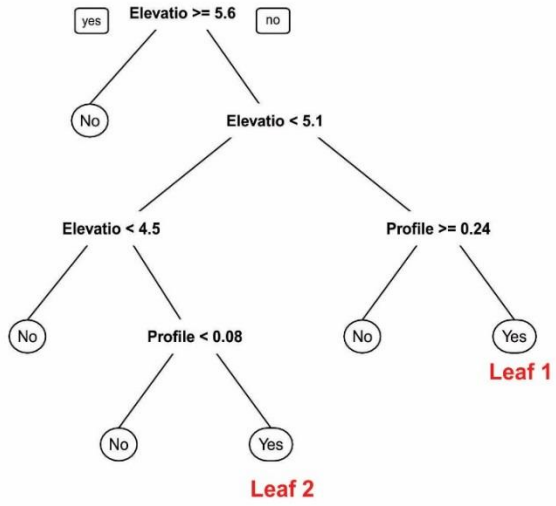

Hardwick 15 m

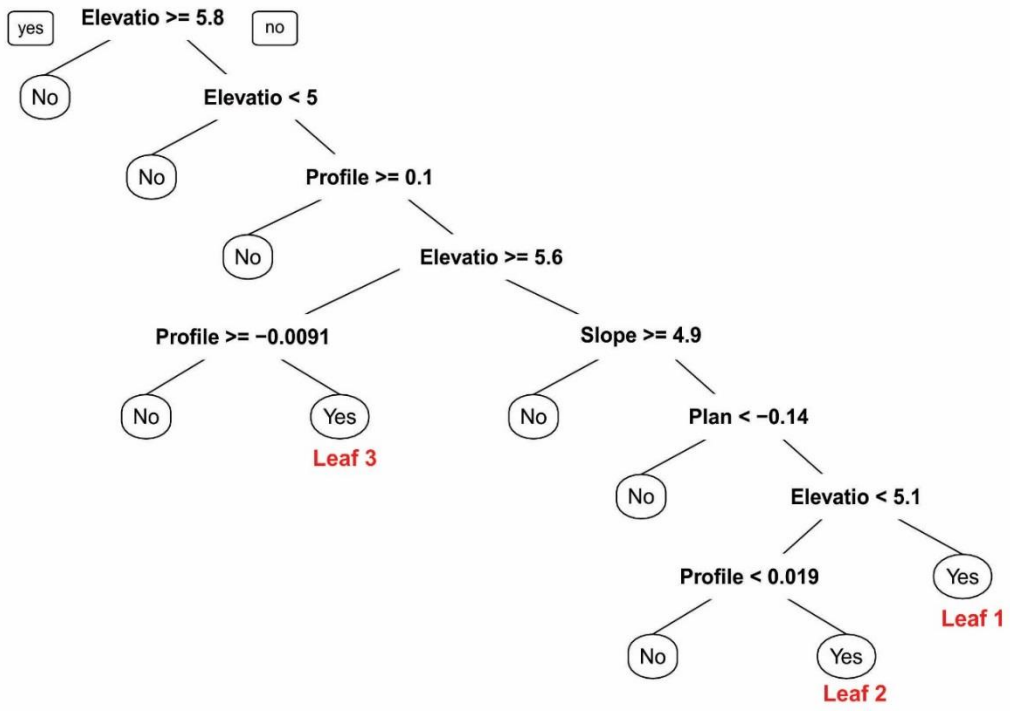

Figure 7. 4 Decision trees of Hardwick site rescaling the DEM of 1 m resolution at 10 m and at 15 m of resolution. The leaf for positive liquefaction surface manifestation are highlighted in red. Elevation in meters, Slope in Percentage rise and Profile and Plan Curvature in 10^{-2} m^{-1}.

Hardwick 20 m

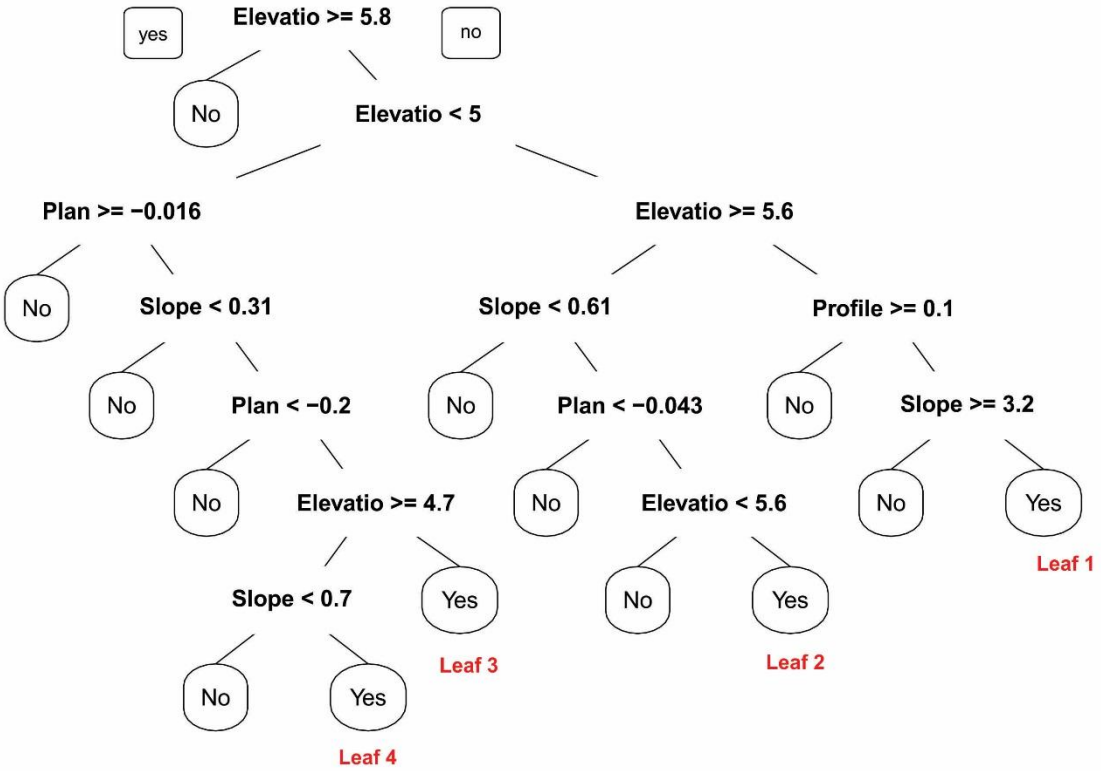

Figure 7.5 Decision tree for Hardwick site rescaling the DEM at 20 m of resolution, the leaves for positive liquefaction manifestation are highlighted in red. Elevation in meters, Slope in Percentage rise and Profile ad Plan Curvature in 1/100.

TABLE 7. 1 List of rules for positive liquefaction surface manifestation at Hardwick site.

	ELEVATION (m)	SLOPE (%)	PROFILE	PLAN 10^{-2} m^{-1}
HWK 10 m				
Test 1	5.1<x<5.6	N.A.	<0.24	N.A.
Test 2	4.5≤x<5.1	N.A.	≥0.08	N.A.
HWK 15 m				
Test 1	5.6≤x<5.8	N.A.	<-0.009	N.A.
Test 2	5.1<x<5.6	<4.9	N.A.	≥-0.14
Test 3	5<x<5.1	<4.9	≥0.019	≥-0.14
HWK 20 m				
Test 1	5≤x<5.6	<3.2	<0.1	N.A.
Test 2	5.6≤x<5.8	>0.61	N.A.	≥-0.043
Test 3	<4.7	≥0.31	N.A.	-0.2≤x<-0.016
Test 4	4.7≤x<5	>0.7	N.A.	-0.2≤x<-0.016

Table 7.1 reveals that at the Hardwick site, liquefaction ejecta occurrence is dominated by Elevation criteria for all DEM resolutions; although Slope is an important secondary parameter at 15 and 20 m resolution. Profile and Plan curvature represent slight upwardly concave surfaces and appear to be less important predictors than elevation and slope.

Turning to the model for the 10 m resolution DEM, the criteria for the two tests identifying ejecta indicate that a band of elevation excluding the extremes (4.5 to 5.6 m AMSL, Fig. 7.3) hosts ejecta, but the profile curvature must not be the most strongly concave for the higher elevation band (5.1 to 5.6 m, Test 1), and it must not be weakly concave or convex for the lower elevation band (4.5 to 5.1 m, Test 2). The geomorphic features identified by Test 1 correspond to higher elevation areas (but not the highest) across point bars and the crevasse splay. In contrast, Test 2 does not correspond to any specific geomorphic element, but instead specifies a consistent set of microtopographic attributes across a range of landforms. In a similar way, all the other tests at 15, and 20 m resolution at the Hardwick site identified the higher elevation part of the study area (e.g. the crevasse splay) and point

bars (Test 3 at 15 m resolution and Test 1 at 20 m resolution, respectively). All the other tests do not have a recognisable geomorphic relevance with respect to genetic landforms.

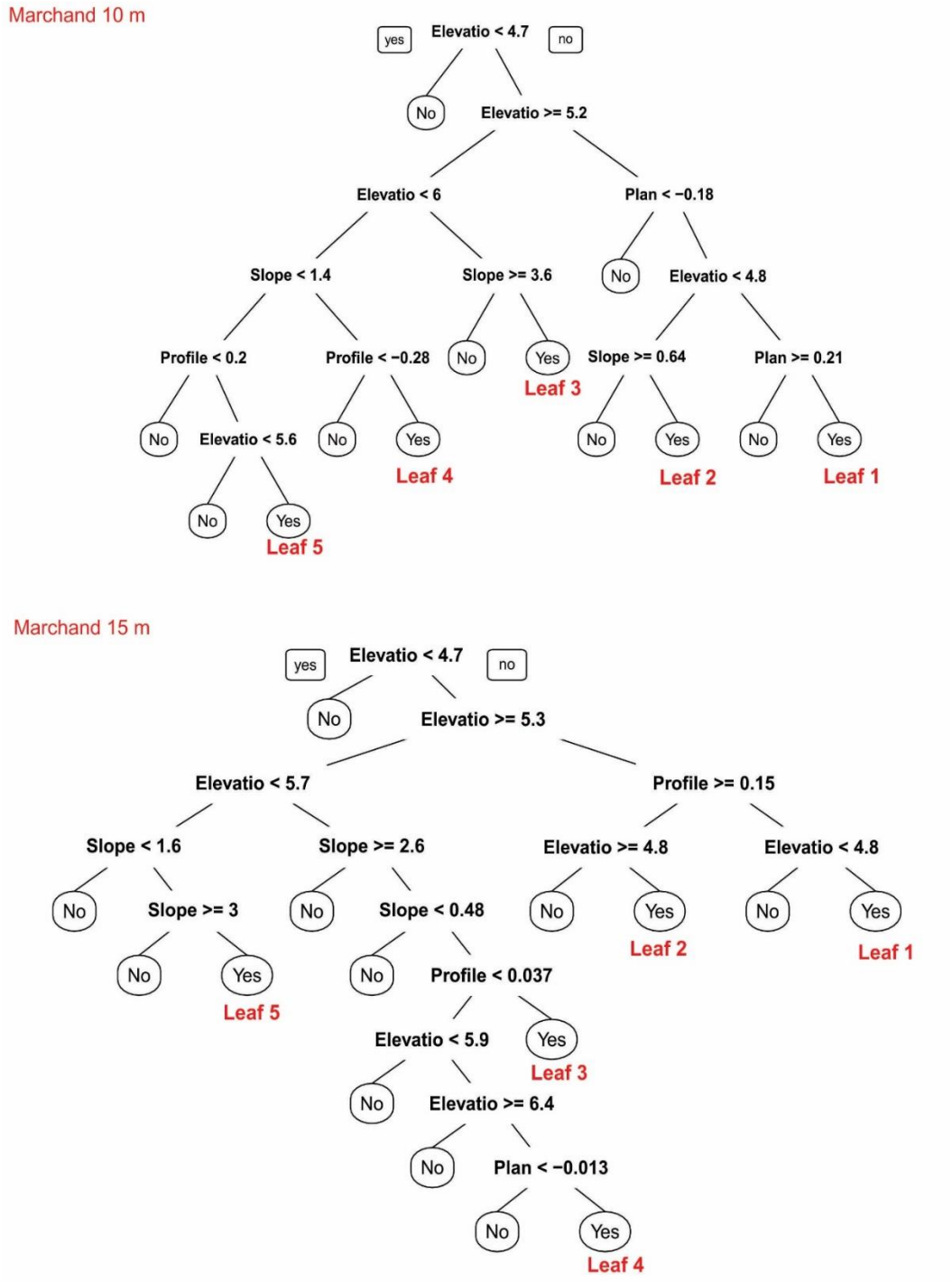

Figure 7.6 Decision trees at the Marchand site, rescaling the 1 m DEM resolution at 10 and 15 m of resolution. Elevation in meters, Slope in Percentage rise and Profile and Plan Curvature in $10^{-2}m^{-1}$.

Marchand 20 m

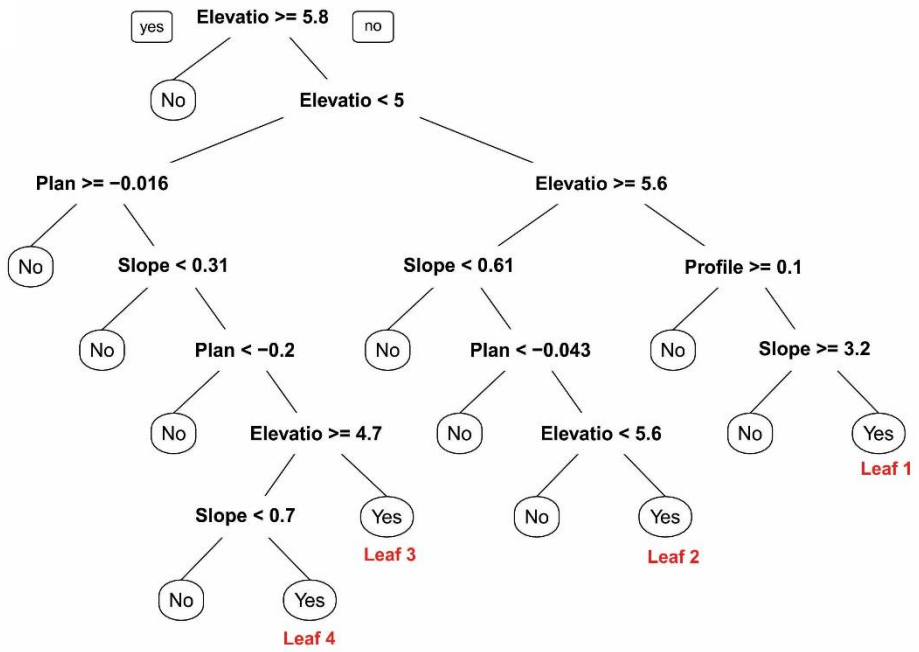

Figure 7. 7 Decision tree at the Marchand site rescaling the 1 m DEM at 20 m resolution. Elevation in meters, Slope in Percentage rise and Profile and Plan Curvature in $10^{-2}m^{-1}$.

TABLE 7. 2 List of rules for positive liquefaction surface manifestation at the Marchand site.

	ELEVATION (m)	SLOPE (%)	PROFILE (1/100)	PLAN (1/100)
MARCH 10 m				
Test 1	4.8≤x<5.2	N.A.	N.A.	0.18≤x<0.21
Test 2	<4.8	<0.64	N.A.	x≥-0.18
Test 3	≥6	<3.6	N.A.	N.A.
Test 4	5.2≤x<6	≥1.4	≥-0.28	N.A.
Test 5	5.6≤x<6	<1.4	≥0.2	N.A.
MARCH 15 m				
Test 1	4.8≤x<5.3	N.A.	<0.15	N.A.
Test 2	4.7≤x<4.8	N.A.	≥0.15	N.A.
Test 3	≥5.7	0.48≤x<2.6	≥0.037	N.A.
Test 4	5.9≤x<6.4	0.48≤x<2.6	<0.037	≥-0.013
Test 5	<5.7	1.6≤x<3	N.A.	N.A.

MARCH 20 m				
Test 1	5≤x<5.6	<3.2	<0.1	N.A.
Test 2	≥5.6	≥0.61	N.A.	≥-0.043
Test 3	<4.7	≥0.31	N.A.	-0.20≤x<-0.016
Test 4	≥4.7	≥0.7	N.A.	-0.20≤x<-0.016

Table 7.2 reveals that at the Marchand site Elevation and Slope are the most important predictors, as for the Hardwick site, followed by Profile and Plan curvature. The curvature criteria identify as liquefaction prone those areas that are near planar or with a gentle concave profile/plan shape. Tests 1, 3 and 4 at 10 m resolution, and Test 1 at both 15 and 20 m resolutions have an obvious association with geomorphic features representative of this study site, such as point bars and levees. All other tests do not represent a clear correspondence with geomorphic features of the study area.

From the decision trees at both the Hardwick and Marchand study sites and from the list of rules in Tables 7.1 and 7.2, Elevation is the most important variable determining liquefaction manifestation, followed by Slope and Profile curvature. Plan Curvature is not part of the decision tree in most of the cases, and when it appears it has only a minor role. The difference in resolution (10-15-20 m pixel resolution) does not seem to affect the sensitivity of the classifier, and the micro topographic variables appear in the same order across all the different pixel resolutions.

The ROC for all the trees is in the range of 0.95-0.99 indicating the model has a very high accuracy, which is also corroborated by the confusion matrix (see Appendix A 13). Consequently, the model is expected to perform well. However, the initial testing of the Hardwick classifier at Marchand site and vice-versa shows a clear over-prediction of the liquefaction ejecta at the two study sites (Figure 7.8). In particular, the classifier does not seem to select a specific geomorphic feature (e.g. crevasse splay or point bars); but to target as liquefaction prone areas different portions of different geomorphic features. This is an unexpected outcome, in disagreement with the confusion matrix and ROC values.

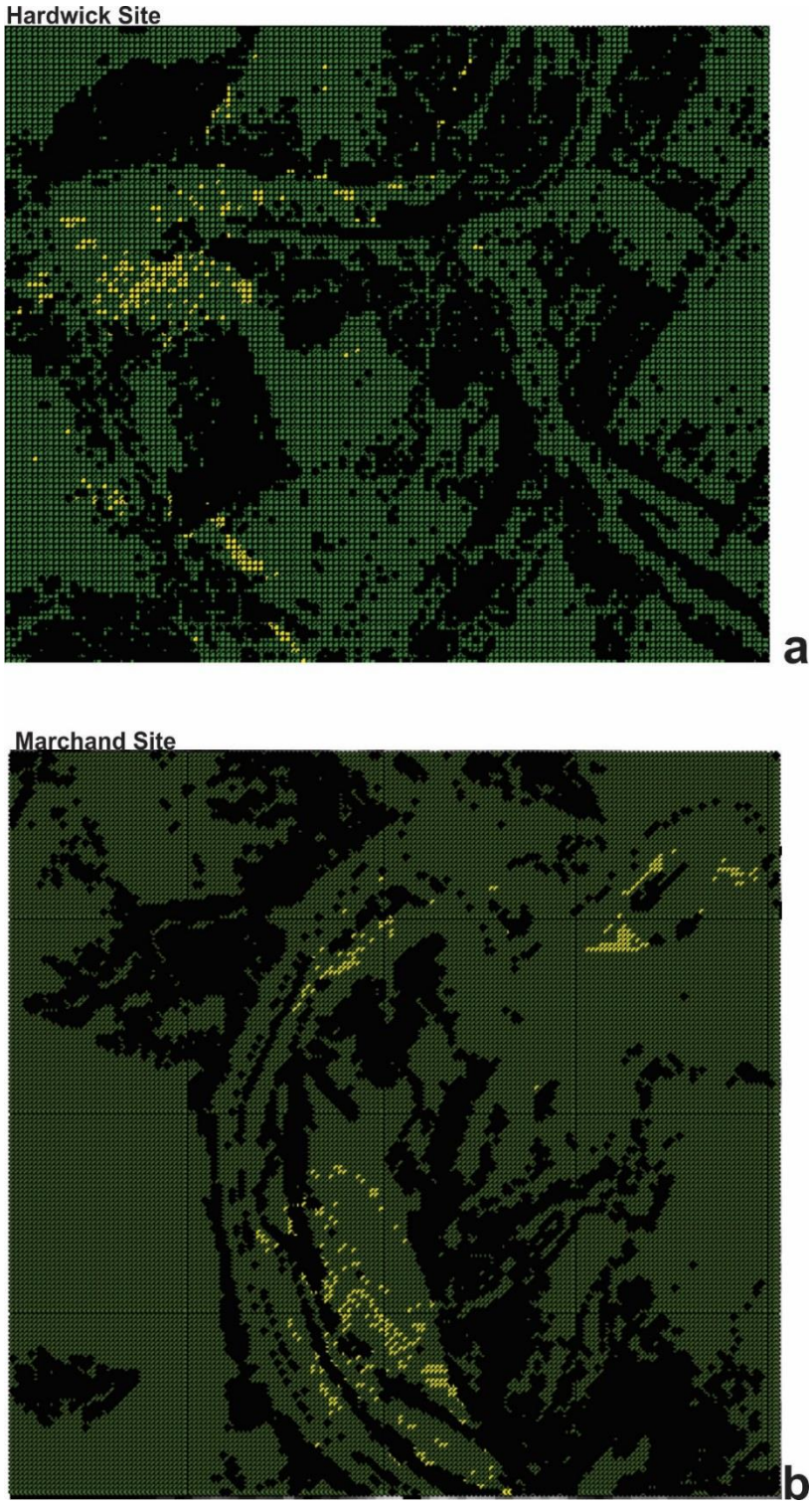

Figure 7. 8 Example of testing of the Random Forest algorithm; a) testing of Marchand Random Forest algorithm on Hardwick site at 10 m resolution; b) testing of Hardwick Random Forest algorithm on Marchand site at 10 m of resolution. The Yellow dots represent the actual liquefaction surface manifestation while the black dots represent the prediction depicted by the Random Forest model. Note the over estimation of this prediction, although the ROC and the confusion matrix showed in Appendix A 13 revealed good performance of the model.

7.4.3 Application of Random Forest technique to predict sites of surface manifestation of liquefaction in the Manawatu River catchment

The detailed geomorphology of the chosen Manawatu River meander is shown in Figure 7.9. The DEM of the Manawatu River was re-sampled at 10-15-20 m in order to be consistent with the resolution of the training dataset and thus the classifier attributes. A geomorphic map was constructed for the meander with the purpose of showing the geomorphic association of the predicted liquefaction ejecta.

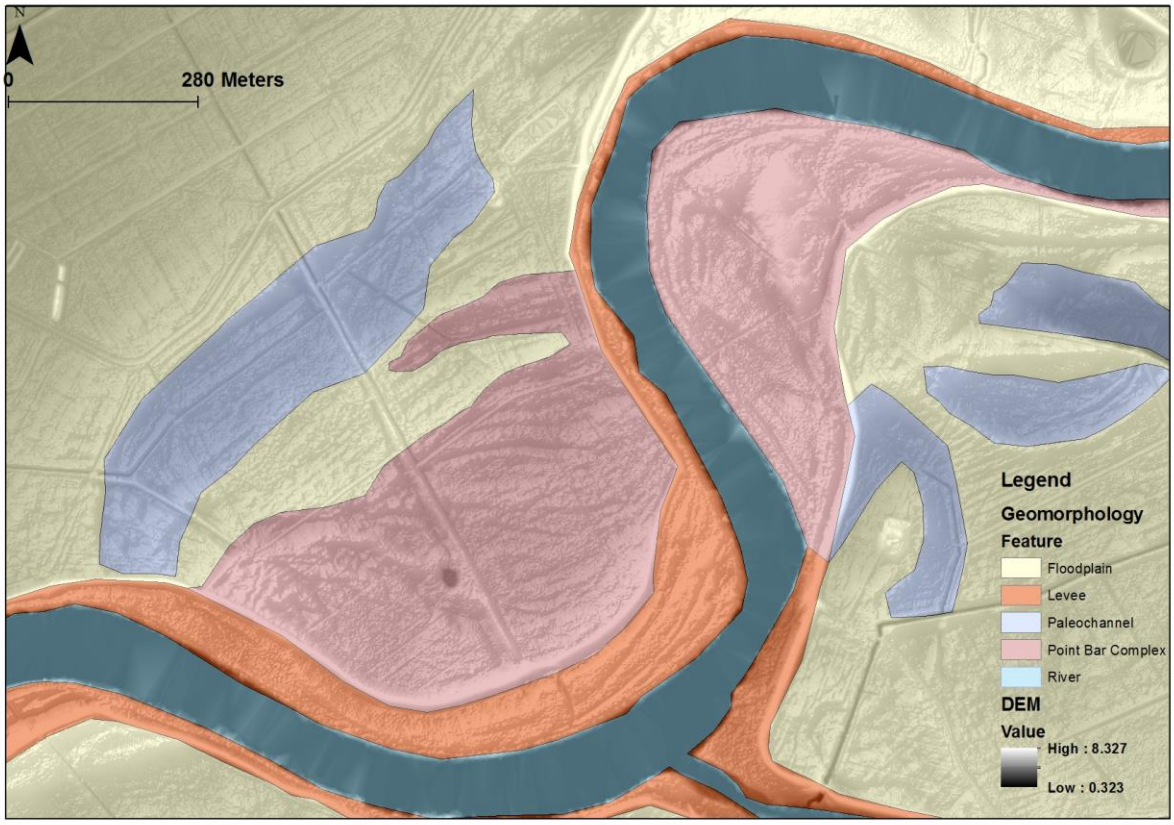

Figure 7. 9 Geomorphic map and DEM of the Manawatu River meander selected as the Random Forest classifier testing site.

Figure 7.10 shows the application of the classifier to the Manawatu River at 10 m resolution. All the predicted liquefaction ejecta are centred along the natural levee and in the inner meander belt of the river, in particular within the point bar area characterized by higher elevation.

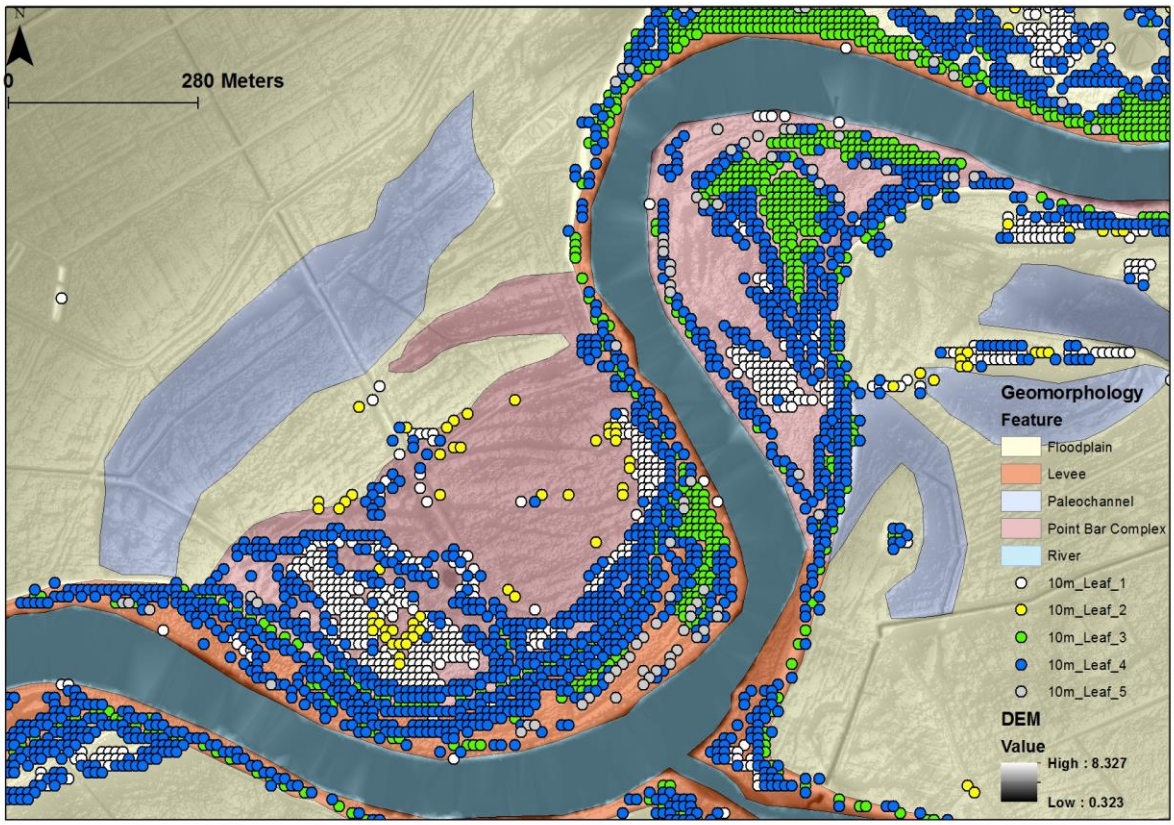

Figure 7. 10 Application of the Classifier at 10 m resolution to the Manawatu meander.

Figure 7.11 (A and B) presents the results of the classifier in the testing area at 15 m resolution. Figure 7.11 A shows that some of the prediction does not have geomorphic validity since liquefaction is predicted also in the river (Leaf n 5, legend of Figure 7.11 A). However, not all the predicted locations of liquefaction surface manifestation of Leaf 5 are necessarily wrong since some of those are still within the point bar complex and along the paleomeander edge. After removing the geomorphically implausible Leaf 5 the final output looks similar to the prediction issued by using the 10 m resolution (Figure 7.11 B).

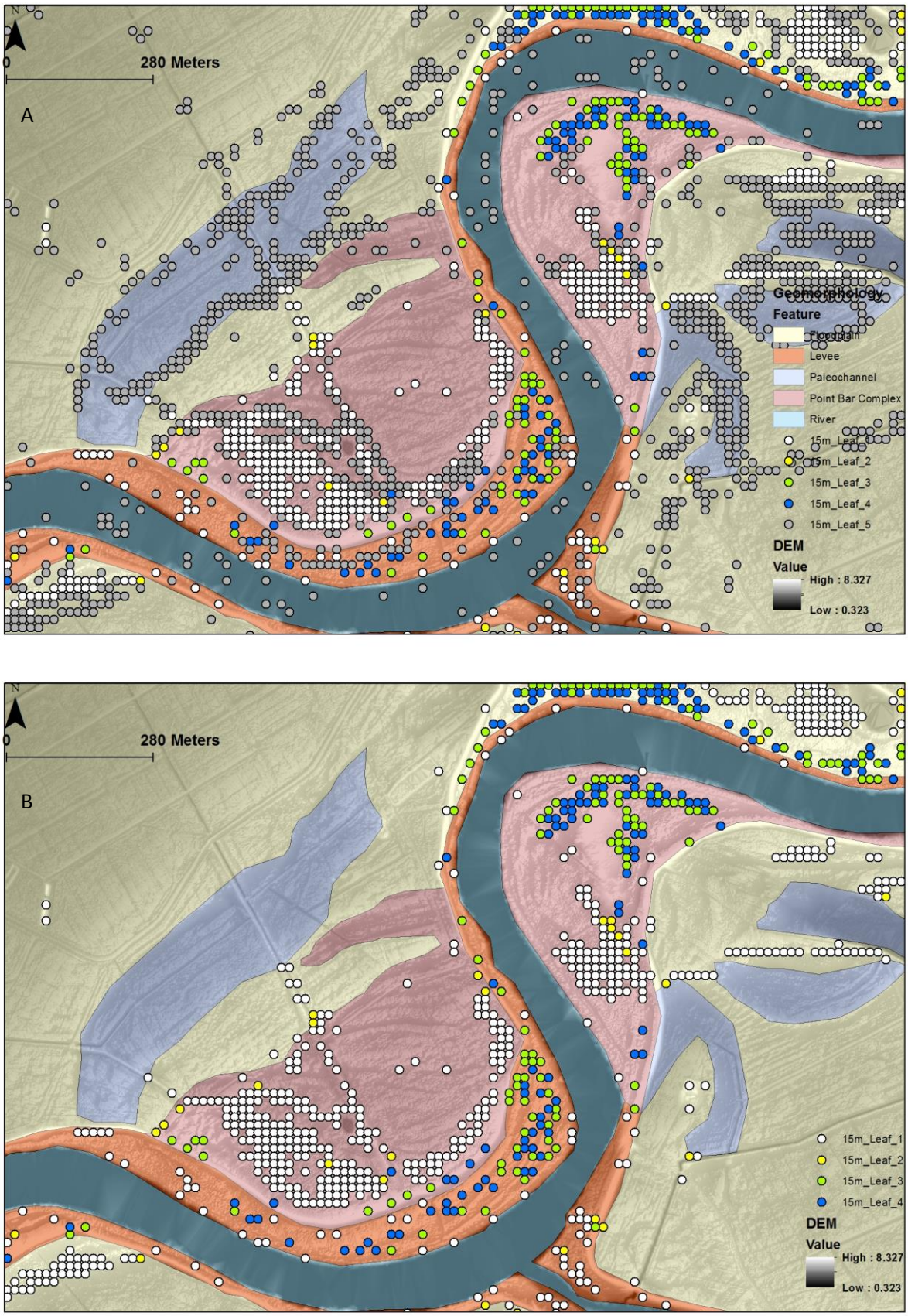

Figure 7. 11 Application of the 15 m classifier at the Manawatu meander A) Application of all the positive leaves of the Marchand 15 m decision tree in Figure 7.4. Note Leaf 5 predicts liquefaction surface manifestation also in the river. The

latter needs to be removed; B) Application of the leaves from the Marchand 15 m decision tree except Leaf 5. See text for more details

Figure 7.12 is the output of the classifier tested at 20 m resolution. Panel A reveals that Leaf 3 predicts liquefaction throughout the whole study area, but also it predicts more abundant liquefaction on the edge of the paleochannel and also in association with other geomorphic features that are known for being liquefaction susceptible (levee and point bars). However, there is also evidence of many more locations of ejecta in the river and all around the floodplain without particular association with geomorphic features. Since Leaf n 3 does not show geomorphic validity it is removed from the final output of Figure 7.12 B.

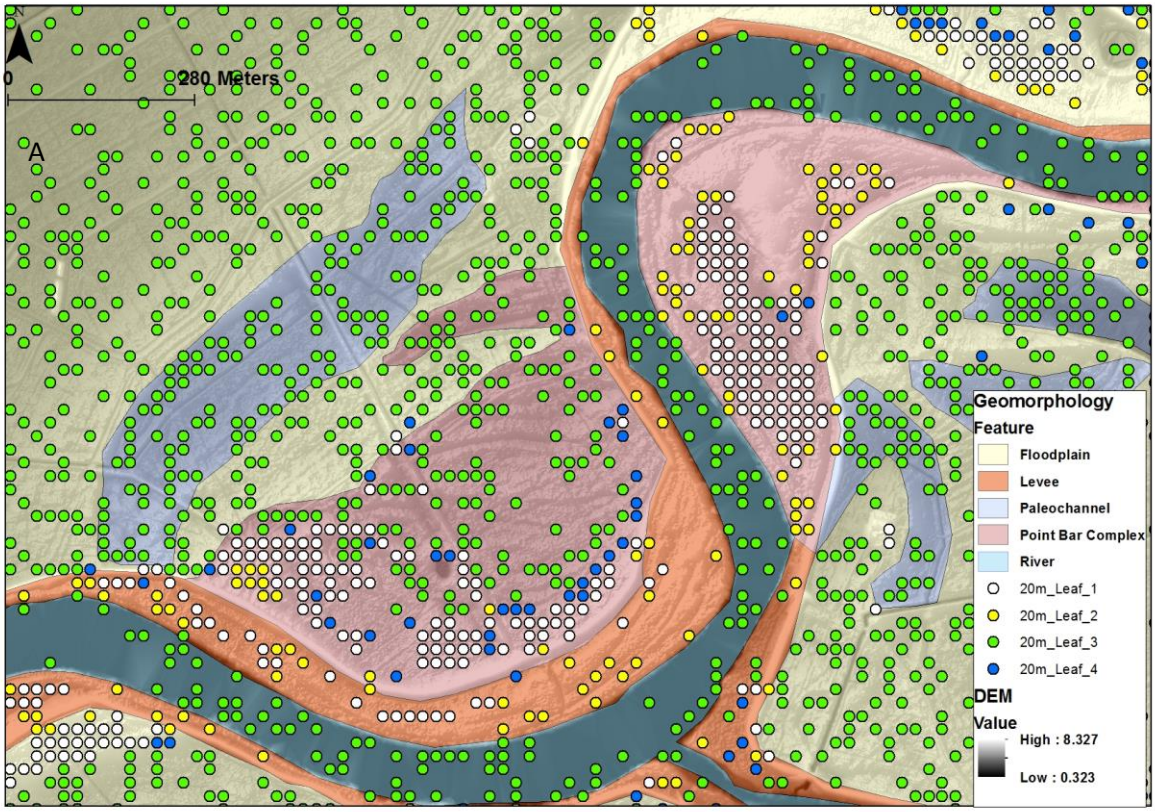

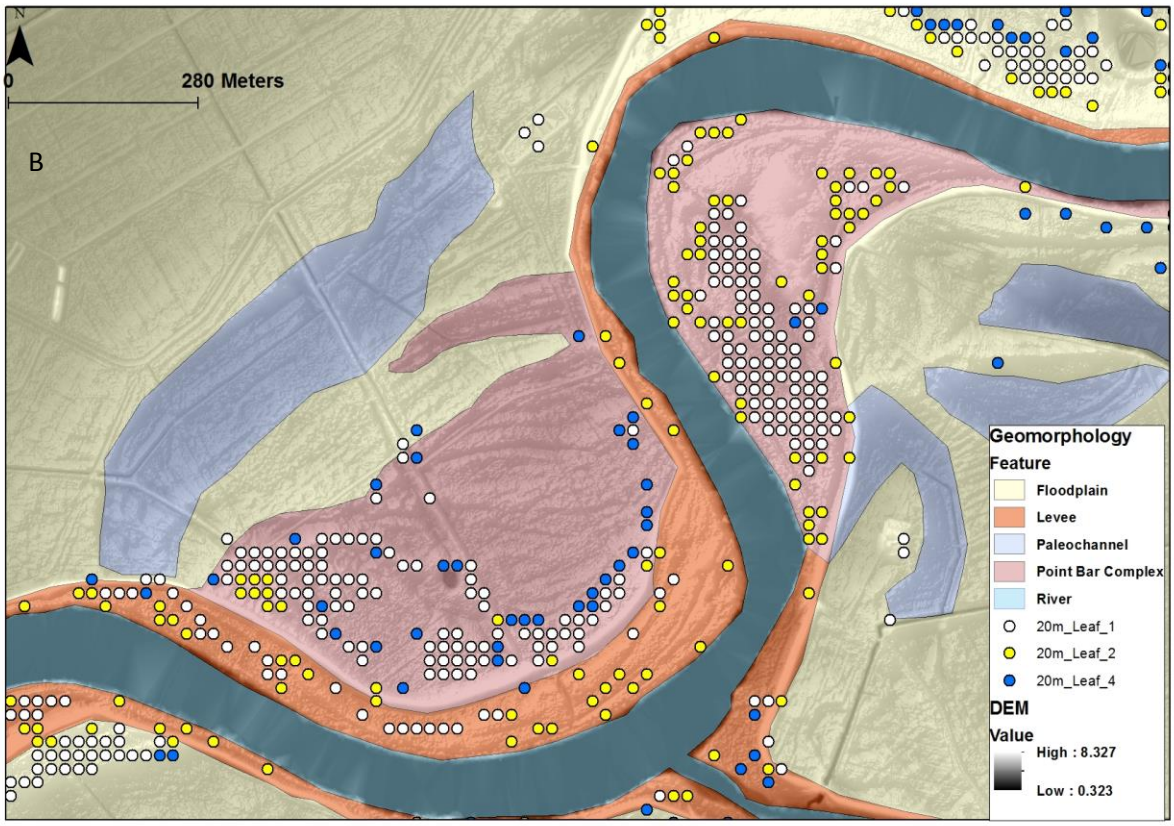

Figure 7. 12 Application of the 20 m classifier at the Manawatu meander detail: A) Testing of all the leaves from Figure 7.7 note that Leaf n 3 predicts liquefaction surface manifestation in the whole area; B) Testing of the 20 m classifier at the Manawatu river meander except Leaf n 3.

7.5 DISCUSSION

This chapter presents a preliminary investigation of the use of the Random Forest classification for determining whether or not landform morphometrics influence the liquefaction surface manifestation. Although several aspects of the model here presented need further improvement, the use of the Random Forest algorithm suggests an association between the micro topographic attributes and liquefaction ejecta. However, the results represent correlation not causation, and it may be that the direct controls on the spatial pattern of liquefaction ejecta are the availability of liquefiable sediment at an appropriate depth, water table conditions and the nature of the surface soils. Nonetheless, the findings are consistent with the hypothesis that surface gravitational stresses control paths for liquefaction ejection (Caputo, 2005), leading some parts of the landform to show greater liquefaction surface manifestation than others.

In a 2-D modelling study of topographic influences on subsurface stress fields Martel et al. (2016) showed that pure gravitational stresses related to topography lead to horizontally oriented compressive stresses on ridges and horizontally oriented tensional stresses in valley bottoms in landscapes of low relief. This may suggest that liquefaction-induced loss of subsurface shear strength could lead to a propensity for cracking and ejection of sediment in the low elevation parts of the landscape. However, these authors also show that where tectonic compressional forces dominate gravitational forces the pattern of tensional and compressive stresses change. Under this condition ridges become zones of vertical tension, while valleys become compressive. An outcome could be the formation of sheeting cracking planes subparallel to the land surface over the ridge, the latter potentially forming sediment flow pathways (dikes). Moon et al. (2017) extended this kind of modelling work to three dimensions and showed that the shape and thickness of the subsurface zone prone to fracturing was dependent on firstly, the ratio of tectonic to gravitational stresses and, secondly, the curvature of the overlying topography; more highly curved parts of the landscape had thicker zones of fracturing, and those zones were thickest near ridges and thinnest under valleys. Although these studies assumed isotropic rock masses and constant tectonic stresses they suggest possible important interactions between topography and imposed external stresses that could provide insights into subsurface fracturing patterns relevant to understanding how liquefied sediment vents to the surface. The appropriateness of the analogies drawn here to cyclical earthquake stresses remains an open question that would require rigorous geomechanical modelling outside the scope of the present research to answer.

7.5.1 Topographic predictors and the Random Forest model

In general it appears that the resolution of the topographic parameters control the sensitivity of the classification but not the parameters involved in making the predictions. In other words, both the Hardwick and Marchand models used the same predictors, and they all played a similar role in the model design. Elevations and slopes are the main predictors, followed by profile and plan curvature,

across all the resolutions used. The range of values for the micro-topographic parameters across the two study sites is listed in Table 7.3.

TABLE 7. 3 Maximum and minimum values with mean for each of the topographic parameters observed.

Resolution	Elevation	Slope	Profile Curvature	Plan Curvature
10 m	[1.96,8.41]mean 5.18	[0,18.39] mean 1.29	[-4,+7] mean -0.01	[-6, +4.88] mean -0.01
15 m	[1.97,8.94]mean 5.42	[0,11.43] mean 0.99	[-2.6, +3.11] mean -0.01	[-3.23, +1.84] mean -0.01
20 m	[2.05,8.7] mean 5.31	[0,8.57] mean 0.81	[-1.30, 1.92] mean -0.01	[-1.83, +1.22] mean -0.01

Table 7.3, when compared with Table 7.1 and 7.2 or with the cumulative frequency distribution curves shown in Figure 7.3, brings to light that the threshold values of the micro-topographic parameters correlated with liquefaction ejecta are close to the mean of the distribution for all the parameters used.

Qualitatively, the classifier at 10 m resolution is the most geomorphically plausible predictor of liquefaction surface manifestation (see Manawatu site application in Figure 7.10). All the leaves from the 10 m classifier predict ejecta on alluvial geomorphic features known for being liquefaction susceptible (scroll bars and more in general inner meander bend) (Holzer et al., 2010). The testing of the classifier at 15 and 20 m resolution revealed that some of the prediction did not have geomorphic validity. However, only the minority of the prediction was implausible as for each test most of the leaves issued a reasonable geomorphic prediction.

7.5.2 General model performance

The ROC parameters and the confusion matrix provide an estimates of how well the model is performing. The values of ROC and confusion matrix suggest the models calibrated at Hardwick and Marchand sites are working well (see Appendix A 13). However, the testing of the Marchand classifier at Hardwick site and vice versa (Figure 7.8 A and B) revealed a large over estimation of liquefaction ejecta at the two study sites. Two possible explanation can be the cause of this type of outcome.

The first explanation is that a large overestimation of surface manifestation of liquefaction may be influenced by the different geomorphic setting characterizing the two study areas. For example, the geomorphology of the Hardwick site features a crevasse splay burying a paleomeander and its related paleo-point bars, while the Marchand site features point bar deposits. The model does not contain any explicit geomorphic information. Although the hypsometric curves of the two training sites do not outline major differences, the geomorphic features of the two sites are different. The differences in the geomorphology may then be one of the causes for the over estimation of liquefaction ejecta at Hardwick and Marchand sites. Other CES sites different to Hardwick and Marchand could be used for further testing.

The second explanation is that the classifier resulting from Hardwick and Marchand incorporates the effects of the SMOTE techniques (Chawla et al., 2002), which (positively) alters the original number of liquefaction pixel already in the training dataset in favour of a more balanced dataset. Consequently, further investigation is required on how the model was built and a better understanding of the site-specific interactions with liquefaction surface ejecta is needed.

7.5.3 Application to a new site

The application at Manawatu River area shows that all models (i.e. at different resolutions) predict the scroll bar and natural levee landforms as sites susceptible to liquefy and be affected by surface ejecta, in line with the literature (Alessio et al., 2013; Civico et al., 2015; De Martini et al., 2015; Tuttle, 2001a; Tuttle et al., 2006; Tuttle and Atkinson, 2010; Tuttle et al., 1999; Tuttle and Hartleb, 2012a; Tuttle et al., 2005) and the findings of Chapter 3. In contrast, the abandoned paleochannels are never identified as potential locations for liquefaction surface manifestation at any of the topographic resolutions employed. From a sedimentology perspective, abandoned meanders are characterized by clay-rich sediment (clay-plug, see reference Ricci-Lucchi, 1980), which notably reduces the liquefaction susceptibility. From a topographic perspective the paleochannels are characterized by a much lower elevation and a general concave shape at the surface (positive values for profile curvature and negative values for plan curvature), a more potentially stable surface (Talebi et al., 2008) less

susceptible to cracking and thus less prone to allow sediment to come up at the surface. However, the ostensible plausibility of the results is not enough to definitively prove that the model is robust and that it can be used for predicting where liquefaction ejecta will occur, or have occurred in the past.

7.5.4 Limits of the Random ForestForest algorithm to predict the liquefaction ejecta

One of the limitations of this Random ForestForest application is the use of only four attributes (elevation, slope, profile and plan curvature) for predicting the surface manifestation of liquefaction. In the Random Forest application here presented, PGA (peak ground acceleration), water table, and distance from the epicentre are not considered as predictors for the model because these variables were either unknown (e.g. water table) or essentially invariant over the small study area (P.G.A., distance from epicentre). In order to test more parameters as predictors of liquefaction ejecta and thus to improve the preliminary model presented in this chapter, it is suggested the selection of a wider study area (e.g. the whole Halswell River, where there is a wealth of geotechnical data available) and the use of relative, rather than absolute, elevation (Sumfleth and Duttmann, 2008) to generalize the application of this model. Across a wider area, PGA values, along with other derived predictors (shear wave velocity, shear modulus and differences in sedimentary settings) would vary and hence be potentially suitable as predictors for the classifier.

In summary, the Random Forest classifier applied to microtopographic parameters shows some potential for being used in an automated prediction of liquefaction surface manifestation. Some tests of the Random Forest algorithm have identified specific geomorphic features as liquefaction prone areas. However, the study does not systematically succeed in identifying these sites, or over-predicts liquefaction occurrence. Finally, this new method may provide necessary but not sufficient conditions for occurrence of liquefaction ejecta, and, therefore, it will not replace other important tools such as geomorphic mapping based on LIDAR and analysis of old aerial photos and subsurface geological, geotechnical and groundwater models for locating study sites for paleoliquefaction investigations.

7.6 CONCLUSION

- Despite the limited modelling undertaken, Random Forest machine learning identifies significant relationships between microtopography and the presence or absence of liquefaction ejecta in a fluvial floodplain setting. The microtopographic control on surface manifestation of liquefaction supports the idea of gravitational stress control for the liquefaction ejection paths as proposed by Caputo (2005).
- Across a range of topographic resolutions, elevation, slope and plan or profile curvature are ranked in that order of decreasing importance for predicting ejecta presence.
- Random Forest trees effectively identify positive relief landforms such as crevasse splays, levees and scroll bars as being the landforms favoured for ejecta occurrence.
- The classifiers do not appear to be systematically identifying elements of landforms with particular topographic characteristics that make them prone to tensional stresses, lateral spreading and consequent ejection of fluidised sediment.
- The training dataset at 10 m resolution resulted in the best prediction of surface manifestation of liquefaction, however a higher dataset resolution (e.g. smaller pixel size of 5 m or 1 m, in relation to the computational efficiency that is available) is suggested, in order to improve the accuracy of the model and reduce the predictions that are not geomorphically plausible.
- A 10 m-resolution Random Forest model trained on a site characterized by point bars geomorphology (the Marchand site) produced a plausible liquefaction distribution when applied to a meander of the Manawatu floodplain with similar geomorphology.
- Although showing promising initial results, the Random Forest model presented is only preliminary and it needs further improvement in the model design to be more robust in its predictions.

8 SUMMARY AND CONCLUSIONS

This thesis presents a detailed analysis of liquefaction surface manifestation, stratigraphy and sedimentology of the alluvial and coastal settings of the Canterbury Plains affected by liquefaction during the Canterbury Earthquake Sequence (2010-2011 CES). The aim of the work has been to support future studies targeting paleoliquefaction and draws the following conclusions.

8.1 Sedimentary environments

- The liquefaction features in the Canterbury Plains were associated with Holocene alluvial and coastal landforms characterized by soil types of recent age (700-2400 years) with poor or imperfectly drained conditions (Chapter 2). The liquefaction ejecta in the alluvial setting is expressed mainly as coalescencing sand blows along fissures aligned following the trend of point bar deposits and the channel current direction, while in the coastal setting the liquefaction ejecta appeared to have a rounded or subrounded shape and no defined orientation or pattern (Chapter 4 and 5).
- The understanding of the architecture of the sedimentary environment was critical to comprehending why liquefaction surface manifestation corresponds to specific geomorphic features, and what is the origin of the liquefaction susceptibility. The case study of this dissertation suggested that subsurface liquefaction can occur in different areas of the floodplain even with no surface manifestation. However, paleochannel and point bar deposits are the main source of liquefaction ejecta owing to their fine to very fine texture, water saturation and sedimentary architecture that facilitates ejection of liquefying sand. Also, the study sites analysed in this research showed that areas with an impermeable crust or with a slightly higher elevation (such as crevasse splays, point bar ridges) may be more prone to show liquefaction at the surface (Chapter 3). The liquefaction source layer in the alluvial setting undergoes substantial sorting when sediment is mobilised by liquefaction. River sediment is characterized by multimodal grain size distribution (Chapter 3); however sand blow grain size samples are relatively well sorted (homogeneous clean fine and very fine sand). Moreover,

sand blows are sorted than dikes because the sediment ejected at the surface leaves behind the coarser grains, and also the winnowing effect of the water ejected during the liquefaction process allows removal of fine sediment (silt and clay). In dikes and sills the liquefaction sorting process is less pronounced; therefore the original grain size subpopulations of the source layer are more preserved. The samples from dikes and sills are better candidates for the analysis of the properties of the source layer. This different degree of sorting has implications in the use of the Tsuchida's (1970) liquefiable soil thresholds as explained below. The fabric of liquefied sand (Chapter 6) also revealed the sorting process during remobilization and ejection . In particular, the thin section analysis showed that within a liquefaction dike there is a grain size gradient from the core to the edge of the dike caused by different flow regimes within the dike (Chapter 6).

- The depositional setting of the alluvial environment characterized by cut and fill, and lateral and vertical accretion can create a complex stratigraphy and multiple source layers (of fine sand and silty sand) susceptible to liquefaction.
- The grain size analysis of samples from cores and trenches confirmed that multiple liquefaction sources are possible, in both alluvial and coastal settings but not all of them may provide sediment for surface ejecta.
- The area of surface manifestation of liquefaction does not outline the extent of the liquefaction source layer or of the liquefaction process in the subsurface. As observed at many study sites, liquefaction features were exposed in the form of sills or blisters or dikes not surfacing, and only visible when a trench was excavated.
- The features found in the alluvial setting of the Canterbury Plains consisted of liquefaction dikes, sand blows, fissure with coalescing sand blows aligned subparallel to river features, rare blisters and abundant lateral spreading (this study and, Almond et al., 2010a; 2012; Bastin et al., 2015; 2016; Tuttle et al., 2017 ; Villamor et al., 2016).

- The unique set of liquefaction features found in the coastal setting included: A horizon splitting, pillow like structures, and blister-collapse systems. Documentation of these features was undertaken for the first time in the coastal setting of the Canterbury Plains, and in particular after the Valentine's Day Earthquake of February 2016 (Chapter 4). The Valentine's Day Earthquake was a fortuitous event, which helped to improve the understanding of the genesis of most of the liquefaction features in the coastal setting.
- Liquefaction features in the coastal setting, in particular at Featherston Avenue Reserve, were associated with interdune deposits, whereas on the dune ridges of the same area, no liquefaction ejecta were observed. No association between liquefaction ejecta and geomorphic features was obvious at the coastal sites studied in the Christchurch urban area (e.g. Wainoni and QEII park), possibly because of intensive recontouring of the land surface.
- The source of the liquefaction features in the coastal setting was very close to the ground surface (near-surface liquefaction), in most cases within 1 m depth. The trenches, along with the visual inspection of cores and grain size analysis, showed that the source layer for surface ejecta was coastal dune sand, but alluvial sand liquefied at depth.
- The surface pattern of liquefaction features in the coastal setting is a consequence of a shallow water table and of better sorted sandy sediment typical of the dune environment. The lack of a thick crust and of fine grains (silt and clay) in the coastal dune sediment prevent the build-up of very high water pressure. As a consequence, the water can vent easily through the sediment. The A horizon of the coastal dune setting is cohesionless and very weak (Chapters 4 and 5), which facilitates the liquefied sand from the B or C horizon to disrupt the A horizon fabric, forming low angle sills or lenses of A horizon (Chapter 4 and 5).
- The thin section (micromorphological) analysis was considered a valid post field work technique to corroborate the stratigraphic interpretation and to determine the different generations of liquefaction identified in the trenches. The micromorphological analysis of the modern liquefaction fabric of both alluvial and coastal sediment is characteristically single

grains with no presence of textural and organic pedofeatures. In contrast, paleoliquefaction features are characterized by a bridged or pellicular microstructure with common presence of textural and organic pedofeatures. The paleoliquefaction features discovered at the study sites investigated by this research revealed paleoliquefaction features at Wainoni and QEII Parks. The age of the paleoliquefaction features at Wainoni Park was AD 1666-1803. However, no age constraints were established for the QEII Park site. At Featherston Avenue Reserve it was particularly challenging to distinguish paleoliquefaction features since the high liquefaction susceptibility of this site and the stratigraphic disruption caused by the liquefaction features created potential superimposition of multiple liquefaction events.

<u>In conclusion, what are the best places to target for finding paleoliquefaction features?</u>

- The research presented showed that the coastal setting, due to a shallower water table and well sorted sandy sediment, is too susceptible to liquefaction. The soil stratigraphy of the coastal sites affected by liquefaction results in a soil profile very disrupted (multiple events of liquefaction means overlapping of different generations of A horizon splitting, collapse features or blisters not distinguishable) which will make the recognition of paleoliquefaction features particularly challenging. The frequency and magnitude of depositional events is also less conducive to creating stratigraphic settings in which relative and numerical ages of paleoliquefaction features can be established (c.f. the alluvial setting, below).

In contrast, the alluvial setting is a better place for looking for paleoliquefaction features. The reasons are as follows:

- Amongst the sandy layers deposited on a floodplain, some can be characterized by a higher content of fines (silt and clay) which prevents the liquefaction susceptibility;
- On a floodplain a high frequency of flooding generates relatively thin volume of sediment superposed on each other. Injection (dikes and sills) and ejections (sand blows or blisters) of sediment during liquefaction episodes has a high chance of being embedded by depositional

event showing clear cross cutting relations with soil sedimentary features. Also wet floodplain environments conducive to liquefaction host abundant organic material that can be dated by ^{14}C. The alluvial study case showed also that point bar deposits of sandy bed rivers with bed-load channel deposits are good source of potential liquefaction sediment.

8.2 Techniques

With regard to the techniques used to investigate the liquefaction features in alluvial and coastal setting, this research leads to the following conclusions.

- The acquisition of LiDAR elevation data is critical to study the geomorphology of areas affected, or that can be affected, by liquefaction and investigate subtle changes of topography that may be relevant for liquefaction surface manifestation. In order to use this research and best target places for paleoliquefaction investigation, it is recommended to select areas with a LiDAR existing coverage or fly new surveys.
- The paleoseismic trench is the premier tool to investigate liquefaction features and study the stratigraphy as it fully exposes them. However, in the coastal setting the shallow water table limited excavation to shallow depths. This limit was partially solved by hand-dug pits in proximity of the trenches. Hand-dug pits were useful to understand the stratigraphic variations that were not exposed in the trenches. In places with high water table, supporting information can be extracted from cores as they can be analysed for soft sediment deformation, and deeper sedimentary architecture and properties. Two-dimensional high resolution GPR (400 to 1500Hz) was confirmed as an important tool to detect changes in sediment geophysical properties and define the uppermost stratigraphic units such as crevasse splay at Hardwick site and point bar architecture (Chapter 3) at Marchand, but high water table conditions limit its use for deeper sections (Villamor et al., 2016; 2014). The 3D GPR was a valid tool to image the subsurface anomalies caused by liquefaction. In the study case presented here the 3D GPR improved the efficiency of the trenching campaign, since it

accurately localized the liquefaction features at various depths (between 0.25 and 1.25 m below the ground) (Chapter 3).

- This research suggests that Tsuchida's (1970) boundaries may not be representative of certain liquefiable soil types. Tsuchida's (1970) soil boundaries are derived from sand that has already experienced liquefaction (mainly sand blows) and thus has undergone substantial grain size sorting (Koester and Tsuchida, 1989). Therefore they do not include liquefiable soil types that contain a larger component of silt (e.g. silty sand in the alluvial setting) and that can also experience liquefaction, as shown in Chapter 3.
- The mixdist analysis (Du, 2002) was tested to analyse liquefiable sediment for the first time in this thesis. The analysis can successfully identify the liquefiable source layer characteristics and its stratigraphic location by comparing the grain size distribution of liquefied sediment collected at the surface or exposed in the trench (sand blows, dikes and sills) with the grain size distribution of sediment in the core (similarity metric, Chapter 2) regardless of sorting effects during liquefaction. These results have been corroborated by a new compositional data analysis (Aitchison, 2011; Hodge, 2016).

8.3 Future Studies

- Improve the Random Forest algorithm to have a more reliable and robust prediction of places to target paleoliquefaction investigation. For example, it is suggested to use a wider training area and relative elevation to make a better classification.
- Use the micromorphology technique to assess which parts of the deeper sediment as revealed in cores liquefied. The scope of this study was to define the microfabric of liquefied soils and assess whether or not this technique can be used as a diagnostic tool. Now that this study has proven the validity of the technique, it can be applied to the cores to assess which core sections liquefied. This can be an additional tool to the visual

inspection of core (identification of soft sediment deformation), grain size and sCPT analysis.

- Further integration of techniques and additional ones (e.g., CT scanning of cores) with a more in depth analysis of sCPT. In particular, a better understanding of the sediment properties along a core, and knowing what specific layers liquefied, could help to discriminate the meaning of the sCPT parameters and perhaps help refine sCPT data interpretations; sCPT is quick and economic but has not given a refined result in this study. More studies will be needed to be able to integrate the geological results (sediment properties, presence of liquefaction) with geotechnical parameters.
- Use the micromorphology techniques to improve the understanding with regards to the weathering of the liquefaction features occurring in different type of settings (alluvial/coastal/estuarine) and also in relation to the age of the sediment (Holocene vs late Pleistocene liquefaction features).
- Use the knowledge gathered in this research to refine the magnitude-bound relations (Castilla and Audermard, 2007; Galli, 2000; Olson et al., 2005b; Papadopoulos and Lefkopoulos, 1993; Papathanassiou et al., 2005; Pirrotta et al., 2007) for liquefaction surface manifestation, in order to improve the liquefaction susceptibility maps throughout New Zealand and elsewhere.

8.3 REFERENCE LIST

Aitchison, J., 2011, A concise guide to compositional data analysis, Department of Statistics University of Glasgow, 134 p.:

Al-Shukri, H., Mahdi, H., and Tuttle, M. P., 2006, Three-Dimensional Imaging of Earthquake-induced liquefaction features with Ground penetrating Radar near Marianna, Arkansas: Seismological research letters, v. 77, no. 4.

Alessio, G., Alfonsi, L., Brunori, C. A., Burrato, P., Casula, G., Cinti, F. R., Civico, R., Colini, L., Cucci, L., De Martini, P. M., Falcucci, E., Galadini, F., Gaudiosi, G., Gori, S., Mariucci, M. T., Montone, P., Moro, M., Nappi, R., Nardi, A., Nave, A., and Pantosti, D., 2013, Liquefaction phenomena associated with the Emilia earthquake sequence of May–June 2012 (Northern Italy): Natural Hazards and Earth System Sciences, v. 13, p. 935–947.

Alfaro, P., Estevez, A., Moretti, M., and Soria, J.-M., 1999, Sedimentary deformation structures interpreted as seismites in the Quaternary of the Low Segura basin (Eastern Betic Cordillera): Comptes rendus de l' academie des sciences serie ii fascicule a-sciences de la terre et des planetes, v. 328, no. 1, p. 17-22.

Alfaro, P., Galindo Zaldívar, J., Jabaloy, A., López-Garrido, A. C., and Sanz de Galdeano, C., 2001 Evidence for the activity and paleoseismicity of the Padul fault (Betic Cordillera, southern Spain): Acta Geológica Hispánica, v. 36, no. 3, p. 283-295.

Alfaro, P., Gibert, L., Moretti, M., Garcia-Tortosa, F. J., de Galdeano, C. S., Galindo-Zaldivar, J., and Lopez-Garrido, A. C., 2010, The significance of giant seismites in the Plio-Pleistocene Baza paleo-Lake (S Spain): Terra Nova, v. 22, p. 172-179.

Allen, J. R. L., 1982, Sedimentary structures, their character and physical basis New York, Elsevier.

-, 1985, Principles of Physical Sedimentology, University of Reading, Springer, Dordrecht.

Almond, P., Shanhun, F., Eger, A., and Wilson, T., 2010a, Liquefaction in the Tai Tapu – Greenpark areas, Selwyn District following the 4 September Darfield (Canterbury) Earthquake: Patterns, sources of liquefiable materials, and remediation: In: Eccles, J.D., Grigor, M.R., Hoskin, P.W.O. and Hikuroa, D.C.H. (Editors). GeoNZ 2010 Conference, The University of Auckland, v. Geoscience Society of New Zealand, Miscellaneous Publication no. 129A.

Almond, P., Villamor, P., Tuttle, M., Langridge, R., Clark, K., Eger , A., Bastin, S., Quigley, M., Barker, P., and Vandergoes, M., Liquefaction induced by the 2010-2011 Canterbury earthquake sequence and implications from recently discovered paleoliquefaction features, *in* Proceedings GSA Annual meeting, 4-7 November Charlotte North Caroline, 2012.

Almond, P., Wilson, T., Shanhun, F. L., Whitman, Z., Eger, A., Moot, D., Cockcroft, M., and Nobes, D., 2010b, Agricultural land rehabilitation following the 2010 Darfield (Canterbury) Earthquake: A preliminary report. : Bulletin of the New Zealand Society for Earthquake Engineering, v. 43, no. 4, p. 432-438.

Ambraseys, N. N., 1988, Engineering seismology: Earthquake Engineering and Structural Dynamics, v. 17, p. 1-105.

Amick, D., Gelinas, R., Maurath, G., Cannon, R., Moore, D., Billington, E., and Kemppinen, H., 1990, Paleoliquefaction features along the Atlantic Seabord: Division of Engineering Office of Nuclear Regulatory Research U.S Nuclear Regulatory Commission Washington DC 20555 NRC FIN D1682.

Andrus, R. D., and H., S. K., 2000, Liquefaction Resistance of Soils from Shear-Wave Velocity: Journal of Geotechnical and Geoenvironmental Engineering, v. 126, no. 11, p. 1015-1025.

Andrus, R. D., Hayati, H., and Mohanan, N. P., 2009, Correcting liquefaction resistance for aged sands using measured to estimated velocity ratio: Journal of Geotechnical and Geoenvironmental Engineering, v. 135, no. 6, p. 735-744.

Anggraeni, D., 2010, Modelling the impact of topography on seismic amplification at regional scale [Master of Science in Geo-Information Science: ITC.

Anketell, J. M., Cegla, J., and Dzulinsky, S., 1970, On the deformational structures in systems with reversed density gradients: Annales de la Societe Geologique de Pologne, v. 40, p. 3-30.

Arango, I., Lewis, M. R., and Kramer, C., 2000, Update liquefaction potential analysis eliminates foundation retrofitting of two critical structures: Soil Dinamics Earthquake Engineering, Elsevier limited, v. 20, p. 17-25.

Arango, I., and Migues, R. E., 1996, Investigation of the seismic liquefaction of old sand deposits: Report on Research, Betchel Corporation, National Science Foundation Grant No CMS 94 16169 San Francisco, CA.

Bannister, S., and Gledhill, K., 2012, Evolution of the 2010-2012 Canterbury earthquake sequence, New Zealand: Journal of Geology and Geophysics, v. 55, no. 3, p. 295-304.

Bannister, S. C., Fry, B. l., Reyners, M. E., Ristau, J., and Zhang, H., 2011, Fine-scale relocation of aftershocks of the 22 February M2 6.2 Christchurch Earthquake using double-difference tomography: Seismological research letters, v. 82, no. 6, p. 839-845.

Barnes, P. M., Castellazzi, C., Gorman, A., and Wilcox, S., 2011, Submarine faulting beneath Pegasus Bay, offshore Christchurch. Short-term Canterbury Earthquake Recovery Project 2: Offshore faults.: National Institute of Water & Atmosphere (NIWA)

Barrell, D. J. A., 2015, Geomorphological map of the eastern Canterbury area. IN Begg, J.G.; Jones, K.E.; Barrell, D.J.A. 2015: Geology and geomorphology of urban Christchurch and eastern Canterbury. GNS Science Geological Map 3. : GNS Science.

Basher, D. J. A., Litchfield, N. J., Townsend, D. B., Quigley, M., Van Dissen, R. J., Cosgrove, R., Cox, S. C., Furlong, K., Villamor, P., Begg, J. G., Hemmings-Sykes, S., Jongens, R., Mackenzie, H., Noble, D., Stahl, T., Bilderback, E., Duffy, B., Henham, H., Klahn, A., Lang, E. M. W., Moody, L., Nicol, R., Pedley, K., and Smith, A., 2011, Strike-slip ground surface rupture (Greendale Fault) associated with the 4 September 2010 Darfield Earthquake, Canterbury, New Zealand: Quarterly Journal of Engineering Geology and Hydrogeology, v. 44, p. 283-291.

Basher, L. R., Hicks, M. D., McSaveney, M. J., and Whitehouse, I. E., 1988, The lower Waimakariri River Floodplain: a geomorphological perspective: Division of Land and Soil Sciences Department of Scientific and Industrail Research.

Bastin, S., Quigley, M., and Bassett, K., 2015, Paleoliquefaction in Eastern Christchurch, New Zealand: Geological Society of America Bullettin v. 127, no. 9-10, p. 1348-1365.

Bastin, S. H., Bassett, K., Quigley, M. C., Maurer, B., Green, R. A., Bradley, B., and Jacobson, D., 2016, Late Holocene Liquefaction at Sites of Contemporary liquefaction during the 2010-2011 Canterbury Earthquake Sequence, New Zealand: Bullettin of Seismological Society of America, v. 106, no. 3, p. 881-903.

Beaven, J., Fielding, E., Motagh, M., Samsonov, S., and Donnelly, N., 2011, Fault location and slip distribution of the 22 February 2011 Mw 6.2 Christchurch, New Zealand, earthquake from geodetic data: Seismological Research letters, v. 82, no. 6, p. 789-799.

Beaven, J., Motagh, M., Fielding, E. J., Donnelly, N., and Collett, D., 2012, Fault slip models of the 2010-2011 Canterbury, New Zealand, earthquakes from geodetic data and observations of postseismic ground deformation. : New Zealand Journal of geology and Geophysics v. 55, no. 3, p. 207-221.

Beetham, D., Begg, J., Barker, P., Levick, S., and Beetham, J., 2011, Assessment of liquefaction and related ground failure hazards in Palmerston North, New Zealand: GNS Science consultancy report 2011/108, v. July 2011.

Begg, J. G., and Johnston, M. R., 2000, Geology of the Wellington area. Institute of Geological and Nuclear sciences 1:250000 geological map 10.1 sheet+64p Lower Hutt, New Zealand.

Begg, J. G., Jones, K. E., and Barrell, D. J. A. c., 2015, Geology and geomorphology of urban Christchurch and eastern Canterbury GNS Science.

Berrill, J. B., Mulqueen, P. C., and Ooi, E. T. C., 1994, Liquefaction at Kaiapoi in the 1901 Cheviot, New Zealand, earthquake Bullettin of the New Zealand national society for earthquake engineering, v. 27 no. 3, p. 178-190.

Berryman, K., 2012, Geosciences as a component of response and recovery from the Canterbury earthquake sequence of 2012-2011: New Zealand Journal of Geology and Geophysics v. 55, no. 3, p. 313-319.

Berryman, K., Cooper, A., Norris, R., Villamor, P., Sutherland, R., Wright, T., Schermer, E., Langridge, R., and Biasi, G., 2012, Late Holocene Rupture History of the Alpine Fault in South Westland, New Zealand: Bullettin of the Seismological Society of America, v. 102, no. 2, p. 620-638.

Birkeland, P. W., 1999, Soils and Geomorphology, 198 Madison Avenue, New York, 10016, Oxford University Press.

Blake, G. J., 1964, Coastal Progradation in Pegasus Bay Unpublished Master thesis, lodged in the Library, University of Canterbury, Christchurch.

-, 1968, The rivers and the foreshore sediment of Pegasus Bay, South Island, New Zealand: New Zealand Journal of Geology and Geophysics, v. 11, p. 225-235.

Blott, S. J., and Pye, K., 2001, Gradistat: A grain size distribution and statistics package for the analysis of unconsolidated sediments: Earth Surface Processes and Landforms, v. 26, p. 1237-1248.

Boulanger, R. W., and Idriss, I., M., 2014, CPT and SPT Based Liquefactin Triggering Procedures: University of California, Davis, CA.

Brackley, H. L., Almond, P., Barrell, D. J., Begg, J., Berryman, K., Christensen, S., Dellow, G., Fraser, J., Grant, H., Harwood, N., Irwin, M., Jacka, M., Jones, K., Lee, J., McCahon, I., McMorran, T., Scott, D., and Townsend, D., 2012, Review of liquefaction hazard information in eastern Canterbury, including Christchurch City and parts of Selwyn, Waimakariri and Hurunui Districts: GNS Science Consultancy Report 2012/218, 99p.

Bray, J., Cubrinovski, M., Zupan, J., and Taylor, M., 2014, Liquefaction effects on buildings in the central business district of Christchurch: Earthquake Spectra, v. 30, no. 1.

Breiman, L., 1996, Bagging Predictors: Machine Learning, v. 24, p. 123-140.

-, 2001, Random Forests: Machine Learning, v. 45, p. 5-32.

-, 2004, Consistency for a simple model of Random Forest: University of California.

Breiman, L., Friedman, J. H., Olshen, R. A., and Stone, C. J., 1984, Classification and regression Trees: Wadsworth International Group.

Brewer, R., and Sleeman, J. R., 1960, Soil Structure and Fabric, their definition and description: Journal of Soil Science, v. 11, no. 1.

Brown, L. J., and Weeber, J. H., 1992, Geology of the Christchurch Urban Area.: Institute of Geological and Nuclear Science

Brown, L. J., Wilson, D. D., Moar, N. T., and Mildenhall, D. C., 1988, Stratigraphy of the late Quaternary deposits of the northern Canterbury Plains, New Zealand: New Zealand Journal of Geology and Geophysics, v. 31, no. 3, p. 305-335.

Browne, G. H., Field, B. D., Barrell, D. J. A., Jongens, R., Bassett, K. N., and Wood, R. A., 2012, The geological setting of the Darfield and Christchurch earthquakes: New Zealand Journal of Geology and Geophysics, v. 55, no. 3, p. 193-197.

Browne, G. H., and Naish, T. Y., 2003, Facies development and sequence architecture of a late Quaternary fluvial-marine transition, Canterbury Plains and shelf, New Zealand: implications for forced regressive deposits: Sedimentary Geology, v. 158, p. 57-86.

Bryant, G., Monegato, G., and Miall, A., 2013, An example of liquefaction-induced interdune sedimentation from the early Jurassic Navajo Sandstone USA: Sedimentary Geology, v. 297, p. 50-62.

Buckley, A., 2010, Understanding curvature rasters, Volume 2017, ArcGIS Blog.

Bullock, P., N. Fedoroff, Jongerius, A., Stoops, G., and Tursina, T., 1985, Handbook for soil thin section description, Mount Pleasant, Beamish Lane, Albrighton, Wolverhampton, WV7 3JJ, Waine Research Publication.

Caputo, R., 2005, Stress variability and brittle tectonic structures: Earth-Science Reviews, v. 70, no. 1-2, p. 103-127.

Caputo, R., Iordanidou, K., Minarelli, L., Papathanassiou, G., Poli, M. E., Rapti-Caputo, D., Sboras, S., Stefani, M., and Zanferrari, A., 2012, Geological evidence of pre-2012 seismic events, Emiliar-Romagna, Italy: Annals of Geophysics, v. 55, no. 4.

Casagrande, A., 1975, Liquefaction and Cyclic Deformation in sands: a critical review: Proceeding of the Fifth Pan American Conference in Soil Mechanics and Foundation Engineering, Buenos Aires, Argentina; also puyblished as Harward Soil Mechanics Series No 88 January 1976, Harward Univerisy, Cambridge, Massachusetts.

Castilla, R. A., and Audermard, F. A., 2007, Sand blows as a potential tool for magnitude estimation of pre-instrumental earthquakes: Journal of Seismology, v. 11, p. 473-487.

Castro, G., 1969, Liquefaction of sands, Harward University, Cambridge, Harvard Soil Mechanics Series.

Celebi, M., 1985, Topographical and geological amplifications determined from strong motion and aftershock records of the 3 March 1985 Chile earthquake: BSSA, v. 77, no. 4, p. 1147-1167.

CGD0200, 2013, Liquefaction interpreted from Aerial Photography.

Chan, M. A., and Bruhn, R. L., 2014, Dynamic liquefaction of Jurassic sand dunes: processes, origins and implications: Earth Surface Processes and Landforms, v. 39, p. 1478-1491.

Chawla, N. V., Bowyer, K. W., Hall, L. O., and Kegelmeyer, W. P., 2002, SMOTE: Synthetic Minority Over-Sampling Technique: Journal of Artificial intelligence research, v. 16, p. 321-357.

Chini, M., Albano, M., Saroli, M., Pulvirenti, L., Moro, M., Bignami, C., Falcucci, E., Gori, S., Modoni, G., Pierdicca, N., and Stramondo, S., 2015, Coseismic liquefaction phenomenon analysis by COSMO-SkyMed: 2012 Emilia (Italy) earthquake: International Journal of Applied Earth Observation and Geoinformation, v. 39, no. 2015, p. 1-14.

Christensen, S. A., 1995, Liquefaction of Cohesionless Soils in the March 2, 1987 Edgecumbe Earthquake, Bay of Plenty, NZ and other Earthquakes: Department of Civil Engineering University of Canterbury.

Civico, R., Brunori, C. A., De Martini, P. M., Pucci, S., Cinti, F. R., and Pantosti, D., 2015, Liquefaction susceptibility assessment in fluvial plains using airborne lidar: the case of the 2012 Emilia earthquake sequence area (Italy): Natural Hazards and Earth System Sciences, v. 15, p. 2473-2483.

Clayden, B., and Hewitt, A. E., 1994, Horizon Notation for New Zealand Soils, Lincoln New Zealand, Whenua Press, Landcare Research

Clement, A. J., Sloss, C. R., and Fuller, I. C., 2010, Late Quaternary geomorphology of the Manawatu coastal plain, North Island, New Zealand: Quaternary International, v. 221, p. 36-45.

Clough, B., 2005, Christchurch Liquefaction Study: Stage IV (addendum report): Environment Canterbury report U04/25/2 Beca, Carter, Hollings and Ferner Ltd, Christhchurch.

Cowie, J. D., and Kimpton, D. C., 1976, Soil map of Palmerston North city and environs, New Zealand. Part of NZ Soil Survey Report 24. Department of Scientific and Industrial Research. Wellington.

Cox, J. E., and Mead, C. B., 1963, Soil Evidence relating to post-glacial climate on the Canterbury Plains (Soil Bureau, Department of Scientific and Industrial): New Zealand Ecological Society, v. 10, p. 28-38.

Cox, S. C., Rutter, H. K., Sims, A., Manga, M., Weir, J. J., Ezzy, T., White, P. A., Horton, T. W., and Scott, D., 2012, Hydrological effects of the Mw7.1 Darfield (Canterbury) earthquake, 4 September 2010, New Zealand: Journal of Geology and Geophysics, v. 55, no. 3, p. 231-247.

Creeser, M., Killham, K., and Edwards, A., 1993, Soil Chemistry and its applications, The Pitt Building, Trumpington Street, Cambridge CB2, 40 West 20th Street, New York, NY 10011-4211 USA, Press Syndacate of the University of Cambridge

Csontos, R., and Van Arsdale, R., 2008, New Madrid Seismic zone fault geometry: Geosphere, v. 4, no. 5, p. 802-813.

Cubrinovski, M., Bray, J. D., Taylor, M., Giorgini, S., Bradley, B., Wotherspoon, L., and Zupan, J., 2011a, Soil liquefaction effects in the central business district during the February 2011 Christchurch Earthquake: Seismological Research Letters, v. 82, no. 6, p. 893-904.

Cubrinovski, M., Green, R. A. E., Allen, J., Ashford, S., Bowman, E., Bradley, B., Cox, B., Cubrinowski, M., Green, R., Hutchinson, T., Kavazanijan, E., Orense, R., Pender, M., Quigley, M., and Wotherspoon, L., 2010, Geotechnical Reconnaissance of the 2010 Darfield (Canterbury) Earthquake Bullettin of the New Zealand Society for Earthquake Engineering, v. 43, no. 4, p. 243-320.

Cubrinovski, M., Hughes, M., Bradley, B., McCahon, I., McDonald, Y., Simpson, H., Cameron, R., Christinson, M., Henderson, B., Orense, R., and O'Rourke, T., 2011b, Liquefaction impacts on pipe networks.

De Martini, P. M., Alfonsi, L., Brunori, C. A., Campagnoli, P., Cinti, F. R., Civico, R., Cucci, L., Gambillara, R., Livio, F., Michetti, A. M., Molisso, F., Pantosti, D., Pinzi, S., Pucci, S., and Venuti, A., 2015, Geological and geophysical approaches for the definition of the areas prone to liquefaction and for the identification and characterization of paleoliquefaction phenomena, the case of the 2012 Emillia Epicentral Area, Italy: Engineering Geology for Society and Territory, v. 5.

Dellow, G. D., Coote, T. P., and Beetham, R. D., 1994, Assessment of liquefaction induced ground failure susceptibility in the Manawatu-Wanganui region. Institute of Geological and Nuclear Sciences Clien report 333902.4D.ii, p. 31p.

Dietterich, T. G., 1998, Approximate statistical tests for comparing supervised classification learning algorithms: Neural Computation, v. 10, no. 7, p. 1895-1923.

Downes, G., Dowrick, G., Van Dissen, R., Taber, J., Hancox, G., and Smith, E., 2001, The 1942 Wairarapa, New Zealand Earthquakes: analysis of observational and instrumental data: Bulletin of the New Zealand Society for Earthquake Engineering, v. 34, no. 2.

Downes, G., and Yetton, M., 2012, Pre-2010 historical seismicity near Christchurch, New Zealand: The 1869 MW 4.7-4.9 Christchurch and 1870 Mw 5.6-5.8 Lake Ellesmere earthquakes. : New Zealand Journal of Geology and Geophysics, v. 55, no. 3, p. 199-205.

Downes, G. L., 1995, Atlas of isoseismal maps of New Zealand earthquakes. Institute of Geological and Nuclear sciences monograph 11, 304 p., Lower Hutt, New Zealand: Institute of Gelogical and Nuclear Sciences Limited.

Du, J., 2002, Combined Algorithms for fitting finite mixture distributions [M.Sc. project: McMaster University.

Earthquake, G. J., 2011, https://www.youtube.com/watch?v=DlhIHhadTqc: Japan, Youtube.

Elder, D. M. G., McCahon, I. F., and Yetton, M. D., 1991, The Earthquake Hazard in Christchurch: A detailed evaluation: Soils & Fundations Ltd, Christchurch. Report funded by the Earthquake Commission.

Fairless, G. J., and Berrill, J. B., 1984, Liquefaction during historic earthquakes in New Zealand: Bulletin New Zealand National Society for Earthquake Engineering, v. 17, no. 4.

Field, B. D., and Atkins, C., 2012, Characterization of fine grained sediment in the AND-2A drillhole core (southern McMurdo Sound, Antarctica) using QEMSCAN: GNS Science.

Fitzpatrick, E. A., 1984, Micromorphology of Soils, The University of Michigan, Chapman and Hall Ltd.

Fontana, D., Lugli, S., Marchetti Dori, S., Caputo, R., and Stefani, M., 2015, Sedimentology and composition of sands injected during the seismic crisis of May 2012 (Emilia, Italy): clues for source layer identification and liquefaction regime: Sedimentary Geology, v. 325, p. 158-167.

Gage, M., 1958, Late Pleistocene Glaciations of the Waimakariri Valley, Canterbury, New Zealand: New Zealand of Geology and Geophysics, v. 1, p. 123-155.

Galli, P., 2000, New empirical relationshipts between magnitude and distance for liquefaction: Tectonophysics, v. 324, p. 169-187.

Giona Bucci, M., Almond, P., Villamor, P., Ries, W., Smith, C., and Tuttle, M., 2017, When the earth blisters: exploring recurrent liquefaction features in the coastal system of Christchurch, New Zealand: Terra Nova, v. 29, p. 162-172.

Green, A. R., Maurer, B. W., Brendon, B., Wotherspoon, L., and Cubrinovski, M., 2013, Implications from liquefaction observations in New Zealand for interpreting paleoliquefaction data in the central eastern united states (CEUS): U.S. Geological Society Final Technical Report, p. 97.

Haberlah, D., and Mctainsh, G. H., 2011, Quantifying particle aggregation in sediments: Sedimentology, v. 58, no. 5, p. 1208-1216.

Hancox, G. T., Archibald, G. C., Cousins, W. J., Perrin, N. D., and Misra, S., 2013, Reconnaissance report on liquefaction effects and landslides caused by the M_L 6.5 Cook strait earthquake of 21 July 2013, New Zealand: GNS Science.

Haslett, S. K., 2009, Coastal System Second Edition, University of Wales Press, Taylor & Francis.

Hastie, T., Tibshirani, R., and Friedman, J., 2009 The elements of statistical learning. Data mining, Inferences, and Prediction, Stanford, California, Springer-Verlag, Second edition

Hayati, H., Andrus, R., D., Gassman, S., L., Hasek, M., Camp, W. M., and Talwani, P. e., 2008, 4th Geotechnical Earthquake Engineering and Soil Dynamics American Society of Civil Engineers Geotechnical Special publication, v. 181, p. 1-32.

Herzer, R. H., 1981, Structure of the Canterbury Plains, New Zealand from gravity modelling: Geophysics Division, Department of Scientific and Industrial Research.

Hewitt, A. E., 2010, New Zealand Soil Classification Lincoln, New Zealand, Manaaki Whenua Press 2010.

Hodge, M., 2016, Comparison of liquefaction data: An application of a logistic normal distribution in the simplex sample space. , International Conference on Statistical Distributions and Applications,: Niagara Falls, Canada.

Hogg, A. G., Hua, Q., Blackwell, P. G., Niu, M., Buck, C. E., Guilderson, T. P., Heaton, T. J., Palmer, J. G., Reimer, P. J., Reimer, R. W., Turney, C. S. M., and Zimmerman, S. R. H., 2013, SHCaol 13 Southern Hemisphere Calibraton 0-50,000 years cal BP: Radiocarbon, v. 55 no. 4, p. 1889-1903.

Holzer, T. L., Noce, T. E., and Bennett, M. J., 2010, Liquefaction Probability Curves for Surficial Geologic Deposits: Environmental & Engineering Geoscience, v. XVII, no. 1, p. 1-21.

Holzer, T. L. c., 1998, The Loma Prieta, California, Earthquake of October 17, 1989-Liquefaction: United States Geological Survey.

Hughes, M. W., Quigley, M. C., Van Ballegooy, S., Deam, B. L., Bradley, B. A., Hart, D. E., and Measures, R., 2015, The sinking city: Earthquakes increase flood hazard in Christchurch, New Zealand: GSA Today, v. 25, no. 3-4.

Idriss, I. M., and Boulanger, R. W., Semi-Empirical procedures for evaluating liquefaction potential during earthquakes, *in* Proceedings 11th International Conference Soil Dynamics and earthquake engineering Berkeley, CA, 2004, Volume 1, p. 32-46.

-, 2006, Semi-empirical procedures for evaluating liquefaction potential during earthquakes: Soil Dynamics and Earthquake Engineering, v. 26, p. 115-130.

Idriss, I. M., and Boulanger, R. W., 2008, Soil Liquefaction during Earthquakes, Oakland, CA, Earthquake Engineering Research Institute.

Iwasaki, T., Tatsouka, F., Tokida, K., and Yasuda, S., A practical method for assessing soil liquefaction potential based on case studies at various sites, Japan., *in* Proceedings 2nd international conference on Microzonation, San Francisco CA, 1978, p. 885 -896.

Johnston, J. A., 1958, Recent climate changes in South Island, New Zealand, a geographic analysis [PhD: University of Canterbury.

Kaiser, A., Beavan, J., Beetham, D., Benites, R., Celentano, A., Collett, D., Cousins, J., Cubrinovski, M., Dellow, G., Denys, P., Fielding, E., Fry, B., Gerstenberger, M., Holden, C., Massey, C., Motagh, M., McVerry, G., Ristau, J., Stirling, M., Thomas, J., Uma, S., and Zhao, J., 2012, The Mw 6.2

Christchurch earthquake of February 2011: preliminary report.: New Zealand Journal of Geology and Geophysics., v. 55, no. 1.

Kaiser, A. E., Holden, C., Hamling, I. J., Hreinsdottir, S., Horspool, N. A., Massey, C. I., Villamor, P., Rhoades, D. A., Fry, B., D'Anastasio, E., Benites, R. A., Christophersen, A., Ristau, J., Ries, W., Goded, T., Archibald, G. C., Little, C., Bannister, S. C., Ma, Q., Denys, P., Pearson, C., Giona-Bucci, M., Almond, P., Van Ballegooy, S., and Wallace, S., The 2016 Valentine's Day Mw 5.7 Christchurch earthquake : preliminary report. paper no. O-20 *in* Proceedings Reducing risk raising resilience New Zealand Society for Earthquake Engineering Technical Conference Christchurch, 1-3 April 2016 2016, New Zealand Society for Earthquake Engineering.

Kirk, R. M., 1987, Dynamics and management of sand beaches in southern Pegasus Bay: Christchurch City Council

Kleyburg, M. A., Moon, V. G., Lowe, D. J., and Nelson, C. S., Paleoliquefaction in Late Pleistocene alluvial sediments in Hauraki and Hamilton basins, and implications for paleoseismicity, *in* Proceedings Proceedings of 12th Australia New Zealand Conference on Geomechanics (ANZ 2015), Wellington, 22-25 February 2015, New Zealand Geotechnical Society.

Koester, J. P., and Tsuchida, T., 1989, Earthquake induced liquefaction of fine-grained soils considerations from Japanese research: Department of the US Army, Corps of Engineers

Lafrenz, M. D., Bean, R. A., and Uthman, D., 2013, Soil ripening following dam removal: Physical Geography, v. 34, no. 2, p. 124-135.

Langridge, R. M., and Berryman, K. R., 2005, Morphology and slip rate of the Hurunui section of the Hope Fault, South Island, New Zealand.: New Zealand Journal of Geology and Geophysics, v. 48, p. 43-58.

LCR, 2010, Soil map for the Upper Plains and Downs of Canterbury.

-, 2016, S-map- a new soil spatial information sistem for New Zealand (current- September 2016): Landcare Research.

Lee, J. M., and Begg, J. G., 2000, Geology of the Wairarapa area. QMAP Wairarapa. Institute of Geological and Nuclear Sciences 1:250 000 geological map 11.1. sheet+66p. Lower Hutt, New Zealand.

Lee, S.-J., Komatitsch, D., Huang, B.-S., and Tromp, J., 2009, Effects of Topography on Seismic-Wave Propagation: An Example from Northern Taiwan: Bulletin of Seismological Society of America, v. 99, no. 1, p. 314-325.

Lewis, M. R., Arango, I., Kimball, J. K., and Ross, T. E., 1999, Liquefaction resistance of old sand deposits: Proceeding of the 11th Panamerican Conference on Soil Mechanics and geotechnical engineering, Foz to Iguassu, Brazil, p. 821-829.

Lewis, M. R., McHood, M. D., and Arango, I., 2004, Liquefaction evaluations at the Savannah River Site, A case History: Proc., Fifth Int, Conf. on Case Histories in Geotechnical engineering, New York, NY.

Leys, J., McTainish, G., Koen, T., Mooney, B., and Strong, C., 2005, Testing a statistical curve-fitting procedure for quantifying sediment populations within multi-modal particle-size distributions: Earth Surface Processes and Landforms, v. 30, p. 579-590.

LINZ, 2011, Christchurch Post-Earthquake Aerial Photos, Flown on 24 February 2011 by NZ Aerial Mapping for the Christchurch Response Centre (CRC).

Lui, L., and Li, Y., 2001, Identification of liquefaction and deformation features using ground penetrating radar in the New Madrid seismic zone, USA. : Journal of Applied Geophysics, v. 47, p. 199-215.

MacLeod, G., 2008, Thin Section & Micromorphology at the University of Stirling: Stirling University.

Martel, S., 2016, Effects of small-amplitude periodic topography on combined stresses due to gravity and tectonics: International Journal of Rock Mechanics and Mining Sciences, v. 89, p. 1-13.

Mc Lauchlan, D., 2012, Geotechnical Assessment report, 131 Hudson Road, Lincoln: Golder Associates.

Molloy, L., 1989, Soils in the New Zealand Landscape the living mantle, Mallison Rendel.

Monaco, P., Santucci de Magistris, F., Grasso, S., Marchetti, S., Maugeri, M., and Totani, G., 2011, Analysis of the liqueafction phenomena in the village of Vittorino (L'Aquila): Bulletting of Earthquake Engineering, v. 9, no. 1, p. 231-261.

Moon, S., Perron, J. T., Martel, S., Holbook, W. S., and Clair, J. S., 2017, A model of three-dimensional topographic stresses with implications for bedrock fractures, surface processes and landscape evolution Journal of Geophysical Research, v. 122, no. 4, p. 823-846.

Moran, C. J., McBratney, A. B., Ringrose-Voase, A. J., and Chartres, C. J., 1989, A method for dehydration and impregnation of clay soil: European Journal of Soil Science, v. 40, no. 3, p. 569-575.

Moretti, M., 2000, Soft-sediment deformation structures interpreted as seismites in middle-late Pleistocene aeolian deposits (Apulian foreland, southern Italy): Sedimentary Geology, v. 135, no. 1-4, p. 167-179.

Moretti, M., Alfaro, P., Caselles, O., and Canas, J. A., 1999, Modelling seismites with a digital shaking table: Tectonophysics, v. 304, p. 369-383.

Moretti, M., Pieri, P., and Tropeano, M., 2002, Late-Pleistocene soft-sediment deformation structures interpreted as seismites in paralic deposits in the city of Bari (Apulian foreland, Southern Italy), *in* Ettensohn, F. R., N; Brett, CE, ed., Volume 359: Boulder, Colorado, Geological Society of America Special Papers, p. 75-85.

Moretti, M., and Sabato, L., 2007, Recognition of trigger mechanisms for soft-sediment deformation in the Pleistocene lacustrine deposits of the Sand-Arcangelo Basin (Southern Italy): Seismic shock vs overloading: Sedimentary Geology, v. 196, p. 31-45.

Murphy, C. P., 1986, Thin section preparation of soils and sediments The University of Michigan.

Nichols, G., 2009, Sedimentology and stratigraphy, Wyley-Blackwell, Second edition, 432 p.

NIWA, 2015, NIWA Core funded project Climate Present and Past CAOA1501 (500 cell size).

Nobes, D. C., Wilson, M. T., Cockcroft, M., Almond, P., and Whitman, Z., 2012, Agricultural ground penetrating radar response to deep cultivation across a fault scarp after the 4 September 2010 Darfield earthquake, Canterbury, New Zealand.: Proceeding of the 14th International Conference on Ground Penetration Radar v. June 4-8, Shangai.

Obermeier, S. F., 1996, Use of liquefaction-induced features for paleoseismic analysis- An overview of how seismic liquefaction feature can be distinguished from other feature and how their regional distribution and properties of source sediment can be used to infer the location and strength of Holocene paleo-earthquakes.: Engineering Geology v. 44, p. 1-76.

Obermeier, S. F., 1998, Liqueafaction evidence for strong earthquakes of Holocene and latest Pleistocene ages in the states of Indiana and Illinois, USA: Engineering Geology, v. 50, p. 227-254.

Obermeier, S. F., Pond, E. C., Olson, S. M., and Green, R. A., 2002, Paleoliquefaction studies in continental settings: Geological Society of America Special Paper 359, v. 359, p. 13-27.

Obermeier, S. F., Scott M. O, and Green, R. A., 2005, Field occurrences of liquefaction-induced features:a primer for engineering geologic analysis of paleoseismic shaking: Engineering Geology, v. 76, p. 209-234.

Oborn, L. E., and Suggate, R. P., 1959, Sheet 21. Christchurch Geological map of New Zealand 1:250 000. : Department of scientific and Industrial Research.

Olson, S. M., Green, R. A., and Obermeier, S. F., 2005a, Field occurrences of liquefaction induced features: a primer for engineering and geologic analysis of paleoseismic shaking: Engineering Geology v. 76, p. 209-234.

Olson, S. M., Russell, A. G., and Obermeier, S. F., 2005b, Revised Magnitude-bound Relation for the Wabash Valley Seismic Zone of the Central United States: Seismological research letters, v. 76, no. 6.

Orense, R. P., Kiyota, T., Yamada, S., Cubrinovski, M., Hosono, Y., Okamura, M., and Yasuda, S., 2011, Comparison of liquefaction features observed during the 2010 and 2011 Canterbury Earthquakes: Seismological research letters, v. 82, p. 905 - 918.

Palmer, A. P., Lee, J. A., Kemp, R. A., and Carr, S. J., 2008, Revised laboratory procedures for the preparation of thin sections from unconsolidated material. : University of London.

Papadopoulos, G. A., and Lefkopoulos, G., 1993, Magnitude distance relations for liquefaction in soil from earthquakes: Bullettin of the Seismological Society of America, v. 83, no. 3, p. 925-938.

Papathanassiou, G., Pavlides, S., Christaras, B., and Pitilakis, K., 2005, Liquefaction case histories and empirical relations of earthquake magnitude versus distance from the broader aegean region: Journal of Geodynamics, v. 40, p. 257-278.

Persaud, M., Villamor, P., Berryman, K. R., Ries, W., Cousins, J., Litchfield, N., and Alloway, B. V., 2016, The Kerepehi Fault, Hauraki Rift, North Island, New Zealand: active fault characterisation and hazard: New Zealand Journal of Geology and Geophysics, v. 59, no. 1, p. 117-135.

Pettinga, J. R., Yetton, M. D., Van Dissen, R. J., and Downes, G., 2001, Earthquake source identification and characterisation for the Canterbury Region, South Island, New Zealand: Bulletin of the New Zealand Society for Earthquake Engineering, v. 34, no. 4.

Phillips, E., 2006, Micromorphology of a debris flow deposit: evidence of basal shearing, hydrofracturing, liquefaction and rotational deformation during emplacement: Quaternary Science Reviews, v. 25, p. 720-738.

Phillips, E., Lipka, E., and van der Meer, J. J. M., 2013, Micromorphological evidence of liquefaction injection and sedinment deposition during basal sliding of glaciers: Quaternary Science Reviews, v. 81, p. 114-137.

Pirrotta, C., Barbano, M. S., Guarnieri, P., and Gerardi, F., 2007, A new dataset and empirical relationshipts between magnitude/ intensity and epicentral distance for liquefaction in central-eastern Dicitly: Annals of Geophysics, v. 50, no. 6, p. 763-774.

Pons, L. J., and Zonneveld, I. S., 1965, Soil ripening and soil classification: initial soil formation of alluvial deposits with a classification of the resulting soils: International Institute for Land Reclamation and Improvement

Powers, M. C., 1953, A new roundness scale for sedimenrary particles: Journal of Sedimentary Research, v. 23, no. 2, p. 117-119.

Quigley, M., Van Dissen, R., Litchfield, N., Villamor, P., Duffy, B., Barrell, D., Furlong, K., Stahl, T., Bilderback, E., and Noble, D., 2012, Surface rupture during the 2010 Mw 7.1 Darfield (Canterbury) earthquake: implications for fault rupture dynamics and seismic-hazard analysis: Geology, , v. 40(1), p. 55-58.

Quigley, M. C., Bastin, S., and Bradley, B. A., 2013, Recurrent liquefaction in Christchurch, New Zealand, during the Canterbury earthquake sequence Geology, v. 41 No 4, p. 419-422.

Ramsey, B., 2008, Depositional models for chronological research: Quaternary Science Rev., v. 27, p. 42-60.

-, 2009, Bayesian analysis of radiocarbon dates: Radiocarbon, v. 51, p. 337-360.

Reed, J. J., 1951, Marine sediments near Summer, Canterbury, New Zealand: New Zealand Journal of Science and Technology, v. B 33, no. 129-137.

Reid, C. M., Thompson, N. K., Urvine, J. R. M., and Laird, T. E., 2012, Sand Volcanoes in the Avon-Heathcote Estuary produced by the 2010-2011 Christchurch Earthquakes: implications for geological preservation and expression, New Zealand: Journal of Geology and Geophysics, v. 55, no. 3, p. 249-254.

Ricci-Lucchi, F., 1980, Sedimentologia Bologna, Italy, CLUEB, 1980 548 p.

Robertson, P. K., 1990, Soil classification using the cone penetration test: Canadian Geotechnical Journal v. 27, p. 151-158.

-, Evaluating Soil Liquefaction and Post-Earthquake DEformations using the CPT, Geotechnical and Geophysical Site Characterization, *in* Proceedings ISC-2, Porto, Rotterdam, 2004, Millpress.

Robertson, P. K., Campanella, R. G., and Gillespie, D., 1986, Seismic CPT to measure in situ shear Wave velocity: Journal of Geotechnical Engineering, v. 112, no. 8, p. 791-803.

Robertson, P. K., and Wride, C. E., 1998, Evaluating cyclic liquefaction potential using the cone penetration test: Canadian Geotechnical Journal, v. 35, no. 3, p. 442-159.

Robertson, P. K., Wride, C. E., List, B. R., Atukorala, U., Biggar, K. W., Byrne, P. M., Campanell, R. G., Cathro, D. C., Chan, D. H., Czajewski, K., Finn, W. D. L., Gu, W. H., Hammamji, Y., Hofmann, B. A., Howie, J. A., Hughes, J., Imrie, A. S., and Konrad, J.-M. K., A.; Lw, T.; Lord, E. R. F.; Monahan, P.A.; Morgenstern, N. R.; Phillips, R.; Piche, R.; Plewes, H. D.; Scott, D.; Sego, D.C.; Sobkowics, J.; Stewart, R. A.; Watts, B. D.; Woeller, D. J.; Youd, T. L.; Zavodni, Z., 2000, The Canlex project: summary and conclusions: Canadian Geotechnical Journal, v. 37, p. 563-591.

Rodriguez-Pascua, M. A., Silva, P. G., Perez-Lopez, R., Giner-Robles, J. L., Martin-Gonzalez, F., and Del Moral, B., 2015, Poligenetic sand volcanoes: On the features of liquefaction processes generated by a single event (2012 Emilia Romagna 5.9 M_w e=earthquake: Quaternary International, v. 357, p. 329-335.

Rydelek, P. A., and Tuttle, M., 2004, Explosive craters and soil liquefaction. Curious dry craters formed in the aftermath of a disastrous earthquake are explained. Brief communiations: Nature, v. 427.

Santucci de Magistris, F., Lanzano, G., Forte, G., and Fabbrocino, G., 2013, A database for PGA threshold in liquefaction occurrence: Soil Dynamics and Earthquake Engineering, v. 54, no. 0, p. 17-19.

Saucier, R. T., 1989, Evidence for Episodic Sand Blow Activity during the 1811-12 New Madrid (Missouri) Earthquake Series: Geology, v. 17, p. 103-106.

Schaetzl, R. J., and Thompson, M. L., 2015, Soils, Genesis and Geomorphology, University of Cambridge, Cambridge University Press.

Schoeneberger, P. J., Wysocki, D. A., Benham, E. C., and Staff, a. S. S., 2012, Field book for describing and sampling soils, Version 3.0 Lincoln, Nebraska, U.S.A., National Soil Survey Centre, Natural Resources Conservation Service, U.S. Department of Agriculture.

Seed, H. B., 1979, Soil liquefaction and cyclic mobility evaluation for level ground during earthquakes,: Journal of the Geotechnical Eng. Div., v. 105, no. 2, p. 201-255.

Seed, H. B., and Idriss, I. M., 1971, Simplified procedure for evaluating soil liquefaction potential: Journal of the Soil mechanics and foundations division (American Society of Civil Engineers), v. 97 (SM9) p. 1249-1273.

Seed, H. B., and Idriss, I. M., 1982, Ground motions and soil liquefaction during earthquakes. Earthquake Engineering Research Institute University of California Berkeley, 134 p. .

Seed, H. B., and Peacock, W. H., 1971, Test Procedures for measuring soil liquefaction characteristics: Journal of the soil mechanics and foundations division ASCE, v. 97, p. 1099-1119.

Seilacher, A., 1969, Fault-graded beds interpreded as seismites: Sedimentology, v. 13, p. 155-159.

Shulmeister, J., and Kirk, S. M., 1993, Evolution of a mixed sand and gravel barrier system in North Cantebury, New Zealand, during Holocene sea level rise and still-sand: Sedimentary Geology, v. 87, p. 215-235.

-, 1996, Holocene history and thermoluminescence based chronology of coastal dune ridges near Leithfield, North Canterbury, New Zealand: New Zealand Journal of Geology and Geophysics, v. 39, no. 1, p. 25-32.

-, 1997, Holocene fluvial- coastal interactions on a mixed sand and sand and gravel beach system, North Canterbury, New Zealand: Catena, v. 30, p. 337-355.

Sims, J. D., and Garvin, C. D., 1995, Recurrent liquefaction induced by the 1989 Loma Prieta earthquake and 1990 and 1991 aftershocks: Implications for paleoseismicity studies: Bullettin of the Seismological Society of America v. 85, p. 51-65.

Soons, J. M., and Selby, M. J., 1985 Landforms of New Zealand Auckland, New Zealand, Longman Paul.

Stark, T. D., and Olson, S. M., 1995, Liquefaction resistance using CPT and field case histories: Journal of Geotechnical Engineering ASCE, v. 121, no. 12, p. 856-869.

Stirling, M., Gerstenberg, M., Litchfield, N., McVerry, G., Smith, W., Pettinga, J., and Barnes, P., 2008, Seismic Hazard of the Canterbury region, New Zealand: new earthquake source moderl and methodology: Bulletting of the New Zealand Society for Earthquake Engineering, v. 41, p. 56-67.

Stirling, M., Yetton, M., Pettinga, J., Berryman, K. R., and Downes, G. L., 1999, Probabilistic seismic hazard assessment and earthquake scenarios for the Canterbury region, and historic earthquakes in Christchurh. Stage 1 (Part B) of Canterbury Regional Council's earthquake hazard and risk assessment study: GNS Report 1999/53.

Stirling, M. W., Pettinga, J., Berryman, K. R., and Yetton, M., 2001, Probabilisti seismic hazard assessment of the Canterbury region, New Zealand: Bullettin of the New Zealand Society for Earthquake Engineering, v. 34, p. 318-334.

Stoops, G., 1998, Key to ISSS: Natuurwet. Tijdschr., v. 78, p. 193-203.

Stoops, G., and Verpraskas, J., 2003, Guidelines for Analysis and Description of Soil and Regolith Thin Sections, Madison, Wisconsin, Soil Science Society of America, 184 p.:

Stuiver, M., Reimer, P. J., and Reimer, R. W., 2017, CALIB 7.1 Radiocarbon Calibration at http://calib.org, accessed 2017-4-7, *in* Database, M. R. C., ed.

Suggate, R. P., 1958, Late Quaternary Deposits of the Christchurch metropolitan area, New Zealand: New Zealand Journal of Geology and Geophysics, v. 1, p. 103-122.

-, 1963, The fan surfaces of the central Canterbury Plain: New Zealand Journal of Geology and Geophysics, v. 6, no. 2, p. 281-287.

Suggate, R. P., 1965, Late Pleistocene geology of the northern part of the South Island, New Zealand.: New Zealand Geological Survey bullettin, v. 77.

Suggate, R. P., 1990, Late Pliocene and Quaternary glaciations of New Zelanad: Quaternary Science Reviews, v. 9, p. 175-197.

Sumfleth, K., and Duttmann, R., 2008, Prediction of soil property distribution in paddy soil landscapes using terrain data and satellite information as indicators: Ecological indicators, v. 8, no. 5, p. 485-501.

Suzuki, Y., Tokimatsu, K., Koyamanda, K., Taya, Y., and Kubota, Y., 1995, Field correlation of soil liquefaction based on CPT data: Proceeding Int. Symposium on Cone Penetration Testing v. 2, p. 583-588.

Talebi, A., Troch, P. A., and Uijlenhoet, R., 2008, A steady-state analytical slope stability model for complex hillslopes: Hydrological Processes, v. 22, no. 4, p. 546-553.

Talwani, P., Amick, D. C., and Schaeffer, W. T., 1999, Paleoliquefaction studies in the South Caroline Coastal Plain: Division of Engineering Technology, Office of Nuclear Regulatory Research, U.S. Nuclear Regulatory Commission.

Talwani, P., and Schaeffer, W. T., 2001, Recurrence rates of large earthquakes in the South Carolina Coastal Plain based on paleoliquefaction data: Journal of Geophysical Research, v. 106, no. (B4), p. 6621-6642.

Terzaghi, K., Peck, R. B., and Mesri, G., 1996, Soil Mechanics in Engineering Practice, Wiley-Interscience publication, Canada, John Wiley & Sons.

Tinsley, J. C., Egan, J. A., Kayen, R. E., Bennet, M. J., Kropp, A., and Holzer, T. L., 1998, Appendix: Maps and descriptions of liquefaction and associated effects in Holzer, T.L.; ed.; The Loma Prieta, California, Earthquake of October 17 1989.

Tonkin and Taylor, L., 2015, Geotechnical information on horizontal land movement due to the Canterbury Earthquake Sequence: Tonkin & Taylor Environmental and Engineering Consultants.

Tonkin and Taylor Ltd, 2014, North East Industrial Zone Liquefaction Assessment-interpretive Geotechnical Report & Desk Top Ground Contamination Assessment: Tonkin and Taylor Environmental and Engineering Consultants.

Townsend, D., Lee, J., Strong, D., Jongesen, R., Smith Lyttle, B., Ashraf, S., Rosser, B., Perring, N., Cubrinovski, M., Taylor, M., Hughes, M., Wilson, T., Almond, P., Jacka, M., McCahon, I., and

Christensen, S., 2016, Mapping surface liquefaction caused by the September 2010 and February 2011 Canterbury earthquakes- a digital dataset: New Zealand Journal of Geology and Geophysics, v. 59, no. 4, p. 496-513.

Townsend, D. B., Vonk, A., and Kamp, P. J. J., 2008, Geology of the Taranaki area. 1:250 000 geological map 7.1 sheet +77p.: Institute of Geological and Nuclear Sciences (GNS).

Tsuchida, H., Prediction and Countermeasure Against the Liquefaction in Sand Deposits, *in* Proceedings Seminar of the Port and Harbor Research Institute Yokosuka, Japan, 1970, Volume 3, p. 1-3.

Tuttle, M., 2001a, The use of liquefaction features in paleoseismology : lessons learned in the New Madrid Seismic Zone, central United States: Journal of Seismology v. 5, p. 361-380.

Tuttle, M., and Barstow, N., 1996, Liquefaction-related ground failure: a case study in the New Madrid Seismic Zone, Central United States: Bullettin of the Seismological Society of America, v. 86 No3, p. 636-645.

Tuttle, M. P., 1999, Late Holocene earthquakes and their implications for earthquake potential of the New Madrid seismic zone, central United States [PhD: University of Maryland, 247 p.

-, 2001b, Towards a paleoearthquake chronology for the New Madrid seismic Zone: Collaborative research, M. Tuttle & Associates and Central Region Geologic Hazards Team, USGS.

-, 2010, Search for and study of sand blows at distant sites resulting from prehistoric and historic New Madrid earthquakes. Collaborative Research. M. TUttle & Associates and Central REgion Hazards Team: U.S Geological Survey.

Tuttle, M. P., Al-Shukri, and Mahdi, H., 2006, Very large Earthquake centered southwest of the New Madrid Seismic Zone 5000-7000 years ago: Seismological research letters v. 77 no. Numner 6.

Tuttle, M. P., and Atkinson, G. M., 2010, Localization of large earthquakes in the Charlevoix seismic zone, Quebec, Canada during the past 10,000 years. : Seismological Research Letters, v. 81, no. (1), p. 18-25.

Tuttle, M. P., Collier, J., Wolf, L. W., and Lafferty, R. H., 1999, New evidence for a large earthquake in the New Madrid seismic zone between A.D. 1400 and 1670: Geology, v. 27, no. (9), p. 771-774.

Tuttle, M. P., and Hartleb, R., 2012a, Appendix E, Central and Eastern U.S. paleoliquefaction database: Uncertainties associated with paleoliquefaction data, and guidance for seismic source characterization. , The Central and Eastern U.S. Seismic Source Characterization for Nuclear Facilities, Technical Report: Palo Alto, California, U.S. Department of Energy and U.S. Nuclear Regulatory Commission, p. 135 p. plus database.

Tuttle, M. P., and Hartleb, R., 2012b, Appendix E: Central and Eastern US paleoliquefaction database, uncertainties associated with paleoliquefaction data, and guidance for seismic source characterization, in the Central and Eastern U.S. Seismic Source Characterization for Nuclear Facilities: DOE, and U.S. NRC.

Tuttle, M. P., Hengesh, J., and Lettis, W., 2002a, Liquefaction induced by the 2001 Bhuj earthquake in India: Earthquake Spectra, v. 18, p. 79-99.

Tuttle, M. P., Schweig, E., Campbell, J., Thomas, P. M., Sims, J. D., and Lafferty, R. H., 2005, Evidence for New Madrid earthquakes in AD 300 and 2350 BC: Seismological Research Letters, v. 76, no. (4), p. 489-501.

Tuttle, M. P., Schweig, E. S., Sims, J. D., Lafferty, R. H., Wolf, L. W., and Haynes, M. L., 2002b, The earthquake potential of the New Madrid Seismic Zone: Bullettin of the Seismological Society of America, v. 92 no. 6, p. 2080-2089.

Tuttle, M. P., Villamor, P., and Almond, P., 2012, Paleoliquefaction lessons learned from the 2010-2011 Canterbury, New Zealand, earthquakes,: Geological Society of America, Abstracts with Programs, v. 42, no. 5, p. p 460.

Tuttle, M. P., Villamor, P., Almond, P., Bastin, S., Giona Bucci, M., Langdridge, R., Clark, K., and Hardwick, C., 2017 Liquefaction induced by the 2010-2011 Canterbury, New Zealand,

Eartquake Sequence and Lessons Learned for the Study of Paleoliquefaction features: Seismological Research Letters, v. 88, no. 4.

Tuttle, M. P., Wolf, L. W., Mayne, P. W., Dyer-Williams, K., and Lafferty, R. H., 2017, Guidance document: Conducting paleoliquefaction studies for earthquake source characterization: U.S. Nuclear Regulatory Agency (NUREG).

van Ballegooy, S., Malan, P., Lacrosse, V., Jacka, M. E., Cubrinovski, M., Bray, J. D., O.Rourke, T. D., Crawford, S. A., and Cowan, H., 2014, Assessment of liquefaction-induced land damage for residential Christchurch: Earthquake Spectra, v. 30, no. 1, p. 31-55.

van Bellegooy, S., Cox, S. C., Agnihotri, R., Reynolds, T., Thurlow, C., Rutter, H. K., Scott, D. M., Begg, J. G., and McCahon, I., 2014, Median water table elevation in Christchurch and surroundings area after the 4 September 2010 Darfield Earthquake (version 2): GNS Science consultancy report 2013/1.

Van der Meer, J. J. M., Kjaer, K. H., Kruger, J., Rabassa, J., and Kilfeather, A. A., 2009, Under pressure: clastic dykes in glacial settings: Quaternary Science Reviews, v. 28, no. 2009, p. 708-720.

Van der Meer, J. J. M., and Menzies, J., 2011, The micromoprhology of unconsolidates sediments: Sedimentary Geology, v. 238, p. 213-232.

Van Dissen, R., Barrel, D., Licthfield, N., Villamor, P., and Quigley, M., Surface rupture displacement on the Greendale Fault during the Mw7.1 Darfield (Canterbury) earthquake, New Zealand, and its impact on man-made structures., *in* Proceedings Ninths Pacific Conference on Earthquake Engineering, Auckland, New Zealand, 14-16 April 2011.

Van Dissen, R., McSaveney, M., Townsend, D., Hancox, G., Little, T. A., Ries, W., Perrin, N., Archibald, G., Dellow, G., Massey, C., and Misra, S., 2013, Landslides and liquefaction generated by the Cook Strait and Lake Grassmere earthquakes: a reconnaissance report: Bullettin of the New Zealand Society for Earthquake Engineering, v. 46, no. 4.

Vanneste, K., Mees, F., and Verbeeck, K., 2008, Thin-Section analysis as a tool to aid identification of paleoearthquakes on the "slow", active Geleen Fault, Roer Valley Graben: Technophysics, v. 453, p. 94-109.

Vermeulen, J., Grotenhuis, J. T. C., Joziasse, J., and Rulkens, W. H., 2003, Ripening of a clayey dredged sediments during temporary upland disposal, a bioremediation technique.: Journal of Soils and Sediments, v. 3, no. 1, p. 49-59.

Villamor, P., Almond, P., Tuttle, M. P., Giona Bucci, M., Langridge, R. M., Clark, K., Ries, W., Bastin, S. H., Eger, A., Vandergoes, M., Quigley, M. C., Barker, P., Martin, F., and Howarth, J., 2016, Liquefaction features produced by the 2010-2011 Canterbury earthquake sequence in southwest Christchurch, New Zealand and preliminary assessment of paleoliquefaction features: Bulletin of Seismological Society of America v. 106, no. 4.

Villamor, P., Giona Bucci, M., Almond, P., Tuttle, M., Langrindge, R., Clark, K., Ries, W., Vandergoes, M., Barker, P., Martin, F., Bastin, S., Watson, M., Howarth, J., and Quigley, M., 2014, Exploring Methods to assess paleoliquefaction in the Canterbury area: GNS Science consultancy report 2014/183.

Villamor, P., Litchfield, N., Barrell, D., Van Dissen, R., Hornblow, S., Quigly, M., Levick, S., Ries, W., Duffy, B., Begg, J., Townsend, D., Stahl, T., Bilderback, E., Noble, D., Furlong, K., and Grant, H., 2012, Map of the 2010 Greendale Fault surface rupture, Canterbury, New Zealand: application to land use planning: New Zealand Journal of Geology and Gephysics, v. 55, no. 3, p. 223-230.

Wang, C., 2007, Liquefaction beyond the Near Field: Seismological research letters, v. 78, no. 5, p. 512-517.

Wang, C., and Manga, M., 2010, Hydrologic responses to earthquakes and a general metric: Geofluids, v. 10, p. 206-2016.

Webb, T. H., 2008, "Soils", in The Natural History of Canterbury: Christchurch, New Zealand, Canterbury University Press, p. 923 p.

Witten, I., H., Frrank, E., Hall, M., A., and Pal, C. J., 2016, Data mining: practical machine learning tools and techniques. Third edition, Waikato University, New Zealand, Morgan Kaufmann Publisher, Elsevier, 654 p.:

Wotherspoon, M. L., Pender, M. J., and Orense, P. R., 2012, Relationship between observed liquefaction at Kaiapoi following the 2010 Darfield earthquake and former channels of the Waimakariri River: Engineering Geology, v. 125, p. 45-55.

Yasuda, S., Harada, K., Ishiwaka, K., and Kanemaru, Y., 2012, Characteristics of liquefaction in Tokyo Bay area by the 2011 Great East Japan Earthquake: Soils and Foundations-Tokyo, v. 52, no. 5, p. 793-810.

Youd, T. L., 2001, Liquefaction Resistance of soils: summary report from the 1996 NCEER and 1998 NCEER/ NSF Workshop on Evaluation of Liquefaction Resistance of Soils: Journal of Geotechnical and Geoenvironmental Engineering, v. 127, p. 817-833.

Youd, T. L., and Hoose, S. N., 1977, Proceedings of the Sixth World Conference on Earthquake Engineering: Indian Society of Earthquake Technology, v. III, p. 2189-2194.

Youd, T. L., and Idriss, I. M., 1997, Proceeding, NCEER Worshop on Evaluation of liquefaction resistance of soils: Natural Centre for Earthquake engineering Reearch State University of New York at Buffalo.

Youd, T. L., and Perkins, D. M., 1978, Mapping liquefaction-induced ground failure potential: Journal of geotechnical engineering division, v. 104, no. 4, p. 433-446.

Ziony, I. J. c., 1985, Evaluating Earthquake Hazards in the Los Angeles Region- An Earth-Science Perspective